Fall 2022

Evaluating the Impact of Submarine Groundwater Discharge on Nutrients and Trace Elements in Coastal Systems: The Examples of the Tuckean Swamp (Australia) and the Mississippi Sound (USA)

Amy Moody

EVALUATING THE IMPACT OF SUBMARINE GROUNDWATER DISCHARGE ON NUTRIENTS AND TRACE ELEMENTS IN COASTAL SYSTEMS: THE EXAMPLES OF THE TUCKEAN SWAMP (AUSTRALIA) AND THE MISSISSIPPI SOUND (USA)

by

Amy A. Moody

A Dissertation
Submitted to the Graduate School,
the College of Arts and Sciences
and the School of Ocean Science and Engineering
at The University of Southern Mississippi
in Partial Fulfillment of the Requirements
for the Degree of Doctor of Philosophy

Approved by:

Dr. Alan Shiller, Committee Chair
Dr. Troy Pierce
Dr. Natasha Dimova
Dr. Christopher Hayes
Dr. Davin Wallace
Dr. Stephan Howden

December 2022

Published by the Graduate School

ABSTRACT

Submarine groundwater discharge (SGD) is the advective flow of both fresh terrestrial groundwater and recirculating seawater through aquifer sediments, which is released into the coastal ocean. In this dissertation, I evaluated the impact of SGD on the distributions and input of trace metals and nutrients. In the Tuckean Swamp, an estuary in Australia dominated by coastal acid sulfate soils, I determined the impact of groundwater on Ba and U during the flood season, when the local aquifer is flushed out after a rapid increase in water table elevation. For Ba and U, groundwater contributed up to 18 and 66 % to the total surface water flux out of the Tuckean Swamp, respectively. This can have implications for the use of these elements as proxies of river influences, upwelling, and sea surface temperature on a regional scale. In the Mississippi Sound, an estuary in the northern Gulf of Mexico, the main sources of nutrients and trace metals to the estuary are thought to be from inputs of local rivers, and the occasional input of the Mississippi River from the opening of the Bonnet Carré Spillway. Using radium and radon, I evaluated the magnitude and distribution of SGD in the Mississippi Sound. I found that submarine groundwater discharge can dominate nutrient fluxes when the river discharge is low, suggesting that during the drier months of the year, SGD was main source of dissolved nutrients to the Sound. This has implications for biological parameters, as the dissolved materials from SGD are often reducing with a high oxygen demand (i.e., ammonium and methane), and the groundwater in itself is often lacking oxygen. This has potential to cause bottom up hypoxia along the coastline and in the western Sound, where the majority of the SGD is infiltrating into the Sound. Trace element inputs to the Mississippi Sound were dominated by river inputs and were affected by the opening of the Bonnet

Carré Spillway. This work explores the importance of SGD versus river and surface runoff, and how all of these parameters combined can affect the water quality of coastal systems.

ACKNOWLEDGMENTS

I would like to thank my advisor, Dr. Alan Shiller for providing me the opportunity to conduct research at the University of Southern Mississippi, and for his mentorship throughout my PhD. I would also like to thank Dr. Troy Pierce for his guidance as my ORISE advisor, Dr. Isaac Santos for his support as my LOREX collaborator, and to Dr. Natasha Dimova, Dr. Christopher Hayes, Dr. Davin Wallace, and Dr. Stephan Howden for serving on my committee and providing much needed insight on this work.

The Shiller and Hayes lab groups and all those that volunteered also have my deepest gratitude for their help with the immense amount of field and lab work. A special thanks to Melissa Gilbert for her analytical help in the lab, as well as to all those that helped in the lab and field including Haley Spaid, Rachel Kriner, Sarah Raney, Neil Redmond, Allie Savoie, Sam Glasscock, Jessalyn Davis, Elora Pierce, Talon Washington, Dr. Laura Whitmore, Dr. Peng Ho, Dr. Shaily Rahman, Dr. Virginie Sanial, and to any who I missed with this list; thank you again. I owe many thanks to Captain Alex Almario, who worked alongside me for the much of this work; thank you for everything.

This research was supported in part by an appointment to the U.S. Environmental Protection Agency (EPA) Research Participation Program administered by the Oak Ridge Institute for Science and Education (ORISE) through an interagency agreement between the U.S. Department of Energy (DOE) and the U.S. Environmental Protection Agency. ORISE is managed by ORAU under DOE contract number DE-SC0014664. All opinions expressed in this dissertation are the author's and do not necessarily reflect the policies and views of US EPA, DOE, or ORAU/ORISE.

DEDICATION

For my friends and family; all your love and support has made this possible.

TABLE OF CONTENTS

LIST OF TABLES

LIST OF ILLUSTRATIONS

LIST OF ABBREVIATIONS

α	Solubility Coefficient of Radon at
…	Equilibrium
AR_{Snd}	Average $^{224}Ra/^{228}Ra$ Activity Ratio in Sound
…	Water
AR_{SGD}	Average $^{224}Ra/^{228}Ra$ Activity Ratio in
…	Submarine Groundwater Discharge
b	Wind Speed Coefficient
BCS	Bonnet Carré Spillway
CASS	Coastal Acid Sulfate Soils
C_{GW}	Constituent Concentration in Groundwater
CLAS	Coastal Lowland Aquifer System
CONCORDE	Consortium of Coastal-River Dominated
…	Ecosystems
CRDS	Cavity Ring-Down Spectroscopy
D	Depth in Meters
d-excess	Deviation from the Global Meteoric Water
…	Line
DI	Ultrapure Deionized Water
DIN	Dissolved Inorganic Nitrogen
DIP	Dissolved Inorganic Phosphorus
DIVA	Data-Interpolating Variational Analysis
DO	Dissolved Oxygen

DOC	Dissolved Organic Carbon
DON	Dissolved Organic Nitrogen
D_{Rn}	Diffusion Coefficient of Radon in Water
$dRn_{bound}/dSal_{bound}$	Slope of Radon vs Salinity at the Boundary
…	between Sound and Bight
DSi	Dissolved Silica
E	Evaporation
EDCF	Empirical Distribution Curve Function
EL-USB-TC	EasyLog Thermocouple Temperature Data
…	Logger
f_{FSGD}	Fresh Groundwater Fraction in Coastal
…	Aquifer
F_{SGD}	Water Flux from SGD
FSGD	Fresh Submarine Groundwater Discharge
f_{SGD}	Total SGD Fraction in Coastal Aquifer
f_{Sound}	Fraction of Sound Water in Coastal Aquifer
HAB	Harmful Algal Bloom
HAHCl	Hydroxylamine Hydrochloride
HCl	Hydrochloric Acid
HR-ICP-MS	High Resolution Inductively Coupled
…	Plasma Mass Spectrometer
ICP-MS	Inductively Coupled Mass Spectrometer
J_{dif}	Passive Diffusion of Tracer from Sediments

J_{off}	Input of Tracer from Offshore
J_{out}	Advection of Tracer Out of Sound
J_{riv}	Input of Tracer from Rivers
J_{SGD}	Input of Tracer from SGD
J_{λ}	Radioactive Decay of Tracer
k_{Rn}	Radon Gas Transfer Velocity
K-S Test	Kolmogorov–Smirnov Test
MEAS	Mississippi Embayment Aquifer System
MIS2	Marine Isotope Stage 2
n	Sediment Porosity
$O_{2\text{-}demand}$	Oxygen Demand for a Constituent
Obs_{conc}	Observed Concentration
ODV	Ocean Data View
P	Precipitation
PCA	Principal Component Analysis
PNEC	Predicted No Effect Concentration
Q_{off}	Water Flux into Sound from Bight
Q_{out}	Water Flux out of Control Volume
Q_{riv}	Water Flux into Sound from Rivers
Q_{SGD}	Total SGD Water Flux to Sound
RaDeCC	Radium Delayed Coincidence Counter
Ra_{dif}	Radium Diffusion Flux
Ra_{GW}	Radium Groundwater Endmember

Ra_I	Radium Inventory
Ra_{Iex}	Radium Excess Inventory
Ra_{pred}	Ra Activity Predicted from Salinity
Ra_{SGD}	Radium Flux from SGD
Ra_{SurfW}	Surface Water Activity of Ra
Rn_{air}	Radon in Air
Rn_{atm}	Atmospheric Evasion of Rn
Rn_{bound}	Radon Activity at Boundary between
…	Sound and Bight
Rn_{dif}	Diffusive Flux of Rn from Sediments
Rn_{ex}	Radon Excess After Parent Isotope
…	Correction
Rn_{GW}	Groundwater Activity of Rn
Rn_{out}	Advective Loss of Rn
Rn_{PW}	Radon Activity in Pore Water
Rn_{SGD}	Radon Flux from SGD
Rn_{Snd}	Average Radon Concentration in the Sound
Rn_w	Radon in Water
RQ	Risk Quotient
$RSGD$	Recirculated Submarine Groundwater
…	Discharge
Rn_λ	Radioactive Decay of Rn
$Salinity_{bound}$	Salinity at Boundary between Sound

…	and Bight
Sc_{CO2}	Schmidt Number for CO_2
Sc_{Rn}	Schmidt Number for Rn
SGD	Submarine Groundwater Discharge
SLB	St. Louis Bay
SPM	Suspended Particulate Matter
T	Temperature (°C) at the Water-Gas Interface
$T_{1/2}$	Half-Life
TN	Total Nitrogen
TP	Total Phosophorus
T_w	Apparent Age of Water
V_S	Volume of Sound
VSMOW	Vienna Standard Mean Ocean Water
λ_{Rn}	Radon Decay Rate
λ_{224}	Decay Constant ^{224}Ra
$(^{224}Ra/^{228}Ra)i$	Initial Activity of ^{224}Ra/^{228}Ra in
…	Groundwater
$(^{224}Ra/^{228}Ra)obs$	Observed Activity of ^{224}Ra/^{228}Ra in
…	Groundwater
$^{224}J_{Ra\text{-}dif}$	^{224}Ra Sediment Diffusion
$^{224}Ra_{Off}$	^{224}Ra Activity in Bight
$^{224}Ra_{Riv}$	^{224}Ra Activity in Rivers
$^{224}Ra_S$	^{224}Ra Activity in Sound

$^{224}Ra_{SGD}$	^{224}Ra Activity in SGD
$^{228}J_{Ra\text{-}dif}$	^{228}Ra Sediment Diffusion
$^{228}Ra_{Off}$	^{228}Ra Activity in Bight
$^{228}Ra_{Riv}$	^{228}Ra Activity in Rivers
$^{228}Ra_{S}$	^{228}Ra Activity in Sound
$^{228}Ra_{SGD}$	^{228}Ra Activity in SGD
$\delta^{18}O_{FSGD}$	Oxygen Isotope Ratio FSGD
$\delta^{18}O_{SGD}$	Oxygen Isotope Ratio SGD
$\delta^{18}O_{Sound}$	Oxygen Isotope Ratio Sound

CHAPTER I – INTRODUCTION

Submarine groundwater discharge (SGD) is a global phenomenon that occurs mostly as diffuse input along coastlines and is defined as "any and all flow of water on continental margins from the seabed to the coastal ocean, regardless of fluid composition, or driving force" (Burnett et al., 2003). This definition expresses that SGD is not defined by composition, origin, or what drives the flow, as these can vary based on the area where SGD is observed (Burnett et al., 2003). Fresh SGD is estimated to be 6-10% of total runoff to the coastal ocean, but it's overall input, including seawater circulation, is close to or even larger than total river input (Burnett et al., 2006), and therefore can be highly important for the input of dissolved materials to the coastal ocean. In recent years, SGD is gaining more traction as a major source to the ocean of trace metals (e.g., Beck et al., 2007; Rodellas et al., 2014), nutrients (e.g., Santos et al., 2021), and carbon (e.g., Liu et al., 2014), and therefore should be considered in global oceanic models.

The concentration of dissolved materials such as trace metals, nutrients, and carbon in SGD is usually higher than that of rivers, making it a significant source to the coastal ocean, especially locally (Moore, 2010). That, combined with its total flux being equal or greater than rivers, can make SGD an important and often overlooked part of oceanic margin fluxes (Moore et al., 2008; Moore, 2010). Even though SGD may be a significant source of dissolved materials such as nutrients, it can be difficult to measure it and determine the driving force of the fluxes (Burnett et al., 2006). Various methodologies have been employed to determine SGD water fluxes, including water balance models (Allen, 1976; Sekulic and Vertacnik, 1996), seepage meters (e.g., Lee, 1977; Taniguchi and Fukuo,1993), and geochemical tracers (e.g., Dulaiova et al., 2005;

Moore, 1996), with the majority of studies concluding that SGD is extremely important for nutrient and trace metal fluxes to the coastal ocean (Moore, 2010).

In this work, we consider the influence of SGD on nutrients and trace metals on coastal systems, in particular how it may affect water quality. Previous research has demonstrated the SGD can lead to eutrophication and hypoxia in coastal systems (e.g., McCoy et al., 2011; Sanial et al., 2021), and in some cases lead to organism mortality (e.g., Montiel et al., 2019). The processes that affect SGD distribution in coastal systems and how that will affect water quality are also considered in this dissertation.

In Chapter 2, the input of Ba and U to the coastal ocean from a coastal acid sulfate system that is highly affected by groundwater is investigated. Previous studies calculated the SGD input to the system, and determined that groundwater flux to the Tuckean Swamp in Australia during the 2010 flood period was between 12 – 18% of the total surface flow, and the dominant source of acidity to estuary (de Weys et al., 2011). We found that groundwater discharge can export up to 18% of Ba and 66% of U loads via surface water. Since Ba and U are important proxies for processes such as river input, sea surface temperature, and upwelling, studies that use these proxies in areas affected by acid sulfate soils need to consider how this will affect the methods they are using.

The groundwater that percolates out as SGD has unique geochemical signatures from its passage through the aquifers. Geochemical changes in the SGD may occur seasonally, including the fresh/salt interface where the fresh groundwater meets the seawater, and mixing occurs. Therefore, the different signatures of dissolved tracers (such as radium and radon) in groundwater are unique enough to distinguish them from surface waters, allowing the ability to determine the impact of SGD both qualitatively and

quantitatively. In Chapters 3 and 4, the tracers radium and radon are used to calculate the water flux of SGD to the Mississippi Sound, an estuary in the northern Gulf of Mexico that experiences seasonal eutrophication and hypoxia. These fluxes are determined both spatially and temporally, allowing us to understand how this compares to other important influences on the system, such as local rivers and a Mississippi River flood diversion structure, the Bonnet Carré Spillway. Chapter 3 mainly focuses on a time series along the coastline, and highlighted how there was a shift in the sources that dominate nutrient input seasonally. Chapter 4 examines the Sound as a whole, and focused mainly on spatial changes and what that means for water quality. This work contributes to the total understanding of how SGD affects water quality, including hypoxia, and how it compares to other stressors such as rivers, spillways, and surface runoff (Figure 1.1).

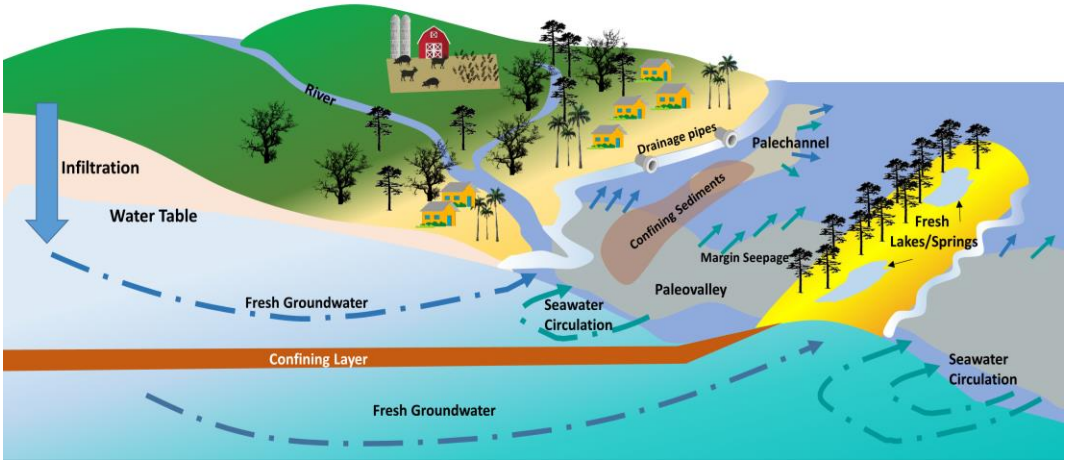

Figure 1.1 *Conceptual model of the Mississippi Sound SGD and forcing mechanisms.*

The mainland has agriculture upriver than can deliver nutrients to the local rivers. Along the coastline is urbanized, with a high density of houses and several cities. Drainage pipes deliver surface runoff directly into the Sound. The barrier islands are undeveloped, but previous studies have found high radium near the island chain, suggesting that there is SGD input from these areas. The coastal aquifer is split into two main aquifer systems, one is confined until offshore, the other is unconfined and freely exchanges with the Sound. Palleovalleys and paleochannels line the coast, potentially inputting SGD near the margins, however dense surface sediments such as clays and silts can block seepage from the relict channels.

1.1 References

Allen, A.D., 1976. Outline of the hydrogeology of the superficial formations of the Swan Coastal Plain. Western Australia Geol Surv Ann Rep, 31–42.

Beck, A.J., Tsukamoto, Y., Tovar-Sanchez, A., Huerta-Diaz, M., Bokuniewicz, H.J., Sañudo-Wilhelmy, S.A., 2007. Importance of geochemical transformations in determining submarine groundwater discharge-derived trace metal and nutrient fluxes. Appl. Geochemistry 22, 477–490. https://doi.org/10.1016/J.APGEOCHEM.2006.10.005

Burnett, W.C., Aggarwal, P.K., Aureli, A., Bokuniewicz, H., Cable, J.E., Charette, M.A., Kontar, E., Krupa, S., Kulkarni, K.M., Loveless, A., Moore, W.S., Oberdorfer, J.A., Oliveira, J., Ozyurt, N., Povinec, P., Privitera, A.M.G., Rajar, R., Ramessur, R.T., Scholten, J., Stieglitz, T., Taniguchi, M., Turner, J. V, 2006. Quantifying submarine groundwater discharge in the coastal zone via multiple methods. Sci. Total Environ. 367, 498–543. https://doi.org/10.1016/j.scitotenv.2006.05.009

Burnett, W.C., Bokuniewicz, H., Huettel, M., Moore, W.S., Taniguchi, M., 2003. Groundwater and pore water inputs to the coastal zone. Biogeochemistry 66, 3–33. https://doi.org/10.1023/B:BIOG.0000006066.21240.53

De Weys, J., Santos, I.R., Eyre, B.D., 2011. Linking groundwater discharge to severe estuarine acidification during a flood in a modified wetland. Environ. Sci. Technol. 45, 3310–3316. https://doi.org/10.1021/ES104071R/ASSET/IMAGES/LARGE/ES-2010-04071R_0001.JPEG

Dulaiova, H, Peterson, R, Burnett, W.C., 2005. A multi-detector continuous monitor for assessment of ^{222}Rn in the coastal ocean. J Radioanal Nucl Chem. 263(2), 361–365.

Lee, D.R., 1977. A device for measuring seepage flux in lakes and estuaries. Limnol Oceanogr. 22, 140–147.

Liu, Q., Charette, M.A., Henderson, P.B., McCorkle, D.C., Martin, W., Dai, M., 2014. Effect of submarine groundwater discharge on the coastal ocean inorganic carbon cycle. Limnol. Oceanogr. 59(5), 1529-1554.

Mccoy, C., Viso, R., Peterson, R.N., Libes, S., Lewis, B., Ledoux, J., Voulgaris, G., Smith, E., Sanger, D., 2011. Radon as an indicator of limited cross-shelf mixing of submarine groundwater discharge along an open ocean beach in the South Atlantic Bight during observed hypoxia. Cont. Shelf Res. 31, 1306–1317. https://doi.org/10.1016/j.csr.2011.05.009

Montiel, D., Lamore, A., Stewart, J., Dimova, N., 2019. Is Submarine Groundwater Discharge (SGD) Important for the Historical Fish Kills and Harmful Algal Bloom Events of Mobile Bay? Estuaries Coast. 42, 470–493. https://doi.org/10.1007/s12237-018-0485-5

Moore, W.S., 1996. Large groundwater inputs to coastal waters revealed by ^{226}Ra enrichments. Nature. 380, 612–614.

Moore, W.S., 2010. The Effect of Submarine Groundwater Discharge on the Ocean. Ann. Rev. Mar. Sci. 2, 59–88. https://doi.org/10.1146/annurev-marine-120308-081019

Moore, W.S., Sarmiento, J.L., Key, R.M., 2008. Submarine groundwater discharge revealed by ^{228}Ra distribution in the upper Atlantic Ocean. Nat. Geosci. 1:309–11.

Rodellas, V., Garcia-Orellana, J., Tovar-Sánchez, A., Basterretxea, G., López-Garcia, J.M., Sánchez-Quiles, D., Garcia-Solsona, E. and Masqué, P., 2014. Submarine groundwater discharge as a source of nutrients and trace metals in a Mediterranean bay (Palma Beach, Balearic Islands). Mar. Chem. 160, 56-66.

Sanial, V., Moore, W.S., Shiller, A.M., 2021. Does a bottom-up mechanism promote hypoxia in the Mississippi Bight? Mar. Chem. 235, 104007. https://doi.org/10.1016/J.MARCHEM.2021.104007

Santos, I.R., Chen, X., Lecher, A.L., Sawyer, A.H., Moosdorf, N., Rodellas, V., Tamborski, J., Cho, H.M., Dimova, N., Sugimoto, R., Bonaglia, S., 2021. Submarine groundwater discharge impacts on coastal nutrient biogeochemistry. Nat. Rev. Earth Environ. 2(5), 307-323.

Sekulic, B, Vertacnik, A, 1996. Balance of average annual fresh water inflow into the Adriatic Sea. Water Resour Dev. 12, 89–97.

Taniguchi, M, Fukuo, Y, 1993. Continuous measurements of ground-water seepage using an automatic seepage meter. Ground Water. 31, 675–679.

CHAPTER II – GROUNDWATER-DERIVED U AND BA EXPORTS FROM A COASTAL ACID SULFATE SOIL (CASS) CATCHMENT FOLLOWING RAIN EVENTS

Co-authors: Isaac R. Santos and Alan M. Shiller

Published in: Estuarine, Coastal and Shelf Science, Volume 270, 5 June 2022, 107838.

2.1 Abstract

Coastal acid sulfate soil (CASS) catchments are regions of enhanced weathering due to sulfur mineral oxidation following drainage of anoxic wetland soils. Heavy rainfall flushes CASS soils, releasing dissolved metals to nearby estuaries and the coastal ocean. The importance of CASS environments on the release of uranium (U) and barium (Ba) to the coastal ocean is not well understood. Here, we discuss daily observations of dissolved Ba and U in an extensively drained CASS system in Australia under contrasting hydrological conditions. Radon-traced groundwater discharge following rain events released trace metals to surface waters. Groundwater fluxes of Ba and U were on average 10% and 30% of the total surface fluxes in the Tuckean Swamp, respectively. The average local surface water fluxes from the Tuckean Swamp were 1692 and 1.6 μmol/m^2/yr from the catchment. On a global scale, dissolved Ba and U derived from CASS systems may be equivalent to 1.0% and 2.5% of rivers, respectively, even though CASS cover only ~0.1% of the global continental area. While CASS may not be a major contributor of dissolved Ba and U to the global ocean, fluxes on a square meter basis indicate that CASS may be highly important to regional U and Ba budgets.

2.2 Introduction

Coastal acid sulfate soils (CASS) are formed when coastal floodplains and wetlands are drained, often to create arable land for agriculture and grazing. These areas are broadly distributed along the world's coastlines (Ljung et al., 2009; Proske et al., 2014). Sediments that are enriched in organic matter and iron sulfides often underlie these floodplains and wetlands. When drained, sulfidic minerals such as pyrite oxidize and produce acid that is then flushed to adjacent waterways (Ward et al., 2004). Exposure of CASS occurs not only due to direct drainage, but also following post-glacial rebound (e.g., Boman et al., 2010) and drought (e.g., Mosley et al., 2017). Climate change will increase droughts in many areas (Cook et al., 2020) leading to enhanced exposure of sulfidic materials, which along with expansion of anthropogenic pressures on floodplains and wetlands (Newton et al., 2020) will increase CASS surface area. This will cause CASS acidification to become more widespread (Fanning et al., 2017), leading to more occurrences of acidic conditions in coastal waterways and atmospheric release of sulfidic gases (Kinsela et al., 2011). The acidity in coastal drainage waters caused by CASS results in enhanced release of several trace metals (Johnston et al., 2010). These CASS areas are thus often associated with extremely high trace metal loads and concentrations exceeding water quality guidelines, creating devastating effects on estuary health (Wong et al., 2010).

While trace metal dynamics in CASS has been studied in various locations over the past few decades (Karimian et al., 2018, Ljung et al., 2009) it remains unknown how CASS affect uranium (U) and barium (Ba) loads, concentrations, and cycling in nearby estuaries. Coastal flooding followed by groundwater discharge is known to enhance

dissolved metal concentrations due to decreased pH (Santos et al., 2011a). Both Ba and U are often used as tracers in the global ocean for understanding export production, paleoenvironments, river inputs, and oceanic alkalinity (Carter et al., 2020; Cao et al., 2016; Hsieh and Henderson, 2017). A greater understanding of U and Ba sources and sinks is important for using them as proxy tracers in both global and regional settings. In this paper, we focus on Ba and U due to their contrasting behaviors (Santos et al., 2011b), providing mechanistic insight into both groundwater discharge and surface discharge from a CASS environment.

Dissolved U concentrations are usually higher in seawater than in rivers and groundwater draining to the ocean. In estuaries, U concentrations are controlled by mixing, iron (Fe) and manganese (Mn) oxide cycling, and reduction of soluble U(VI) to less soluble U(IV) under anoxic conditions (Swarzenski et al., 2004). Processes such as colloidal aggregation, flocculation, and adsorption onto resuspended sediments in intermediate salinities can drive non-conservative behavior in surface and subterranean estuaries (Sanders et al., 2017; Toole et al., 1987; Windom and Niencheski, 2003). Uranium is also associated with Fe oxide cycling, precipitating near the redox level needed for Fe reduction (Charette and Sholkovitz, 2005; Waite et al., 1994). Cycles of U reduction/oxidation due to hypoxic/anoxic conditions are often important in coastal systems (Porcelli and Swarzenski, 2003), but these processes have not been investigated in CASS waters subject to extreme shifts in pH and oxygen conditions (Johnston et al., 2005, Karimian et al., 2018). Pyrite (FeS_2) has been associated with uptake and release of U, depending on the redox condition of the environment (Descostes et al., 2010; Scott et

al., 2007). Oxidized species of Fe and S can sorb U onto the surface of FeS_2, reducing U and removing it from solution (Scott et al., 2007; Wersin et al., 1994).

Barium concentrations in surface and subterranean estuaries are controlled primarily by mixing, ion exchange reactions, Fe and Mn oxide cycling, and weathering of solids (Moore and Shaw, 2008; Shaw et al., 1998). Concentrations of Ba often decrease with distance from shore due to dilution. During ion exchange, seawater cations substitute for Ba on suspended materials (Charette and Sholkovitz, 2006). Barium adsorption occurs in freshwater, such as rivers or in fresh groundwater, and desorption from particles occurs when fresh water meets seawater. While Ba does not have a redox chemistry cycle of its own, it can be recycled at the oxic/anoxic boundary as part of the Mn/Fe oxide cycle (Charette and Sholkovitz, 2006; Coffey et al., 1997; Gonneea et al., 2013). Slow weathering minerals within an aquifer allows for the exposure of ion exchangeable Ba (Gonneea et al., 2013). All these processes are likely active in CASS and can potentially produce large Ba fluxes and rapid cycling.

In this paper, we hypothesize that CASS are hotspots that disproportionally contribute to U and Ba fluxes to the coastal ocean. We quantify the fluxes of dissolved Ba and U from groundwater to surface waters, and from surface waters to the estuary in a subtropical CASS catchment during multiple rain events. We compare our observations to other CASS sites to discuss the global context and possible relevance of CASS to U and Ba fluxes to the coastal ocean.

2.3 Materials and Methods

2.3.1 Experimental Site

Observations were performed in the main creek draining the Tuckean Swamp in New South Wales, Australia from January to June 2010 (Figure 2.1). This area has been extensively cleared and drained since the early 1900s to reduce periodic inundation, which resulted in a large portion of the swamp developing into CASS (Taffs et al., 2008). The Swamp drains into the Tuckean Broadwater, a major tidal tributary of the Richmond River estuary. Average annual rainfall to the region is ~1800 mm, with the majority falling from December to April. The pH levels remain low year round, due to groundwater discharge that often peaks a few days after rain events. This area has been extensively investigated from deoxygenation (Wong et al., 2010), groundwater (de Weys et al., 2011), nutrient (Santos et al., 2013), and heavy metal (Santos et al., 2011a) perspectives. Here, we assess how flood events and groundwater discharge release U and Ba from CASS.

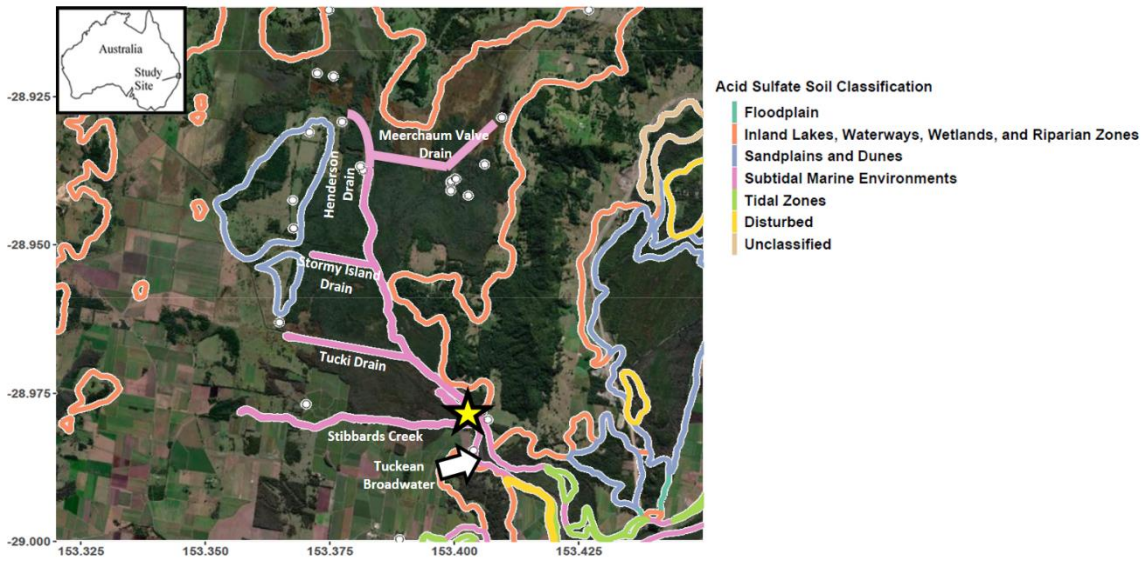

Figure 2.1 *Map of Tuckean Swamp.*

Combined satellite (ESRI) and soil classification map of the Tuckean Swamp. The yellow star indicates the location of the monitoring station. Groundwater samples are indicated by the white dots.

2.3.2 Experimental Approach

Daily samples were collected for 4 months from 28 January 2010 to 1 June 2010 from surface waters during low tide in the Tuckean Broadwater. This period started during dry conditions, captured a flood event, and ended when pH levels and radon concentrations approached those of the dry conditions. Thirty-one groundwater samples were collected from shallow wells installed with a hand auger and monitoring wells installed by the Department of Environmental Protection. A peristaltic pump was used to retrieve samples after purging the well. Samples were collected and filtered using a 0.45 μm disposable acetate filter. Filtered samples were acidified with high-purity HNO_3 and stored in acid cleaned vials. Samples were analyzed for dissolved metals using a Perkin-Elmer DRCe Inductively Coupled Plasma Mass Spectrometer (ICP-MS). Calibrations

were conducted before and after running the samples. Instrument drift and blank corrections of the samples are described in Santos et al. (2011a). Briefly, instrument drift was taken into account using a standard – 10 samples – standard bracketing scheme, and blanks were run by treating ultrapure deionized (DI) water as a sample.

Water level, pH, conductivity, and temperature parameters were monitored at 1-hr intervals using data loggers maintained by the Richmond River County Council (calibrated biweekly). Radon (^{222}Rn, $T_{1/2}$ = 3.84 days) concentration was determined using a continuous, automated radon-in-air monitor (RAD7; Durridge Co.) adapted for radon-in-water (RAD Aqua). While ancillary, radon and Fe data have been published elsewhere (De Weys et al., 2011; Santos et al., 2011a), all of the U, Ba, Cl, and SO_4 data reported here are original. Daily groundwater discharge rates were calculated from a radon mass balance approach as reported by De Weys et al. (2011). This approach determined the possible range (minimum and maximum) of groundwater discharge to the CASS drainage network. U and Ba fluxes from groundwater to surface water were estimated by multiplying the average concentrations in regional groundwater by the radon-derived groundwater discharge rates assuming no temporal variability in the groundwater endmember. U and Ba export fluxes from surface waters to the nearby estuary were estimated by multiplying daily concentrations by water fluxes. Principal component analysis (PCA) was conducted in R using the FactoMineR package and plotted using the ggplot package.

2.4 Results

2.4.1 Time Series in surface waters

Daily observations collected over 117 days showed variation in both hydrological and geochemical conditions (Figure 2). Four different hydrological stages (dry, flood, post flood, and minor rains) were defined (Santos et al., 2011a) to describe radon and Fe distributions. Dry periods had the highest pH due to the intrusion of seawater into the time series station. Net water flow during this time approached zero through a tidal cycle and Ba and U concentrations reached their maximums (Ba max = 310 nM, U max = 1250 pM) due to higher conductivity. Rainfall began in early February, driving down the conductivity and decreasing both Ba and U.

Flood periods were characterized by a rapid increase in rainfall after some more minor rainfalls in February (Figure 2.2). During the first major rain event on 2 March, 213 mm of rainfall inundated the swamp for one week. This led to surface runoff and groundwater discharge reaching maximums of 120 m^3/s and 5 m^3/s, respectively. pH levels dropped significantly from 6 to 4.5 immediately following the rainfall event. Radon concentration increased during the flood recession. Dissolved Ba had started to slightly increase right before the intense rainfall, when pH initially started to decrease, and decreased slightly after the rain ended. Ba increased as the radon concentrations and groundwater flows increased. When groundwater discharge reached its maximum following the flood, the dissolved Ba experienced a spike of 130 nM. Dissolved U concentrations dropped just after the rainfall event, and continued to decline through the entire flood period.

The post flood period had little rainfall, and was dominated by groundwater discharge (Figure 2.2). Peak radon coincided with the minimum surface water pH of about 4. Near the end of the post flood period, radon concentrations started to drop, coinciding with an increase in pH. Dissolved Ba concentrations remained steady through this period, averaging 110 nM. Dissolved U concentrations experienced a small peak from 19 to 23 March, coinciding with the lowest pH. After this peak, dissolved U levels dropped and remained low.

After the post flood period, two minor rain events on 20 April and 4 May (both 37 mm), were captured (Figure 2.2). The first rainfall event caused a drop in pH to 3.62. A less intense drop in pH occurred after the second rainfall event, and by 28 May, pH returned to >5. After both rain events, there were increases in the radon and Ba concentrations. The Ba concentrations were higher than the ones noted during the highest groundwater discharge. Interestingly, dissolved U also increased after each rainfall, coinciding with radon even though it was negatively correlated with radon during the flood period. Concentrations of both metals leveled off near the end of the minor rainfall events.

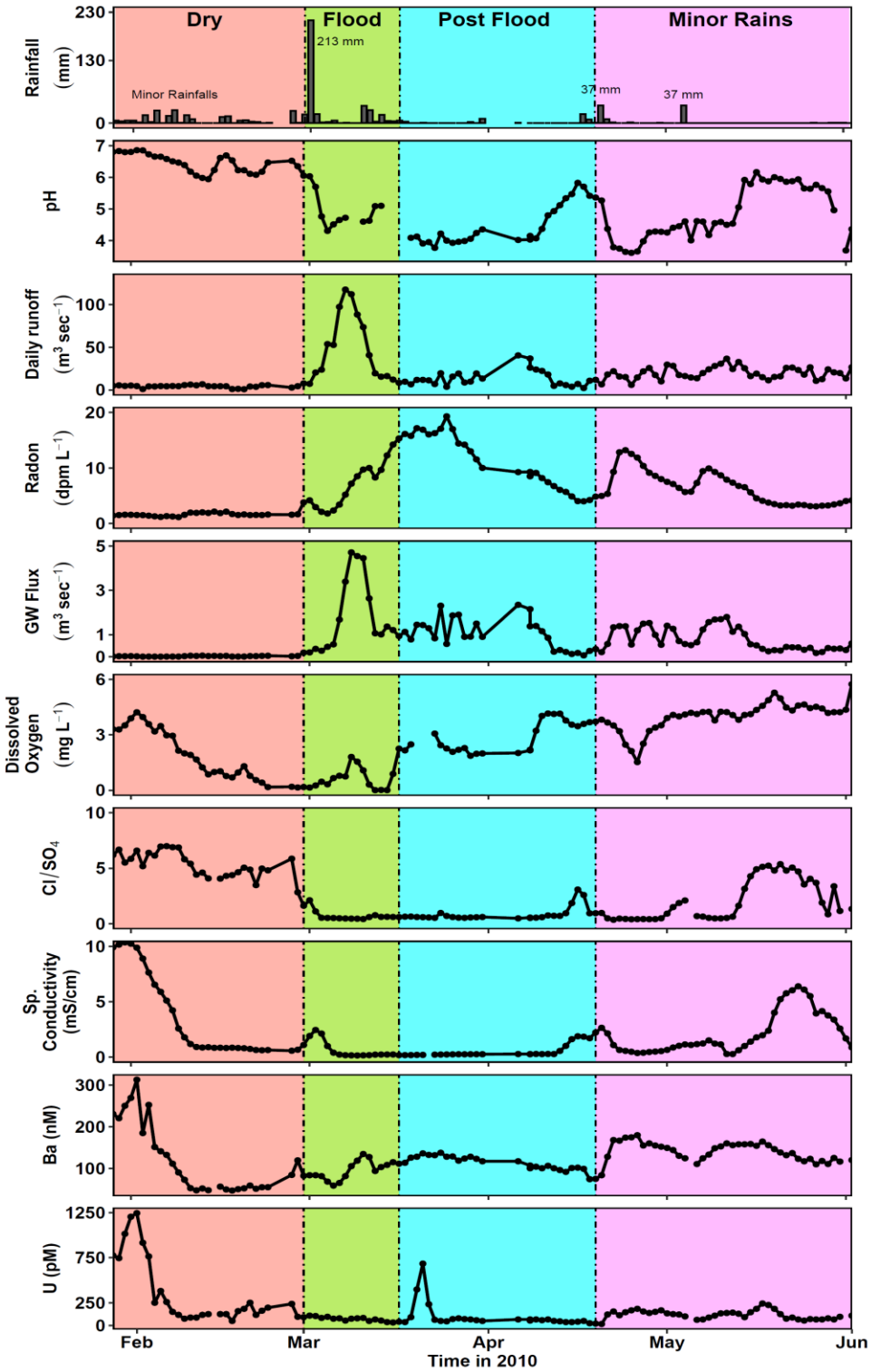

Figure 2.2 *Time series measurements in Tuckean Swamp.*

Time series measurements of trace metals and associated parameters in the Tuckean Broadwater. Ba, U, and Cl/SO_4 measurements are original observations, while the ancillary parameters were reported elsewhere (Santos et al 2011a).

2.4.2 Statistical analysis

Both metals significantly correlated with pH, conductivity, and dissolved oxygen (DO) during the dry season, and significantly correlated with radon during the flood season. ($|r| > 0.5$, $p < 0.001$, Figures 2.3 and 2.4). The correlation to radon during the flood season was opposite for each metal, with Ba being positively correlated, and U negatively correlated. During the post flood season, Ba was significantly correlated to pH, radon, conductivity, and DO, and during the minor rains season, Ba was significantly correlated to radon, conductivity, and DO ($|r| > 0.5$, $p < 0.001$, Figures 2.3 and 2.4). Ba negatively correlated with pH, conductivity, and DO during the post flood and minor rains periods. Both Ba and U were significantly negatively correlated to Fe during the dry season ($|r| > 0.5$, $p<0.001$, Figures 2.3 and 2.4), with U also negatively correlated to Fe during the flood season ($|r| > 0.5$, $p\leq0.05$, Figures 2.3 and 2.4). Ba was significantly positively correlated to Fe and Mn during the post flood season while Ba and U were both positively correlated to Fe and Mn during minor rains ($|r| > 0.5$, $p<0.01$ and $p<0.05$, respectively, Figures 2.3 and 2.4).

The chloride:sulfate ratio (Cl/SO_4) can be used as a proxy for CASS-influenced water (Macdonald et al., 2004). Typical seawater ratios of Cl/SO_4 are around 7.2, and ratios lower than 4 are indicative of an acidic sulfate source from sulfide oxidation (Macdonald et al., 2004, Mulvey, 1993). Cl/SO_4 was also positively correlated with pH, further indicating its use as a tracer of reducing waters (Figure 2.4). These levels of Cl/SO_4 occurred directly after the 213 mm rainfall event, and did not recover until the minor rains period before rapidly falling again at the end of the time series. The Cl/SO_4 ratio was negatively correlated to radon during the dry, post flood, and minor rains season

(Figure 2.4), and is only positively correlated to Ba during the dry and flood period (Figures 2.3 and 2.4).

There was a noticeable counter clockwise hysteresis pattern for Ba versus discharge plot due to a delay in metal release from the catchment following rainfall. At days 8-10 during the flood period (March 2 – 17), Ba concentrations reached their peak, and slowly declined, coinciding with peak groundwater discharge. However, Ba concentrations did not fall completely back to concentrations seen before the flood period, and stayed relatively elevated during the post flood season and minor rain events (Figure 2.3). The radon concentrations also remained elevated through this time, indicating there was still delayed groundwater seepage into the catchment from the shallow aquifer recharge during the flood.

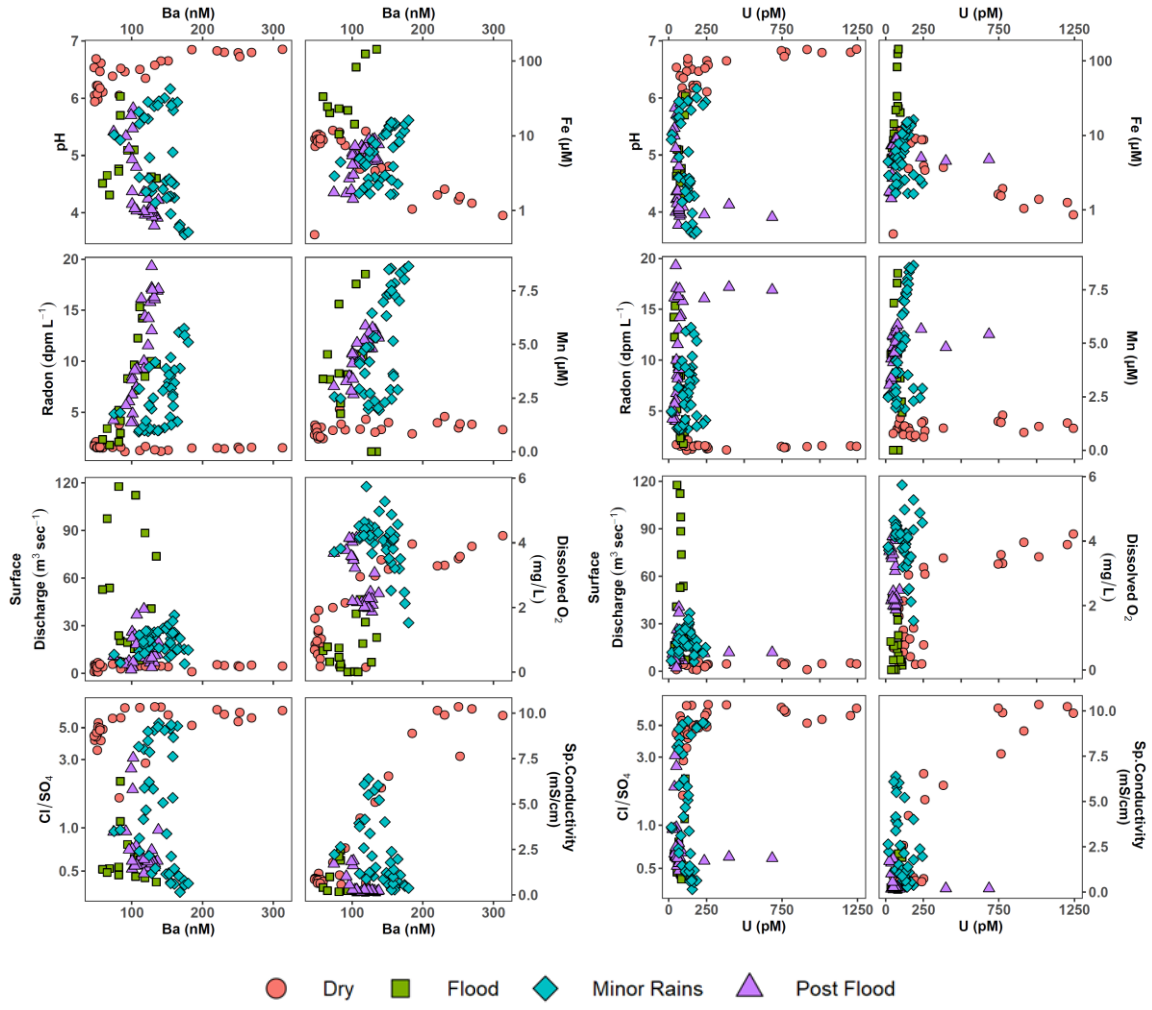

Figure 2.3 *Barium and uranium scatter plots.*

Barium (left) and uranium (right) concentrations versus pH, radon, surface discharge chloride:sulfate ratio (Cl/SO4), iron (Fe), manga nese (Mn), DO, and specific conductivity.

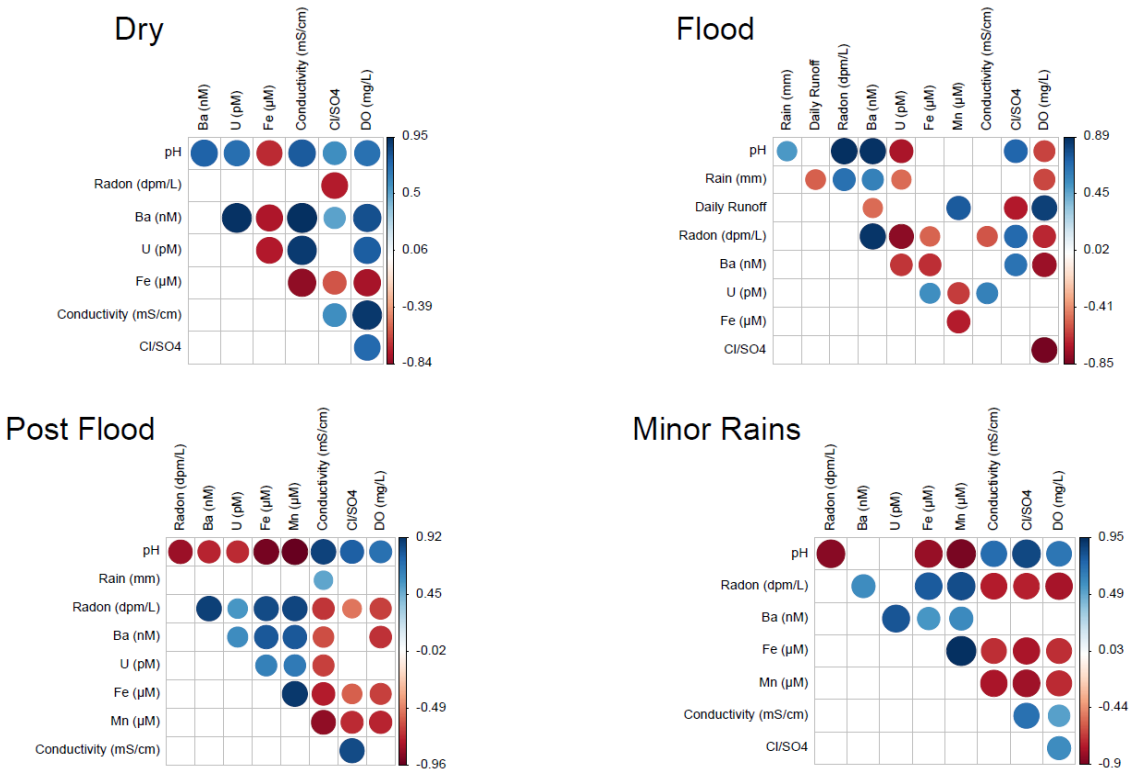

Figure 2.4 *Seasonal correlation plots.*

Pearson correlation plots of the key parameters. Relationships have an r value >0.5 (blue) or <-0.5 (red), and each correlation is significant ($p<0.05$). Non-significant correlations appear as blank spaces.

To gain further insight into the complex driving forces behind surface water trace metal concentrations, a PCA analysis was conducted (Figure 2.5). The two main PCA axes revealed clear clusters representing the four hydrological stages. The majority of the variation in the data was explained by the Cl/SO_4 ratio, pH, radon, and conductivity (46 % of the variance in the dataset, dimension 1), representing groundwater seepage from CASS. The dry season variance was mainly explained by the pH, Cl/SO_4, and conductivity, and was negatively correlated to radon concentration, representing seawater intrusion. The data for the period of post flooding and minor rains is well spread across the vectors of radon, conductivity, and Cl/SO_4. However, the post flood period shifted

more to the left indicating groundwater dominance. During the flood season, the confidence ellipse opposed the other three seasons, and was aligned along the Y-axis (dimension 2), which is dominated by rainfall and DO (19.4 % of the variance in the dataset). However, this is mainly due to an outlier in the 2nd quadrant (lower right) representing a sample on the day with the highest rainfall of 213 mm. If this outlier is removed from the dataset, pH and radon become the main variables affecting the dataset. With the majority of the flood season data in the 1st and 2nd quadrants (top and bottom left), the data for this time is more strongly correlated with radon than pH.

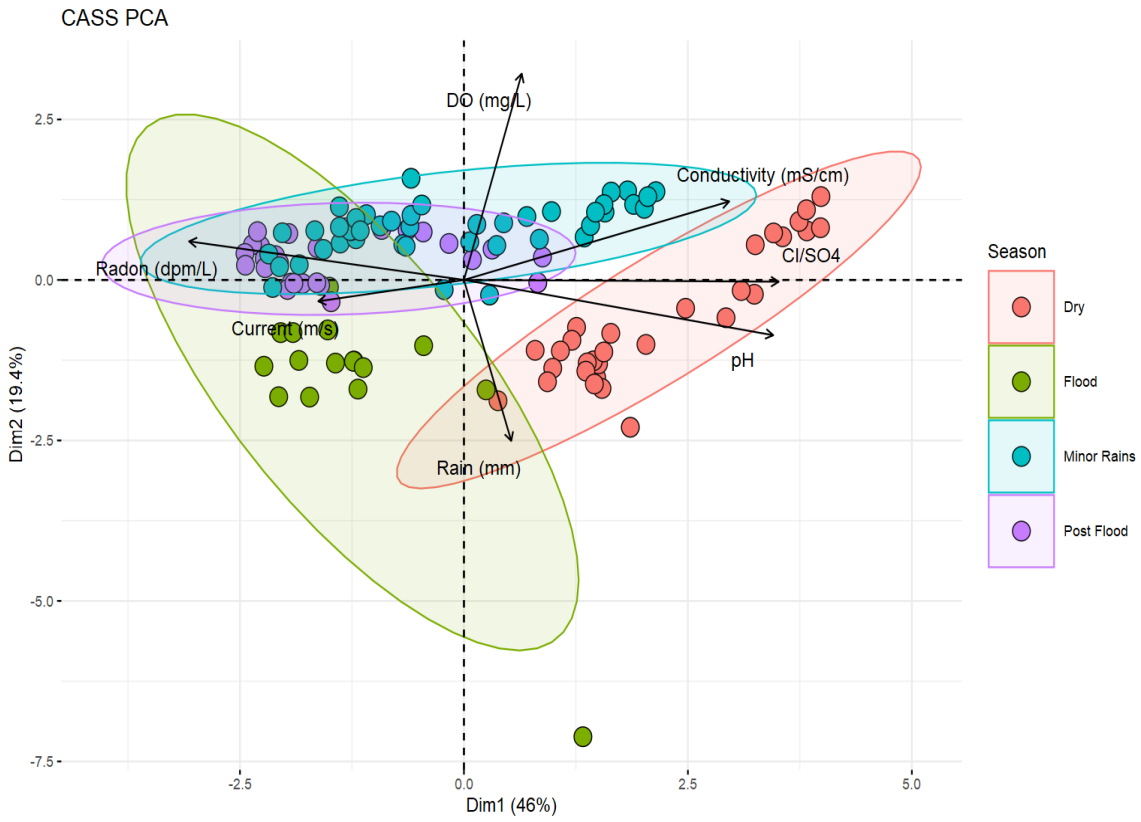

Figure 2.5 *Surface water PCA.*

PCA analysis of surface water time series observations revealing clusters associated with the four hydrological stages. Groundwater seepage from CASS as traced by radon and Cl/SO_4 ratios was the main factor explaining variability.

2.4.3 Groundwater samples

Groundwater samples were separated into two distinct groups as in de Weys et al. (2011): CASS and non-CASS groundwater. The CASS samples were defined as having a pH < 5. These samples were all collected in < 2.5 m depth, and had pH as low as 3.11. All groundwater samples had a specific conductivity of less than 9 mS/cm, i.e., below levels needed to desorb Ba, and the oxygen concentrations ranged between 0.95 – 4.83 mg/L, near hypoxic levels. Concentrations of U in the CASS groundwater samples had a higher range than the non-CASS samples, mainly due to low oxygen and pH. Ba showed a different trend, decreasing with decreasing pH, indicating that the CASS samples had lower Ba concentration than the non-CASS samples. Ba was positively correlated to radon (p = ≤0.05), whereas U was positively correlated to Mn (p≤0.01, Figure 2.6). All the other groundwater samples were scattered, and no other strong correlations were present.

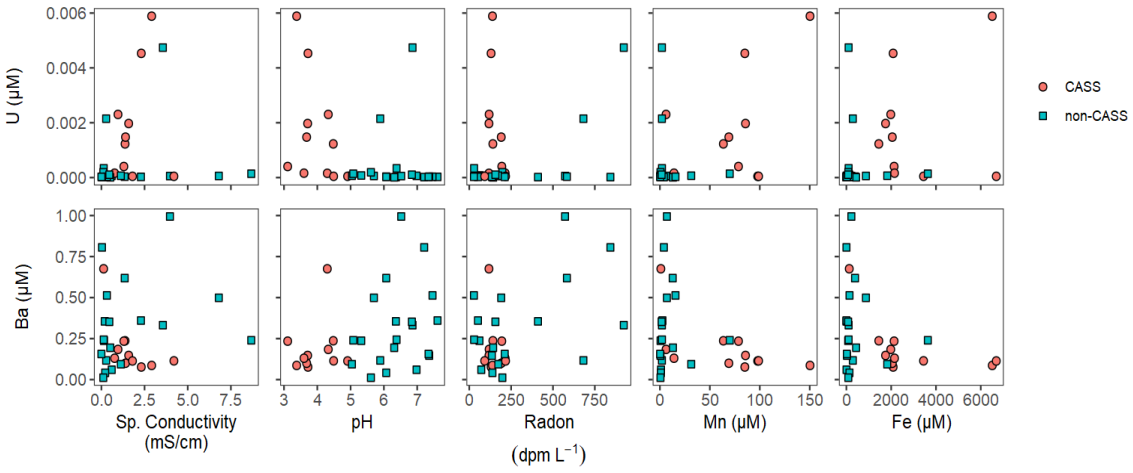

Figure 2.6 *Groundwater scatter plots.*

Groundwater concentration of Ba and U vs specific conductivity, pH, radon, manganese (Mn), and iron (Fe).

2.5 Discussion

2.5.1 Geochemical Controls

U was mainly related to the pH and oxygen when the conductivity levels were below 9 mS/cm, and can be removed to particulate phases in reducing sediments (Sarin and Church, 1993). The elevated U during the very beginning of the dry season was due to tidally-driven seawater intrusion into the estuary. Seawater has high dissolved U concentrations of 13 nM (Turekian and Chan, 1971; Ku et al., 1977). The groundwater influence was negligible during dry conditions. In other CASS-dominated estuaries, conductivity rises due to tidally influenced waters entering the system during times of no rainfall (e.g., Green et al., 2006), and lowering of pH is triggered by rainfall events. Here, the onset of a major flooding event triggered a rapid decline in conductivity and pH. The minor rain events dropped the conductivity, DO, Ba, and U. With those small rainfalls, there is little to no change in pH, Cl/SO_4, or radon, indicating that there was no CASS-related discharge or groundwater influencing the system. The decline in DO indicates there may be some other process occurring such as the formation of Fe oxides, removing oxygen, Ba, and U from the water column (Sammut et al., 1996; Green et al., 2006). Dissolved oxygen, Ba, and U are all negatively correlated to Fe during the dry period, indicating that the formation of Fe oxides control their distribution during conditions of low rainfall conditions and no groundwater discharge.

During the flood period, Ba and U seem to be affected by different processes even though the main control is acid sulfate discharge (Figure 2.7). The significant negative correlation of U to radon during the flood period could be due to two processes: either the groundwater is a net sink for U, or the U concentration is more affected by surface water

discharge, causing a diluting effect as the sediments are flushed (Cánovas et al., 2008). The groundwater fluxes to the surface of U (Table 2.1) revealed a clear source of U especially during the post flood period. During rain events, the shallow groundwaters are initially flushed, releasing U. At a later stage (i.e. minor rains), there was not rapid replacement of U, leading to dilution and a slowly declining concentration in the surface waters. Similar observations were made in an acidic river in Spain where the first rainfall of the year rapidly enhances dissolved metal concentrations. With subsequent rainfalls, the soil store of exchangeable salts and metals became depleted (Cánovas et al., 2008).

Strongly reducing groundwater high in iron and sulfate can be a sink for U (Riedel and Kübeck, 2018). Conditions for threshold redox conditions (Riedel and Kübeck 2018) indicate the groundwater in the Tuckean Swamp is reducing due to its high sulfate and iron content, and low oxygen. While the groundwater in this region is not conducive to U release, there is a considerable source to surface waters (Figure 2.7). This may be due to several factors. First, the Tuckean Swamp is infilled with Quaternary sediments, which contain groundwater that is highly mineralized (Riedel and Kübeck, 2018). Another factor could be the introduction and subsequent reduction of nitrate in the aquifer system could result in U mobilization (Riedel and Kübeck, 2018). Both the direct reduction of nitrate to N_2 and oxidation of pyrite through microbial oxidation of nitrate in the aquifer can release particle-bound U to solution (Riedel and Kübeck, 2018). If high amounts of nitrate are introduced into the groundwater, the natural redox conditions of the aquifer can change, leading to conditions that can enhance U release. During the post flood, the Tuckean Broadwater is mainly dominated by groundwater discharge (de Weys et al., 2011) with high nitrate flushed via surface runoff during the flood (Santos et al.,

2013). This nitrate may have mobilized U and increased its availability through the rest of the time series.

Table 2.1 *Ba and U fluxes.*

	n (days)	Water flux ($m^3 s^{-1}$)	Ba (mol d^{-1})	U (mol d^{-1})
Total surface water				
Dry	30	4.35	44	0.13
Flood	16	89.24	389	0.30
Post Flood	27	13.98	138	0.12
Minor Rains	44	19.73	244	0.20
Groundwater				
Dry	30	0.04	1	0.00
Flood	16	1.92	40	0.13
Post Flood	27	1.19	25	0.08
Minor Rains	44	0.88	19	0.06
% Groundwater to Surface				
Dry		1.0%	1.4%	1.5%
Flood		2.2%	10.4%	41.8%
Post Flood		8.5%	18.0%	66.9%
Minor Rains		4.5%	7.7%	29.0%

Note: Fluxes of Ba and U from surface runoff and groundwater discharge in mol/d.

Ba in surface waters (Figure 2.2) mimicked ^{222}Rn, indicating that the Ba flux is highly sensitive to groundwater discharge. Other studies indicate that Ba is highly influenced by groundwater discharge, and can even be used as a groundwater tracer in the ocean (e.g., Moore, 1997). A counter clockwise hysteresis pattern, or a lag, was also observed in the barium vs. discharge relationship. Barium peaked at 8-10 days after the initial rainfall, correlating with the highest groundwater discharge. Similar patterns were noticed for Mn and Fe (Santos et al. 2011a), but there were no strong correlations

between Ba and Mn, during the flood period, and Ba was negatively correlated to Fe, indicating additional processes affecting concentrations besides groundwater discharge. This hysteresis is not seen in the U concentration, indicating that groundwater may not be as important a source of U during flood periods. However, the main source of Ba is not groundwater at any hydrological stage (Table 2.1), indicating that other geochemical controls, mainly conductivity, play a larger role in determining Ba distribution.

The Ba concentration during post flood was positively correlated not only to radon, but also Fe and Mn, indicating a common source. In other groundwater influenced systems, elements such as Fe, Mn, and Ba are often highly enriched, leading to enhanced fluxes (Charette and Sholkovitz, 2006). The Ba, Fe, and Mn were all negatively correlated to conductivity, pH, and oxygen during this period as well, further providing evidence that groundwater was a source of Ba. This trend continued into the minor rains period, except that Ba was not as negatively correlated to pH as during the post flood period, potentially due to the reduction of groundwater discharge. Post flood times are characterized by a rapid decline in surface waters, but high groundwater levels, creating hydraulic gradients that drive groundwater discharge (Webb et al., 2016). As the CASS system begins to return to a more baseline phase, the groundwater discharge will decline (Webb et al., 2016). Since Ba was so closely tied to radon, it will follow the pattern of highest discharge during flood and post flood, with a decline as the system returns to normal. The Cl/SO_4 ratio during the post flood and minor rains period was strongly negatively correlated to radon, Fe, and Mn, showing that the groundwater is a source of reducing, metal-rich water. Ba and U are not significantly correlated to the Cl/SO_4 ratio,

and therefore may not be as susceptible to loading due to the reducing nature of the CASS site, or they became depleted in the groundwater after the initial flooding statge.

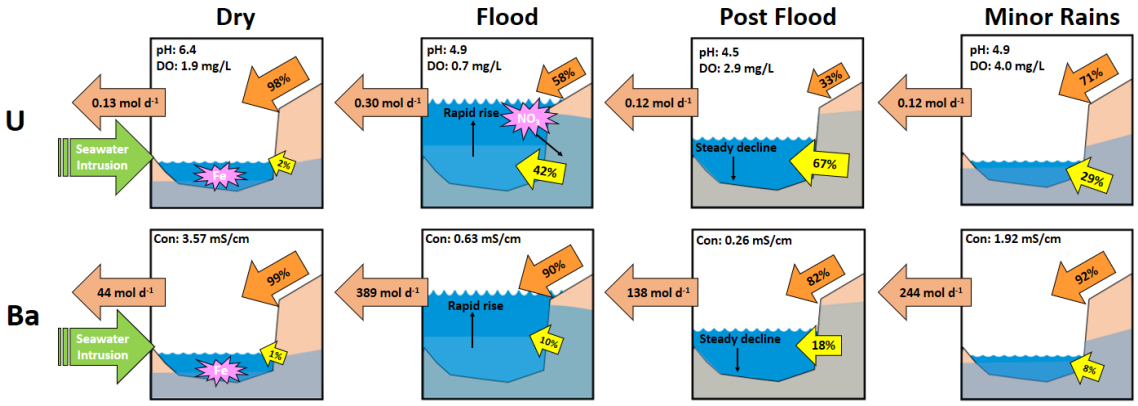

Figure 2.7 *Ba and U flux conceptual model.*

Conceptual model of the key processes affecting Ba and U in the Tuckean Swamp during each hydrological stage. The yellow arrow represents percent groundwater discharge and the orange arrow percent surface water fluxes to the total flux. The total flux of Ba and U is the arrow leaving the system. The purple represents other factors affecting the distributions, including Fe oxide formation and input of NO_3 into the system from surface runoff.

2.5.2 Surface vs Groundwater Loads

The surface water flux of Ba was 21 kmol in 114 days (68 kmol/yr), while for U it was 20 mol in 114 days (64 mol/yr). This value was then divided by the CASS catchment area to determine an area yield for Ba of 1700 mol/m^2/yr, and for U of 1.6 µmol/m^2/yr (Table 2.2). If we assume that the area that groundwater is discharging from the entirety of the Tuckean Swamp area (4000 ha), the fluxes of groundwater metals can be normalized by area and compared to the total surface water fluxes. The areal yield of Ba from groundwater was 169 µmol/m^2/yr, and for U it was 0.5 µmol/m^2/yr. Thus, radon-traced groundwater contributes on average 10% to the Ba flux and 30% to the U flux exported by surface waters. However, Ba in particular, was highly correlated to radon

during the flood, post flood, and minor rains periods. Other sources of radon are considered negligible compared to groundwater, and cannot explain radon levels above 2 dpm/L (Santos and Eyre, 2011). Taken together, these observations imply that shallow soils release some Ba but not radon, creating an additional Ba flux that is not explained by radon-derived groundwater discharge.

The use of all the groundwater samples to determine the flux to surface assumes that the groundwater endmember concentrations are constant. However, both Ba and U endmember concentrations can be temporally and spatially variable (Beck et al., 2007; Charette, 2007) and the low conductivity of groundwater makes Ba adsorb onto particles due to ion exchange interactions (Charette and Sholkovitz, 2006). To obtain the groundwater endmember, concentrations in all samples were averaged. Distinct changes of the groundwater signal with depth were related to conductivity and pH changes (Figure 2.5). Hence, the chosen groundwater endmember may not accurately reflect the groundwater sources to surface waters. In previous studies, desorption of Ba occurred with conductivity increases, while there was sorption with increasing pH (Gonneea et al., 2013). There are no significant correlations of Ba with conductivity. Therefore, other processes such as simple dilution may be affecting the Ba groundwater concentration.

2.5.3 Global Perspective

To understand the impact sulfidic soils may have on the global flux of Ba and U, three acid soil sulfate sites and two rivers affected by acid sulfate soils were compared to rivers, bays, and lagoons that were not affected by sulfidic soils (Table 2.2). The three sulfate soil sites with U and Ba data available are all located in Australia (Santos et al., 2011a; Macdonald et al., 2007). Two rivers in Finland are also affected by acid sulfate

soils (Roos and Åström, 2005), causing them to have slightly decreased pH. Other rivers, bays, and lagoons listed are not affected directly by acidic sulfate soils. The average concentration of Ba and U in the non-CASS areas were 277 ± 164 nM and 217 ± 206 pM, respectively. Average concentrations of Ba and U for the CASS sites were 120 ± 50 nM and 2980 ± 4540 pM. The Tuckean Swamp Ba flux was at least an order of magnitude higher than for non-CASS sites. The other two CASS sites did not have Ba data. The CASS-impacted Finland rivers did not have highly elevated Ba concentrations. For the three CASS areas, U fluxes and concentrations were at least one order of magnitude higher than global rivers away from CASS, driving a disproportionately high flux of U to the coastal ocean from CASS (Table 2.2).

To explore if CASS areas can potentially be an important source of Ba and U to the coastal ocean, we assume that the average CASS fluxes from Table 2.2 represent CASS systems worldwide. Acid sulfate soils cover about 1.7×10^{11} m^2 or 0.1% of the continental surface (Ljung et al., 2009). The average areal fluxes at CASS sites for U and Ba are 591 ± 954 μmol/m^2/d and 4.9 ± 7.5 μmol/m^2/d, respectively. Using these averages for CASS impacted sites, we obtain fluxes of 0.014 Tg/yr and 1.98×10^{-4} Tg/yr for Ba and U, respectively. These fluxes can be compared to the global river fluxes of 1.37 - 2.75 Tg/yr for Ba and 8×10^{-3} Tg/yr for U (Bridgestock et al., 2021; Windom et al., 2000). Hence, CASS systems may release 0.50 – 1.0% of the Ba river flux, and 2.5% of the U river flux.

On a square meter basis, fluxes of Ba and U from CASS are 0.08 g/m^2/yr and 1.2×10^{-3} g/m^2/yr, and from rivers are 9.2×10^{-3} – 0.02 g/m^2/yr and 5.4×10^{-5} g/m^2/yr, respectively. While CASS may not be a major source of dissolved Ba and U to the global

ocean, CASS related fluxes of Ba and U may be important on local to regional scales, depending in part on the time scales considered. For example, monitoring studies that use non-mobile animals, such as corals, may find that CASS systems are a potential "hotspot" of localized acidification, metal loading, and poor water quality (Powell and Martens, 2005). Also, while intermittent flooding and discharge may not cause major changes to monitoring results over longer time scales (i.e., decades), when looking at seasonal and annual fluctuations (e.g., Gou et al., 2020; Min et al., 1995; Sinclair and McCulloch, 2004; Wu et al., 2021), these excess trace metal inputs have the potential to skew results. Short time scale studies using Ba and U ratios to other metals or Ba and U isotopic variation as proxies for records of parameters such as riverine flux (e.g., Gou et al., 2020; Sinclair and McCulloch, 2004), upwelling (e.g., Ourbak et al., 2006), and sea surface temperature (e.g., Min et al., 1995; Wu et al., 2021) in areas that are impacted by terrestrial runoff may need to consider what the impact is on the proxy record of seasonal changes in CASS fluxes. As CASS area increases due to anthropogenic stressors and climate change (Boman et al., 2010; Fanning et al., 2017; Mosley et al., 2017), the flux of Ba, U and several other metals from these systems will also increase. Thus, accounting for CASS contributions may need to be considered when using Ba and U as proxies and when estimating fluxes of Ba and U to coastal regions where CASS are present.

Table 2.2 *CASS and river comparison.*

Site	Geology	Country	pH	Ba (nM)	U (pM)	Area (km^2)	Specific Discharge ($L/m^2/yr$)	Ba ($\mu mol/m^2/yr$)	U ($\mu mol/m^2/yr$)
Tuckean Swamp[1]	Acidic Sulfate Soil Swamp	Australia	3.6-6.9	120	170	40	-	1692	1.60
McLeods Creek[2]	Acidic Sulfate Soil Creek	Australia	3.0-7.0	-	11000	4.5	1500	-	16.4
Black Drain[2]	Acidic Sulfate Soil Swamp	Australia	3.0-7.0	-	1800	5.2	3040	-	5.47
Tillamook Bay[3]	Bay	USA	6.7-7.0	7	-	34	-	130	-
Patos Lagoon[4]	Coastal Lagoon	Brazil	6.0-8.0	-	110	201000	627	-	0.07
Delaware[4,5]	River	USA	8	170	84	17000	588	99	0.05
Geum[4]	River	Korea	8.9	-	240	10000	640	-	0.16
Hudson[4,5]	River	USA	7.5	370	660	34000	353	129	0.23
Humber[5]	River	UK	5.5-9.0	430	-	24240	325	139	-
Maeklong[4]	River	Thailand	7.5	-	54	27000	481	-	0.03
Mississippi[6]	River	USA	8.2	480	-	2980000	88	43	-
Pee Dee[4,7]	River	USA	7.0-8.0	220	270	23000	300	65	0.08
Savannah[4,7]	River	USA	7	260	290	25000	440	114	0.13
Tama[4]	River	Japan	7.3	-	29	1200	500	-	0.01
Lapväärtinjoki [8]	River affected by Acidic Sulfate Soils	Finland	6.71	70	420	1098	301	21	0.13
Sulvanjoki[8]	River affected by Acidic Sulfate Soils	Finland	5.23	170	1500	144	528	61	0.80
Global River Average[4,9]	River	-	-	282	1300	-	-	67-133	0.22

Note: Comparison of acid sulfate soil affected regions to normal regions. (Refs: 1-This study; 2-Macdonald et al., 2007; 3-Colbert and McManus, 2005; 4-Windom et al., 2000; 5-Coffey et al., 1997; 6- – Joung and Shiller, 2014; 7-Shaw et al., 1998; 8- Roos and Åström, 2005; 9-Bridgestock et al., 2021).

2.6 Conclusion

CASS regions are associated with enhanced trace metal loading due to the re-oxidation of minerals following soil drainage. Our continuous, detailed observations captured highly variable Ba and U fluxes in a CASS system before, during, and after a flood event. During dry conditions, seawater intrusion was the main factor impacting U and Ba distribution. As the CASS were inundated with flood waters, the surface runoff controlled the distribution of trace metals. Steady decline in surface waters while the water table remained high caused the system to become groundwater dominated, leading to high export fluxes of Ba and U. The flux of Ba and U from groundwater contributed up to 18% and 66% of the total Ba and U loads via surface water, respectively. Highly variable groundwater endmember concentrations bring uncertainties to these flux estimates, and in this case may underestimate the total fluxes of Ba and U from groundwater over the whole time series.

On a per area basis, CASS systems may contribute an order of magnitude higher Ba and U than rivers. On a local level, this can cause enhanced release of Ba and U during times of flood. While U and Ba loads from CASS are not a large influence on the global system, CASS systems are important from a regional perspective. Studies that focus on using Ba and U as proxies may want to take CASS inputs into account due to the enhanced fluxes to coastal regions. While Ba and U may not be quantitatively important from CASS systems, monitoring these elements could provide useful insight into groundwater influence and redox conditions in CASS affected areas. With the increased need for arable land and urbanization as the population continues to increase, and enhanced droughts due to climate change, draining of wetland areas will continue to

occur, leading to an expansion of CASS. The expansion of CASS will likely change local groundwater and surface water loads of trace metals. Hence, the impact of CASS systems on metal budgets into the coastal ocean is likely to continue growing.

2.7 Acknowledgements

International collaboration was triggered and kindly supported by the ASLO/LOREX program led by Prof. Adina Paytan. Field investigations were supported by a Hermon Slade Foundation grant (09-01) and the Australian Research Council (DP110103638) grants to IRS. We thank Bruce Heynatz and Jason de Weys for performing daily sampling and providing invaluable guidance. The Richmond River County Council provided water quality information. Metal analysis was performed by the NATA certified Environmental Analysis Laboratory in Lismore, Australia.

2.8 References

Beck, A. J., Tsukamoto, Y., Tovar-Sanchez, A., Huerta-Diaz, M., Bokuniewicz, H. J., Sanudo-Wilhelmy, S. A., 2007. Importance of geochemical transformations in determining submarine groundwater discharge-derived trace metal and nutrient fluxes. Applied Geochemistry 22(2), 477-490.

Boman, A., Fröjdö, S., Backlund, K., Åström, M.E., 2010. Impact of isostatic land uplift and artificial drainage on oxidation of brackish-water sediments rich in metastable iron sulfide. Geochimica et Cosmochimica Acta, 74(4), 1268-1281.

Bridgestock, L., Nathan, J., Paver, R., Hsieh, Y.T., Porcelli, D., Tanzil, J., Holdship, P., Carrasco, G., Annammala, K.V., Swarzenski, P.W., Henderson, G.M., 2021. Estuarine processes modify the isotope composition of dissolved riverine barium fluxes to the ocean. Chemical Geology 579, 120340.

Cánovas, C. R., Hubbard, C. G., Olías, M., Nieto, J. M., Black, S., Coleman, M. L, 2008. Hydrochemical variations and contaminant load in the Río Tinto (Spain) during flood events. Journal of Hydrology 350(1-2), 25-40.

Cao, Z., Siebert, C., Hathorne, E. C., Dai, M., Frank, M., 2016. Constraining the oceanic barium cycle with stable barium isotopes. Earth and Planetary Science Letters 434, 1-9.

Carter, S. C., Paytan, A., Griffith, E. M., 2020. Toward an improved understanding of the marine barium cycle and the application of marine barite as a paleoproductivity proxy. Minerals 10(5), 421.

Charette, M. A., Sholkovitz, E. R., 2006. Trace element cycling in a subterranean estuary: Part 2. Geochemistry of the pore water. Geochimica et Cosmochimica Acta 70(4), 811-826.

Charette, M.A., 2007. Hydrologic forcing of submarine groundwater discharge: Insight from a seasonal study of radium isotopes in a groundwater-dominated salt marsh estuary. Limnology and Oceanography 52(1), 230-239.

Coffey, M., Dehairs, F., Collette, O., Luther, G., Church, T., Jickells, T., 1997. The behaviour of dissolved barium in estuaries. Estuarine, Coastal and Shelf Science, 45(1), 113-121.

Colbert, D., McManus, J., 2005. Importance of seasonal variability and coastal processes on estuarine manganese and barium cycling in a Pacific Northwest estuary. Continental Shelf Research 25(11), 1395-1414.

Cook, B.I., Mankin, J.S., Marvel, K., Williams, A.P., Smerdon, J.E., Anchukaitis, K.J., 2020. Twenty-first century drought projections in the CMIP6 forcing scenarios. Earth's Future 8(6), e2019EF001461.

Descostes, M., Schlegel, M. L., Eglizaud, N., Descamps, F., Miserque, F., Simoni, E., 2010. Uptake of uranium and trace elements in pyrite (FeS2) suspensions. Geochimica et Cosmochimica Acta 74(5), 1551-1562.

de Weys, J., Santos, I.R., Eyre, B.D., 2011. Linking groundwater discharge to severe estuarine acidification during a flood in a modified wetland. Environmental Science & Technology 45 3310-3316.

Fanning, D.S., Rabenhorst, M.C., Fitzpatrick, R.W., 2017. Historical developments in the understanding of acid sulfate soils. Geoderma 308, 191-206.

Gonneea, M. E., Mulligan, A. E., Charette, M. A., 2013. Seasonal cycles in radium and barium within a subterranean estuary: Implications for groundwater derived chemical fluxes to surface waters. Geochimica et Cosmochimica Acta 119, 164-177.

Gou, L.F., Jin, Z., Galy, A., Gong, Y.Z., Nan, X.Y., Jin, C., Wang, X.D., Bouchez, J., Cai, H.M., Chen, J.B., Yu, H.M., 2020. Seasonal riverine barium isotopic variation in the middle Yellow River: Sources and fractionation. Earth and Planetary Science Letters 531, 115990.

Green, R., Macdonald, B. C. T., Melville, M. D., Waite, T. D., 2006. Hydrochemistry of episodic drainage waters discharged from an acid sulfate soil affected catchment. Journal of Hydrology 325(1-4), 356-375.

Hsieh, Y. T., Henderson, G. M., 2017. Barium stable isotopes in the global ocean: Tracer of Ba inputs and utilization. Earth and Planetary Science Letters 473, 269-278.

Johnston, S.G., Burton, E.D., Bush, R.T., Keene, A.F., Sullivan, L.A., Smith, D., McElnea, A.E., Ahern, C.R., Powell, B., 2010. Abundance and fractionation of Al, Fe and trace metals following tidal inundation of a tropical acid sulfate soil. Applied Geochemistry 25, 323-335.

Johnston, S.G., Slavich, P.G., Hirst, P., 2005. Changes in surface water quality after inundation of acid sulfate soils of different vegetation cover. Australian Journal of Soil Research 43, 1-12.

Joung, D., Shiller, A. M., 2014. Dissolved barium behavior in Louisiana Shelf waters affected by the Mississippi/Atchafalaya River mixing zone. Geochimica et Cosmochimica Acta 141, 303-313.

Karimian, N., Johnston, S.G. and Burton, E.D., 2018. Iron and sulfur cycling in acid sulfate soil wetlands under dynamic redox conditions: A review. Chemosphere 197, 803-816.

Kinsela, A.S., Denmead, O.T., Macdonald, B.C., Melville, M.D., Reynolds, J.K., White, I., 2011. Field-based measurements of sulfur gas emissions from an agricultural coastal acid sulfate soil, eastern Australia. Soil Research 49(6), 471-480.

Ku, T. L., Knauss, K. G., Mathieu, G. G., 1977. Uranium in the open ocean: concentration and isotopic composition. Deep-Sea Research 24, 1005-1017.

Ljung, K., Maley, F., Cook, A., Weinstein, P., 2009. Acid sulfate soils and human health - A Millennium Ecosystem Assessment. Environment International 35, 1234-1242.

MacDonald, B., I. White, A. Keene, M. Melville, J. Reynolds. 2004. Acidity, metals and acid sulfate soils. 3rd Conference SuperSoil Australian - New Zealand Soils. University of Sydney, Australia. www.regional.org.au/au/asssi/.

Macdonald, B. C. T., White, I., Åström, M. E., Keene, A. F., Melville, M. D., Reynolds, J. K., 2007. Discharge of weathering products from acid sulfate soils after a rainfall event, Tweed River, eastern Australia. Applied Geochemistry 22(12), 2695-2705.

Min, G.R., Edwards, R.L., Taylor, F.W., Recy, J., Gallup, C.D., Beck, J.W., 1995. Annual cycles of UCa in coral skeletons and UCa thermometry. Geochimica et Cosmochimica Acta 59(10), 2025-2042.

Moore, W. S., 1997. High fluxes of radium and barium from the mouth of the Ganges-

Brahmaputra River during low river discharge suggest a large groundwater source. Earth and Planetary Science Letters 150(1-2), 141-150.
Moore, W.S., Shaw, T.J., 2008. Fluxes and behavior of radium isotopes, barium, and uranium in seven Southeastern US rivers and estuaries. Marine Chemistry 108, 236-254.
Mosley, L.M., Biswas, T.K., Cook, F.J., Marschner, P., Palmer, D., Shand, P., Yuan, C., Fitzpatrick, R.W., 2017. Prolonged recovery of acid sulfate soils with sulfuric materials following severe drought: causes and implications. Geoderma 308, 312-320.
Mulvey, P., 1993. Pollution, prevention and management of sulphidic clays and sands. In 'Proceedings National Conference on Acid Sulphate Soils'. (Ed. R Bush). pp.116-129.
Newton, A., Icely, J., Cristina, S., Perillo, G.M., Turner, R.E., Ashan, D., Cragg, S., Luo, Y., Tu, C., Li, Y., Zhang, H., 2020. Anthropogenic, direct pressures on coastal wetlands. Frontiers in Ecology and Evolution 8, 144.
Ourbak, T., Correge, T., Malaizé, B., Le Cornec, F., Charlier, K., Peypouquet, J.P., 2006. A high-resolution investigation of temperature, salinity, and upwelling activity proxies in corals. Geochemistry, Geophysics, Geosystems 7(3).
Porcelli, D., Swarzenski, P. W., 2003. The behavior of U-and Th-series nuclides in groundwater. Reviews in Mineralogy and Geochemistry 52(1), 317-361.
Powell, B., Martens, M., 2005. A review of acid sulfate soil impacts, actions and policies that impact on water quality in Great Barrier Reef catchments, including a case study on remediation at East Trinity. Marine Pollution Bulletin 51(1-4), 149-164.
Proske, U., Heijnis, H., Gadd, P., 2014. Using X-ray fluorescence core scanning to assess acid sulfate soils. Soil research 52(8), 760-768.
Riedel, T., Kübeck, C., 2018. Uranium in groundwater–a synopsis based on a large hydrogeochemical data set. Water research 129, 29-38.
Roos, M., Åström, M., 2005. Hydrochemistry of rivers in an acid sulphate soil hotspot area in western Finland. Agricultural and Food Science, 14(1), 24-33.
Sanders, C.J., Santos, I.R., Sadat-Noori, M., Maher, D.T., Holloway, C., Schnetger, B., Brumsack, H.-J., 2017. Uranium export from a sandy beach subterranean estuary in Australia. Estuarine, Coastal and Shelf Science 198, Part A, 204-212.
Santos, I. R., Burnett W. C., Misra S., Suryaputra, I. G. N. A., Chanton J. P., Dittmar, T., Peterson, R. N. , Swarzenski P. W., 2011b. Uranium and barium cycling in a salt wedge subterranean estuary: the influence of tidal pumping. Chemical Geology 287(1-2), 114-123.
Santos, I.R., de Weys, J., Eyre, B.D., 2011a. Groundwater or floodwater? Assessing the pathways of metal exports from a coastal acid sulfate soil catchment. Environmental Science & Technology 45, 9641-9648.
Santos, I. R., de Weys, J., Tait, D. R., Eyre, B. D., 2013. The contribution of groundwater discharge to nutrient exports from a coastal catchment: post-flood seepage increases estuarine N/P ratios. Estuaries and coasts 36(1), 56-73.
Santos, I. R., Eyre, B. D., 2011. Radon tracing of groundwater discharge into an Australian estuary surrounded by coastal acid sulphate soils. Journal of hydrology 396(3-4), 246-257.

Sammut, J., White, I., Melville, M. D., 1996. Acidification of an estuarine tributary in eastern Australia due to drainage of acid sulfate soils. Marine and Freshwater Research 47(5), 669-684.
Sarin, M. M., Church, T. M., 1994. Behaviour of uranium during mixing in the Delaware and Chesapeake estuaries. Estuarine, Coastal and Shelf Science 39(6), 619-631.
Scott, T. B., Tort, O. R., Allen, G. C., 2007. Aqueous uptake of uranium onto pyrite surfaces; reactivity of fresh versus weathered material. Geochimica et Cosmochimica Acta 71(21), 5044-5053.
Shaw, T.J., Moore, W.S., Kloepfer, J., Sochaski, M.A., 1998. The flux of barium to the coastal waters of the southeastern USA: the importance of submarine groundwater discharge. Geochimica et Cosmochimica Acta 62, 3047-3054.
Sinclair, D.J., McCulloch, M.T., 2004. Corals record low mobile barium concentrations in the Burdekin River during the 1974 flood: evidence for limited Ba supply to rivers?. Palaeogeography, Palaeoclimatology, Palaeoecology 214(1-2), 155-174.
Swarzenski, P., Campbell, P., Porcelli, D., McKee, B., 2004. The estuarine chemistry and isotope systematics of 234,238U in the Amazon and Fly Rivers. Continental Shelf Research 24, 2357-2372.
Taffs, K. H., Farago, L. J., Heijnis, H., Jacobsen, G., 2008. A diatom-based Holocene record of human impact from a coastal environment: Tuckean Swamp, eastern Australia. Journal of Paleolimnology, 39(1), 71-82.
Toole, J., Baxter, M. S., Thomson, J., 1987. The behaviour of uranium isotopes with salinity change in three UK estuaries. Estuarine, Coastal and Shelf Science 25(3), 283-297.
Turekian, K. K., Chan, L. H., 1971. The marine geochemistry of uranium isotopes, 23°Th and 231Pa. In 'Activation Analysis in Geochemistry and Cosmochemistry' (Brunfelt, A. O. & Steinnes, E., eds). Universitetsforlaget, Oslo, pp. 311-320.
Waite, T.D., Davis, J.A., Payne, T.E., Waychunas, G.A., Xu, N., 1994. Uranium(VI) adsorption to ferrihydrite: application of a surface complexation model. Geochimica et Cosmochimica Acta 58, 5465-5478.
Ward, N.J., Sullivan, L.A., Bush, R.T., 2004. Soil pH, oxygen availability, and the rate of sulfide oxidation in acid sulfate soil materials: implications for environmental hazard assessment. Australian Journal of Soil Research 42, 509-514.
Webb, J. R., Santos, I. R., Tait, D. R., Sippo, J. Z., Macdonald, B. C., Robson, B., Maher, D. T., 2016. Divergent drivers of carbon dioxide and methane dynamics in an agricultural coastal floodplain: Post-flood hydrological and biological drivers. Chemical Geology, 440, 313-325.
Wersin, P., Hochella Jr, M.F., Persson, P., Redden, G., Leckie, J.O., Harris, D.W., 1994. Interaction between aqueous uranium (VI) and sulfide minerals: spectroscopic evidence for sorption and reduction. Geochimica et Cosmochimica Acta 58(13), 2829-2843.
Windom, H., Niencheski, F., 2003. Biogeochemical processes in a freshwater-seawater mixing zone in permeable sediments along the coast of Southern Brazil. Marine Chemistry 83 121-130.
Windom, H., Smith, R., Niencheski, F., Alexander, C., 2000. Uranium in rivers and

estuaries of globally diverse, smaller watersheds. Marine Chemistry 68(4), 307-321.
Wong, V.N.L., Johnston, S.G., Bush, R.T., Sullivan, L.A., Clay, C., Burton, E.D., Slavich, P.G., 2010. Spatial and temporal changes in estuarine water quality during a post-flood hypoxic event. Estuarine, Coastal and Shelf Science 87, 73-82.
Wu, Y., Fallon, S.J., Cantin, N.E., Lough, J.M., 2021. Assessing multiproxy approaches (Sr/Ca, U/Ca, Li/Mg, and B/Mg) to reconstruct sea surface temperature from coral skeletons throughout the Great Barrier Reef. Science of the Total Environment 786, 14739

CHAPTER III - THE EFFECTS OF SUBMARINE GROUNDWATER DISCHARGE (SGD) AND THE BONNET CARRÉ SPILLWAY ON NUTRIENT DYNAMICS IN THE WESTERN MISSISSIPPI SOUND

3.1 Abstract

The Mississippi Sound is an estuary in the northern Gulf of Mexico that is susceptible to eutrophication and hypoxia, both of which have led to habitat degradation and organism mortality. In this study, we explore the potential forcing factors that contribute to the Sound's decline in water quality such as local river flooding, submarine groundwater discharge (SGD), and the 2019 opening of the Bonnet Carré Spillway. When the Bonnet Carré Spillway was open, the western part of the Sound experienced rapid and severe drops in salinity, as well as high influxes of nutrients that changed the geochemical composition of the Sound. When the Spillway was closed, broad spatial surveys of radon along the coast and offshore indicated that areas prone to localized fish kills had higher levels of groundwater seepage. Nearshore water measurements of radium (^{224}Ra and ^{228}Ra) were used to calculate the groundwater flux at five stations across the western Sound. These fluxes were on the order of 50 cm d^{-1}. Measured reduced constituents (DON, NH_4^+ and CH_4) introduced to the Sound from SGD have a high potential oxygen demand representing about half of the typical summer oxygen saturation. Addition of unmeasured S^{2-} and DOC may increase the oxygen demand further. Submarine groundwater discharge nutrient fluxes were also higher than that of the local rivers for reduced nitrogen species and phosphate, and when river fluxes are low, the groundwater is the dominant source of all nutrients to the Sound. Therefore,

submarine groundwater discharge is an important part of the Sound biogeochemistry and should be taken into consideration when making management decisions.

3.2 Introduction

Submarine groundwater discharge (SGD) is a global phenomenon that occurs not only as diffuse input along coastlines (Burnett et al., 2003; Taniguchi et al., 2002), but also throughout continental shelves (Moore and Shaw, 1998). SGD represents the advective flow of both fresh terrestrial groundwater and seawater circulating through aquifer sediments into the coastal ocean (Moore, 1999). SGD is not defined by composition, origin, or what drives the flow, as these can vary based on the area where it is observed (Burnett et al., 2003). The concentration of materials such as radium, barium, radon, carbon and nutrients in the water being discharged is often higher than that of rivers, making it a significant source of these constituents to the coastal ocean (Moore, 2010; Slomp and Van Cappellen, 2004). However, SGD inputs are difficult to constrain and, thus, it has been an overlooked part of oceanic margin elemental fluxes (Taniguchi et al., 2002). The role and scope of SGD in the environment is still not completely understood, and depending on the location where it is occurring, SGD may have varying impacts on the ecosystem.

The original intent of this study was to understand the impact of SGD in the Mississippi Sound; however, while sampling was being conducted in 2019, there was a prolonged opening of the Bonnet Carré Spillway (BCS), which diverted Mississippi River flood water into Lake Pontchartrain, and then into the Mississippi Sound (Dzwonkowski et al., 2018; Parra et al., 2020; Figure 3.1). The 2019 opening lasted 123 days, causing extreme salinity declines across the western section of the Mississippi

Sound, leading to organism mortality, and a harmful algal bloom (HAB) (Gledhill et al., 2020; Byrd, 2019). While this was an unprecedented event, as climate change starts to increase precipitation across the continental United States (Davenport and Diffenbaugh, 2021), there is the possibility that such openings will become more frequent, and therefore the impact of the BCS needs to be understood in relation to natural sources of nutrients.

The area of interest for this study is focused on a time series conducted on the western section of the Mississippi Sound from Waveland, MS, to Biloxi, MS. (Figure 3.1). This area was chosen for its close proximity to oyster reefs that line the coastline, and the occurrence of "jubilee" (fish kill) events that occur occasionally during the summer months (Dugas and Joyce, 1997; Overstreet and Hawkins, 2017). The western Sound has a lower salinity than both the central and eastern Sound; the salinity is highly variable depending on river discharge, which is mainly from the Pearl River in this region (NOAA, 1997). The importance of this region to fisheries (Dugas and Joyce, 1997), makes it imperative to understand what affects the local water quality. This region of the Sound also experiences occasional hypoxia which has been attributed to several factors, including extreme heating of the water combined with no wind mixing (MDMR, 2017; Darnell, 1992), the degradation of harmful algal blooms (Darnell, 1992; Soto et al., 2018), and stratification due to the opening of the BCS and increased local river flux that changes seasonally (Eleuterius, 1978; Ho et al., 2019).

The fill kill events occurring in the western Mississippi Sound are often described as "low oxygen events" (https://www.mdeq.ms.gov/water/field-services/fish-kills/). Hypoxic conditions along the shoreline of estuaries leading to fish kills are not

uncommon, and often occur during the summer months when ambient dissolved oxygen levels are already low (e.g., Montiel et al., 2019). Submarine groundwater discharge is often enriched in reduced substances, such as dissolved organic carbon (DOC), ammonium (NH_4^+), methane (CH_4), and sulfide (S^{2-}) which have a high oxygen demand. These substances can have significant dissolved oxygen (DO) demand, which can push a system to hypoxia (e.g., Peterson et al., 2016; Guo et al., 2020; Sanial et al., 2021).

Areas of impermeable surfaces are currently increasing along the Mississippi shoreline as population increases in this agri-urban landscape (Sherif, 2018). Impermeable surfaces increase surface runoff, limiting the ability of aquifers to recharge with fresh water (Vázquez-Suñé et al., 2010). This limited freshwater recharge enhances seawater circulation into and through the aquifer (Vázquez-Suñé et al., 2010). This, along with increased pumping from the aquifer, could cause higher levels of seawater intrusion into the aquifer, which can have impacts such as driving release of ions and ultimately increasing the amount of nutrients and metals that are delivered to coastal waters by SGD (Khublaryan et al., 2008; Moore, 2010). Replacing fresh water with seawater in coastal aquifers introduces a powerful oxidizing agent, sulfate (S042-), that releases dissolved metals, carbon and nutrients from organic matter and adds sulfide to the system (Moore & Joye, 2021). Anthropogenic input of nutrients to coastal aquifers can also increase the amount of nutrients that are released by SGD, which can have detrimental effects on both the quality of the groundwater itself, and the surface water affected by SGD (Greenwood et al., 2013; Moore, 2010b; Slomp and van Cappellan, 2004). Another anthropogenic impact is overall climate change, which is expected to increase total precipitation, and increase the number of severe precipitation events (e.g., Davenport and Diffenbaugh,

2021). This has the potential to require more openings of the BCS, which will in turn cause excess nutrients to enter the Mississippi Sound, leading to eutrophication and hypoxia.

In this paper, we hypothesize that SGD plays an important role in nutrient fluxes to the Mississippi Sound and can be a driving factor behind hypoxic conditions that lead to fish kills. Here, we quantify fluxes of SGD using three radioisotopes (^{224}Ra, ^{228}Ra, and ^{222}Rn), calculate the nutrient fluxes and potential oxygen demand for reduced species to determine the overall impact of SGD in an area that is prone to hypoxia and fish kills. We also investigate the impact of the BCS opening compared to more "normal" conditions, and how the impact of this event compares to SGD and local coastal rivers as a source of nutrients. This work especially highlights the shift in dominant nutrient sources within estuaries seasonally and through episodic events, which has not been well studied.

3.3 Methods

3.3.1 Study Site

The Mississippi Sound is an elongate estuary located along the coastline of Mississippi and parts of Alabama in the southeastern United States (Figure 3.1). It is classified as a well-mixed estuary, but may experience localized stratification, occurring mostly around the shipping channels (Eleuterius, 1978). River flow is highest and salinity lowest from February – April, while August – October typically experiences reduced river flow and higher salinities (Orlando et al., 1993). The Sound is separated from the Mississippi Bight by a string of barrier islands that limit mixing with offshore waters (Figure 3.1). The estuary has diurnal tides with an average range of 0.57 m (Eleuterius, 1978). Several major freshwater sources affect the Sound, including the Pearl and

Pascagoula Rivers, as well as the Tensaw and Mobile Rivers that flow into Mobile Bay before entering the Sound. Minor freshwater sources include the Tchoutacabouffa and Biloxi Rivers as well as the Jourdan and Wolf Rivers that flow into Saint Louis Bay. Occasionally, the Sound is impacted by openings of the BCS, releasing water from the Mississippi River into Lake Pontchartrain, and which then flows through the Rigolets and Chef Menteur Passes into the western Mississippi Sound (Figure 3.1). This can cause the salinity of the Sound, especially in the western section, to decline rapidly to near 0, whereas average salinities in the Sound range from 10 to 25 (USGS). In 2019, the BCS was opened from February 27 – April 11, and May 10 – July 27. This was an unprecedented event in terms of duration, total discharge, and the two openings in one year (https://www.mvn.usace.army.mil/Missions/Mississippi-River-Flood-Control/Bonnet-Carre-Spillway-Overview/).

During the sampling, between July 2017 through November 2019, there were three occasions where dead or dying fish were observed in the water or on the beach. The first kill was in July 2017 and we collected samples two days after the kill was reported; it was labelled a jubilee event due to low oxygen by MDMR (2017). The second kill was on August 28, 2018, with dead fish observed in the water across the entire sampling area; the cause of this fish kill is unknown. The final kill was on September 5, 2019, and dead and dying fish were observed on only one section of beach; this was labeled a jubilee by MDMR officials on site due to low oxygen.

The majority of the bottom sediments within the Sound are silts, which—while often not conducive for SGD—can be easily penetrated by structures and sandy intrusions, allowing for groundwater release (Kim et al., 2005; Neuzil, 1986; Sawyer et

al., 2001). There is also the presence of paleochannels, which have previously been described to enhance SGD flow (Attisano et al., 2013; Mulligan et al., 2007). Renken (1998) has summarized the extensive aquifer formations that lie beneath the state of Mississippi and extend out towards the shelf. There are two major aquifer systems that affect the coastline, one overlain on another (Figure A.1). The surficial system is the Coastal Lowland Aquifer System (CLAS), which extends from southern Texas to westernmost Florida. This aquifer system extends into the Gulf of Mexico across the shelf, but the offshore areas are mostly saline. The CLAS consists of five permeable zones, and the lithology is interbedded sand and clay. The freshwater section of the aquifer is actively pumped for agriculture, industrial, and public use. The Mississippi, Pearl, and Red Rivers flow above this system and are the major contributors, along with rainfall, to recharging the aquifer. Underneath the CLAS is the Mississippi Embayment Aquifer System (MEAS), separated by the Vicksburg-Jackson confining unit. This aquifer system flows from parts of Kentucky and Illinois to offshore of the Mississippi Sound into the Mississippi Bight. A confining unit separates the two aquifer systems and advective SGD is most likely from only the CLAS because the Mississippi embayment aquifer system only breaches the confining layers on land.

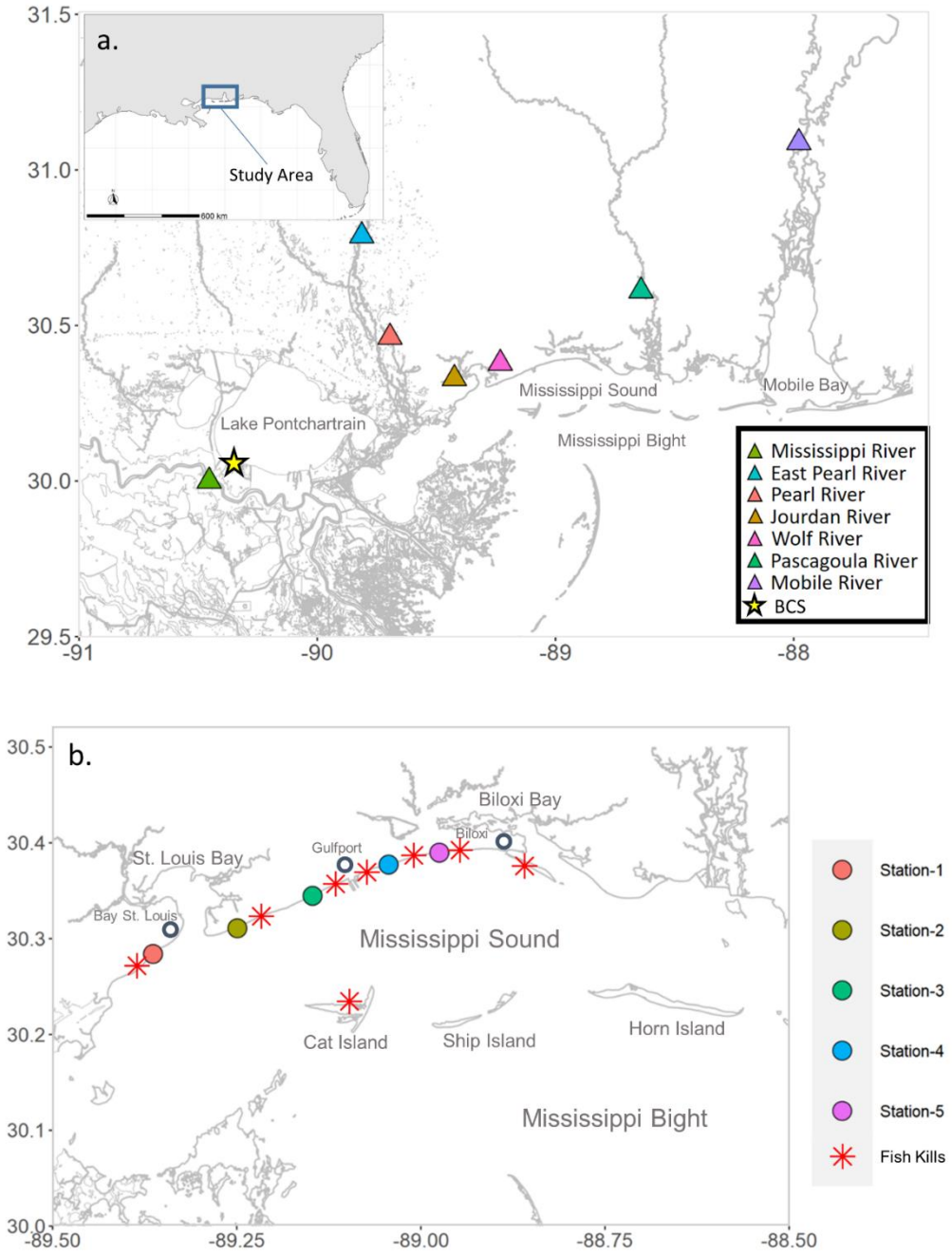

Figure 3.1 *Regional and station map of study area.*

a) Regional map of study area with river station locations denoted by triangles, and the BCS location denoted by a star.

b) Map of the western Mississippi Sound. Stations are colored circles, historic fish kill locations are red stars.

3.3.2 Sample Collection

Nearshore hypoxic events have historically been prevalent along the coastline, especially by Biloxi, MS, and extending westward (Engle et al., 1997; Gunter and Lyles, 1979; Overstreet, 1978). Therefore, we developed a time series of five stations along the beaches of the Sound in this region (Figure 3.1) conducted between July 2017 and November 2019. The time series was conducted in two stages: initial response sampling and the continuous time series. The initial sampling was conducted in July 2017 in response to a fish kill attributed to low oxygen; subsequent samples were collected in October 2017 to begin characterizing the baseline. The majority of the time series measurements were conducted between June 2018 and November 2019 and included surface water samples and push-point groundwater samples. Gaps in the monthly time series occurred when conditions were not suitable for field work (i.e., harmful algal blooms, foul weather, lack of sampling support). In support of the beach sampling, radon surveys along the beaches and further into the Sound were conducted in October and December 2018, February, April, July, and October 2019, February 2020, November 2020, and April 2021.

Beach time series surface water samples were collected by two methods. In summer months, when wind conditions and weather were favorable, an inflatable raft was positioned at the desired location and surface waters were collected. This was done in order to prevent contact with the bottom, which could stir up sediments and instigate a release of pore waters. This is particularly a problem in the summer months when sediments can become anoxic and disturbing them could facilitate release of reduced substances. In winter months, when conditions were often not feasible for the raft,

buckets and trace metal clean grab samplers were used to collect samples from a nearby pier, thereby reducing sediment disturbance. Regardless of the season, samples were collected for radium (20 L), barium (250 mL), nutrients (250 mL), and methane (70 mL); sample methods are described in following section.

Groundwater time series samples were collected using a PushPoint (MHE Products) on the beach. The PushPoint is a thin steel tube with a pointed tip that contains screen zones where water can enter. The device is inserted into the ground with a twisting motion until resistance, and then a guard rod is removed from the inside of the PushPoint to open the tube. Water can then be pumped up. To sample the beach groundwater, holes were dug down to the water table, and then the PushPoint was inserted to max depth (~ 2 m) and a peristaltic pump was used to pump water up the PushPoint, which was then collected. These samples were collected starting in November 2018 and were taken nearly every month until August 2019. Samples included radium (5-10 L), barium (250 mL), nutrients (250 mL), methane (70 mL), and radon (20-40 mL); sample methods are described in following section.

River samples were collected from October 2015 to June 2016. In total, five samples were collected for radium, nutrients, and trace elements. These were collected from the Pearl River, which is the river closest to the study site, and therefore would have the highest impact. One suspended particulate matter (SPM) sample and desorbed sample was also collected from the Pearl River, MS in May 2018 (Figure 3.1). To investigate the ^{224}Ra that could possibly desorb from particulate material delivered by rivers, we followed the same procedure as Sanial et al. (2021). Briefly, two large volume samples were collected. One was immediately filtered through a 0.45 µm capsule filter and then

through a cartridge of manganese coasted acrylic fiber (Mn-fiber; see below). The other sample was taken back to the lab, where the salinity was artificially increased to 29 using solar salt crystals, and then circulated for 24 hours, filtered through a 0.45 µm capsule filter, and then through Mn-fiber. The desorbed ^{228}Ra river sample was reported in Sanial et al. (2021).

Radon survey measurements were collected using a RAD7 radon detector equipped with a RAD AQUA air-water equilibrator (Durridge; Billerica, MA). Water was pumped from the sample location into the RAD AQUA at 7 L min^{-1}, and the internal pump of the RAD7 was used to circulate the air at 1 L min-1. Radon in air measurements were then recalculated to radon in water using the Rn solubility coefficient as a function of water temperature and salinity (Schubert et al., 2012). Temperature measurements in the air-water equilibrator were collected every 2 minutes on a data logger from the air-water equilibrator (Lascar, EL-USB-TC, EasyLog Thermocouple Temperature Data Logger).

Physical parameters (temperature, salinity, and oxygen) were collected using YSI sondes; either a handheld probe (PRO30) for groundwater samples, or multiparameter sonde (EXO2) for surface water samples. Other parameters such as local river discharge and tide data were collected from USGS and NOAA websites, respectively.

3.3.3 Analytical Methods

Radium was extracted from samples for analysis using manganese coated acrylic fiber (Mn-fiber, e.g., Moore, 2008); samples were passed through the Mn-fiber cartridge at no faster than 1 L min^{-1}. Once this was complete, the fiber was washed with radium-free deionized water to remove any sediment/salt, and then partially dried. Fibers were

then weighed, placed into sample tubes, and connected to a Radium Delayed Coincidence Counter (RaDeCC; Scientific Computer Instruments). Samples were run until there were at least 1000 counts for ^{220}Rn, or until the counts stabilized (i.e., counts vs time was a straight line). The samples were each analyzed three times (immediately after sampling, one week after sampling, and one month after sampling) in order to determine ^{223}Ra and ^{224}Ra (Moore and Arnold, 1996). Once the three runs had been completed, the values were determined and corrected through calculations outlined by Garcia-Solsona et al. (2008), Griffin et al. (1963), and Moore and Arnold (1996). Analytical uncertainties are around 7% for ^{224}Ra and 12% for ^{223}Ra (Garcia-Solsona et al., 2008). The longer half-life isotope (^{228}Ra and ^{228}Ra) concentrations were determined through gamma ray spectrometry. To prepare the sample for the gamma ray spectrometer, the Mn-fibers were first leached with a combination of hydroxylamine hydrochloride (HAHCl) and hydrochloric acid (HCl), then coprecipitated with BaSO4. After three weeks, which allows for ^{222}Rn to equilibrate with ^{228}Ra, they were measured on the gamma ray spectrometer (Moore, 1996).

The diffusive Ra flux from sediments was determined experimentally (Rodellas et al., 2012). Surficial sediment samples were collected from the Mississippi Sound in October, 2020. Sediments were placed into an incubation chamber, where they were aerated and water was continuously pumped through a Mn-fiber column to extract the radium (Rodellas et al, 2012). This procedure was repeated five times for different time intervals (24 hr, 48 hr, 72 hr, 96 hr, and 120 hr). The diffusive flux was estimated from the best fit slope of the ^{224}Ra activity per surface area of sediments (dpm m^{-2}) versus time (d) (Figure A.2).

Water samples for oxygen and hydrogen stable isotopes ($^{18}O/^{16}O$ and D/H) were filtered (0.45 µm Whatman Puradisc 25 PP filter) and stored in dark glass bottles that were sealed until measurement to prevent evaporation. The $\delta^{18}O$ and δD analysis was conducted using isotope ratio infrared spectroscopy (L2120-i cavity ring-down spectrometer, Picarro Inc.). The data were calibrated using reference waters that are standardized to the VSMOW reference material and drift corrections were done following van Geldern and Barth (2012). The analytical uncertainty of the $\delta^{18}O$ and δD measurements were 0.07‰ and 0.5‰ (1 σ). The *d-excess*, or deviation from the Global Meteoric Water Line was calculated as d- excess = $\delta D - 8 \times \delta^{18}O$.

Dissolved methane (CH_4) samples were collected and measured according to the method of Roberts and Shiller (2015). Seventy-milliliter water samples were collected in an air-tight 140 mL syringe in the field, taking care to not introduce air bubbles into the syringe. Samples were immediately put on ice to minimize biological activity. Once back in the lab, we introduced a zero air headspace (gas mix with very low methane; 70 mL) to each sample syringe. Samples were then placed on a shaker table for approximately 30 minutes to allow the introduced headspace to reach equilibrium with the water and to allow the water to reach close to room temperature. The equilibrated headspace was then transferred to a clean, dry syringe and analyzed by cavity ring-down spectroscopy (CRDS; Picarro G2301). Zero air gas samples, and transfers of zero air between syringes, were analyzed to determine the concentration of methane in the zero air and the amount of contamination introduced during syringe transfers. The mass balance equation makes use of solubility equations from Wiesenburg and Guinasso (1979) and Henry's Law.

Nutrient samples were collected in 250 mL, acid washed, Nalgene polyethylene bottles. After collection, samples were filtered (0.45 µm Whatman Puradisc 25 PP filter) into a 125 mL acid-washed plastic brown bottle, and frozen. Samples were run on a Seal Auto Analyzer (AA3) for ammonium, nitrate+nitrite, phosphate, and silicate. Regressions of $r > 0.95$ for the standard curves were used for each run to ensure sample accuracy. Organic nutrient concentrations were determined via a chemical method, outlined in the Seal AA3 manual. To make the oxidizing reagent, 15 g of boric acid, 25 g of recrystallized potassium persulfate, and 7.5 g of sodium hydroxide were diluted to 500 mL with water. To digest the samples, 5 mL of the oxidizing reagent was added to 50 mL of sample and heated at 115 ºC for 2 hours. The pH was checked after each digestion to ensure it was around 8. Samples were then run using the phosphate and nitrate methods outlined in the Seal AA3 manual.

Two trace elments, Ba and Cs were examined in this study to help understand distributions of tracers. Barium is a geochemical analog to Ra, but unlike Ra it does not undergo radioactive decay. Cesium is highly enriched in St Louis Bay (Bera et al., 2015). Water from the Bay enters the Sound and therefore may be an important water source at certain times of the year. Trace element samples were collected in 250 mL acid washed HDPE bottles. Once collected, samples were filtered (pre-cleaned 0.45 µM Whatman Puradisc 25 PP filter) into 15 mL acid washed bottles and acidified to $pH < 2$ with 6 N ultraclean HCl (Seastar Baseline). After acidification, samples were stored in a clean space at room temperature until analysis on a high resolution inductively coupled plasma mass spectrometer (HR-ICP-MS) for Ba, Cs, Cr, Fe, Mn, Mo, Re, U and V. Concentrations were determined using an isotope dilution method (Ho et al., 2019; Joung

and Shiller, 2013). Briefly, samples were diluted 20-fold with 0.3 M ultrapure HNO3 (Seastar Baseline) that contained a known amount of In, and enriched ^{50}V, ^{57}Fe, ^{95}Mo, ^{135}Ba and ^{185}Re (Oak Ridge National Laboratories). The In response was used for instrument drift correction and sensitivity checks. Concentrations of V, Fe, Mo, Ba, and Re were calculated from the isotopic ratios and the known isotopic spike. Cs and U were determined in low resolution, and the instrumental drift was corrected by a response factor derived from the instrumental response (cps/nM) of ^{95}Mo and ^{135}Ba. Cr and Mn were determined in medium resolution, and the instrumental drift was corrected by a response factor derived from the instrumental response of ^{57}Fe. Calibrations for Cs, Mn, Cr, and U were performed by standard additions to a seawater sample (Shim et al., 2012).

3.4 Results and Discussion

3.4.1 Qualitative Analysis of SGD

Using water isotope data (δ^{18}O and δD), we can evaluate the main contributors of fresh water to the Sound (Figure 3.2). Sanial et al. (2019) previously showed that the Mississippi River (δ^{18}O ~ -6.6 ± 0.3‰) and local rivers (δ^{18}O ~ -3.6 ± 0.2‰) were the main fresh water contributors to the Mississippi Bight. In the Sound, if there were only mixing between offshore waters and rivers, we would expect the samples to fall along the mixing line between the local rivers and the Bight water or when the BCS is open between the Mississippi River and Bight water. However, for Sound time series samples pre-BCS, during the BCS, in September 2020, and during an April 2021 radon survey, the δ^{18}O samples often fell above the mixing line for Bight waters and the Pearl River (Figure 3.2). There was also a change in the δ^{18}O composition in the water column when the BCS was opened. Post-BCS samplings right after the second closure indicated that

the surface waters were tracking more towards the Mississippi River endmember (Figure 3.2). Thus, while our data are generally compatible with the analysis of Sanial et al. (2019), they also clearly show evidence of an additional isotopically heavier fresh water component for the Mississippi Sound. Since many of the fresh groundwater samples were also isotopically heavy, this implies that the additional fresh endmember is groundwater; and, given that this endmember also influences the mixing trends (Figure 3.2), there must be significant groundwater influence in the Sound time series.

The Mississippi Sound has distinct changes in salinity year round, mainly due to changes in river discharge, wind direction, circulation patterns, and the BCS (Armandei et al., 2021; Cambazoglu et al., 2017; Hode, 2019). Evaporation (E) and precipitation (P) may also be important contributors to the isotopic signatures in the Sound, but there is limited data exploring this part of the freshwater balance. The *d-excess* of the samples was used to investigate the importance of E (Dansgaard, 1964; Figure 3.2b), with negative deviation from the Global Meteroric Water Line (GMWL) suggesting influence of E (Frohlich et al., 2001). Several studies (Dinnel and Wiseman, 1986; Etter et al., 2004) have determined that E in this region is not as important as river influences, though Etter et al., (2004) noted that E can have a potentially significant effect on the freshwater balance during the fall. When plotting *d-excess* vs salinity, the surface water samples plot along a mixing line of the local rivers and higher salinity Sound waters (Figure 3.2). Some samples fall below the 2 sigma intervals of the trend line for all Sound samples,

indicating a higher influence of E. These samples occur during the summer and fall months, when there can be high levels of evaporation due to the temperature.

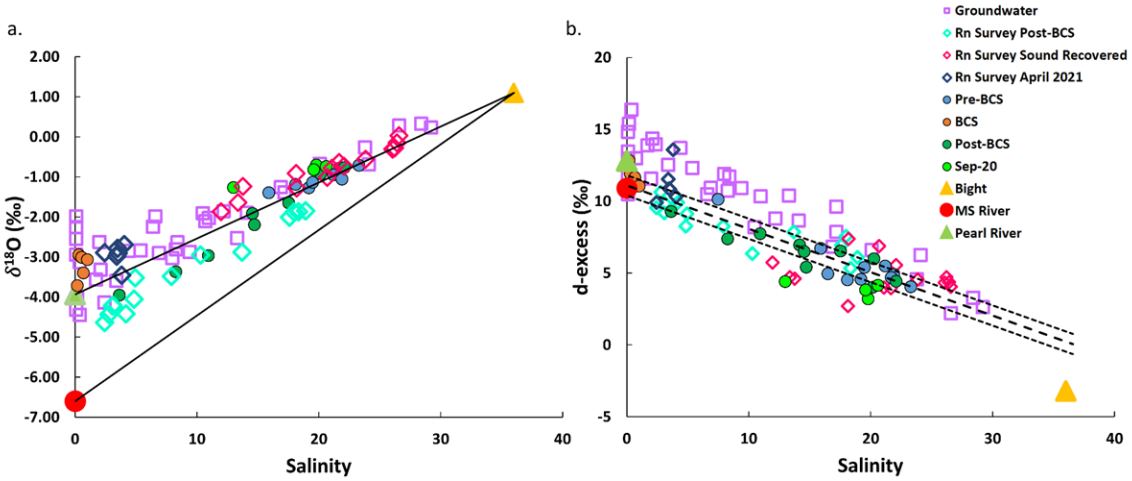

Figure 3.2 *Oxygen isotopes and d-excess versus salinity.*

a) Oxygen isotope composition ($\delta^{18}O$) of groundwater, Pearl River water, Bight water, time series surface samples, and radon survey surface samples. Mixing lines between the Bight water and both the Pearl River and Mississippi River are in black.

b) Deviation of isotopic composition from the Global Meteoric Water Line (*d-excess*=$\delta D - 8\times\delta^{18}O$) as a function of salinity. The black dashed lines indicate the surface water regression and 2-sigma confidence limits.

Other tracers also can be used to determine if there is a distinct groundwater signature in Sound surface waters. Radium is highly enriched in groundwater and has a quartet of isotopes (^{224}Ra $T_{1/2}$ = 3.66 days; ^{223}Ra $T_{1/2}$ = 11.4 days; ^{228}Ra $T_{1/2}$ = 5.75 years; ^{226}Ra $T_{1/2}$ = 1600 years) that can be used to estimate SGD water fluxes (e.g., Rodellas et al., 2017). Often, ^{223}Ra is not used in balances because it is the isotope with the largest uncertainties, and is well correlated with ^{224}Ra (Rodellas et al., 2017). Comparing the percent composition of three radium isotopes (^{224}Ra, ^{228}Ra, ^{228}Ra) between river water, Sound water, and groundwater can help to distinguish the sources (Figure 3.3). Another qualitative assessment that can be made is through the use of fixed nitrogen speciation. Groundwater often has nitrogen in a more reduced form while rivers are often more

oxidized (Santos et al., 2021). When looking at the nitrogen species percent composition (Figure 3.3), it can be seen that Sound water nitrogen is more closely related to the groundwater endmember. However, radium is more complex, with rivers having a large impact on the radium balance, especially that of the short-lived isotope (^{224}Ra). Using the ternary plots, we are able to see distinctions between the groundwater and river water endmembers for radium and for nutrients, which will allow for a quantitative assessment of both. The bioactivity of nutrients and short half-life of ^{224}Ra have the similar problem that there may be changes in composition with time away from sources, but what can be seen is that the nearshore Sound waters seem to be a combination of both river and groundwater (Figure 3.3).

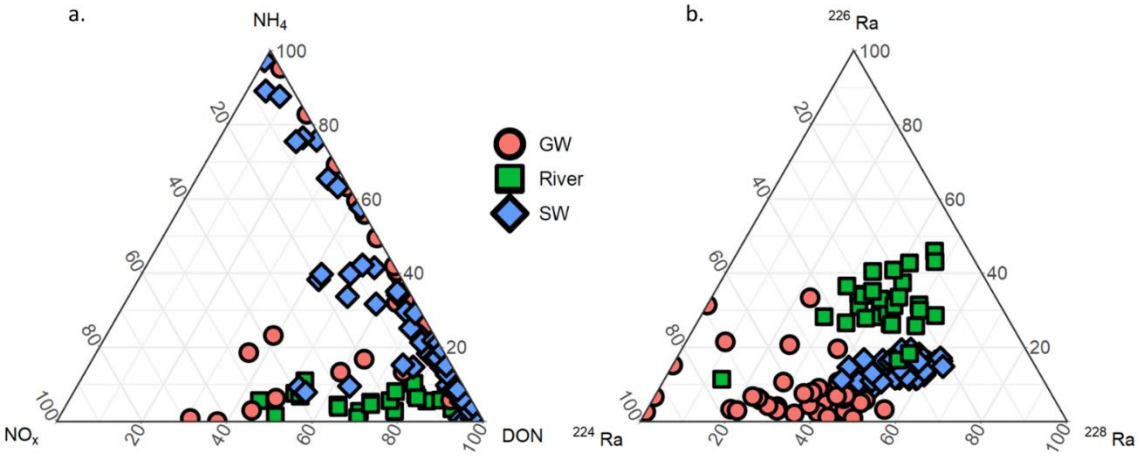

Figure 3.3 *Ternary plots of nitrogen and radium*

a) Ternary plot of nitrogen species (NO_x, NH_4^+, DON) of groundwater (GW), river water (River), and Sound water (SW).

b) Ternary plot of radium isotopes (^{224}Ra, ^{228}Ra, ^{228}Ra) for each water type.

During the summer and fall, there is a distinct radium excess above the mixing lines between river samples and offshore samples (Figure 3.4). These high excess values are most likely indicative of SGD input, as the river flow during this time was at its

lowest (Ho et al., 2019). Contrastingly, the radium activities during the spring and winter fall extremely close to the mixing line, indicating that during this time of the year, river influences dominate the Sound radium budget (Figure 3.4). Most of the ^{228}Ra data, even those during spring and winter, fall either on or above the mixing line, unlike ^{224}Ra. The difference in apparent behavior of the two isotopes is likely due to the conservative nature of the predicted mixing curve. The theoretical dilution line assumes completely conservative mixing, but ^{224}Ra is inherently non-conservative due to decay over the mixing timescale. Even simple mixing of ^{224}Ra without other inputs would lead to a downward curve of the mixing line. However, for simplicity we ignore this and assume conservative mixing, therefore overestimating the impact of rivers on the ^{224}Ra.

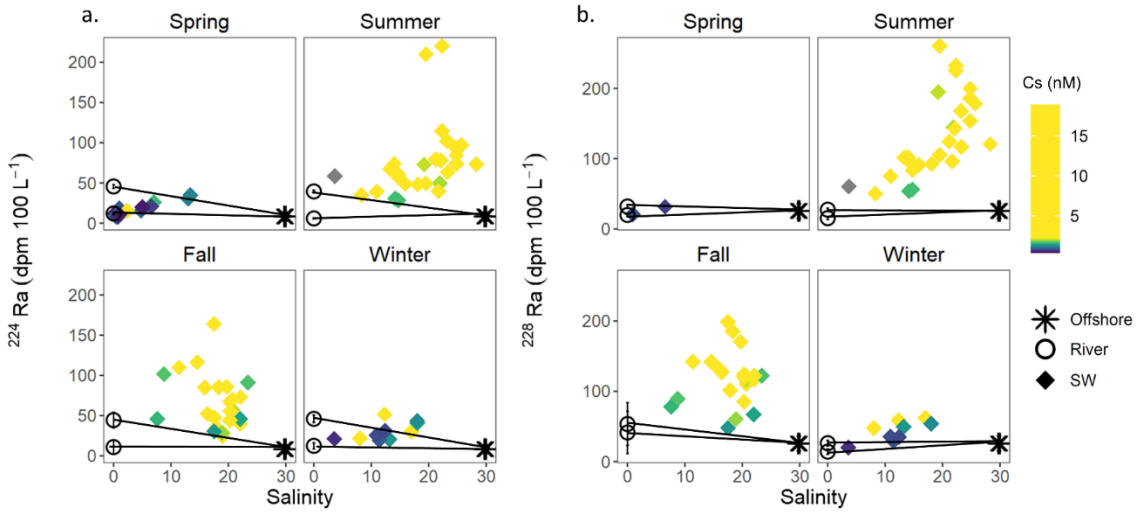

Figure 3.4 *Conservative mixing plots for ^{224}Ra and ^{228}Ra.*

a) Mixing lines for ^{224}Ra river endmembers;

b) Mixing lines for ^{228}Ra river endmembers. Mixing lines are straight lines from the endmember (River) to the offshore concentration (Offshore). The Sound water samples (SW) are colored based on their Cs concentration. Error analysis was conducted using propagation. Spring samples were collected March – May, summer samples from June – August, fall samples from September – November, and winter samples from December – February.

Radon ($T_{1/2}$ = 3.82 days) is an inert gas sourced from the decay of ^{226}Ra, and is highly enriched in groundwater versus surface water, making it a good tracer of SGD (Burnett and Dulaiova, 2003; Cable et al., 1996; Corbett et al., 1997). In order to get a better understanding of the spatial variation of SGD, ^{222}Rn anomalies were calculated for each survey. The anomaly, defined as the positive or negative deviation from the mean, is determined by subtracting the mean of each survey from each radon concentration ($^{222}Rn_{Sound} - {}^{222}Rn_{Survey\ Mean}$; Montiel et al., 2019). Radon in water data for the entire western Sound is shown in Figure A.3. Anomaly calculations allow for comparison of ^{222}Rn across seasons. The ^{222}Rn anomaly indicates that near the beach, we generally have high positive anomalies, but away from the beach in open waters, the western part of the Sound has a higher groundwater influence that declines eastward (Figure 3.5). This pattern can also be seen in ^{222}Rn inventories for each season (Figure A.4), for spring and summer surveys that were conducted in the far western Sound. It is unclear at this time why there was high ^{222}Rn offshore, but possibilities could be paleochannels (e.g., Attisano et al., 2013), high ^{222}Rn in the Pearl River plume at this time, and decay of radium on particles in the water column (e.g., Rodellas et al., 2015). The anomalies in the western Sound ranged from -1.8 to 5.9 dpm/L. The highest ^{222}Rn concentrations are all focused along the coastline and offshore in the most western part of the Sound from longitudes 89.4 – 89.2º W. A section of paleo-Mississippi River delta separates this section of the Sound from offshore, limiting Bight water influence, and contains old river channels since filled in by the last sea level rise ~ 22,000 – 17,000 BP years ago (Adcock, 2019; Otvos, 2001), which could explain the offshore increase.

The qualitative analysis of $\delta^{18}O$, δD, fixed nitrogen, radium isotopes, and ^{222}Rn all indicate that there is SGD entering into the Mississippi Sound, and therefore may be important for biogeochemical processes. From the ^{222}Rn anomaly map, we can infer that a major portion of the SGD is along the coastline, and therefore the time series should capture this signal and show changes that may occur with different seasons.

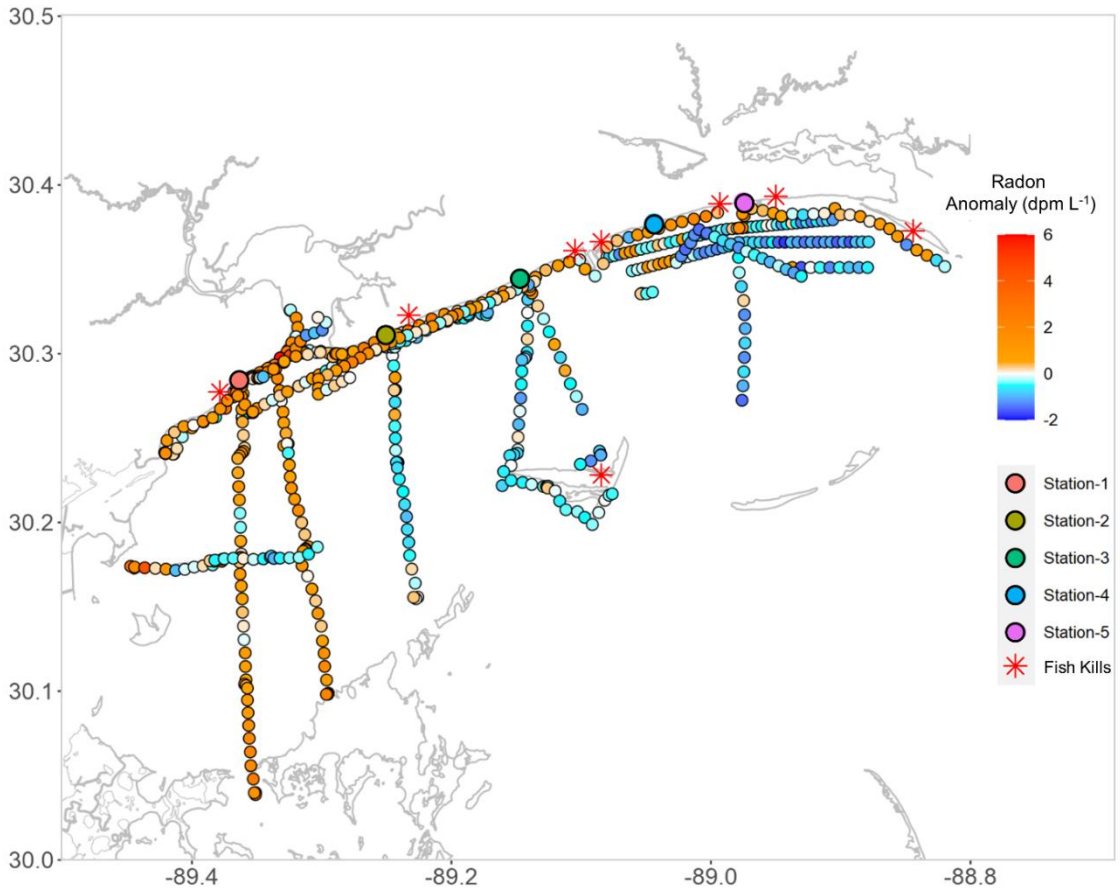

Figure 3.5 *Surface anomaly plot of ^{222}Rn.*

Surface anomaly plot of ^{222}Rn. Activities of ^{222}Rn were subtracted from the mean of each survey. Black dots indicate where samples were taken. Interpolation between points was calculated with ODV DIVA gridding. Beach station locations are denoted by the circles, and station name by the color. Stars indicate locations of historical fish kills according to Overstreet and Hawkins (2017), MDMR (2017), and other news articles dating back to 2013.

3.4.2 Time Series

Sampling for the time series occurred on a seasonal basis, with 16 total samples collected throughout a 3 1/3 year period. This was a sampling frequency of ~5 samples per year. Assuming this system exhibits a yearly cycle, or that each season has its own unique identifier, we would need at least 4 samples per year to resolve the seasonal cycle of SGD. Therefore, sampling on an interval of 5 samples per year should resolve our seasonal cycle. The time series data also exhibit a yearly seasonal cycle, especially when looking at temperature.

Salinity was highest in the summer and fall and declined by the end of fall and through the winter, with lowest salinities in the spring (Figure 3.6). Rainfall typically peaked in the summer months, though rain events throughout the year often resulted in >5 cm accumulations (Figure 3.6. While 2018 sampling occurred during relatively average conditions, and thus set a good baseline, the 2019 sampling was severely impacted by openings of the Bonnet Carré Spillway (BCS). The opening of the Spillway caused salinity values to plummet below 10, and in late May, to near 0. The westernmost station (Station 1) had the lowest salinity consistently during the time series, while it often varied with the other stations (Figure 3.6). However, after the opening of the BCS in February 2019, all stations except 4 and 5 experienced a decline in salinity (Figure 3.6). Stations 4 and 5 had a delayed response to the BCS opening of about 3 months. Due to the opening of the Spillway and the resulting freshwater discharge to the Sound (average 3.1×10^8 m^3 d^{-1} from US Army Corp of Engineers, https://www.mvn.usace.army.mil/Missions/Mississippi-River-Flood-Control/Bonnet-

Carre-Spillway-Overview/Historic-Operation-of-Bonnet-Carre/), the utility of salinity dependent tracers of SGD such as radium and barium, was compromised.

Oxygen concentration through the time series varied as well but was often 80-100% saturated. The oxygen levels dropped below the threshold to cause biological stress (156 µM; Bricker et al., 1999) on five occasions, usually at only one station (Figure 3.6). There were two instances in August 2018 (avg. 145 µM or 70%) and September 2019 (avg. 119 µmol/L or 55% for bottom oxygen) where the oxygen levels were below the threshold at two or more stations. In August 2018, low oxygen was observed from surface to bottom, whereas in September 2019, there was a gradient with lower oxygen at depth at stations 2, 3, and 4. There was no discernable vertical salinity gradient, but temperatures declined about 0.6° C from surface to bottom at these three stations. Typically, waters were too shallow to observe any changes in salinity, temperature, or oxygen with depth during the bulk of the time series. Fish kills were observed during both of these low oxygen events.

Methane has been used as a tracer of groundwater inputs in nearshore waters along the northern Gulf of Mexico (Bugna et al., 1996; Cable et al., 1996), and while not a conservative tracer, if the concentrations in groundwater exceed those in surface waters, it can indicate a presence of SGD (Dulaiova et al., 2010; Santos et al., 2009). While CH_4 data in this study was limited, during the fish kills that have data, the CH_4 concentration was highly elevated in surface waters and exceeded 500 nM at station 4 (Figure 3.6). At times when there was not a fish kill or BCS input (i.e., summer 2018), CH_4 concentrations were not elevated to such extreme levels (Figure 3.6). The lowest observed CH_4 concentrations were during the opening of the BCS.

To track potential inputs of St. Louis Bay (SLB) water into the Sound, dissolved cesium (Cs) was used as a tracer (Figures 3.4 & 3.6). St Louis Bay has elevated concentration of Cs in its waters due to an outfall from a titanium dioxide refinery along the northern shore that contributes Cs to the water (Bera et al., 2015). Movement away from the refinery causes a reduction in the Cs concentration in the water column, but the high Cs levels can be tracked in the nearshore Mississippi Sound (Bera et al., 2015; Ho et al., 2019). Just outside SLB, there is a strong west to east current, meaning that the majority of the Cs to reach the Sound will flow eastward (Cobb and Blain, 2002). For this study, we define Cs levels above 2.2 nM (i.e., typical seawater concentration) to be enriched (Ho et al., 2019), and thus indicative of SLB water influence.

The ^{224}Ra and ^{228}Ra activities ranged from 7.2 ± 0.7 to 220 ± 11 dpm 100L^{-1} and 260±21 to 19.8±7.0 dpm 100L^{-1} respectively, while Ba ranged from 57 – 547 nM with the highest concentrations of both radium and Ba occurring in the summer/early fall months of the time series, and the lowest occurring during the winter and spring months due to increasing freshwater from seasonal changes in hydrology or the BCS influence (Figure 3.6). The radium isotopes and barium had a spatial trend of decreasing eastward, implying the Pearl River and SLB are important sources, or that SGD is more important in the west than the east (Figure 3.6), in agreement with the ^{222}Rn studies. Station 1 often had the highest radium and barium of any station, which could be due to its close proximity to the Pearl River and SLB, both of which can provide increased dissolved materials to the Sound, or enhanced SGD (Figure 3.6). At the height of the BCS opening, both radium isotope concentrations fell to near 0, while Ba reached around 50 nM, lower than the local and Mississippi Rivers (Figure 3.6). Sampling the month after the closure

of the BCS saw full recovery of Ba concentrations to levels similar to before the opening, while the radium isotopes remained low, and even started to decline by November 2019, as salinity began to decrease again (Figure 3.6). All stations showed elevated ^{228}Ra during our fish kill samplings and elevated ^{224}Ra during the latter two fish kill samplings. Since the first fish kill sampling occurred several days after the event, we suspect that the ^{224}Ra ($T_{1/2}$ = 3.6 d) signal had already decayed away.

Pearl River discharge peaked from January – May 2019 (Figure 3.7), with an average discharge of 2.6×10^7 m^3 d^{-1} (Pearl River at Bogalusa, USGS https://waterdata.usgs.gov/nwis). The final two fish kills were sampled when river discharge was below the average, while the first was sampled when river discharge was above the average. The Pearl River plume can affect the salinity of the western Sound; however, the highest flow periods occur in late winter and early spring (Orlando et al., 1993; Figure 3.7). Therefore, during times when the Pearl River discharge was not at peak, we do not expect that it to be a dominant source of nutrients to the Sound, especially in areas where high SGD is indicated.

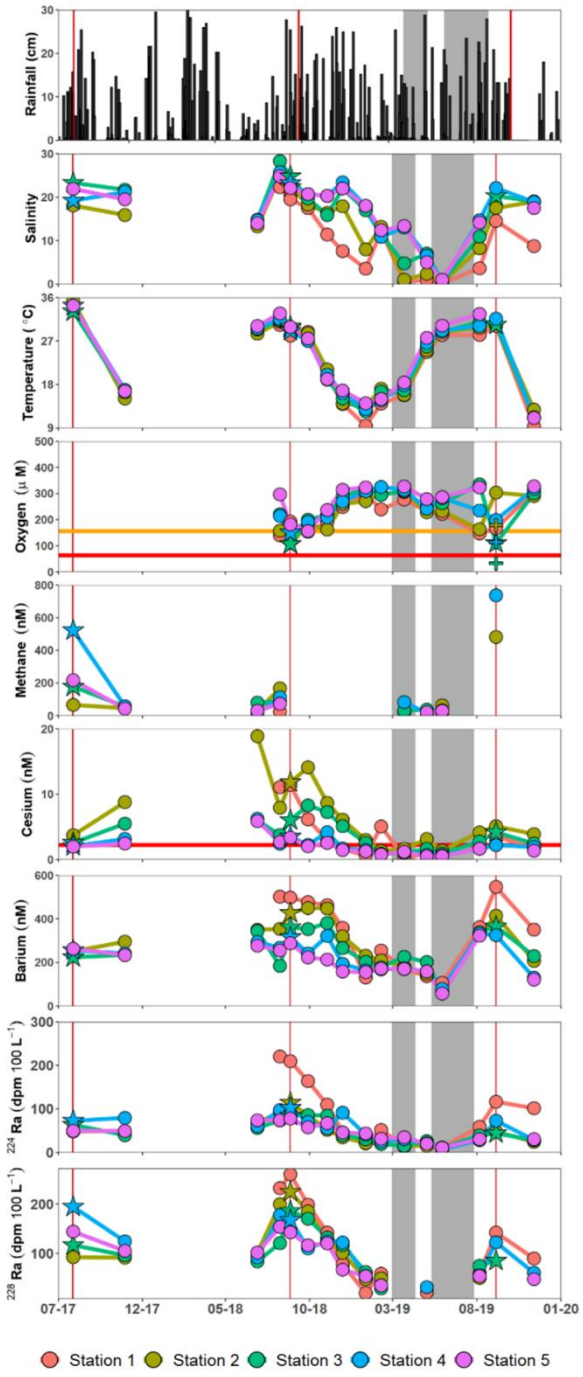

Figure 3.6 *Time series of physical parameters and tracers.*

The vertical red lines indicate when there was an observed fish kill in the Sound. Gray bars are when the Bonnet Carré Spillway was open. Stars on the plot indicate the station of fish kill events. The horizontal red line on the oxygen plot is the hypoxic level and the horizontal orange line is the stressed level. Plus marks show the bottom water oxygen level during September 2019. The horizontal red line on the Cs plot is the open seawater average. Precipitation data was collected from the NOAA GHCN Daily Database.

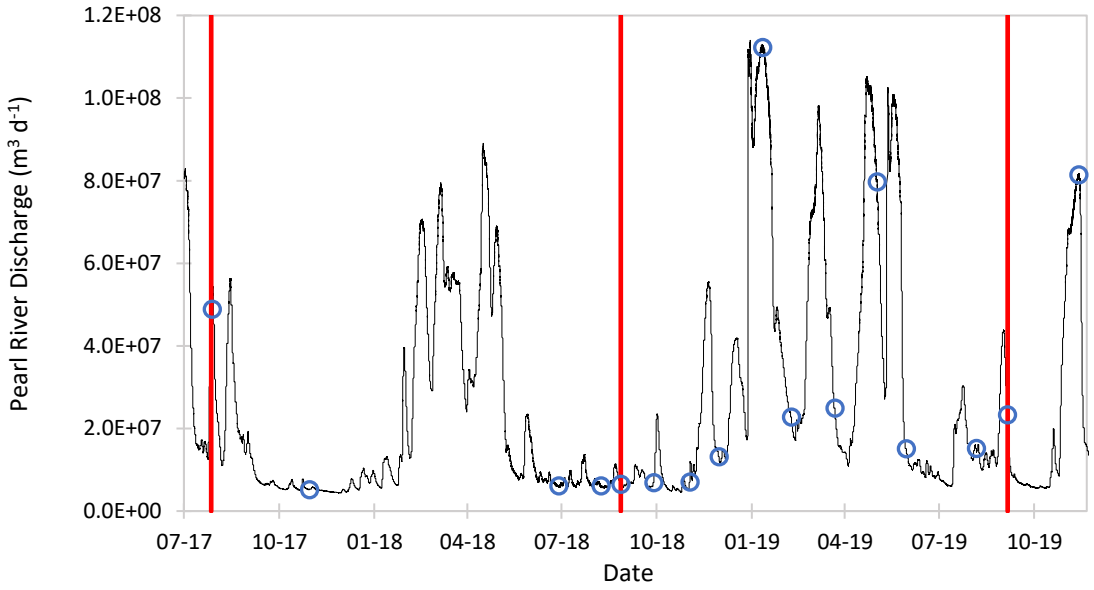

Figure 3.7 *Pearl River Discharge*

Pearl River discharge data from the Pearl River at Bogalusa, LA (data from US Geological Survey: https://waterdata.usgs.gov/nwis). The red lines indicate a fish kill event during the time series, and open circles are when samples were collected.

Recent evidence has indicated that there is a correlation between upwelling favorable winds and SGD (George et al., 2020). The upwelling lowers coastal sea levels, setting up a similar scenario to tidal pumping where hydraulic pressure is relieved and the groundwater is able to flow more easily (George et al., 2020). Two of the three fish kills coincided with westerly winds, which are necessary for upwelling along the Mississippi coast. However, the fish kill occurring in August 2018 had steady easterly winds on days leading up to and throughout the day, and therefore upwelling was unlikely to occur (Figure 3.8). Predicted water levels for July 2017 and September 2019 were higher than the actual verified water levels either preceding the fish kill or during that day, indicating that winds may have lowered the water levels (Figure 3.8). However, for August 2018, the predicted water levels were overall lower than the verified water levels before,

during, and after the fish kill occurred (Figure 3.8). While it is uncertain what role this mechanism may play in enhancing SGD flow, it does correlate with the two fish kills that were jubilees, and therefore cannot be discounted as possible cause of enhanced groundwater flow.

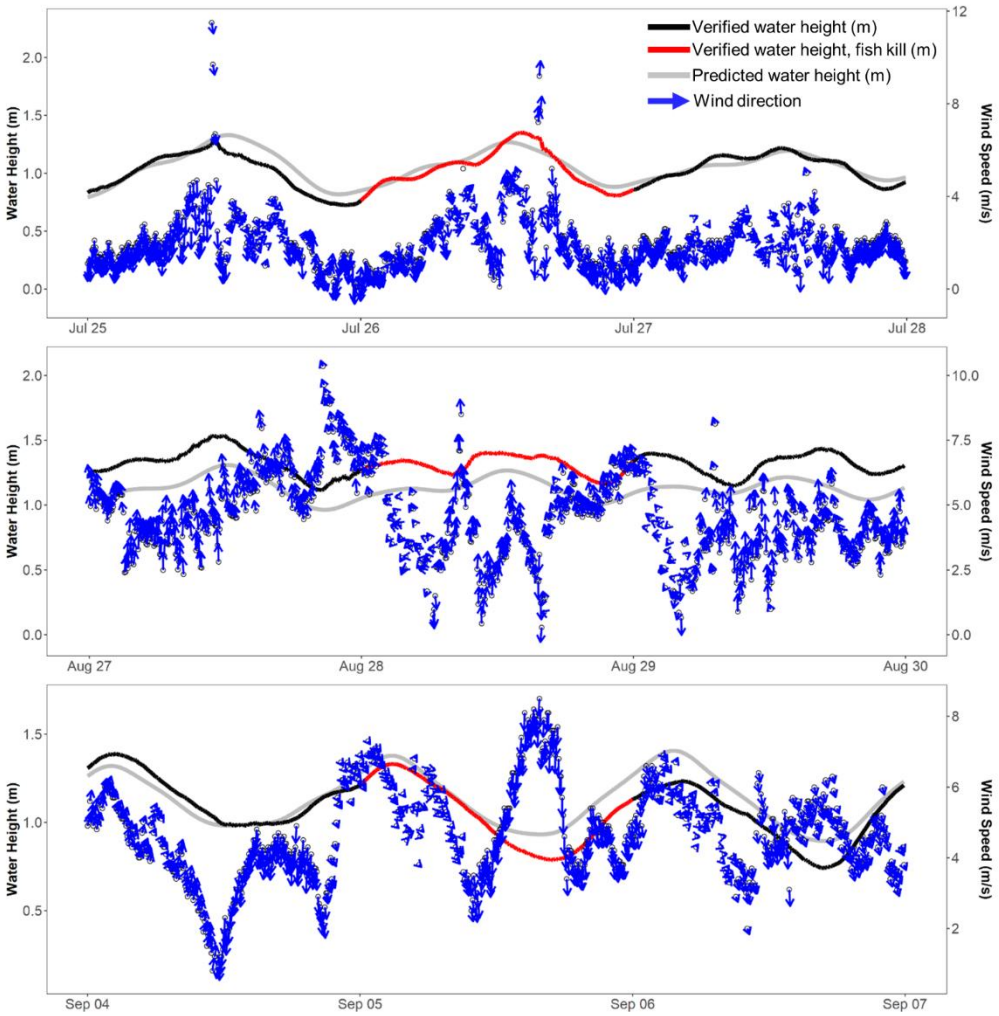

Figure 3.8 *Wind and tidal data.*

Water height and wind speed/direction data from USGS station 8747437 Bay Waveland Yacht Club, MS except for September 2019 wind data, which was obtained from USGS station 8741003 Petit Bois Island, Port of Pascagoula, MS.

Rainfall may help to explain the higher radium activities along the coastline, especially for 2017 and 2018, which are the two wettest years recorded for coastal Mississippi (Williams, 2018). There were significant rainfall events (>10 cm) that occurred less than a week before sampling in July 2017 and August 2018, when two of the fish kills occurred (Figure 3.6). The high permeability of the sediments along the coastline, as well as the unconfined nature of the aquifer, could allow for rapid flushing of the aquifer system. This has been seen before in other unconfined aquifer systems (e.g., Montiel et al., 2019), where high precipitation rates raised the aquifer groundwater table, leading to enhanced SGD.

Nutrient concentrations were highly variable during the time series and seemed to be affected by a variety of factors (Figure 3.9). Nitrate + nitrite (NO_x) concentration reached its maximum during the first opening of the BCS at stations 1, 2, and 3, but stations 4 and 5 were not particularly affected by the BCS. Other than the extreme spike in NO_x during the BCS, the levels remained relatively constant. Ammonium (NH_4^+) was elevated during both sampling periods in August 2018 at stations 2, 3 and 4. There was no enhanced NH_4^+ during the BCS, which may be due to a lower NH_4^+ concentration in Mississippi River (1.72 µM) water compared to the Pearl River (3.4 µM), and modification (i.e., uptake and remineralization) of nitrogen during passage through Lake Pontchartrain. Phosphate concentrations saw two peaks during the time series: on June 28, 2018, and on September 5, 2019. PO_4 did not seem to be highly affected by the BCS opening and remained at a relatively constant level throughout the opening. Silicate concentrations peaked at stations 1-4 on September 5, 2019, the same as PO_4, and the lowest concentrations occurred in August 2019 at all stations (Figure 3.9).

The dissolved inorganic nitrogen (DIN) to dissolved inorganic phosphorus (DIP) molar ratio changed drastically throughout the time series, with a range of about 1 to 50. The highest DIN:DIP ratio occurred at station 4 on August 28, 2018, at the time of the second fish kill (Figure 3.10). On that day, the NH_4^+:DIN molar ratio was also high, near 1, indicating that NH_4^+ was the main nitrogen species in the water. Stations 2, 3, and 4 all had DIN:DIP ratios above 16 on that day, while stations 1 and 5 did not. This may mean that there was an input of NH_4^+ rich water near these stations, which may be indicative of SGD. The next high DIN:DIP ratios occurred at stations 4 and 5 on November 2, 2018, and November 30, 2018. There was a decline in PO_4 concentrations, and slight increases in NH_4^+ concentrations, which could be why the DIN:DIP was elevated (Figure 3.10). Station 2 had an elevated DIN:DIP on January 11, 2019 (Figure 3.10), that coincided with an increase in the NO_x concentration at that station (Figures 3.9 and 3.10). The final DIN:DIP ratios above 16 occurred on March 22, 2019, after the initial opening of the BCS at stations 1, 2, and 3 (Figure 3.10). For these stations, the NO_x:DIN ratio also increased dramatically, which can be seen in the rapid decline of the NH_4^+:DIN ratio (Figure 3.10) . The enhanced NO_x:DIN ratio is due to the opening of the BCS, which allowed for an influx of high NO_x waters. Interestingly, we do not see the same increase in the DIN:DIP ratios with the second BCS opening, even though the dominant nitrogen species was NO_x again (Figure 3.10).

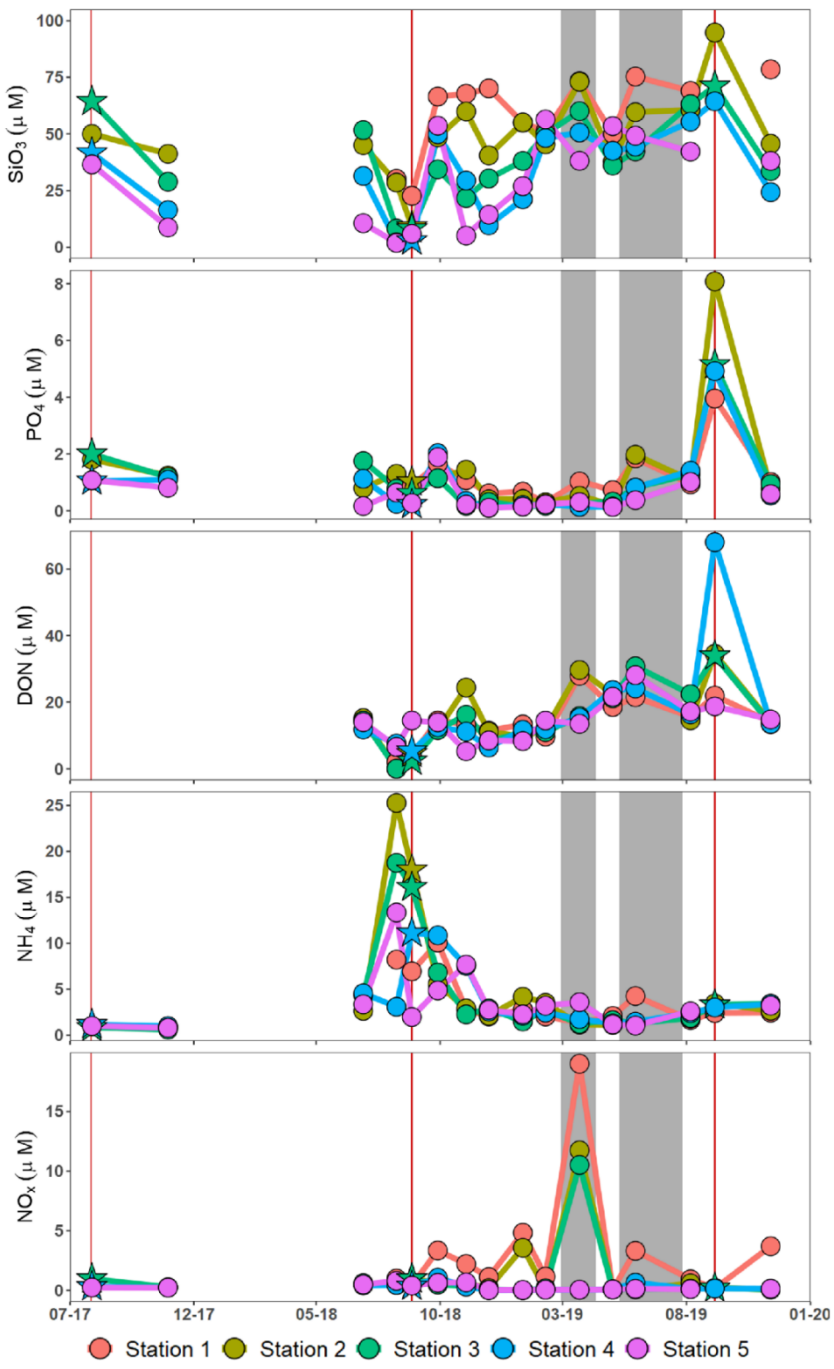

Figure 3.9 *Time series of nutrient concentrations.*

Vertical red lines indicate when there was an observed fish kill and gray bars are when the BCS was open. Stars show the station that had dead fish.

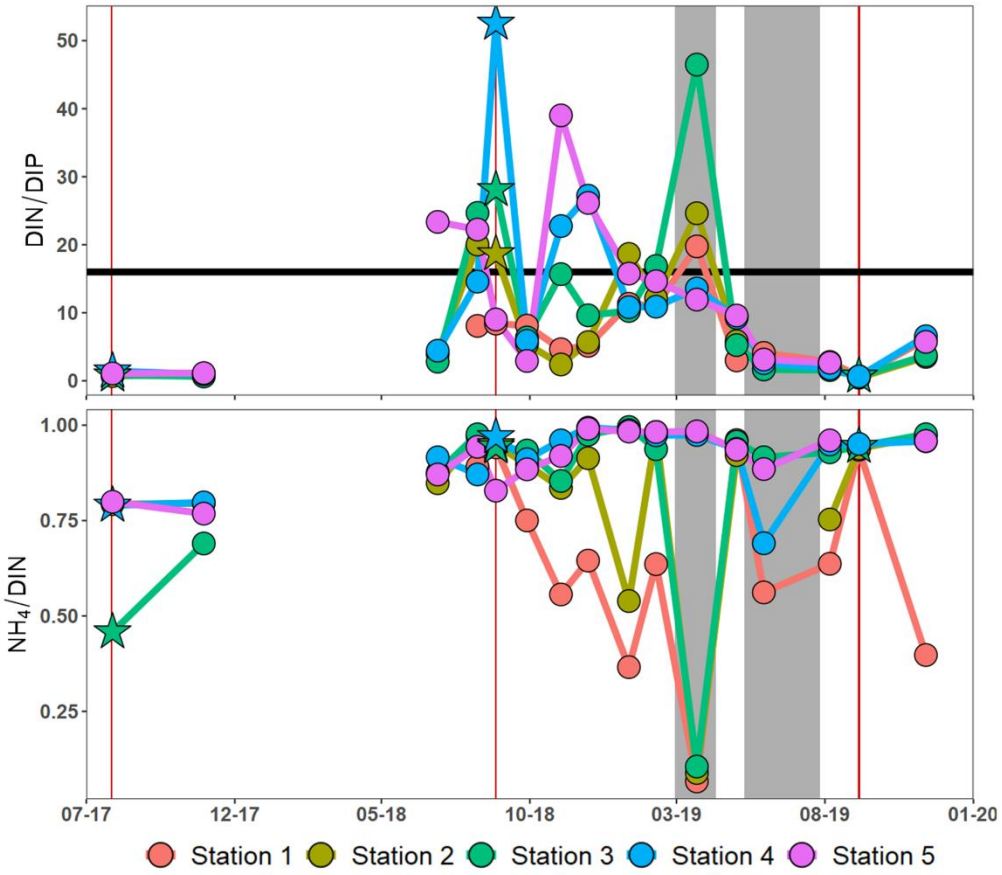

Figure 3.10 *Nutrient ratios.*

Inorganic nitrogen to inorganic phosphorus and ammonium to inorganic nitrogen. Vertical red lines indicate when there was an observed fish kill and gray bars are when the BCS was open. The black line on the N:P plot indicate the 16:1 line. Stars show the location of dead fish.

3.4.3 Mass Balance Calculations of SGD

A typical approach for determining SGD water flux from tracers is to use a steady state mass balance of a tracer enriched in SGD (e.g., Rodellas et al., 2017). A common issue with a mass balance is choosing appropriate endmembers that accurately reflect the system (e.g., Sanial et al., 2021). For this study, we separately calculate the flux of groundwater using three radioisotopes: ^{224}Ra, ^{228}Ra, and ^{222}Rn. At steady state, the

radium fluxes supplied by SGD, rivers, and diffusion must be balanced by advection/mixing with offshore waters and radioactive decay. Therefore, the mass balance equation for radium is:

Eq. 1 $Ra_{out} + Ra_{\lambda} = Ra_{dif} + Ra_{riv} + Ra_{sw} + Ra_{SGD}$

where Ra_{out} is the flux of radium out of the Sound (i.e., mixing loss), Ra_{λ} is the radioactive decay, Ra_{dif} is diffusion of radium from sediments, Ra_{riv} is flux of radium from rivers, Ra_{sw} is the input of radium from offshore waters, and Ra_{SGD} is radium input from SGD. For ^{228}Ra, the decay term can be ignored due to its long half-life (5.75 years) as compared with the residence time of water in the Sound (~ 10 days).

The ^{222}Rn balance is similar to the radium balance, but has an extra removal term for atmospheric evasion and source term from production of ^{222}Rn from decay of the parent isotope ^{226}Ra:

Eq. 2 $^{222}Rn_{out} + {}^{222}Rn_{\lambda} + {}^{222}Rn_{atm} = {}^{222}Rn_{dif} + {}^{222}Rn_{riv} + {}^{222}Rn_{sw} + {}^{222}Rn_{SGD} + {}^{222}Rn_{prod}$

where $^{222}Rn_{atm}$ is the evasion of ^{222}Rn to the atmosphere from the water, $^{222}Rn_{prod}$ is the production of ^{222}Rn from ^{228}Ra, and the other terms represent the same factors as in the Ra balances.

In the next three sections, the specifics for each radioisotope mass balance will be outlined, along with additional assumptions and calculations.

3.4.3.1 ^{224}Ra

For the short-lived radium isotopes, determining their fluxes from rivers and offshore can be problematic as there are many river and bay sources to Sound, and the fluxes from offshore potentially change rapidly depending on wind and tide. For this section of the Sound, we assume the major river source will be the Pearl River, as the

next largest river input directly into the Sound is the Pascagoula River, and the smaller Jourdan and Wolf Rivers feed directly into SLB. Therefore, we created a mixing line between the offshore waters of the Bight (^{224}Ra: 8.3 dpm 100 L^{-1}, salinity: 29) and an estimate of Pearl River ^{224}Ra (Figure 3.4).

However, there is uncertainty in the Pearl River endmember, mainly due to variations with suspended particulate matter (SPM) content, leading to a range in the ^{224}Ra concentration. The SPM is important to the mass balance because when the low salinity river water carrying particulates reaches the higher salinity estuary, desorption of radium from SPM will occur, increasing the amount of radium released by rivers to the estuary (e.g., Rodellas et al., 2015). To determine how much difference a change in river endmember would cause to the SGD flux calculation, two separate mixing lines were created. The first assumed that there was no desorption from the Pearl River as it entered the Sound. This would underestimate the impact of the river on the Sound. The second line utilizes SPM content of the Pearl River and desorbed ^{224}Ra values to estimate a desorbed plus dissolved content that would enter the Sound (Figure 3.4); this likely overestimates the ^{224}Ra supply since it ignores decay during transport from endmember to sampling sites.

The SPM content in the Pearl River sample was 167 mg L^{-1} (Sanial et al., 2021), the desorbed ^{224}Ra in the river was 33.7 dpm 100 L^{-1}, and the average ^{224}Ra in the five non-desorbed samples was 8.41 dpm 100 L^{-1}. In the East Pearl River, Shiller et al. (2012) found SPM often to be <100 mg L^{-1}, and typically around 40 mg L^{-1}. USGS data for the West Pearl River at Bougalusa suggests a higher mean around 80 – 100 mg L^{-1}. Our SPM value is above even this range, and therefore will most likely overestimate the amount of

^{224}Ra added to the Sound from river inputs. The desorbed ^{224}Ra from SPM from the Pearl River was estimated to be 2.01 dpm g^{-1}. Considering this, the average amount of ^{224}Ra added to the Sound from the local rivers was 42 dpm 100 L^{-1}. Moore et al (2008), reports that the maximum desorption of radium from river sediments is around 2 dpm g^{-1}, which is near our ^{224}Ra desorption values, making our estimate within an acceptable range, though at the higher end. We go a step further with this analysis and attempt to break down the river ^{224}Ra by season using the different average river radium concentrations for each season (Figure 3.4).

There is also the issue that SLB may be a significant contributor of SGD to the Mississippi Sound, at least in the vicinity of some of our sampling sites. The Bay is situated between stations 1 and 2 and has been shown to have significant SGD input (Spaid, 2020; Roberts, 2014). Since the Bay has enriched levels of Cs (Bera et al., 2015), we are able to use this as a tracer of SLB influence in the Sound. The majority of Cs above 2.2 nM occurs in the summer and fall, indicating contribution from SLB, coinciding with our highest Ra estimates (Figure 3.4). This suggests that SLB has a larger contribution to the Sound in the summer and fall. However, this may not be important for ^{224}Ra due to decay during transit, but for ^{228}Ra, it could cause an overestimate of SGD along the coastline.

The mixing line equation is used to estimate an expected radium content at the salinity of each Sound sample. The expected radium concentration is subtracted from the actual radium concentration to determine the excess (Ra_{ex}), and correct for both riverine and offshore input to the Sound using equation 3:

Eq. 3 $Ra_{ex} = Ra_{Snd} - Ra_{mix}$

where Ra_{ex} is the excess radium, Ra_{Snd} is the Sound radium concentration, and Ra_{mix} is the calculated radium from the mixing line. This excess term can then be used as a corrected Ra concentration to determine the other terms in Eq. 1. The Ra_{ex} thus represents the SGD and diffusive inputs of Ra minus transport out of the Sound and radiodecay. As noted above, our linear mixing lines do not account for the decay of ^{224}Ra (3.6 d half-life) during transit of waters from endmember locations to the sample sites. As a crude example, the average velocity of the Pearl River indicates it would take about one ^{224}Ra half-life for river water to transit from the Pearl River mouth to Station 1. This is an underestimate of the transit time since on entering the Sound, the river water spreads out and its velocity will decrease significantly. Thus, our upper mixing line and even our lower mixing line probably greatly overestimate the actual river and offshore contributions to ^{224}Ra at each sampling site. In other words, our calculation of SGD input may be biased low. Furthermore, the upper line probably overestimates the desorbed Ra. With this in mind, we utilize the lower endmember concentrations to estimate SGD fluxes using Ra. Choice of mixing line makes minimal difference in our estimates of summer/fall SGD nor does it affect the basic observation that in summer/fall SGD in far more important than in winter/spring (Figure 3.4).

With the excess, we then calculate the excess inventory of the ^{224}Ra from:

Eq. 4 $$Ra_{Iex} = \frac{Ra_{ex}}{0.1} \times d_S$$

where Ra_{Iex} is the excess inventory in dpm m^{-2}, and d_S is the depth of the Sound (m) at a given sampling station. The 0.1 converts from 100 L to m^3.

An estimate of residence time of water in the Sound is needed to estimate the mixing loss term in Eq. 1 (Ra_{out}). The apparent age in days (d) of each sample was calculated based on the $^{224}Ra/^{228}Ra$ activity ratio as outlined in Moore et al. (2000):

Eq. 5 $$T_w = \frac{Ln(\frac{AR_{SGD}}{AR_{Snd}})}{\lambda^{224}\mathrm{Ra}}$$

where AR_{SW} and AR_{SGD} are the averages of the $^{224}Ra/^{228}Ra$ activity ratio in the Sound and in the groundwater, and $\lambda^{224}Ra$ is the decay constant of ^{224}Ra in d^{-1}. This is a point source model that assumes radium coming into the system is only coming in at a certain point, and there are no other sources (Moore et al., 2000). This model is most appropriate for this study site, as it is extremely shallow, and over an area that quickly mixes. We use ^{224}Ra and ^{228}Ra to limit the influence of rivers on the age model. The ages were averaged per station and used as constants through the time series. Averages for stations 1, 2, 3, 4, and 5 were 4.2 ± 1.4, 7.6 ± 0.9, 7.3 ± 1.2, 6.8 ± 1.2, and 6.6 ± 1.4 days, respectively. Estimates of the Sound residence time based on a modelling approach predict that the average time is ~10 days in the spring, and ~20 days in the summer (Bouchard, 2021), which is higher than our estimates. The difference is from the apparent age representing time elapsed since water was enriched in radium, not the amount of time it takes for water to be replaced. The continuous input model from Moore et al (2006), which assumes that radium is constantly added to the system, also predicts ages that are higher than the point source estimates, with average ages per station of 5.8 ± 2.6, 15.5 ± 3.9, 14.4 ± 4.8, 12.6 ± 4.1, and 12.4 ± 4.9 days, respectively. However, these most likely overestimate the apparent age because we expect that the SGD entering the Sound at

these locations will have been in contact with the source recently, and therefore is more similar to a point source of SGD than a continuous source.

With the apparent age, the mixing loss with offshore waters can be calculated by dividing the ^{224}Ra inventory (dpm m^{-2}) by the apparent age at each site, giving a value in dpm m^{-2} d^{-1}. The decay term is determined by multiplying the total inventory (dpm m^{-2}) by the decay constant for ^{224}Ra (0.189 d^{-1}).

The diffusion experiment gave a ^{224}Ra flux of 29 dpm m^{-2} d^{-1}. Often, diffusion is demonstrated to be a negligible source of radium (e.g., Beck et al., 2007), but in shallow waters can be significant to the overall budget (e.g., Rodellas et al., 2015). Our diffusion estimate is a middle range compared to many studies (e.g., Rodellas et al., 2015; Spaid, 2019), but is in the same order of magnitude to studies such as Garcia-Orellana et al. (2014). Since this study location is a shallow environment with silty/muddy sediments, the diffusion term is important for the overall budget, and contribute ~27% of the ^{224}Ra inventory. This particular term has high uncertainty (Garcia-Orellana et al., 2014; Moore et al., 2008; Rodellas et al., 2015), and therefore we assign an uncertainty of ±50%. This approach provides an upper limit estimate of the diffusive flux because the overlying water is consistently being depleted of radium, increasing the gradient between sediments and water, enhancing diffusive fluxes (Rodellas et al., 2012). Thus, here again, our approach biases our SGD flux estimates low.

All together, we can substitute our new terms into the mass balance equation, while also removing river radium and offshore radium due to our excess correction and solve for radium from SGD. The mass balance equation now becomes:

Eq. 6 $$\mathrm{Ra_{SGD}} = \frac{\mathrm{Ra_{Iex}}}{\mathrm{T_w}} + (\mathrm{Ra_I} \times \lambda_{224\mathrm{Ra}}) - \mathrm{Ra_{dif}}$$

where the flux of ^{224}Ra from SGD is in dpm m^{-2} d^{-1}. We then convert this into a water flux or seepage rate (cm d^{-1}) by dividing the RaSGD by the groundwater ^{224}Ra endmember (dpm m^{-3}), which was the average of all our groundwater ^{224}Ra activities:

Eq. 7 $$F_{SGD} = \frac{Ra_{SGD}}{Ra_{GW}} \times 100$$

where F_{SGD} is the water flux in m d^{-1} from the SGD.

Unstated assumptions of our model include: i) that the groundwater radium endmember is constant, ii) that the river radium endmember is constant each season, iii) that the diffusion flux does not change per season, and, iv) that the apparent age model correctly demonstrates the residence time of water in the study area.

3.4.3.2 ^{228}Ra

The mass balance using ^{228}Ra is similar to that of ^{224}Ra, but due to its long half-life (5.75 yr), radio-decay can be ignored. Therefore, Eq. 6 can be rewritten as:

Eq. 8 $$Ra_{SGD} = \frac{Ra_{Iex}}{T_w} - Ra_{dif}$$

for ^{228}Ra. In this case, Ra_{dif} is estimated based on its molecular diffusivity, the differences in Ra activity between pore and surface waters, and an assumed a diffusion length of 10 cm (Rodellas et al., 2017). Similar to ^{224}Ra, the mixing curves between rivers and offshore waters were used to determine ^{228}Ra excess, using Eq. 3. Inventories were calculated using Eq. 4, and ^{228}Ra from SGD was calculated using Eq. 8. Water flux was determined using Eq. 7.

There was no data for ^{228}Ra in SLB waters, so we focus only on the river endmembers. The difference between the high and low mixing lines for ^{228}Ra was within

the error margins calculated for the dataset. Therefore, like ^{224}Ra we use the low endmember values.

3.4.3.3 ^{222}Rn

The mass balance equation for ^{222}Rn (Eq. 2) is similar to the radium mass balances but has an additional term for atmospheric evasion. Each radon measurement is considered individually (e.g., Dulaiova et al., 2010) by correcting each data point for sinks and sources of ^{222}Rn, and then using the groundwater concentration to calculate water flux.

Due to the radioactive decay of ^{222}Rn and degassing, we expect there to be little to no ^{222}Rn added to water column by rivers or from offshore. We also expect that offshore ^{222}Rn would not increase the near shore ^{222}Rn levels, due to the decreasing concentration as we move offshore, and the anomaly map, which indicates that the majority of ^{222}Rn is entering the Sound from the shoreline (Figure 3.5). Therefore, we can rearrange Eq. 2:

Eq. 9 $$Rn_{SGD} = Rn_{atm} + Rn_{\lambda} + Rn_{out} - Rn_{dif}$$

where Rn_{SGD} is the flux of ^{222}Rn derived from groundwater (dpm m^{-2} d^{-1}), Rn_{atm} is atmospheric evasion, Rn_{out} is the loss due to advection and mixing with offshore water, Rn_{Dec} is the decay of Rn, and Rn_{dif} is the diffusion of ^{222}Rn from sediments. Each term is determined using a ^{222}Rn value corrected for in situ production from the parent isotope ^{226}Ra.

Rn_{dif} was modeled by the equation (Schubert and Paschke, 2015):

Eq. 10 $$Rn_{dif} = \sqrt{n \times D_{Rn} \times \lambda_{Rn}} \times (Rn_{PW} - Rn_{Snd})$$

where n is the porosity of the sediments (~0.35 for silty sands), D_{Rn} is the diffusion coefficient of radon in water (avg±stdv: 1.06×10^{-4} m^2 d^{-1} $\pm1.5\times10^{-5}$ m^2 d^{-1}; Schubert and

Paschke, 2015) , λ_{Rn} is the radon decay rate (0.181 d^{-1}), Rn_{PW} is the radon concentration in pore water (avg±stdv: 5.2×10^4 $\pm4.9\times10^4$ dpm m^{-3}) calculated from the average of the high salinity groundwater samples, and Rn_{Snd} is the average radon concentration in the Sound (2.19×10^3 $\pm1.26\times10^3$ dpm m^{-3}).

The age model approach for ^{222}Rn was calculated using the ^{224}Ra/^{223}Ra activity ratios of water samples instead of ^{224}Ra/^{228}Ra due to data limitations. These were then plugged into Eq. 5. The average age for the radon survey locations was 9.5 d. Where there was ^{224}Ra/^{228}Ra data, the apparent age was calculated as well. The average age from these isotopic ratios was 9.7 days (i.e., similar to the ^{224}Ra/^{223}Ra age). The average apparent ages throughout the western Sound align well with the model results from Bouchard (2021).

The atmospheric loss of radon (Rn_{atm}) is determined by the concentration gradient between ^{222}Rn in air (Rn_{air}) and water (Rn_w) and the gas transfer velocity (k_{Rn}) as outlined below:

Eq. 11 $$Rn_{atm} = k_{Rn} \times \frac{24}{100} \times (Rn_W - \alpha \times Rn_{air})$$

where α is the solubility coefficient of radon at equilibrium (Dimova et al., 2013; Lambert and Burnett, 2003):

Eq. 12 $$\alpha = 0.105 + 0.405e^{-0.05027T}$$

Eq. 13 $$k_{Rn} = .0.45u_{10}^{1.6}(Sc_{Rn}/Sc_{CO2})^{-b}$$

where b = 0.5 for wind speed > 3.6 m s^{-1} or 0.667 for wind speed < 3.6 m s^{-1}, ScRn and ScCO2 are the Schmidt numbers for ^{222}Rn and CO_2 respectively, u_{10} is the wind speed at 10 m, and T is the temperature (°C) at the water–gas interface.

Rn_{Dec} and Rn_{out} and the inventories were modeled the same as radium. Our values for each term were plugged into the mass balance (Eq. 9). We then convert the F_{SGD} flux into a discharge (cm d^{-1}) using the equation:

Eq. 14 $$F_{SGD} = \frac{Rn_{SGD}}{Rn_{GW}} \times 100$$

where Rn_{GW} is the average groundwater endmember of ^{222}Rn, calculated from the average of all groundwater ^{222}Rn samples ($4.2\times10^4 \pm 3.5\times10^4$ dpm m^{-3}).

3.4.3.4 SGD Rates

SGD calculated from ^{224}Ra ranged from <0 to 68±16 cm d^{-1}, with an average of 10.3±11.5 cm d^{-1}, while rates calculated from ^{228}Ra ranged from <0 to 45±17 cm d^{-1}, with an average of 10.0±8.9 cm d^{-1} (Figure 3.11). Uncertainty was calculated using propagation of error for each component of the equation, and standard deviations on the averages. The estimated fluxes are similar to other coastal studies that have examined SGD at the shoreline (e.g., McCoy et al., 2011; Montiel et al., 2019). We exclude negative values calculated from the ^{224}Ra balance, as those occurred when the BCS had been opened, causing both a drastic drop in salinity, and enhanced flushing of coastal waters. The fluxes for both radium isotopes indicate that SGD is highest in the summer and early fall, a timing which aligns with that of a recent study from Mobile Bay, Alabama (Table 1; e.g., Montiel et al., 2019). Station 1 consistently had higher SGD (except for ^{224}Ra when the BCS was open), with the highest radium concentrations (Figure 3.11). This matches with the ^{222}Rn anomaly plot, which shows that the western most part of the Sound has the highest anomalies (Figures 3.5 & 3.6).

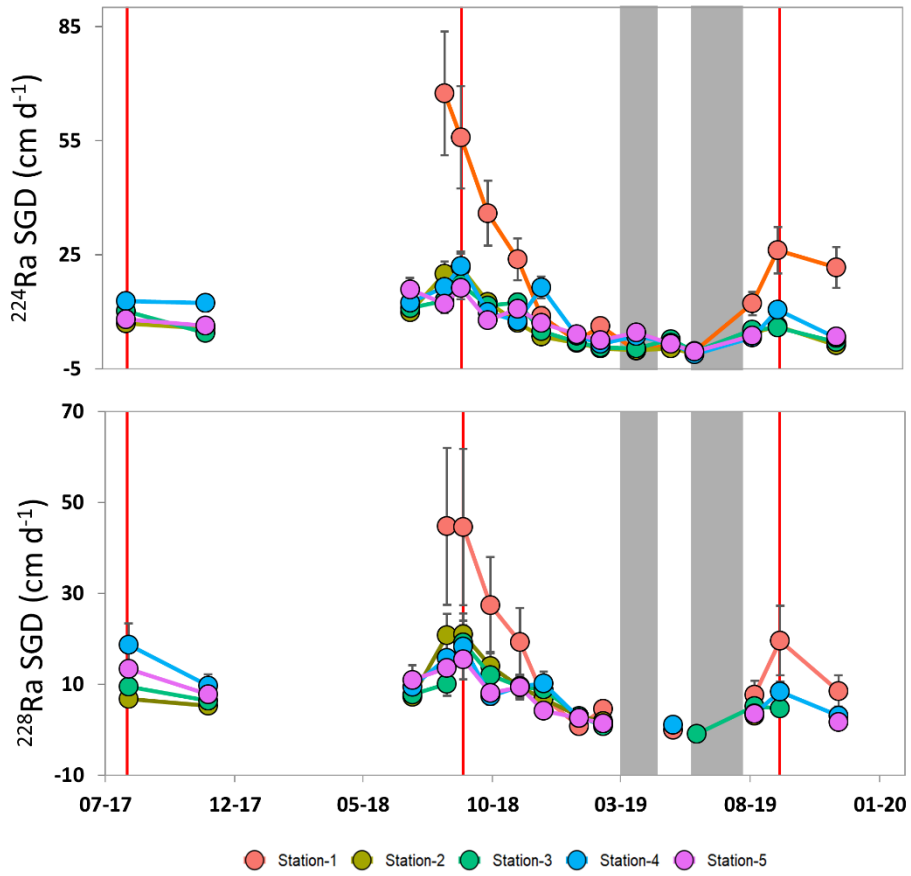

Figure 3.11 *SGD rates for ^{228}Ra and ^{224}Ra and their associated errors.*

Vertical red lines indicate when there was an observed fish kill and gray bars are when the BCS was open.

Table 3.1 *SGD rates averaged per season for 2017 – 2019.*

	SGD (cm d^{-1})		
	^{222}Rn	^{224}Ra	^{228}Ra
Spring	3.1±3.2	2.0±1.5	1.0±0.4
Summer	4.7±3.1	16.4±15.4	14.3±11.1
Fall	6.7±3.3	10.8±8.6	10.0±6.1
Winter	5.0±2.9	4.4±4.1	3.9±3.0

The Mobile Bay study (Montiel et al., 2019), showed that SGD supports fish kill (jubilee) events along the coast, and may also trigger harmful algal blooms. During our study, there were three fish kill events occurring on July 26, 2017 (sampling occurred on July 28, 2017), August 27, 2018, and September 5, 2019 (Figure 3.6). Two of these fish kills were due to low oxygen (MDMR, 2017; MDMR pers. com.), while the cause for the August 2018 fish kill was unknown. The highest groundwater discharge occurred on August 8, 2018, when there was no fish kill event (Figure 3.11). This may indicate that SGD is not the dominant cause of hypoxia, or that groundwater composition changes on short time scales, and may not always be reducing. However, SGD input along the coast may push an already at risk system over the edge under the right conditions. Sanial et al. (2021) observed that oxygen demand due to both low oxygen water and reduced species from groundwater was highest in the summer and can push an already oxygen depleted system into hypoxia. Therefore, this process is most likely occurring in the Mississippi Sound as well.

The ^{222}Rn SGD fluxes helped us examine spatial variations across the Sound for each season. Therefore, while the temporal resolution is low, the spatial resolution is more refined than for the time series data. Only samples collected along the shoreline were used to calculate SGD in order to better compare to the time series data (Figure 3.12). These survey data were collected at different times than the time series data, with the first sampling for ^{222}Rn beginning in October 2018. However, we assume that seasonal changes in the hydrology and SGD flow will be broadly similar year to year (Michael et al., 2005). The full range of the ^{222}Rn calculated SGD was from <0 cm d^{-1} to

16.4 cm d^{-1}, which is lower than our nearshore estimates due to the samples being collected slightly further offshore. There was a distinct change in the ^{222}Rn-based SGD flux from season to season, with spring having the lowest average discharge (3.1 ± 3.2 cm d^{-1}), and fall having the highest (6.7 ± 3.3 cm d^{-1}). There are similarities in the spatial distribution of radon in each season, with the section west of BSL having the highest discharge rates (except for winter where there is no data, Figure 3.12). This indicates that the area around station 1 has enhanced discharge, as can be seen for all three radioisotope tracers.

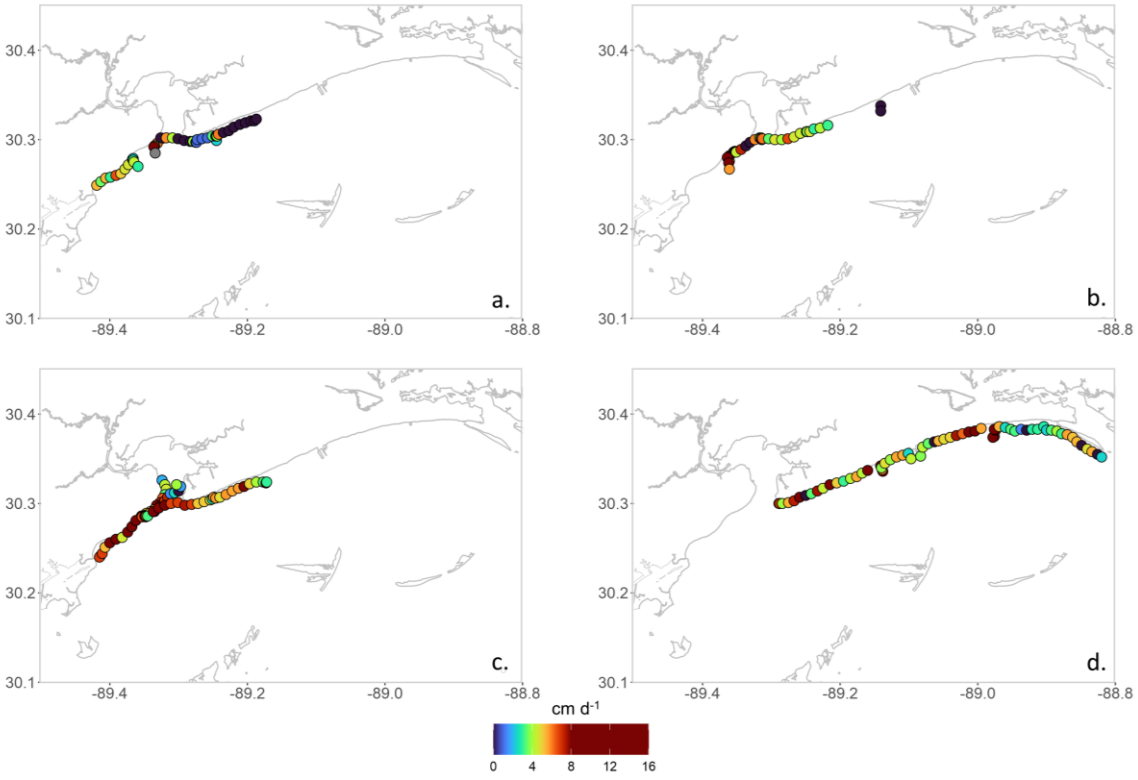

Figure 3.12 *SGD fluxes (cm d^{-1}) calculated from ^{222}Rn.*

a) Spring (2019, BCS open), b) summer (2019), c) fall (2018, 2019), and d) winter (2018).

Seasonal and daily variations with radon tracers have been noted in multiple studies and can be due to the lag time between precipitation and discharge (Cheng et al., 2020; Lou et al., 2020). However, our study site has the highest rainfall in the summer months, with a drop off through the fall and into spring. The highest discharges occur in the fall, winter, and then summer, with spring as the lowest. This may be due to rapid flushing of the aquifer in summer with heavier rainfall, with a continuation of higher discharge through fall and winter due to elevated aquifer groundwater levels (de Weys et al., 2011).

3.4.3.5 Contribution of SGD to Nutrient Fluxes

Hypoxia may or may not result from eutrophication through enhanced nutrient release by SGD, depending in part on stratification. We estimate SGD nutrient fluxes (Table 2) by multiplying the discharge by the groundwater nutrient endmembers. First, average SGD seepage fluxes from our radium and radon estimates in cm d^{-1} are converted to m^3 d^{-1} discharges by multiplying by the seepage face area (m^2). This is estimated by calculating the area of the positive ^{222}Rn anomaly along the coastline of mainland Mississippi in ArcGIS online. The seepage face area was estimated to be 2.2×10^7 m^2. These are then compared to the Pearl River flux, the nearest river to the study site. The average Pearl River discharge (2.6×10^7 m^3 d^{-1}) (USGS), was then multiplied by the river endmember. Another important nutrient source, when open, was the BCS. We estimate the impact of the BCS using average discharge data from the US Army Corps of Engineers website (https://www.mvn.usace.army.mil/Missions/Mississippi-River-Flood-Control/Bonnet-Carre-Spillway-Overview/Spillway-Operation-Information/) for the 2019 year. This average discharge (3.12×10^8 m^3 d^{-1}) and the Mississippi River nutrient

endmembers were used to calculate the impact of the BCS. This was likely an overestimate of the BCS endmember entering the Sound, since nutrients will be removed during the water transit through Lake Pontchartrain, and not all BCS water will enter the Sound (Parra et al., 2020). Both the local river and BCS influences to the study area were probably overestimated, since the river input gets more broadly dispersed through the Sound while SGD impacts are most pronounced near the seepage face.

Table 3.2 *Fluxes of different constituents from SGD, the Pearl River, and the BCS.*

	Dsi (kmol d^{-1})	DIN (kmol d^{-1})	DIP (kmol d^{-1})	DON (kmol d^{-1})	NH_4^+ (kmol d^{-1})	Ba (kmol d^{-1})
Pearl River Flux	1400	350	20	780	90	5.8
SGD Flux (^{224}Ra)	360	85	20	130	100	0.5
SGD Flux (^{228}Ra)	400	90	30	150	110	0.6
SGD Flux (^{222}Rn)	100	20	6	35	30	0.1
Bonnet Carre Spillway Flux	29000	39400	750	38000	540	140

When comparing fluxes, the BCS dominates the flux of nutrients and Ba to the Sound when it is open (Table 2). Again, this is an overestimate, since the discharge rate to the Sound will not be as high after traveling through Lake Pontchartrain. However, it was noticed that the opening of the BCS greatly affected the overall biogeochemistry of the Sound, and caused harmful algal blooms and organism mortality in 2019 (Gledhill et al., 2020; Byrd, 2019). The average Pearl River nutrient fluxes were dominant over SGD for DSi and Ba but were nearly the same order of magnitude for DIN, DIP, DON, and NH_4^+. This only takes into account average fluxes. Figure 3.13 looks at the average, minimum, and maximum fluxes of each constituent into the Sound. From this, we can

conclude that the fluxes from rivers and SGD overlap each other, and therefore SGD is a significant contributor of nutrients to the Sound, especially when the river flux is low. Our fluxes are higher than those recently estimated in the Mississippi Bight (Sanial et al., 2021), but are within range of estimates from multiple SGD studies in other estuaries for DIN, DIP, and DSi (Slomp and Van Capellan, 2004; Santos et al., 2021).

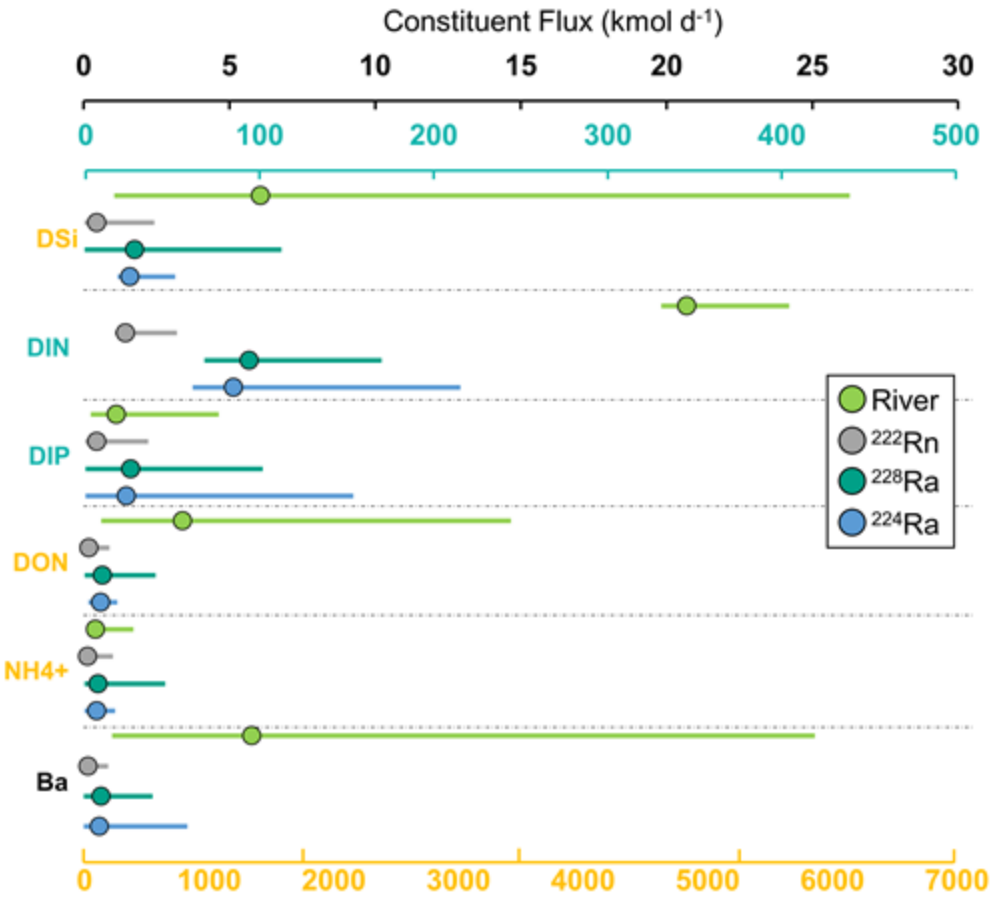

Figure 3.13 *Fluxes of various constituents from SGD and the Pearl River.*

The marker is the calculated average flux, and the bars are the range of the minimum and maximum flux. Colors of the y-axis match the scales of the appropriate x-axis.

Using the fish kill period estimates for ^{224}Ra and ^{228}Ra, we can calculate a potential oxygen demand (Sanial et al., 2021) for our reduced species of nitrogen, and

carbon during the times when we had low oxygen. This will allow us to determine if SGD input is enough to convert a system to hypoxia, especially if the system is already experiencing lower oxygen. NH_4^+, DON, and CH_4 have a molar oxygen demand of 2:1. To calculate oxygen demand, we use the equation:

Potential oxygen demand = $(Ra_{SurfW} - Ra_{pred}) \div Ra_{SurfW} \times C_{GW} \times O_{2\text{-demand}}$

where Ra_{SurfW} is the surface activity of radium in the Sound water during each sampling point, Ra_{pred} is radium activity predicted from salinity based on the river to offshore mixing curve, C_{GW} is the constituent concentration in the groundwater, and $O_{2\text{-demand}}$ is the oxygen demand for that constituent. This calculates the percentage of Sound water that is groundwater, and then how much of a certain constituent will make it to the surface with an oxygen demand (Figure 3.14). While this almost certainly underestimates the oxygen demand, because we neglect sulfide, DOC and other components, it nonetheless provides a minimum estimate of how much oxygen depletion there can be with SGD. From ^{224}Ra, we get an average potential oxygen demand of 162 µM, and from ^{228}Ra, 178 µM. Previous work done in the Mississippi Bight predicted a potential oxygen demand ranging from 22 – 78 µM, depending on seasonality (Sanial et al., 2021). This only examined the oxygen demand from groundwater of DON, NH_4^+, and CH_4 as there can be oxygen demand from sulfide, organic carbon and other constituents as well. However, this simple calculation shows that there is enough of an oxygen demand to reduce low oxygen waters to hypoxic/anoxic conditions if there is high enough groundwater flow. Indeed, these potential oxygen demand estimates represent roughly half of the typical summer saturation value of oxygen.

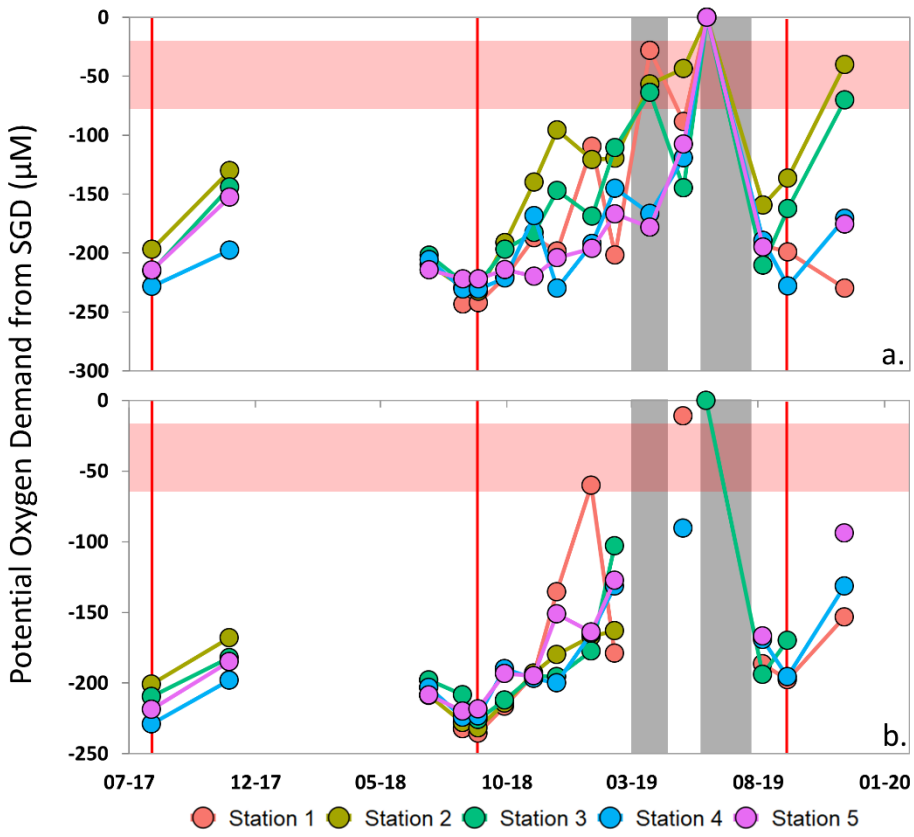

Figure 3.14 *Potential oxygen demand from SGD.*

Based on a) ^{224}Ra activities and b) ^{228}Ra activities. Vertical red lines indicate when there was an observed fish kill and gray bars are when the BCS was open. The horizontal red bar shows the potential oxygen demand in the Mississippi Bight (Sanial et al., 2021).

3.5 Conclusion

The effect of SGD on estuarine biogeochemistry has been shown to be important, but it is still relatively unknown globally how SGD changes seasonally and thus triggers episodic events such as fish kills, harmful algal blooms, or hypoxia. Previous work in the Mississippi Sound and Bight (e.g., Ho et al., 2019; Sanial et al., 2021) and episodic hypoxic events along the coast indicated that SGD may play a role in the Mississippi Sound biogeochemistry. Using three radioisotope tracers (^{224}Ra, ^{228}Ra, and ^{222}Rn), we were able to quantify SGD rates infiltrating the coastal waters of the Mississippi Sound.

Our approaches using radium for the time series data along the coastline gave us a range of SGD values, ranging from 0 (negligible) to 67.5±16.3 cm d^{-1} for ^{224}Ra, and 0.7±0.4 to 44.7±17.3 cm d^{-1} for ^{228}Ra, which are of the same order of magnitude, allowing for confidence in our calculations. These are also in line with previous coastal estimates. Radon SGD estimates were taken further offshore and at broader time scale intervals to obtain spatial distribution of SGD. The fluxes from ^{222}Rn ranged from 0 cm d^{-1} to 16.4 cm d^{-1}, which fall within our radium shoreline estimates.

The summer and fall had the highest discharge rates for our radium tracers, and the fall and winter had the highest discharge for radon. This can cause interesting dynamics for the Mississippi Sound, including differences in nutrient domination between rivers and SGD, which can greatly impact the geochemistry of the Sound due to their highly different endmember concentrations. Three of the sampling days during the time series had a connection to a fish kill event, either a 'jubilee' or unexplained dead fish in the water column and on the beach. While it is still uncertain if SGD was the major cause, the release of increased SGD, and therefore increased reduced species such as NH_4^+ and DON, may drive oxygen levels down enough to tip and already at risk system into hypoxia. We found that for an average input of ^{224}Ra and ^{228}Ra during fish kill events, there is an estimated average potential oxygen demand between 162 – 178 µM (this does not include sulfide and DOC), which would be enough to drive an already low oxygen environment to hypoxia. Overall, SGD in this system plays a highly important role in nutrient fluxes, and can potentially be a sink of oxygen, leading to both eutrophication and hypoxia along the coastline.

3.6 References

Armandei, M., Linhoss, A.C., Camacho, R.A., 2021. Hydrodynamic modeling of the Western Mississippi Sound using a linked model system. Reg. Stud. Mar. Sci. 44, 101685. https://doi.org/10.1016/J.RSMA.2021.101685

Attisano, K. K., Santos, I. R., Ferreira De Andrade, C. F., Lopes De Paiva, M., Milani, I. C. B., Niencheski, L. F. H., 2013. Submarine groundwater discharge revealed by radium isotopes (Ra-223 and Ra-224) near a paleochannel on the southern Brazilian continental shelf. Brazilian J. Oceanogr. 61, 195–200.

Beck, A.J., Rapaglia, J.P., Cochran, J.K., Bokuniewicz, H.J., 2007. Radium mass-balance in Jamaica Bay, NY: Evidence for a substantial flux of submarine groundwater. Marine Chemistry, 106(3-4), 419-441.

Bera, G., Yeager, K.M., Shim, M., Shiller, A.M., 2015. Anthropogenic stable cesium in water and sediment of a shallow estuary, St. Louis Bay, Mississippi. Estuar. Coast. Shelf Sci. 157, 32–41. https://doi.org/10.1016/j.ecss.2015.02.004.

Bricker, S.B., C.G. Clement, D.E. Pirhalla, S.P. Orlando, and D.R.G. Farrow. 1999. National Estuarine Eutrophication Assessment: Effects of Nutrient Enrichment in the Nation's Estuaries. NOAA, National Ocean Service, Special Projects Office and the National Centers for Coastal Ocean Science. Silver Spring, MD: 71 pp.

Bouchard, C., 2021. Exploring the Influence of Diurnal Forcing on Tidal Inlet Exchange and the Impact on the movement of Oxygen Depleted Waters in the Mississippi Sound and Bight Region. Masters thesis, Univ. of Southern Mississippi.

Bugna, G.C., Chanton, J.P., Cable, J.E., Burnett, W.C., Cable, P.H., 1996. The importance of groundwater discharge to the methane budgets of nearshore and continental shelf waters of the northeastern Gulf of Mexico. Geochimica et Cosmochimica Acta, 60(23), 4735-4746.

Burnett, W.C., Bokuniewicz, H., Huettel, M., Moore, W.S., Taniguchi, M., 2003. Groundwater and pore water inputs to the coastal zone. Biogeochemistry 66, 3–33. https://doi.org/10.1023/B:BIOG.0000006066.21240.53

Byrd, J., 2019. Fishery Disaster Due to the Opening of the Bonnet Carré Spillway. Water Log 39:4, 10-12. http://masglp.olemiss.edu/waterlog/pdf/dec19/wl39.4_article3.pdf

Cambazoglu, M.K., Soto, I.M., Howden, S.D., Dzwonkowski, B., Fitzpatrick, P.J., Arnone, R.A., Jacobs, G.A., Lau, Y.H., 2017. Inflow of shelf waters into the Mississippi Sound and Mobile Bay estuaries in October 2015. J. of Applied Remote Sensing, 11(3), 032410. https://doi.org/10.1117/1.JRS.11.032410 11, 032410.

Cable, J.E., Bugna, G.C., Burnett, W.C., Chanton, J.P., 1996. Application of ^{222}Rn and CH_4 for assessment of groundwater discharge to the coastal ocean. Limnology and Oceanography, 41(6), 1347-1353.

Cheng, K.H., Luo, X., Jiao, J.J., 2020. Two-decade variations of fresh submarine groundwater discharge to Tolo Harbour and their ecological significance by coupled remote sensing and radon-222 model. Water Research, 178, 115866.

Cobb, M., Blain, C.A., 2002. A coupled hydrodynamic-wave model for simulating wave

and tidally-driven 2D circulation in inlets. Estuarine and Coastal Modeling, 725-742.
Dansgaard, W., 1964. Stable isotopes in precipitation. Tellus 16, 436–468. https://doi.org/10.3402/tellusa.v16i4.8993.
Darnell, R.M., 1992. Ecological history, catastrophism, and human impact on the Mississippi/Alabama continental shelf and associated waters: a review. Gulf and Caribbean Research, 8(4), 375-386.
Davenport, F.V., Diffenbaugh, N.S., 2021. Using machine learning to analyze physical causes of climate change: A case study of US Midwest extreme precipitation. Geophysical Research Letters, 48(15), p.e2021GL093787.
de Weys, J., Santos, I.R., Eyre, B.D., 2011. Linking groundwater discharge to severe estuarine acidification during a flood in a modified wetland. Environ. Sci. Technol. 45, 3310–3316. https://doi.org/10.1021/es104071r
Dimova, N.T., Burnett, W.C., Chanton, J.P., Corbett, J.E., 2013. Application of radon-222 to investigate groundwater discharge into small shallow lakes. J. Hydrol. 486, 112–122. https://doi.org/10.1016/J.JHYDROL.2013.01.043
Dinnel, S.P., Wiseman, W.J., 1986. Fresh water on the Louisiana and Texas shelf. Cont. Shelf Res. 6, 765–784. https://doi.org/10.1016/0278-4343(86)90036-1.
Dugas, R. J., Joyce E. A., Berrigan, M. E., 1997. History and status of the oyster, Crassostrea virginica, and other molluscan fisheries of the U.S. Gulf of Mexico, p. 187–210. In Mackenzie Jr., C. L., V. G. Burrell Jr., A. Rosenfield, and W. L. Hobart [eds.], The history, present condition, and future of the molluscan fisheries of North and Central America and Europe. Volume 1, Atlantic and Gulf Coasts. U.S. Dep. Commer., NOAA Tech. Rep. 127, 234 p.
Dulaiova, H., Camilli, R., Henderson, P.B., Charette, M.A., 2010. Coupled radon, methane and nitrate sensors for large-scale assessment of groundwater discharge and non-point source pollution to coastal waters. J. Environ. Radioact. 101, 553–563. https://doi.org/10.1016/j.jenvrad.2009.12.004
Dzwonkowski, B., Fournier, S., Reager, J.T., Milroy, S., Park, K., Shiller, A.M., Greer, A.T., Soto, I., Dykstra, S.L., Sanial, V., 2018. Tracking sea surface salinity and dissolved oxygen on a river-influenced, seasonally stratified shelf, Mississippi Bight, northern Gulf of Mexico. Cont. Shelf Res. 169, 25–33. https://doi.org/10.1016/j.csr.2018.09.009.
Eleuterius, C.K., 1978. Classification of Mississippi Sound as to Estuary Hydrological Type. GulfResearch Reports 6, 185–187. https://doi.org/10.18785/grr.0602.12
Engle, V.D., Kevin Summers, J., Macauley, J.M., 1999. Dissolved oxygen conditions in northern Gulf of Mexico estuaries. Environ. Monit. Assess. 57, 1–20. https://doi.org/10.1023/A:1005980410752
Etter, P.C., Howard, M.K. and Cochrane, J.D., 2004. Heat and freshwater budgets of the Texas-Louisiana shelf. J. Geophys. Res. Oceans. 109(C2). https://doi.org/10.1029/2003JC001820
Frohlich, K., Gibson, J.J., Aggarwal, P.K., 2001. Deuterium Excess in Precipitation and its Climatological Significance, Vol. 13 International Atomic Energy Agency, Vienna.

Garcia-Solsona, E., Garcia-Orellana, J., Masqué, P., Dulaiova, H., 2008. Uncertainties associated with ^{223}Ra and ^{224}Ra measurements in water via a Delayed Coincidence Counter (RaDeCC). Mar. Chem. 109, 198–219. https://doi.org/10.1016/J.MARCHEM.2007.11.006

Garcia-Orellana, J., Cochran, J.K., Bokuniewicz, H., Daniel, J.W.R., Rodellas, V., Heilbrun, C., 2014. Evaluation of ^{224}Ra as a tracer for submarine groundwater discharge in Long Island Sound (NY). Geochim. Cosmochim. Acta 141, 314–330. https://doi.org/10.1016/J.GCA.2014.05.009

Gledhill, J.H., Barnett, A.F., Slattery, M., Willett, K.L., Easson, G.L., Otts, S.S., Gochfeld, D.J., 2020. Mass mortality of the Eastern Oyster Crassostrea virginica in the western Mississippi Sound following unprecedented Mississippi River flooding in 2019. Journal of Shellfish Research, 39(2), 235-244.

George, C., Moore, W.S., White, S.M., Smoak, E., Joye, S.B., Leier, A., Wilson, A.M., 2020. A new mechanism for submarine groundwater discharge from continental shelves. Water Resources Research, 56(11), p.e2019WR026866.

Greenwood, J. E., Symonds, G., Zhong, L., Lourey, M., 2013. Evidence of submarine groundwater nutrient supply to an oligotrophic barrier reef. Limnol. Oceanogr. 58, 1834–1842.

Gunter, G., Lyles, C. H., 1979. Localized Plankton Blooms and Jubilees on the Gulf Coast. Gulf Res. Reports 6, 297–299. https://doi.org/10.18785/grr.0603.12

Guo, X., Xu, B., Burnett, W.C., Wei, Q., Nan, H., Zhao, S., Charette, M.A., Lian, E., Chen, G. and Yu, Z., 2020. Does submarine groundwater discharge contribute to summer hypoxia in the Changjiang (Yangtze) River Estuary?. Science of the Total Environment, 719, 137450.

Ho, P., Shim, M.J., Howden, S.D., Shiller, A.M., 2019. Temporal and spatial distributions of nutrients and trace elements (Ba, Cs, Cr, Fe, Mn, Mo, U, V and Re) in Mississippi coastal waters: Influence of hypoxia, submarine groundwater discharge, and episodic events. Cont. Shelf Res. 175, 53–69. https://doi.org/10.1016/j.csr.2019.01.013

Hode, L., 2019. Establishing the Role of the Mississippi-Alabama Barrier Islands in Mississippi Sound and Bight Circulation Using Observational Data Analysis and a Coastal Model. Ph.D dissertation, Uni. of Southern Mississippi.

Joung, D.J., Shiller, A.M., 2014. Dissolved barium behavior in Louisiana Shelf waters affected by the Mississippi/Atchafalaya River mixing zone. Geochim. Cosmochim. Acta 141, 303–313. https://doi.org/10.1016/j.gca.2014.06.021

Kim, G., Ryu, J. W., Yang, H. S., Yun, S. T., 2005. Submarine groundwater discharge (SGD) into the Yellow Sea revealed by ^{228}Ra and ^{228}Ra isotopes: Implications for global silicate fluxes. Earth Planet. Sci. Lett. 237, 156–166. https://doi.org/10.1016/J.EPSL.2005.06.011

Khublaryan, M. G., Frolov, A. P., Yushmanov, I. O., 2008. Seawater intrusion into coastal aquifers. Water Resour. 35, 274–286.

Lambert, M.J., Burnett, W.C., 2003. Submarine groundwater discharge estimates at a Florida coastal site based on continuous radon measurements. Biogeochemistry, 66(1), 55-73.

Loesch, H. 1960. Sporadic mass shoreward migrations of demersal fish and crustaceans in Mobile Bay, Alabama. Ecology 41 (2): 292–298.
Luo, M., Zhang, Y., Li, H., Wang, X., Xiao, K., 2020. Submarine groundwater discharge in a coastal bay: Evidence from radon investigations. Water, 12(9), 2552.
Mccoy, C., Viso, R., Peterson, R.N., Libes, S., Lewis, B., Ledoux, J., Voulgaris, G., Smith, E., Sanger, D., 2011. Radon as an indicator of limited cross-shelf mixing of submarine groundwater discharge along an open ocean beach in the South Atlantic Bight during observed hypoxia. Cont. Shelf Res. 31, 1306–1317. https://doi.org/10.1016/j.csr.2011.05.009
Michael, H.A., Mulligan, A.E., Harvey, C.F., 2005. Seasonal oscillations in water exchange between aquifers and the coastal ocean. Nature 436, 1145–1148. https://doi.org/10.1038/nature03935
Mississippi Department of Marine Resources (MDMR). (2017, July 27). *Jubilee occurring in Mississippi Sound; Seafood safe to eat, but people should use caution* [Press Release]. https://dmr.ms.gov/wp-content/uploads/2019/07/17-47-MMS-Jubilee-occurring-in-Mississippi-Sound.pdf. Access date: May 5, 2022.
Montiel, D., Lamore, A., Stewart, J., Dimova, N., 2019. Is Submarine Groundwater Discharge (SGD) Important for the Historical Fish Kills and Harmful Algal Bloom Events of Mobile Bay? Estuaries and Coasts 42, 470–493. https://doi.org/10.1007/s12237-018-0485-5
Moore, W. S., 1996. Large groundwater inputs to coastal waters revealed by 226Ra enrichments. Nature 380, 612–614.
Moore, W.S., 1999. The subterranean estuary: a reaction zone of ground water and sea water. Mar. Chem. 65, 111–125. https://doi.org/10.1016/S0304-4203(99)00014-6
Moore, W.S. 2000. Determining coastal mixing rates using radium isotopes. Continental Shelf Research 20(15), 1993–2007.
Moore, W.S., 2010. The effect of submarine groundwater discharge on the ocean. Ann. Rev. Mar. Sci. 2, 59–88. https://doi.org/10.1146/annurev-marine-120308-081019
Moore, W.S. and Arnold, R., 1996. Measurement of ^{223}Ra and ^{224}Ra in coastal waters using a delayed coincidence counter. J. Geophys. Res. 101, 1321–1329.
Moore, W.S., Blanton, J.O., Joye, S.B., 2006. Estimates of flushing times, submarine groundwater discharge, and nutrient fluxes to Okatee Estuary, South Carolina. J. Geophys. Res. 111, C09006. https://doi.org/10.1029/2005JC003041
Moore, W.S. and Joye, S.B., 2021. Saltwater Intrusion and Submarine Groundwater Discharge: Acceleration of Biogeochemical Reactions in Changing Coastal Aquifers. Front. Earth Sci. 9:600710. doi: 10.3389/feart.2021.600710
Moore, W. S. and Shaw, T.J., 1998. Chemical signals from submarine fluid advection onto the continental shelf. J. Geophys. Res. 103, 21543-21552.
Moore, W.S. and Shaw, T.J., 2008. Fluxes and behavior of radium isotopes, barium, and uranium in seven Southeastern US rivers and estuaries J. Geophys. Res. 101, 236–254. https://doi.org/10.1016/j.marchem.2007.03.004
Mulligan, A.E., Evans, R.L., Lizarralde, D., 2007. The role of paleochannels in groundwater/seawater exchange. J. Hydrol. 335, 313–329. https://doi.org/10.1016/J.JHYDROL.2006.11.025

Neuzil, C.E., 1986. Groundwater flow in low-permeability environments. Water Resour. Res. 22, 1163–1195. https://doi.org/10.1029/WR022i008p01163
National Oceanic and Atmospheric Administration (NOAA). 1997. NOAA's Estuarine Eutrophication Survey, Volume 4: Gulf of Mexico Region. Silver Spring, MD: Office of Ocean Resources Conservation and Assessment. 77 pp.
Orlando, S.P. Jr., Rozas, L.P., Ward, G.H., Klein, C.J. 1993. Salinity Characteristics of Gulf of Mexico Estuaries. Silver Spring, MD: National Oceanic and Atmospheric Administration, Office of Ocean Resources Conservation and Assessment. 209 pp.
Otvos, E.G., 2001. Mississippi coast: stratigraphy and Quaternary evolution in the Northern Gulf Coastal Plain framework. Stratigraphic and Paleontologic Studies of the Neogene and Quaternary Sediments in Southern Jackson County, Mississippi. US Geological Survey Open File Report, pp.01-415.
Overstreet, R.M., Hawkins, W.E., 2017. Diseases and mortalities of fishes and other animals in the Gulf of Mexico, in: Habitats and Biota of the Gulf of Mexico: Before the Deepwater Horizon Oil Spill. Ward, C.H. ed, Springer New York, pp. 1589–1738. https://doi.org/10.1007/978-1-4939-3456-0_6
Peterson, R.N., Moore, W.S.; Chappel, S.L., Viso, R.F., Libes, S.M., Peterson, L.E., 2016. A New Persective on Coastal Hypoxia: The Role of Saline Groundwater. Marine Chemistry, 179, 1-11.
Renken, R.A., 1998. Ground Water Atlas of the United States: Segment 5, Arkansas, Louisiana, Mississippi (No. 730-F, pp. F1-F28). US Geological Survey.
Roberts, H.M., 2014. Methane Dynamics in St. Louis Bay, Mississippi. Masters thesis, Univ. of Southern Mississippi.
Roberts, H.M. and Shiller, A.M., 2015. Determination of dissolved methane in natural waters using headspace analysis with cavity ring-down spectroscopy. Analytica Chimica Acta, 856, pp. 68-73.
Rodellas, V., Garcia-Orellana, J., Garcia-Solsona, E., Masqué, P., Domínguez, J.A., Ballesteros, B.J., Mejías, M., Zarroca, M., 2012. Quantifying groundwater discharge from different sources into a Mediterranean wetland by using ^{222}Rn and Ra isotopes. J. Hydrol. 466–467, 11–22. http://dx.doi.org/10.1016/j.jhydrol.2012.07.005.
Rodellas, V., Garcia-Orellana, J., Masqué, P., Font-Muñoz, J.S., 2015. The influence of sediment sources on radium-derived estimates of Submarine Groundwater Discharge. Mar. Chem. 171, 107–117. https://doi.org/10.1016/j.marchem.2015.02.010
Rodellas, V., Garcia-Orellana, J., Trezzi, G., Masqué, P., Stieglitz, T.C., Bokuniewicz, H., Cochran, J.K., Berdalet, E., 2017. Using the radium quartet to quantify submarine groundwater discharge and porewater exchange. Geochim. Cosmochim. Acta 196, 58–73. https://doi.org/10.1016/J.GCA.2016.09.016
Sanial, V., Moore, W.S., Shiller, A.M., 2021. Does a bottom-up mechanism promote hypoxia in the Mississippi Bight?. Marine Chemistry, 235, 104007.
Sanial, V., Shiller, A.M., Joung, D.J., Ho, P., 2019. Extent of Mississippi River water in the Mississippi Bight and Louisiana Shelf based on water isotopes. Estuar. Coast. Shelf Sci. 226, 106196. https://doi.org/10.1016/j.ecss.2019.04.030
Santos, I.R., Chen, X., Lecher, A.L., Sawyer, A.H., Moosdorf, N., Rodellas, V., Tamborski, J., Cho, H.M., Dimova, N., Sugimoto, R., Bonaglia, S., 2021. Submarine

groundwater discharge impacts on coastal nutrient biogeochemistry. Nature Reviews Earth & Environment, 2(5), 307-323.

Santos, I.R., Dimova, N., Peterson, R.N., Mwashote, B., Chanton, J., Burnett, W.C., 2009. Extended time series measurements of submarine groundwater discharge tracers (^{222}Rn and CH_4) at a coastal site in Florida. Mar. Chem. 113, 137–147. https://doi.org/10.1016/J.MARCHEM.2009.01.009

Savoie, A., 2020. Freshwater Endmembers Impacting Carbonate Chemistry in the Mississippi Sound. Masters thesis, Univ. of Southern Mississippi.

Sawyer, W.B., Vaughan, C., Lavoie, D., Furukawa, Y., Carnaggio, N., Maclean, J., Populis, E., 2001. Northern Gulf Littoral Initiative (NGLI), Geology and Physical Properties of Marine Sediments in the N.E. Gulf of Mexico: Data Report. Report NRL/Mr-MM/7430--01-8548; Naval Research Laboratory, Washington, D.C.

Schubert, M., Paschke, A., Lieberman, E., Burnett, W.C., 2012. Air-water partitioning of ^{222}Rn and its dependence on water temperature and salinity. Environ. Sci. Technol. 46, 3905–3911. https://doi.org/10.1021/es204680n

Schubert, M., and Paschke, A., 2015. Radon, CO_2 and CH_4 as environmental tracers in groundwater/surface water interaction studies − comparative theoretical evaluation of the gas specific water/air phase transfer kinetics. The European Physical Journal Special Topics, 224: 709-715. DOI: 10.1140/epjst/e2015-02401-4.

Sherif, A.R., 2018. Urban Landscape Assessment of the Mississippi and Alabama Gulf Coast Using Landsat Imagery 1973-2015. Masters thesis, Mississippi State University.

Shiller, A.M., Shim, M.J., Guo, L., Bianchi, T.S., Smith, R.W., Duan, S., 2012. Hurricane Katrina impact on water quality in the East Pearl River, Mississippi. Journal of Hydrology, 414, 388-392.

Shim, M.J., Cai, Y., Guo, L., Shiller, A.M., 2017. Floodplain effects on the transport of dissolved and colloidal trace elements in the East Pearl River, Mississippi. Hydrol. Process. 31, 1086–1099. https://doi.org/10.1002/hyp.11093.

Slomp, C.P., and Van Cappellen, P., 2004. Nutrient inputs to the coastal ocean through submarine groundwater discharge: Controls and potential impact. J. Hydrol. 295, 64–86. https://doi.org/10.1016/j.jhydrol.2004.02.018

Soto, I.M., Cambazoglu, M.K., Boyette, A.D., Broussard, K., Sheehan, D., Howden, S.D., Shiller, A.M., Dzwonkowski, B., Hode, L., Fitzpatrick, P.J. and Arnone, R.A., 2018. Advection of Karenia brevis blooms from the Florida Panhandle towards Mississippi coastal waters. Harmful Algae, 72, pp.46-64.

Spaid, H., 2020. Contribution of Submarine Groundwater Discharge to Select Biogeochemical Fluxes in St. Louis Bay, Mississippi. Masters thesis, Univ. of Southern Mississippi.

Taniguchi, M., Burnett, W.C., Cable, J.E., Turner, J.V., 2002. Investigation of submarine groundwater discharge. Hydrological Processes, 16(11), pp.2115-2129. https://doi.org/10.1002/hyp.1145

van Geldern, R., and Barth, J.A.C., 2012. Optimization of instrument setup and post-run corrections for oxygen and hydrogen stable isotope measurements of water by isotope ratio infrared spectroscopy (IRIS). Limnol Oceanogr. Methods 10, 1024–1036. https://doi.org/10.4319/lom.2012.10.1024.

Vázquez-Suñé, E., Suñé, S., Carrera, J., Tubau, I., Sánchez-Vila, X., Soler, A., 2010. Hydrology and Earth System Sciences An approach to identify urban groundwater recharge. Hydrol. Earth Syst. Sci 14, 2085–2097. https://doi.org/10.5194/hess-14-2085-2010

Wiesenburg, D.A., and Guinasso, N.L.J., 1979. Equilibrium solubilities of methane, carbon monoxide, and hydrogen in water and sea water. J. Chem. Eng. Data 24, 356–360.

Williams, W. (2018, December 31). *2018: One of Gulfport's hottest and wettest years on record.* [News Article]. https://www.wlox.com/2018/12/31/one-gulfports-hottest-wettest-years-record/. Access date: August 12, 2022.

CHAPTER IV – THE INFLUENCE OF SUBMARINE GROUNDWATER DISCHARGE (SGD), LOCAL RIVER DISCHARGE, AND THE BONNET CARRÉ SPILLWAY (BCS) ON THE GEOCHEMICAL MAKEUP OF THE MISSISSIPPI SOUND

4.1 Abstract

The Mississippi Sound, an estuary in the northern Gulf of Mexico, is impacted by a variety of water sources, all of which contribute to its geochemical makeup. In this study, we determine how each water source contributes to nutrients and trace metal dynamics in the Mississippi Sound. Fourteen surveys between 2018 and 2021 were conducted across the entire Sound to determine SGD fluxes using ^{222}Rn and the radium quartet. To account for uncertainty, Monte Carlo simulations were implemented into our mass balance calculations, providing a broad scope of the error associated with SGD fluxes. Distinct spatial variation of the magnitude of SGD was found, with the western Sound having the highest SGD, and the eastern Sound the lowest. Wet and dry season SGD fluxes were similar in magnitude, but the dry season had a larger input of fresh groundwater compared to the wet season, indicating a lag time in recharge and discharge. Average water fluxes of SGD were at least one order of magnitude lower than local rivers and the Bonnet Carré Spillway. Nutrient and trace metal distributions were influenced by the opening of the BCS, local rivers, and SGD. In general, the local rivers dominated the nutrient input, but SGD was highly important for dissolve inorganic phosphorus and ammonium. Trace element distributions were dominated by river inputs, but SGD was shown to potentially be important for Re, Ba, and V. Overall, SGD was concluded to be important for both nutrient and trace metal dynamics.

4.2 Introduction

Estuaries are transition zones between terrestrial water sources such as rivers and the coastal ocean and are regions with high biodiversity, a variety of habitats, and act as a natural filter of nutrients and sediments (Elliot et al., 2019; Kennish, 2002). These areas are important regions of nutrient, carbon, and trace metal cycling, and are often susceptible to negative impacts such as excessive sediment and pollutant inputs, eutrophication, and hypoxia (Bricker et al., 1999; Elliot et al., 2019; Kennish, 2002). The main influences on estuaries are typically thought to be river and marine inputs that determine not only the salinity gradient of the system, but also the concentrations of various constituents (Bricker et al., 1999). These regions worldwide have been shown to be important not only ecologically, but also socially and economically (Elliot et al., 2019). Therefore, understanding the mechanisms that affect these sensitive ecosystems is important.

The Mississippi Sound is a subtropical estuary along the coast of Mississippi and Alabama that experiences seasonal hypoxia, eutrophication, and, on occasion, harmful algal blooms (HABs), all of which lead to organism mortality (NOAA, 1997; Rabalais and Turner, 2001). The Sound is an important habitat for oysters (Linhoss and Mickle, 2022), and negative impacts on water quality can affect the viability of oyster reefs (e.g., Lowe et al., 2017). Oysters provide ecosystem services such as filtration, benthic and pelagic coupling, and the creation of nesting and feeding habitats (Coen et al., 2007). Negative impacts on the oyster reefs in the Mississippi Sound have led to economic impacts and destruction of hard bottom habitat that many species rely on (Morgan and Rakochinski, 2020; Schulte et al., 2010). The most recent oyster reef die-off occurred in

2019 due to diversion of Mississippi River water into the Sound, which exposed the Sound to nutrient enriched, low salinity water (Bonnet Carré Spillway Overview, 2019; Morgan and Rakochinski, 2020). The Bonnet Carré Spillway (BCS), which is the source of the Mississippi River diversion, is located near New Orleans, and prevents flooding by diverting a portion of the Mississippi River to Lake Pontchartrain and surrounding lakes, and which can eventually flow into the Mississippi Sound and Bight (Dortch et al., 2007; Dzwonkowski et al., 2018). During years of extended openings of the BCS, the Sound experiences extreme drops in salinity, and increased nutrient inputs (Dortch et al., 2007; Gledhill et al., 2020; Byrd, 2019). While this is a relatively infrequent occurrence, during 2019 the BCS was open for an unprecedented number of days, leading to mass organism mortality, hypoxia, and HABs. This release of Mississippi River water led to ~ 90% oyster mortality (Morgan and Rakochinski, 2020). With climate change, it is highly probable that there will more openings of the BCS due to enhanced precipitation (e.g., Davenport and Diffenbaugh, 2021), leading to more frequent drops in the Mississippi Sound salinity, eutrophication, and hypoxia, causing more mortality events.

While rivers and offshore waters are known to affect biogeochemical cycles in estuaries, a relatively unquantified component of these systems is submarine groundwater discharge. Submarine groundwater discharge (SGD) is a broad term that encompasses the advective flow of fresh groundwater and recirculating seawater through an aquifer, often coined as the subterranean estuary due to the chemical reactions between the mixing waters (Burnett et al., 2003; Moore, 1999). This process is driven by hydraulic forcing, and pressure gradients due to waves, tides, and/or density driven water circulation (Santos et al., 2012). SGD usually has a small volumetric flux of water compared to both

river and marine sources, and is often not typically considered in estuarine models and balances (Moore, 2010). However, unlike the BCS, SGD has the potential to be a continuous source of elevated nutrients year round, as groundwater often has higher concentrations of many dissolved materials than rivers (Moore, 2010). Depending on the total water flux from SGD, and the concentration of dissolved constituents, the impact of SGD on coastal oceans can be very similar to rivers, or an even greater source of materials such as nutrients, trace metals, and carbon (Moore, 2010). Recent work has shown that oyster reef locations can be affected by the presence of SGD (e.g., Carroll et al., 2021; Spalt et al., 2018; Spalt et al., 2020). Submarine groundwater discharge can sometimes increase the survivability of oysters by having a moderating influence on temperature, salinity, and nutrients (Bighash and Murgulet, 2015; Hwang et al., 2005; Spalt et al., 2020), or it can have negative impacts on oyster reefs by providing low oxygen and low pH water (Carroll et al., 2021). Therefore, identifying locations of high SGD, and its impact on the water quality is important for oyster reef management.

It is well known that SGD often influences coastal waters, but the reasons why SGD impacts are higher or lower in different coastal environments are often unclear. Previous work has indicated that factors such as hydrologic conditions, sediment type, and paleochannels within the underlying sediment can all play a role in SGD influence (Spalt et al., 2018). For hydrologic conditions, it is thought that elevation of the terrestrial water table in coastal aquifers and movement of the fresh-saline groundwater interface can impact the total SGD fluxes on a seasonal basis (Santos et al., 2012). During the wet season, rainfall recharges aquifers with fresh groundwater, which can move the interface seaward. Then during the dry season, the interface moves landward (Michael et al.,

2005). When the interface moves landward, the seawater infiltrates the aquifer, and then discharges as the interface moves seaward again (Michael et al., 2005). This has implications for how groundwater dynamics change with season, especially if there is pronounced wet/dry season variability. Surficial sediment type is also thought to play a role in SGD fluxes (Douglas et al., 2020). Sediment types with fine grain size such as clay and silt create dense barriers to advective flow through sediments, and therefore may be areas that are not conducive to SGD (Douglas et al., 2020). Lastly, paleochannels and paleovalleys have been hypothesized to be conduits of SGD from the shore to the coastal zone, and even further offshore (Attisano et al., 2013; Burnett et al., 2006; Mulligan et al., 2007). Paleochannels and paleovalleys are infilled ancient river channels from when sea level was lower (Kolker et al., 2013; Mulligan et al., 2007). These locations are typically filled with permeable sediments, and can be hydraulic connections between terrestrial aquifers and the coastal ocean (Mulligan et al., 2007). When breached, paleochannels can be sources of fresh or saline groundwater, especially if there is pumping of groundwater onshore for human use (Mulligan et al., 2007). Studies in other regions with paleovalleys have indicated that oyster reefs tend to live along the margins of paleochannels, where the highest SGD fluxes occur (e.g., Spalt et al., 2018).

Nutrients and trace metals are extremely important in estuarine systems, as they not only provide the essential building blocks for life, but can also become harmful if at too high of levels. High levels of nutrient fluxes from SGD have been well reported (e.g., Slomp and Van Cappellen, 2004), and have been shown to potentially lead to hypoxia due to the high oxygen demand from reduced constituents (e.g., Sanial et al., 2021). Trace metal input from SGD is not as widely reported, but some studies have reported

that SGD can have an impact on trace metal cycling and input (e.g., Prakash et al., 2021; Santos et al., 2011). Trace metals can also be used as indicators of redox conditions, tracers of different water sources, are utilized as micronutrients, and can become pollutants if concentrations become too high.

In this study, we aim to determine the overall flux of SGD to Mississippi Sound using a non-deterministic approach with multiple tracers to understand the spatial and seasonal variation of SGD within the Sound. In particular, we look at the variability of SGD, including the distinction of fresh and recirculated SGD, and how this is affected by seasonality, paleovalley location, and surficial sediment variations. With our estimated fresh and recirculated SGD fluxes, we then compare local river, BCS, and groundwater sources of nutrients, including inorganic and organic, and trace metals. Based on these, we construct an environmental risk assessment based on the concentrations in the surface waters and predicted no effect concentration, which can be used to predict the effect on the oyster reef population. The Mississippi Sound is highly dynamic system, with many factors influencing the water quality. Therefore, it is important to understand which factors have the most influence on the Sound, which is vital for future policy and management strategies.

4.3 Methods

4.3.1 Study Site

The Mississippi Sound is an elongate estuary located along the coastline of Mississippi and parts of Alabama (Figure 4.1). It is classified as a well-mixed estuary, but during January through June it may experience localized stratification, occurring mostly around the shipping channels (Eleuterius, 1978). The estuary has diurnal tides with an

average range of 0.57 m (Eleuterius, 1978). Several major freshwater sources affect the Sound, including the Pearl River, Pascagoula River, and Mobile Bay. Minor freshwater sources include the Tchoutacabouffa River, Saint Louis Bay, and Biloxi Bay. The majority of the bottom sediments within the Sound are silts, which—while not conducive for SGD—can be easily penetrated by man-made structures, dredging, and sandy intrusions, allowing for groundwater release (Kim et al., 2005; Neuzil, 1986; Sawyer et al., 2001). For the Mississippi Sound, salinity is often dependent on the river input, rainfall, surface currents, and whether or not the BCS has been opened. While there are variations year to year, the typical pattern is that from January to June, salinity in the Sound decreases due to riverine input and surface current patterns. In July surface salinity starts to increase, with the highest salinities occurring between September and December (Hode, 2019). Rainfall along the coast of Mississippi peaks in August, and is lowest in October (Bianchi et al., 1999).

According to NOAA's Estuarine Eutrophication Survey, the Mississippi Sound is prone to periods of hypoxia and nuisance algal blooms. Each section of the Sound has distinct river and offshore influences, causing them to be affected somewhat independently. The eastern Sound is affected by the Pascagoula River, Mobile Bay through Pass aux Herons, and the offshore waters of the Mississippi Bight through Petit Bois Pass (Figure 4.1). This section extends from Dauphin Island to just west of the Pascagoula River. The western section of the Sound extends from the Mississippi state line near the Pearl River over to the Gulfport shipping channel. This section is highly affected by St. Louis Bay, the Pearl River, and the BCS when open. Salinity structure in this region is determined by how intense the freshwater influence is. The central Sound

sits between the west and eastern sections, and is primarily affected by offshore water influence through winds and tides. When the BCS is open, water flows from the south western part of Lake Pontchartrain (Figure 4.1) and through the Chef Menteur and Rigolets Passes that connect the Sound to the Lake (Dzwonkowski et al., 2018). Not all the water from the BCS gains access to the Sound, but for the portion that does, it mainly affects the western part of the Sound, and can drop the salinity to near zero (Morgan and Rakochinski, 2022).

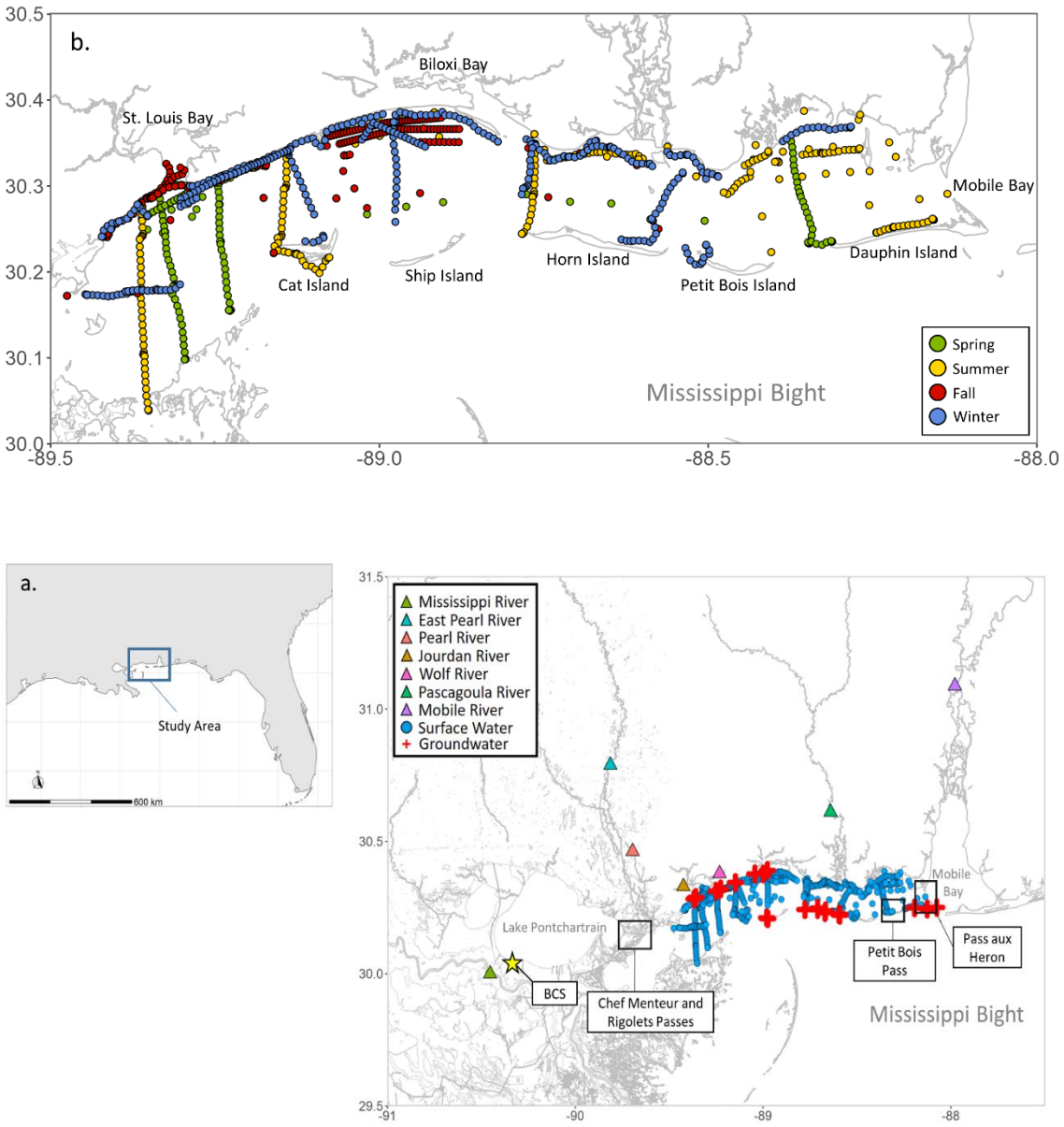

Figure 4.1 *Map of study site.*

a) Map of the Mississippi Sound and surrounding region, including surface water samples, groundwater samples are river samples.

b) In depth look at surface water samples; the color correlates to the season the samples were taken.

Renken, (1998) summarized the extensive aquifer formations that lie beneath Mississippi and extend out towards the shelf. There are two major aquifer systems that affect the coastline, one overlain on the other. The surficial system is the coastal lowland

aquifer system, which extends from the Rio Grande to the westernmost parts of Southern Florida. This aquifer system extends into the Gulf of Mexico across the shelf, but the offshore areas are mostly saline. The coastal lowlands aquifer system consists of five permeable zones, and the lithology is interbedded sand and clay. Much of the water in the aquifers is pumped and utilized for agriculture, industrial, and public use. The Mississippi, Pearl, and Red Rivers flow into this system and are the major contributors, along with rainfall, to recharging the aquifers. Underneath the coastal lowland aquifer system is the Mississippi embayment aquifer system. This aquifer system extends from offshore Mississippi up into parts of Kentucky and Illinois. A confining unit separates the two aquifer systems and advective SGD is from only the coastal lowland aquifer system because, although the Mississippi embayment aquifer system is sequestered to more nearshore areas, it only breaches the surface on land, though there may be paleochannels that incise into that aquifer in the Sound and offshore.

Oyster reefs in the Mississippi Sound are mainly clustered in the western Sound, with a few around the Pascagoula River and Biloxi Bay (Figure 4.2). The western Sound reefs contain the largest and most profitable commercial reefs (Linhoss and Mickle, 2022), and historically had some of the most productive oyster stocks in the Southeastern US (Gore, 1992). The reefs in the western Sound contain restored relic shell sites, restored limestone sites, and reference sites (Morgan and Rakocinski, 2022; Figure 4.2). These reefs are an important part of the local economy, and are affected by the low salinity waters from the BCS. It is unknown how SGD impacts the oyster reefs, or if there are connections between their locations and SGD input.

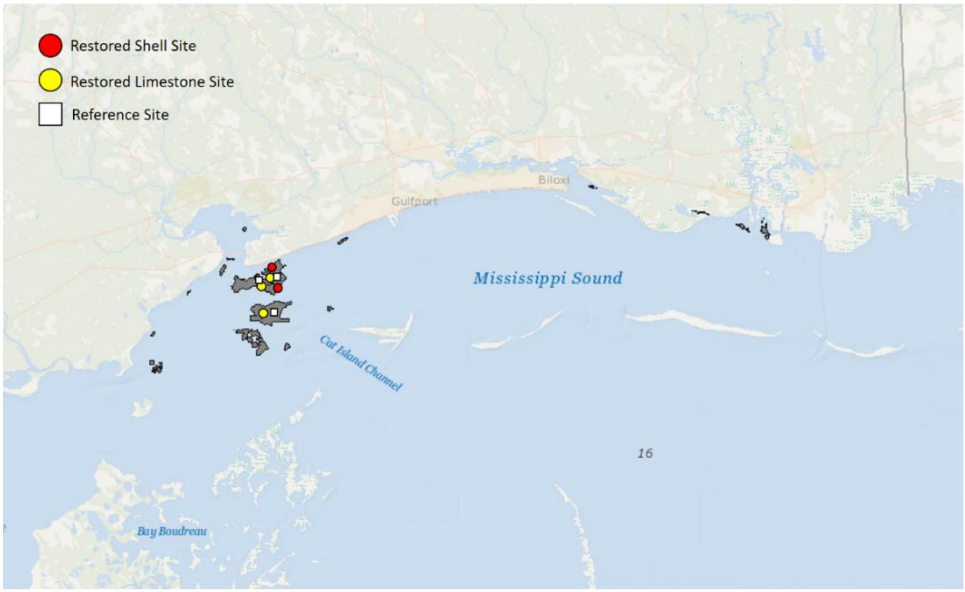

Figure 4.2 *Oyster reef locations in the Mississippi Sound.*

Reefs are in gray, with restored and reference sites in the western Sound indicated by the colors.

4.3.2 Sample Collection and Analysis

Between of 2018-2021, 14 radon surveys were conducted by a small boat moving at 2-4 km/hr both parallel and perpendicular to the shoreline (Figures 4.1 & 4.3) to determine SGD seepage extent. Continuous ^{222}Rn ($T_{1/2}$ = 3.84 days), dissolved oxygen (DO), salinity, and temperature, and discrete dissolved radium (^{224}Ra $T_{1/2}$ = 3.66 days; ^{223}Ra $T_{1/2}$ = 11.4 days; ^{228}Ra $T_{1/2}$ = 5.75 years; ^{226}Ra $T_{1/2}$ = 1600 years), dissolved nutrients (SiO3, NH4, NO_x, PO_4, DON, DOP), stable isotopes of water (δ^{18}O), dissolved methane (CH4), and dissolved trace metals were collected from the surface waters during each survey. DO, salinity, and temperature were collected every 5 minutes during the surveys using a YSI EXO sonde, with an accuracy of ±0.1 mg L^{-1}, ±0.1 ppt, and ±0.01°C, respectively.

GPS measurements (Garmin GPSMAP 640) were taken in conjunction with the continuous data. River samples were collected from the Mississippi, Jourdan, Wolf, Pascagoula, Pearl, and Mobile Rivers between October 2015 and June 2016 as part of the Consortium of Coastal-River Dominated Ecosystems (CONCORDE; data available at Gulf of Mexico Research Initiative Information & Data Cooperative (GRIIDC) at https://data. gulfresearchinitiative.org), as well as several samples during 2016 in the central and east Sound (Figures. 4.1 & 4.3). From chapter 2, we know that a sampling regimen of 4 times per year, once a season, was enough to resolve seasonal changes. For this work, we averaged 14 separate radon surveys over a 4-year period, with only a 3.5 times per year frequency of sampling. Due to this, we cannot resolve changes per season. However, looking at the data in terms of wet and dry seasonality, we would only need 2 samples per year. Therefore, broad changes between wet (often spring and summer), and dry (often fall and winter) seasonality are explored in this study. While the wet season is often spring and summer, and the dry season is fall and winter, there are exceptions, which can be seen in Figure 4.3.

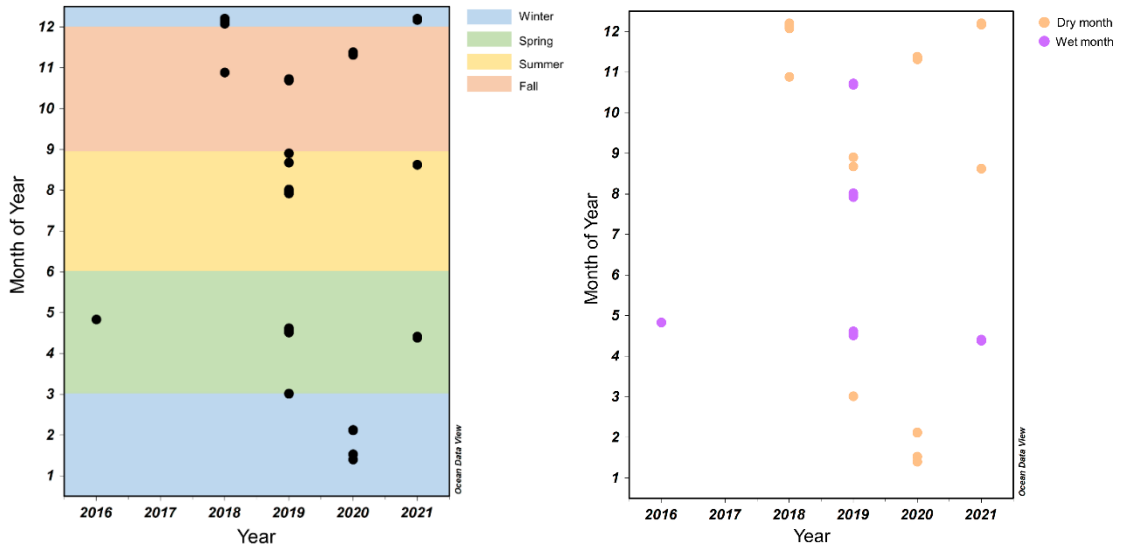

Figure 4.3 *Sampling periods throughout the study*

Each point represents one week of sampling.

Groundwater samples were collected on both mainland beaches of Mississippi, and from the Mississippi/Alabama barrier islands between April 2016 and August 2019 for both CONCORDE and additional time series beach sampling along the coastline (Figure 4.1). Groundwater samples were collected using a PushPoint (MHE Products), from wells, or from groundwater fed ponds. The PushPoint is a thin steel tube with a pointed tip that contains screen zones where water can enter. The instrument is inserted into the ground with a twisting motion until resistance, and then a guard rod is removed from the inside of the PushPoint to open the tube. Water can then be pumped up. To sample the beach groundwater, holes were dug down to the water table (~ 0.5 m to ~ 1 m), and then the push point was inserted to maximum depth (~ 2 m) and a peristaltic pump was used to pump water up the push point, which was then collected.

Rivers were sampled five times between October 2015 and June 2016 with samples collected for determination of radium, nutrients, and trace elements. These were collected from all the main rivers that empty directly into the Sound, including the East Pearl River, the Pearl River, and the Pascagoula River, as well as rivers that empty into other bays and tributaries that can release water to the Sound, such as the Jourdan River, the Wolf River, and the Mobile River (Figure 4.1). Samples were also collected in the Mississippi River, which generally only influences the Sound when the BCS is open. Groundwater and river salinity were determined using a YSI ProDSS sonde with an accuracy of ±0.1 ppt.

Radon was determined through use of gas equilibration with the sample water, which allowed for solid-state detection of alpha particles from the radon decay change. Radon measurements were conducted using a RAD7 with RAD AQUA air-water equilibrator (Durridge; Billerica, MA). Water was pumped from the sampling location at 7 L/min into the RAD AQUA. The equilibrated air was then pumped (by the RAD7) through a dessicant holder, which dries the air before it enters the instrument. Once dry, the air was measured for radon by the RAD7. Groundwater radon was determined through use of gas equilibration with the sample water. Samples were collected by letting bubble-free water pump into the sample bottle (250 mL) and overflow for about 15-20 seconds, to remove any air from the atmosphere. The sample bottle was then capped, and the sample was checked to ensure there were no bubbles. The sample was then run on the RAD H2O system as outlined in the manual (Durridge RAD H2O manual, 2018). Radon anomalies were plotted using Ocean Data View (ODV; Schlitzer, Reiner, Ocean Data

View, https://odv.awi.de, 2021) and gridded using Data-Interpolating Variational Analysis (DIVA).

Radium samples (20 L) were filtered through a manganese coated acrylic fiber (Mn-fiber) at no faster than 1 L min-1. Once this was complete, the fiber was washed with radium free deionized water to remove any sediment/salt, and then partially dried. Fibers were then weighed, placed into sample tubes, and connected to a Radium Delay Coincidence Counter (RaDeCC). Samples were run until there were 1000 counts for 220Rn, or until the counts stabilized. The samples were analyzed three times total (immediately after sampling, one week after sampling, and one month after sampling) in order to determine 223Ra and ^{224}Ra (Moore and Arnold, 1996). Once three runs had been completed, the values were determined and corrected through calculations outlined in Garcia-Solsona et al., 2008, Griffin et al., 1963, and Moore and Arnold, 1996. The longer half-life isotope (^{226}Ra and ^{228}Ra) activities were determined through gamma ray spectrometry. To prepare the sample for the gamma ray spectrometer, the manganese fibers were first leached with a combination of hydroxylamine hydrochloride (HAHCl) and hydrochloric acid (HCl), then coprecipitated with barium sulfate (BaSO4). After three weeks, which allows for ^{222}Rn to equilibrate with ^{226}Ra, they were measured on a gamma spectrometer (Moore, 1996).

Water samples for oxygen stable isotopes (δ^{18}O = deviation of O18/O16 isotopic ratios from the international reference Vienna standard mean ocean water (VSMOW)) were filtered with 0.45 μm pore size polypropylene syringe filters (Whatman Puradisc 25 PP) and stored in glass bottles that were sealed with Parafilm until measurement to prevent evaporation. The δ^{18}O was analyzed using isotope ratio infrared spectroscopy

(L2120-i cavity ring-down spectrometer, Picarro Inc.). The data were calibrated using reference waters that were standardized to the VSMOW and drift corrected following van Geldern and Barth (2012). Analytical uncertainties associated with $\delta^{18}O$ were 0.07‰. The $\delta^{18}O$ values are expressed in per mille (‰), and defined as:

$$\delta^{18}O = \left[\frac{\left(\frac{^{18}O}{^{16}O}\right)_{sample} - \left(\frac{^{18}O}{^{16}O}\right)_{VSMOW}}{\left(\frac{^{18}O}{^{16}O}\right)_{VSMOW}} \right] \times 1000 \quad (1)$$

Nutrient samples were collected in a 250 mL, acid washed, Nalgene bottles. After collection, samples were filtered (0.45 µM Whatman Puradisc 25 PP) into a 125 mL acid washed brown bottle, and frozen. Samples were run on a Seal Auto Analyzer (AA3) for ammonium, nitrate+nitrite, phosphate, and silicate. Regressions of $r > 0.95$ were used for each run to ensure sample accuracy. Total nitrogen (TN) and total phosphorus (TP) were determined by adding 5 mL of oxidizing reagent to 50 mL of sample. To make the oxidizing reagent, 15 g of boric acid, 25 g of potassium persulfate, and 7.5 g of sodium hydroxide were diluted to 500 mL with water. These were then autoclaved for 2 hours at 115 C. After cooling, samples were run for nitrate+nitrite and phosphate as outlined in the SEAL manual. Organic concentration of nitrogen and phosphorus were determined by subtracting the inorganic concentration from the total.

Trace element samples were collected in 250 mL acid washed HDPE bottles. Once collected, samples were filtered (pre-cleaned 0.45 µM Whatman Puradisc 25 PP filter) into 15 mL acid washed bottles, and acidified to $pH < 2$ with 6 N ultraclean HCl (Seastar Baseline). After acidification, samples were stored in a clean space at room temperature until analysis on a high resolution inductively coupled plasma mass spectrometer (HR-ICP-MS) for Ba, Cs, Cr, Fe, Mn, Mo, Re, U, V, As, Cd, Cr, Cu, Pb,

and Ni. Concentrations were determined using an isotope dilution method (Ho et al., 2019; Joung and Shiller, 2013). Briefly, samples were diluted 20-fold with 0.3M ultrapure HNO3 (Seastar Baseline) that contained a known amount of In, and enriched ^{111}Cd, ^{207}Pb, ^{62}Ni, ^{65}Cu, ^{50}V, ^{57}Fe, ^{95}Mo, ^{135}Ba and ^{185}Re. The In response was used for instrument drift correction and sensitivity checks. Concentrations of V, Fe, Mo, Ba, and Re were calculated from the isotopic ratios and the known isotopic spike. Cs and U were determined in low resolution, and the instrumental drift was corrected by a response factor derived from the instrumental response (cps/nM) of ^{95}Mo and ^{135}Ba. Cr and Mn were determined in medium resolution, and the instrumental drift was corrected by a response factor derived from the instrumental response of ^{57}Fe. Calibrations for Cs, Mn, Cr, and U were performed by standard additions to a seawater sample (Shim et al., 2012).

4.3.3 Monte Carlo Simulations

For this study, we used Monte Carlo simulations (Raychaudhuri, 2008) to estimate the error range of SGD, river, and the BCS input in the Sound, and their associated nutrient and trace metal fluxes. All terms were considered uncertain, and were treated stochastically in order to comprehensively account for the full flux ranges. Histograms of the initial data were used to determine the distribution curve, which was either lognormal or normal. The Monte Carlo simulations were used to define the ^{222}Rn, ^{224}Ra, ^{228}Ra, salinity, and nutrient endmembers for SGD, local rivers, offshore, and the BCS. The Monte Carlo simulations were conducted in several stages. First, all data were first boosted to 1000 values based on the empirical distribution curve function (edcf), and then μ and σ of the boosted distribution were input into the Monte Carlo simulation. The 1 million values were either substituted into a simultaneous mass balance (Eqs. 9-12), or

underwent matrix computation (Eq. 4), depending on the SGD model. The statistics of the mean, median, mode, and interquartile ranges were used to describe the data. To determine differences in the simulated data, we use the Kolmogorov–Smirnov (K-S) test and Cohen's D (Becker, 2000; Raychaudhuri, 2008) to calculate the statistical difference and effect size between distributions. The K-S test checks the distance between the empirical distribution function and determines if they are statistically different, while Cohen's D determines the standardized difference between the means of the distributions, and expresses this in standard deviations. A Cohen's D below 0.2 indicates negligible differences, 0.2-0.4 is small differences, 0.5-0.8 is medium differences, and >0.8 is large differences. This approach allows us to grasp the high uncertainty in SGD flux calculations, which is often overlooked, as well as provide a range of SGD fluxes, which can be highly variable.

4.4 Results

An important assumption with mass balance approaches is that the endmember values are an accurate representation of the various sources. In this study, we had three main endmembers; rivers, offshore, and SGD. Endmember values for ^{222}Rn, ^{224}Ra, ^{228}Ra, and salinity were used to calculate SGD water fluxes, while nutrient endmembers were used to calculate the nutrient fluxes into the Sound from the various sources. The next three sections go into detail on the various endmembers and their distributions in the Sound, rivers, offshore, and SGD. All statistics for endmembers are shown in Appendix B.

4.4.1 Sound water tracer composition

During this study, ^{222}Rn concentrations were measured during boat surveys that extended across the entirety of the Sound. The activities of ^{222}Rn are often 1000-fold or higher in groundwater compared to surface water, making it an ideal tracer of SGD (Dulaiova et al., 2005). Another advantage is that ^{222}Rn is inert, and therefore there are no biogeochemical reactions that need to be considered (Dulaiova et al., 2005). Radon is also not susceptible to rapid changes in salinity, and in situ monitoring can provide a large amount of data points, helping to constrain error. To compare all radon surveys, the anomaly of the ^{222}Rn concentrations was calculated by subtracting the mean concentration of ^{222}Rn per season from the data that were taken during that season (e.g., Montiel et al., 2019). Since ^{222}Rn was collected across the whole Sound for each season, this allows for removal of bias and potential changes in SGD flux season to season. Radon concentrations and positive anomalies were often highest in the western part of the Sound and right along the coastline (Figure 4.4). Persistently low ^{222}Rn values and anomalies occurred farther offshore, and in the far eastern sections of the Sound (Figure 4.4). Anomaly values ranged from -1.3 – +5.9 dpm L^{-1}, -1.8 – +2.2 dpm L^{-1}, and -1.5 – +2.4 dpm L^{-1} in the western, central, and eastern sections of the Sound, respectively. Oyster reefs are shown in green on the map, and fall in areas that are near locations with a high radon anomaly, but not directly over them. The western Sound data is the same as the data used in Chapter 2, but now will be used more in depth to predict changes across the whole Sound.

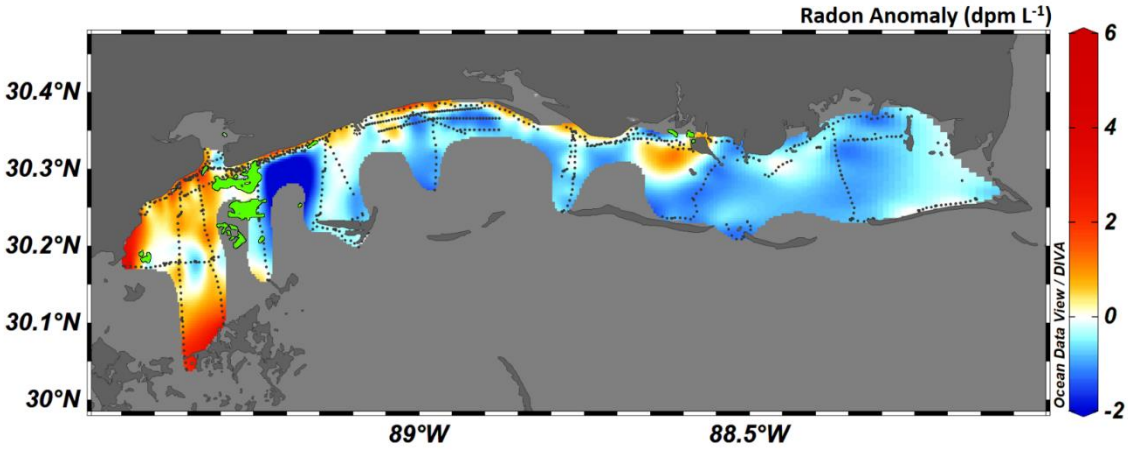

Figure 4.4 *Distribution map of ^{222}Rn anomalies in the Mississippi Sound in dpm L^{-1}.*

Black dots indicate individual sampling points. Data was gridded using ODV DIVA setting, with a quality limit of 1.0. Oyster reef locations are marked on the map in green.

Radium samples for analysis of the full quartet (^{224}Ra, ^{223}Ra, ^{228}Ra, and ^{226}Ra) were also collected during the boat surveys for ^{222}Rn. When examining radium versus salinity, we noticed an increase in activities around salinities 10-15, especially in the western Sound (Figure 4.5). As water moves from the low salinity rivers to the Sound, there is the potential that there may be desorption of radium from SPM, which can also increase radium concentrations at higher salinities.

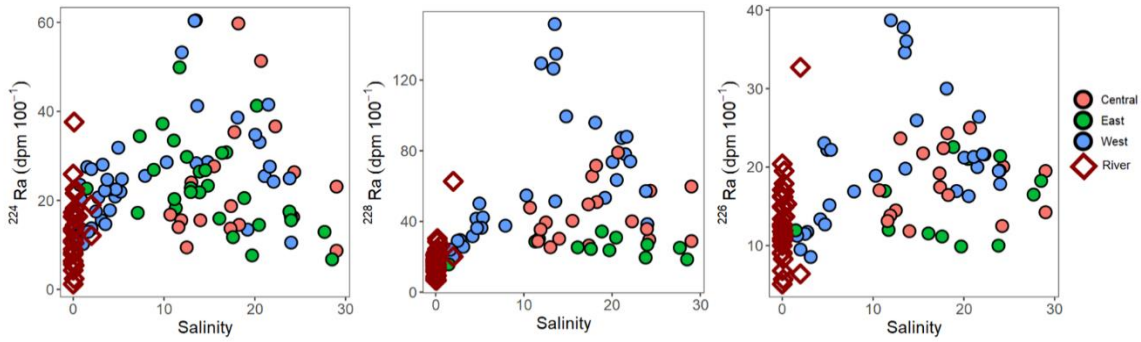

Figure 4.5 *Radium isotopes vs salinity.*

Blue samples represent the western Sound, orange the central Sound, and green the eastern Sound. Red diamonds are river samples.

Radium isotopes can also be used to qualitatively determine the influence of various sources (e.g., Moore and Shaw, 1998). The ^{228}Ra vs ^{226}Ra activity plot (Figure 4.6) shows that the samples fall between the river and groundwater lines, with the eastern Sound falling closer to the river line, and the western Sound closer to the groundwater line. This aligns well with our ^{222}Rn anomaly plot which clearly shows there was a higher presence of excess ^{222}Rn in the western Sound compared to the eastern Sound (Figure 4.4). The plot of ^{224}Ra vs ^{228}Ra activities shows samples falling along a line more similar to that of rivers than groundwater (Figure 4.6). However, the Sound samples have higher radium than the rivers, so there was either desorption of river radium leading to elevated Sound activities, or there was decay of ^{224}Ra derived from SGD to give the Sound the trends observed in the ^{224}Ra vs ^{228}Ra activity plot. Considering that the ^{228}Ra vs ^{226}Ra activity plot indicates that the Sound was clearly a mixture of river water and SGD, we assume the latter. Looking at a ternary plot of percent composition for radium samples (Figure 4.7), what we notice was that the Sound samples display a distribution that

indicates a mixture of groundwater and river water, as the Sound radium activities (western Sound in particular) have a lower composition of ^{226}Ra and higher composition of ^{224}Ra and ^{228}Ra compared to rivers. Groundwater has a higher influence of ^{224}Ra and ^{228}Ra, while rivers and Sound waters have a composition of about 50% for each isotope (Figures 4.6 & 4.7). This shows that the shorter lived isotopes are most likely decaying in the rivers and Sound waters, and that the groundwater, since it was recently in contact with source sediments, has a higher abundance of short lived radium.

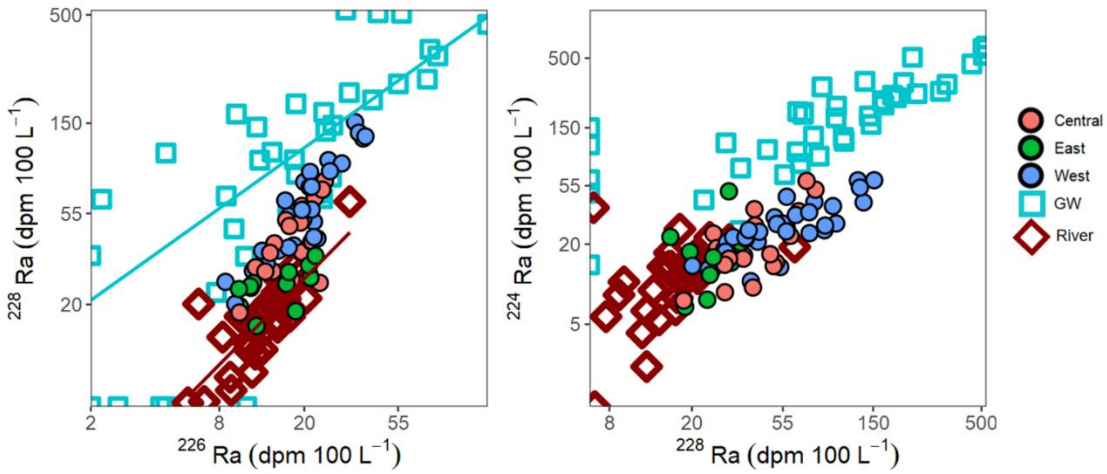

Figure 4.6 *Radium activities of ^{228}Ra to ^{226}Ra and ^{224}Ra to ^{228}Ra.*

Sound samples (circles), groundwater samples (squares), and river samples (diamonds). Sound samples are colored by sample location. Note that the axes are logarithmic. Linear axis figures are in Appendix II (Figure B.1).

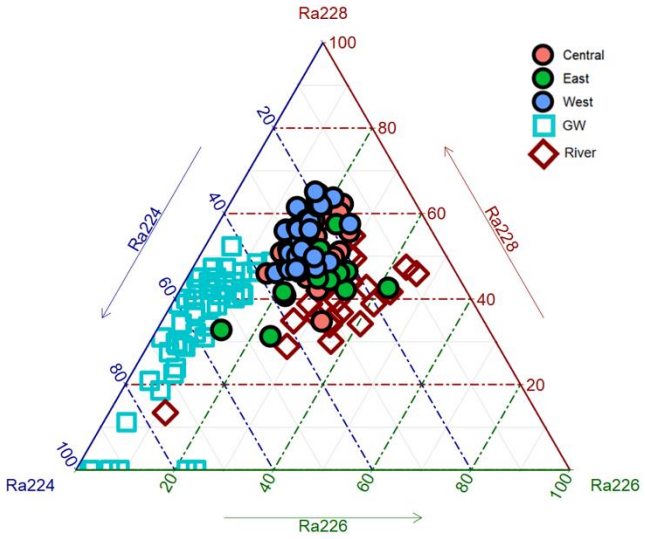

Figure 4.7 *Ternary plot of radium compositions for ^{224}Ra, ^{226}Ra, and ^{228}Ra.*

Sound samples are colored by location, river samples are red, and groundwater samples are light blue.

Using this information, we can assume that groundwater and river contributions to the Sound are both important sources of radium. Therefore, to calculate apparent water age, we assume the main source of ^{224}Ra and ^{228}Ra was groundwater or rivers. Apparent water age was calculated using $^{224}Ra/^{228}Ra$ activity ratios following equations from Moore, 2006:

$$t = \frac{\left(\frac{^{224}Ra}{^{228}Ra}\right)i - \left(\frac{^{224}Ra}{^{228}Ra}\right)obs}{\left(\frac{^{224}Ra}{^{228}Ra}\right)obs \times \lambda_{224}} \quad (2)$$

where t is the apparent water age (d), $(^{224}Ra/^{228}Ra)_i$ is the initial activity ratio in the source (groundwater), $(^{224}Ra/^{228}Ra)_{obs}$ is the activity ratio of the samples, and λ is the decay constant of ^{224}Ra (0.189 d^{-1}). This method assumes that the system is in steady state, and that radium will be continuously added to the system from sediments and groundwater (Moore et al., 2006). The activity ratio of $^{224}Ra/^{228}Ra$ in groundwater is on

average 1.8, and in rivers that affect the eastern Sound it was on average 1.1. This was applied separately to each sample collected in order to understand water age variability within the Sound, and to calculate ages based on location and seasonality. Groundwater endmember activity ratios were used for the west and central Sound, while the river activity ratio was used for the eastern Sound. This was based on Figure 4.6, where the western and central Sound fall more in line with the groundwater $^{228}Ra/^{226}Ra$ line, and the eastern Sound falling more in line with the river $^{228}Ra/^{226}Ra$ line. We broke the data into wet and dry seasonality based on the Köppen climate classification, where less than 60 mm of precipitation per month is classified as dry. The average age model value was 12.5±8.2 days, which is similar to previous modelling work conducted in the Sound (Bouchard, 2021). Therefore, we have confidence that our model is an accurate prediction. The eastern Sound had the lowest apparent age at 5.1±3.3 days, followed by the western (13.7±7.5 days) and then the central Sound (15.4±9.1). The differences between the wet and dry season were within error of each other, with average ages of 13.4±8.7 and 11.5±7.7, respectively.

A Monte Carlo approach, as stated above, was used for this study in order to estimate the uncertainty in tracer calculations for SGD, and provide the full range of SGD error. To do this, each dataset for ^{222}Rn ^{224}Ra, ^{228}Ra, and salinity in the Sound water was simulated (Table B.1). Our K-S testing indicated that all empirical distributions were significantly different from each other, but from here on we use Cohen's D to determine how large that difference is. The mean activities of ^{222}Rn in the west, central, and east Sound after simulation were 1.9±1.2, 1.4±0.8, and 0.6±0.6 dpm L^{-1}, with the wet and dry seasons having mean activities of 1.2±0.9 and 1.6±1.1 dpm L^{-1}, respectively. The eastern

Sound distribution was statistically different from the other sections of the Sound, (Cohen's D>1), but the wet and dry seasons only had small effect sizes between distributions (Cohen's D = 0.4) (Figure 4.8). The mean activities of the simulated ^{224}Ra in the west, central, and east Sound were 25±11, 23±12, and 24±9.1 dpm 100L^{-1}, with the wet and dry seasons having mean activities of 25±11 and 24±11 dpm 100L^{-1}, respectively. The Cohen's D showed no major differences between the distributions for ^{224}Ra due to the small differences in the means and overall error range of activities (Figure 4.8). For ^{228}Ra, the mean activities for the west, central, and east Sound were 64±34, 43±15, and 26±4.5 dpm 100L^{-1}, with the wet and dry seasons having mean activities of 55±30 and 41±22 dpm 100L^{-1}, respectively. Like the ^{222}Rn distribution, there were only major differences between the eastern sound distributions and all other distributions (Cohen's D > 1), while the central Sound was moderately different (Cohen's D < 0.8) (Figure 4. 8). Salinity between all locations and wet and dry seasons were statistically different from each other (Cohen's D > 0.9). This was seen in the distributions as well, with the western Sound having the lowest salinity and the central the highest, and the dry season having a higher salinity than the wet season (Figure 4.8). Mean salinities for the west, central, and east Sound were 8.6±7.8, 22±4.6, and 17±4.8, with the wet and dry seasons having means of 9.7±7.2 and 18±8.1, respectively.

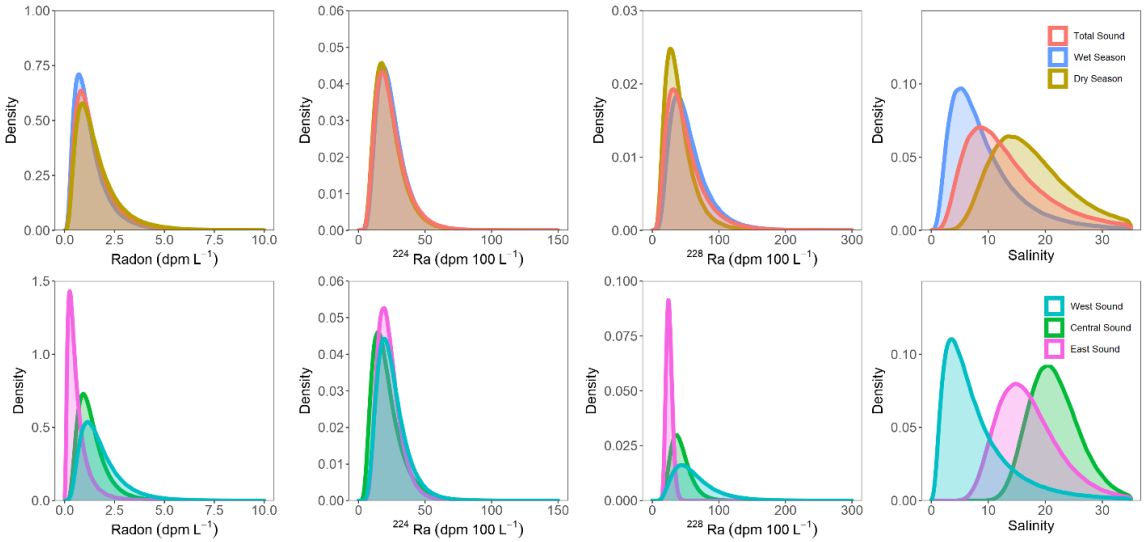

Figure 4.8 *Distributions of ^{222}Rn, ^{224}Ra, ^{228}Ra, and salinity for the total Sound, wet and dry seasons, and the west, central, and eastern Sound.*

Our δ^{18}O values ranged from -4.64 to -0.01 ‰ (Figure 4.9a). The majority of the less negative values were concentrated in the central part of the Sound, due to the influence of offshore waters (Sanial et al., 2019), while the western and eastern Sound had more negative values due to higher river influence (Sanial et al., 2019), which are also shown by the salinity (Figure 4.9b). The δ^{18}O values were -1.9±0.95, -2.2±1.0, -1.3±0.5, -2.2±0.8, -1.6±1.0, and -2.2±0.8 ‰ for the entire Sound, for the west, central, and east sections, and the wet and dry seasons, respectively. Time periods for sampling are shown in Figure B.2.

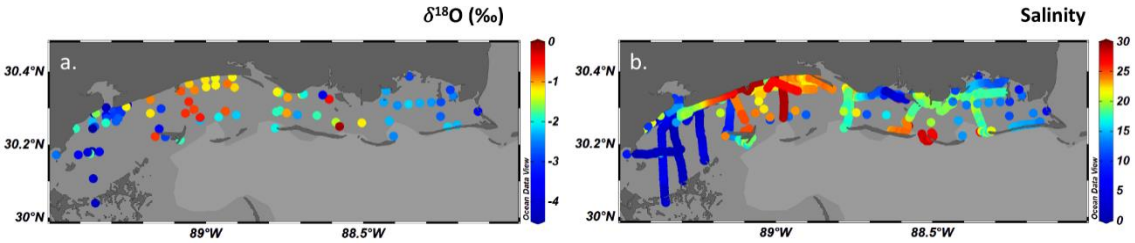

Figure 4.9 *δ^{18}O values (‰) and surface salinity in the Sound.*

4.4.2 River, offshore, and groundwater tracer composition

Groundwater samples were collected from both mainland beaches and on the barrier islands that define the boundary between the Mississippi Sound and Mississippi Bight (Figure 4.1). The salinity of the groundwater ranged from 0 – 29.2, with a mean of 7.7 (n = 62). Activities for ^{224}Ra and ^{228}Ra ranged from 7.1 – 1152 dpm 100L^{-1} and from below detection to 528 dpm 100L^{-1}, respectively. To estimate the SGD fluxes to the Sound with radium, we need to choose endmember activities that accurately reflect the water that enters the Sound from SGD. SGD is a mixture of both fresh groundwater (FSGD) and recirculating seawater (RSGD). The recirculating seawater component would be reflective of the Sound salinity, as that would be the water infiltrating the aquifer. However, the Sound has a wide range of salinities, depending on the season, as there are changes in rainfall, currents, and wind patterns throughout the year. Previous studies have shown that the RSGD is often the dominant water flux from SGD (Burnett et al., 2003). Due to this, we assume that the groundwater salinities will be just as variable as those of the Sound, and therefore we use the full salinity range of the groundwater samples to simulate the range of our endmember for radium (Figure 4.10). The ^{222}Rn activities in the groundwater ranged from 0 to 144 dpm L^{-1}, and since ^{222}Rn is not affected by salinity, the entire distribution is used in the Monte Carlo simulation (Figure 4.10; Table B.2).

The δ^{18}O of the fresh groundwater ranged from -4.45 to -1.99 ‰, with the salinity of the fresh groundwater ranging from 0 to 3. We consider the fresh component to be the terrestrial groundwater endmember that is comprised of percolating rainwater into the aquifer. The δ^{18}O of the mid salinity SGD, or the component that is comprised of a

mixture of infiltrating Sound water and the fresh terrestrial groundwater (salinity 5 – 20) ranged from -3.03 to -1.26 ‰. The average $\delta^{18}O$ of the fresh groundwater was -3.38 ‰ and the SGD was -2.22 ‰. These are used as components in Eq. 14 to determine the fraction of FSGD to RSGD in the total SGD.

River endmember activities were again simulated by Monte Carlo methods (Figure 4.10). Each river's distribution calculated separately according to the methods in section 2.3, and then they were added together to estimate the potential error on all river input. This should take into account activities that may occur due to desorption from particles, and therefore be a good estimate of our river values. Endmember activities of ^{224}Ra and ^{228}Ra ranged from 1.2 – 148, and 6.7 – 286 dpm 100 L-1, respectively. To account for riverine sources of ^{222}Rn, we use the activity of the parent isotope ^{226}Ra under the assumption that the daughter isotopes will be in radioactive steady state. This correction is applied before the Monte Carlo simulation on the excess ^{222}Rn content in the Sound. The ^{226}Ra activities ranged from 3.5 – 97.3 dpm 100 L-1. The $\delta^{18}O$ of the waters entering the Sound from rivers and Lake Pontchartrain range from -4.4 – +0.9 ‰. Lake Pontchartrain can potentially contribute up to15% of water entering the Sound on average; however, this will vary temporally (Sikora and Kjerfve 1985; Savoie, 2020).

Offshore endmember activities were considered to be those of the Mississippi Bight. The Bight has been shown to have an SGD component of its own (Sanial et al., 2021), and therefore needs to be considered a potential source of both radium and radon. Offshore radon data was collected on two separate occasions; October 2018, and September 2019. The average activity of radon for each trip was 0.5±0.04 and 0.8±0.07 dpm L^{-1}, respectively. The highest radon activities in the Bight occurred near the

Mississippi barrier islands and the Chandeleur Islands, indicating that these are the primary source to the Bight (Figure 4.11a). The average activity of the offshore radon was 0.6±0.5 dpm L^{-1}. Farther offshore, radon activities were continuously near 0 dpm L^{-1} (detection limit 0.06 dpm L^{-1} radon activities in water). The offshore ^{222}Rn correction was conducted pre-Monte Carlo. Bight radium activities have been previously reported (Sanial et al., 2021), but for choosing an offshore endmember, we chose to use data that was within 30 km of the barrier islands, as this would be more indicative of waters entering the Sound from the Bight. Our offshore ^{224}Ra and ^{228}Ra endmembers were therefore 7.3±7.6 and 20.9±11.5 dpm $100L^{-1}$ respectively, with a salinity of 29.9±5.6 (Figures. 4.11b & 4.11c).These data were then simulated through our Monte Carlo method (Figure 4.10; Table B.2). The offshore activities of the short-lived isotopes ^{222}Rn and ^{224}Ra are small compared to those in the Sound, and we would expect that there is substantial decay of these isotopes before the water reaches the Sound. However, we still correct for the offshore endmember even though it is trivial, as to not overestimate our SGD fluxes.

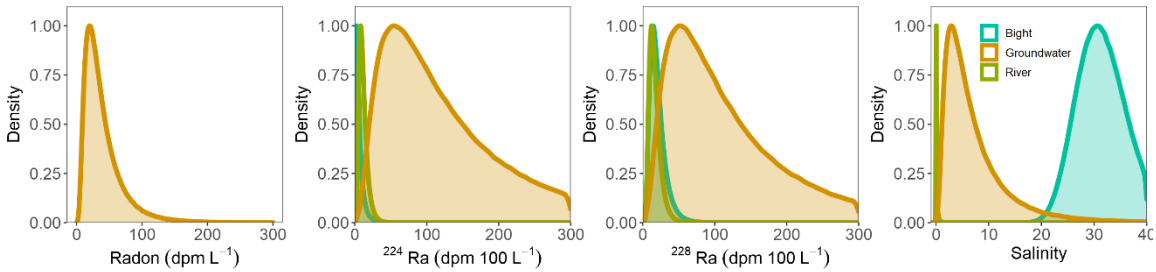

Figure 4.10 *Endmember distributions of ^{222}Rn, ^{224}Ra, ^{228}Ra, and salinity in the Mississippi Bight, groundwater, and the local rivers.*

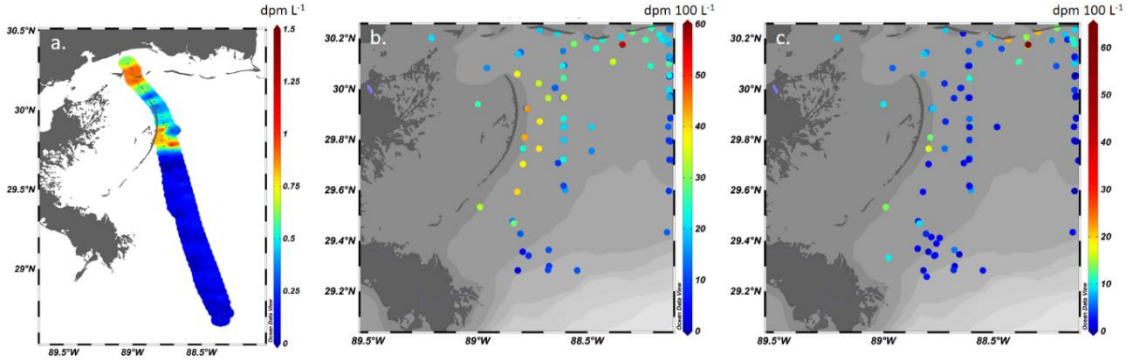

Figure 4.11 *Surface water radon, ^{228}Ra, and ^{224}Ra in the Mississippi Bight.*

a) ^{222}Rn (dpm L^{-1}) taken as individual data points through RAD AQUA system set to 30 min intervals. The majority of the ^{222}Rn is near the barrier islands, and within 30 km off the Sound.

b) ^{228}Ra (dpm 100 L-1) activities collected as part of CONCORDE (Sanial et al., 2021).

c) ^{224}Ra (dpm 100 L-1) activities collected as part of CONCORDE (Sanial et al., 2021).

4.4.3 Nutrient endmembers

Of the 14 radon surveys that were conducted, 8 of them had nutrient data collected (Figure 4.12). There were gaps in the data that occurred when conditions were not suitable for field work (i.e., harmful algal blooms, foul weather, lack of sampling support, global pandemic). The main sources of nutrients to the Sound were the local rivers, the BCS, offshore, and groundwater (Table 4.1). The discrete endmember concentrations of these sources were used to qualitatively examine nutrient distributions during three main Sound conditions: no BCS impact, when the BCS was open, and directly after the BCS closed (Section 4.5.4). We did this mainly because changes in nutrients can be rapid, and affected by biological activity. Concentrations of NH_4^+, DSi, and DIP were highest in the groundwater, while river sources (local and Mississippi Rivers) were a similar concentration, or on the same order of magnitude, as groundwater

for DON and NO_x (Table 4.1). The Bight NH_4^+ and DIP average concentrations were similar to those of the local rivers (Table 4.1).

Table 4.1 *Nutrient endmember concentrations.*

Refs: * - CONCORDE (Sanial et al., 2021); + - This Study

	Local Rivers *	Mississippi River*	Mississippi Bight*	Fresh Groundwater *,+	Mixing Zone Groundwater *,+	Saline Groundwater* ,+
NH_4^+ (µM)	2.7	1.7	2.1	44	68	99
NO_x (µM)	9.8	124	2.9	2	4.6	4.6
DIN (µM)	13	126	5.1	48	75	103
DON (µM)	34	126	-	31	80	39
DSi (µM)	32	94	9.4	161	158	146
DIP (µM)	0.5	2.4	0.6	9.2	11	7.8
DIN:DIP	36	62	10	6.1	15	9.7
NH_4^+:DIN	0.3	0.01	0.5	0.9	0.7	0.7
DON:TDN	0.7	0.3	-	0.6	0.6	0.5

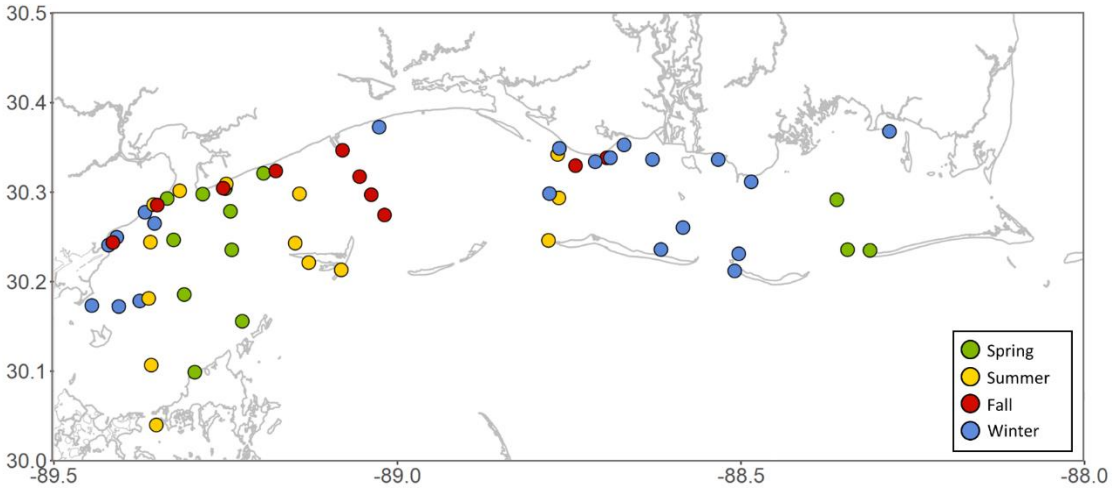

Figure 4.12 *Distribution of nutrient samples collected throughout the time series by season.*

Spring: March 2019; Summer: August 2019; Fall: October 2019; Winter: February 2019, January and February 2020.

The local rivers, groundwater, and Mississippi River endmembers were all run through the Monte Carlo simulation to obtain the distributions (Figure 4.13). Statistics of all the nutrient endmembers are shown in Table B.3. To calculate the flux of nutrients from various sources into the Sound, we used matrix multiplication on our nutrient endmember distributions (Figure 4.13) and water flux distributions (Section 4.5.6). Groundwater was divided into fresh and recirculated components in order to look at the difference between 'new' and 'recycled' nutrient fluxes from SGD into the Sound. The differences in the distributions of DIN for FSGD and RSGD were moderately different ($D > 0.5$), while differences between NH_4^+, NO_x, DSi, DIP, and DON were small (D 0.2 – 0.4). Distributions of endmembers for the local rivers and the Mississippi River were moderately different for NH_4^+ ($D = 0.8$), but largely different for NO_x, DSi, DIP, DIN, and DON ($D > 0.8$). Local rivers and FSGD were negligibly different for DON ($D < 0.2$)

and had small differences for DIN (D = 0.4). There were medium differences between river and FSGD NH_4^+ (D = 0.5), and large differences for NO_x, DIP, and DSi (D > 0.8). Distribution differences between local rivers and RSGD were large for all nutrients (D > 0.8) except DON, which had a negligible difference (D < 0.2).

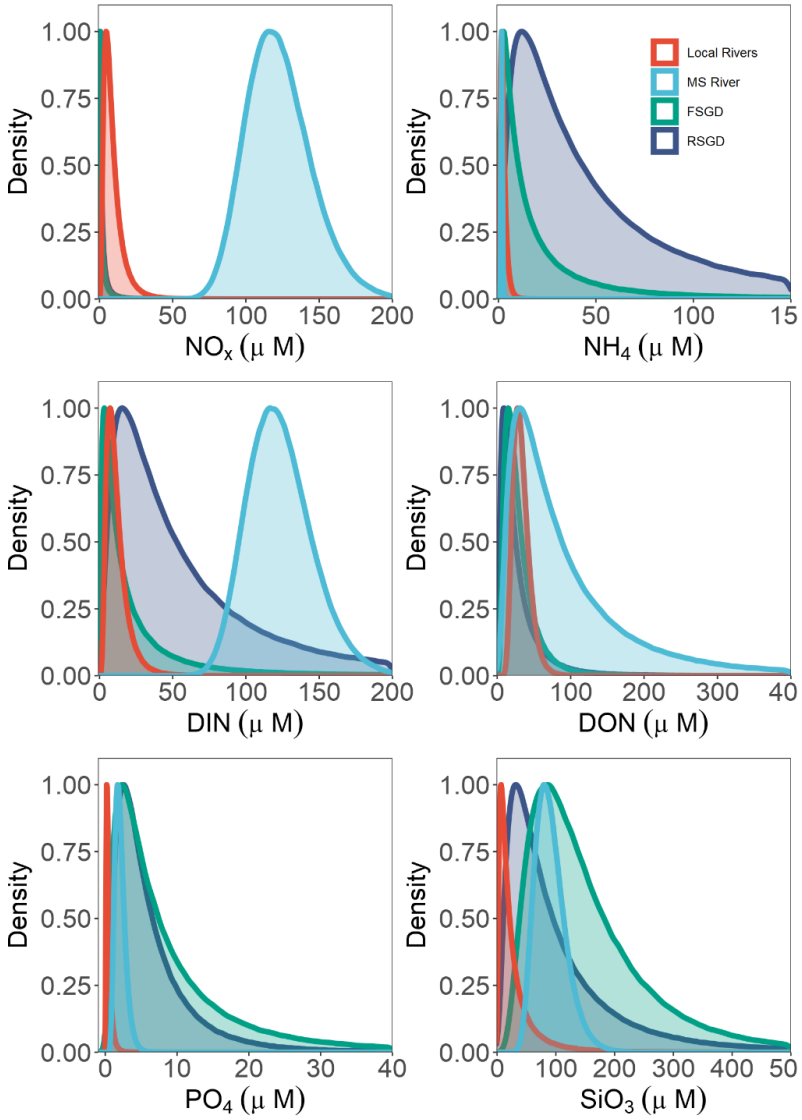

Figure 4.13 *Nutrient concentration endmembers in FSGD, RSGD, the local rivers, and the Mississippi River.*

4.4.4 Trace metal composition

As with nutrients, trace metal concentrations in the Sound are influenced by local rivers, BCS influence, offshore water, and SGD. Strong temporal variability previously has been noted for trace metal concentrations in the Sound (Ho et al., 2019), thus implying seasonal changes in trace metal fluxes. Endmember concentrations of local rivers, the Mississippi River, groundwater, and offshore water can be used to determine mixing trends in the data and allow for further understanding of how these various endmembers influence trace metal distributions. Trace metal collection during all the sampling is shown in Figure 4.14. In total, 14 trace metals were examined for their behavior across salinity gradients in the Sound and groundwater.

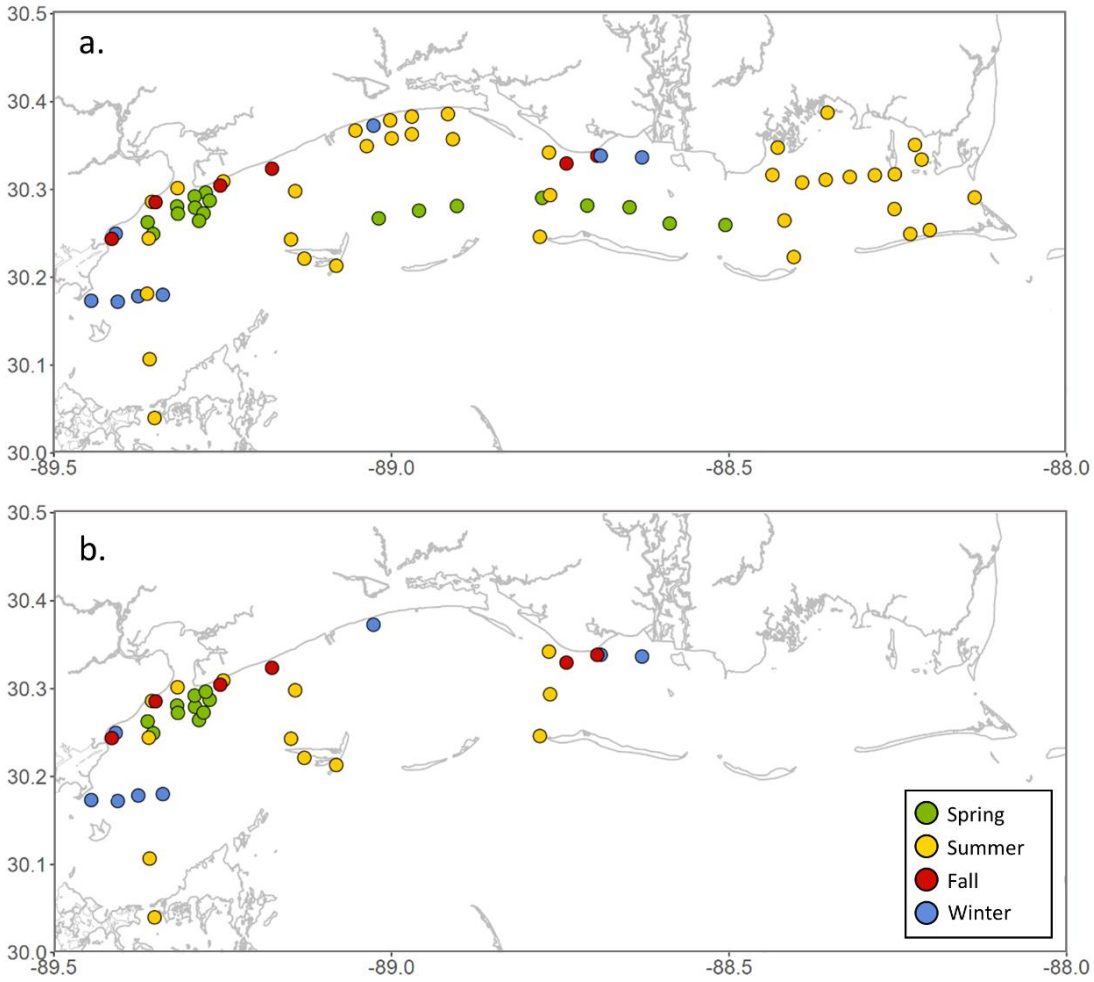

Figure 4.14 *Distribution of trace metal sampling.*

a) Ba, Cs, and Mo.

b) U, Re, Mn, Fe, V, As, Cd, Cr, Cu, Pb, and Ni.

The flux of metals to the Sound from various water sources was not calculated due to the majority of trace metals being highly influenced by RSGD, and it was uncertain if input from RSGD may simply be due to the seawater intrusion in the aquifer having the same signature as the surface water rather than excess being added in the subsurface. Therefore, we conduct qualitative analysis using salinity gradient plots and

redox indicators (Section 4.5.7). Endmember concentrations of the metals listed above are shown in Table 4.2.

Table 4.2 *Surface water trace metal endmember concentrations.*

Refs: + – This study; * – Concorde Data (Sanial et al., 2021); 1 – Brewer et al., 1972; 2 – Ku et al., 1977; 3 – Danish et al., 2021 & Goswami et al., 2012; 4 – Neff, 2009; 5 – Joung and Shiller, 2013.

Metal (nM)	Local Rivers*	Mississippi River*	Offshore	Fresh Groundwater *,+	Mixing Zone Groundwater *,+	Saline Groundwater *,+
Cs	0.6	0.3	2.2 [1]	0.4	1.1	1.4
Mo	2.2	10	97*	16	26	58
U	0.4	5.4	13 [2]	2.0	1.4	-
Re	0.0	0.1	0.04 [3]	0.0	0.0	-
Ba	221	443	103*	109	373	271
Mn	870	394	20.4*	1495	3927	-
Fe	10299	2478	44.4*	6663	11423	-
V	24	49	30.1*	51	27	-
As	11	22	23 [4]	139	407	-
Cd	0.1	0.2	0.06*	0.2	0.1	-
Cr	10	4.3	2.0 [5]	15	5.8	-
Cu	12	21	4.55*	9.9	2.4	-
Pb	1.8	0.6	0.03*	2.9	0.4	-
Ni	17	22	5*	16	13	-

4.5 Discussion

4.5.1 SGD Estimation

Quantifying SGD rates can be accomplished in several different ways including direct measurement (e.g., Sholkovitz et al., 2003), salinity balances (e.g., Knee et al., 2016), oxygen isotopes (e.g., Wang et al., 2021), and radioisotopes (e.g., Santos et al., 2009; Rodellas et al., 2017). For this study, we use both ^{222}Rn, two radium isotopes (^{224}Ra and ^{228}Ra), and δ^{18}O to estimate discharge. A typical approach using these tracers is to create a mass balance, equating sinks and sources, and assuming steady state for the study site.

The Mississippi Sound is a complex system with rapidly changing winds, salinity, and volume (due to tides, storms, river flow, etc.). This is further complicated with the shallow nature of the Sound, which can increase the impact of sediment diffusion (e.g., Rodellas et al., 2015), and SGD fluxes that come from not only onshore, but also from the barrier islands that separate the Sound from the Bight (Sanial et al., 2021). Our system is well bounded by the coastline and the islands, but assuming the entire volume is affected by SGD can also lead to an overestimation (Montiel et al., 2019). Therefore, when creating a mass balance, we need to determine the most important sources of tracers to the water column, and exclude those that may have a more limited effect, as well as pick an appropriate control volume. To start, we first create a balance of sources and sinks for the Sound:

$$J_{out} + J_{\lambda} = J_{riv} + J_{diff} + J_{off} + J_{SGD} \quad (3)$$

where the J indicates a flux of tracer (amount/time), the left side of the equation contains removals from the Sound, and the right side has inputs to the Sound. Our application of this equation assumes steady state. The removal terms are advection of a tracer out of the Sound (J_{out}) and radioactive decay of the tracer (J_{λ}). The sources of a tracer are rivers (Jriv), passive diffusion from sediments (J_{diff}), input of tracer from offshore (J_{off}), and SGD (J_{SGD}). Many studies ignore the input of tracers from sedimentary diffusion (e.g., Sanial et al., 2021). However, due to the shallow nature of the Sound, diffusion may be important (e.g., Rodellas et al., 2015). In order to estimate the diffusive process for radium, we use a diffusion estimation equation outlined in Rodellas et al. (2017) and, for radon, we use an equation outlined in Martens et al. (1980).

Based on this mass balance, we create two models using the ^{222}Rn and the radium isotopes. The first model relies on ^{222}Rn activities, and corrects the ^{222}Rn for all sources and sinks before plugging into an equation based on several previous studies (Dulaiova et al., 2010; Peterson et al., 2010; Santos and Eyre, 2011; Savatier and Rocha, 2021), and solving for SGD. For this method, we use parent isotope, river, and offshore corrected ^{222}Rn activities, age models, and groundwater endmember composition in our Monte Carlo simulation, and use matrix multiplication to determine the range of SGD fluxes. The second model simultaneously solves four mass balances, for water fluxes into and out of a control volume, as described by Sanial et al. (2021). The third model uses δ^{18}O to solve for the fresh groundwater fraction in our SGD fluxes by calculating the relative fraction of FSGD and RSGD in SGD and multiplying by the total SGD, and solving for the fraction of the water balances to independently find FSGD and RSGD (Wang et al., 2021).

4.5.1.1 Radon Model

Our first model focuses on the ^{222}Rn measurements across the Sound, and creates a budget for each section of the Sound based on changes in the apparent age, parent isotope (^{226}Ra) correction, and seepage area. We convert the ^{222}Rn measurements from the surveys into water fluxes using an equation based on previous studies (Dulaiova et al., 2010; Peterson et al., 2010; Santos and Eyre, 2011; Savatier and Rocha, 2021):

$$Q_{SGD} = \frac{\left[Rn_{ex} + Rn_{dec} + \left(Rn_{atm} \times \frac{t}{D}\right) - Rn_{dif}\right] \times V_S}{\left[Rn_{GW} - \left(Rn_{bound} - Sal_{bound} \times \frac{dRn_{bound}}{dSal_{bound}}\right)\right] \times t} \quad (4)$$

where Q_{SGD} is the total SGD water flux to the Sound in $m^3\ d^{-1}$. Equation 3 has been rearranged from Eq. 2 to solve for SGD instead of balancing inputs and outputs of tracer

into the system. Rn_{ex} (dpm m^{-3}) is the radon excess after parent isotope, offshore, and river correction, Rn_{dec} (dpm m^{-3}) is the decay correction applied to the radon, Rn_{atm} (dpm m^{-2} d^{-1}) is the atmospheric evasion correction multiplied by the apparent age (d) calculated from the $^{224}Ra/^{228}Ra$ continuous source discharge equation (t; Eq. 2) and depth (m; D), and Rn_{dif} (dpm m^{-3}) is the diffusion correction. V_S is the volume of the coastal seepage face (m^3) and Rn_{Gw} is the average radon in groundwater (dpm m^{-3}). Rnbound (dpm m^{-3}) and Sal_{bound} are the ^{222}Rn and salinity at the boundary between the Sound and Bight, and $dRn_{bound}/dSal_{bound}$ is the slope of the radon vs salinity relationship at the boundary. J_{out} and J_{λ} from Eq. 3 are corrected for by the Rn_{dec} term and the boundary correction of the groundwater endmember (Rn_{GW}). J_{riv} and J_{off} were removed from all the ^{222}Rn activities, resulting in excess ^{222}Rn (Rn_{ex}). J_{diff} is corrected for by the Rn_{dif} term. An additional term in the ^{222}Rn balance is atmospheric evasion, which affects ^{222}Rn because it is a gas.

To calculate our corrected ^{222}Rn, we correct for various sources and sinks, indicated by Eq. 4, which are summarized below:

1. In situ production of ^{222}Rn from dissolved ^{226}Ra, input of ^{222}Rn from river ^{226}Rn, and input from offshore ^{222}Rn from the Mississippi Bight is corrected for by calculating ^{222}Rn excess from:

$$^{222}Rn_{ex}\ (\text{dpm } m^{-3}) = {}^{222}Rn - {}^{226}Ra_{Prod} - {}^{226}Ra_{Riv} - {}^{222}Rn_{Bight} \quad (5)$$

   where $^{226}Ra_{Prod}$ is production of ^{222}Rn from the parent isotope ^{226}Ra, $^{226}Ra_{Riv}$ is the input of ^{226}Ra to the Sound by rivers, and $^{222}Rn_{Bight}$ is the input of ^{222}Rn from offshore.

2. Loss of ^{222}Rn due to radioactive decay is calculated using the apparent age of the water in the Sound and the decay constant of radon (0.181 d^{-1}).

$$^{222}Rn_{dec} = \lambda_{Rn} \times {}^{222}Rn_{ex} \times t \quad (6)$$

3. Loss of ^{222}Rn due to atmospheric evasion is calculated from measured wind speeds and the gradient between ^{222}Rn concentration in the air and the water:

$$Rn_{atm} = k_{Rn} \times (Rn_w - \alpha \times Rn_{air}) \quad (7)$$

where k_{Rn} is the radon gas transfer velocity, α is Ostwald's solubility coefficient, and Rn_w and Rn_{air} are the activities of ^{222}Rn in water and air respectively.

4. Input of radon due to sedimentary diffusion was calculated using an equation outlined in Martens et al (1980), formatted for use with ^{222}Rn:

$$Rn_{dif} = \sqrt{n \times D_{Rn} \times \lambda_{Rn}} \times (Rn_{PW} - Rn_{Snd}) \quad (8)$$

where n is the porosity of the sediments (~0.35 for silty sands), D_{Rn} is the diffusion coefficient of radon in water (Schubert and Paschke, 2015) , λ_{Rn} is the radon decay rate (0.181 d-1), Rn_{PW} is the radon concentration in pore water (avg±stdv: $5.2\times10^4 \pm 4.9\times10^4$ dpm m^{-3}) calculated from the average of the high salinity groundwater samples, and Rn_{Snd} radon activity in the Sound. The diffusion equation was applied to each ^{222}Rn sample.

5. Loss of radon due to advection was calculated using a method outlined in Savatier and Rocha (2021), which estimates the net exchange of radon from estuary to ocean. This was estimated using the slope of the radon vs salinity curve (Figure B.3). The average radon, salinity, and the slope was added as a correction to the groundwater endmember of radon.

To calculate the volume of the seepage face, we use the radon anomaly map (Figure 4.4). In areas where the anomaly is positive, we define that as a seepage area. Combined, the area of the seepage face is ~ 4×10^8 m^2. This is multiplied by the average depth to determine volume. Our apparent age was calculated from our $^{224}Ra/^{228}Ra$ continuous model, and our groundwater endmember is defined as the distribution of the groundwater ^{222}Rn. Monte Carlo simulation is applied to all equation components except for the volume of the seepage face, which is assumed to remain relatively constant.

4.5.1.2 Radium Model

The next model is based on using the radium concentrations from the Sound and various sources and sinks in a system of equations to determine an SGD component compared to rivers and offshore water inputs. This model simultaneously solves four mass balances applied to the volume of the region affected by SGD in the Sound (Sanial et al., 2021). The equations include a continuity balance (Eq. 9), ^{224}Ra balance including a decay term (Eq. 10), a ^{228}Ra balance (Eq. 11), and a salinity balance (Eq. 12). The equations are based on a balance by Sanial et al. (2021):

$$Q_{Out} = Q_{Off} + Q_{Riv} + Q_{SGD} \quad (9)$$

$$Q_{Out} \times {}^{224}Ra_S + \lambda \times V_S \times {}^{224}Ra_S - {}^{224}J_{Ra\text{-}dif} = Q_{Off} \times {}^{224}Ra_{Off} + Q_{Riv} \times {}^{224}Ra_{Riv} + Q_{SGD} \times {}^{224}Ra_{SGD} \quad (10)$$

$$Q_{Out} \times {}^{228}Ra_S - {}^{228}J_{Ra\text{-}dif} = Q_{Off} \times {}^{228}Ra_{Off} + Q_{Riv} \times {}^{228}Ra_{Riv} + Q_{SGD} \times {}^{228}Ra_{SGD} \quad (11)$$

$$Q_{Out} \times Sal_S = Q_{Off} \times Sal_{Off} + Q_{Riv} \times Sal_{Riv} + Q_{SGD} \times Sal_{SGD} \quad (12)$$

where Q_{Out}, Q_{Off}, Q_{Riv}, and Q_{SGD} are the fluxes of water out of the control volume, into the Sound from the Mississippi Bight, into the Sound from rivers, and into the Sound from SGD, respectively. Radium endmembers are from the Sound (Ra_S), offshore (Ra_{Off}),

rivers (Ra_{Riv}), and SGD (Ra_{SGD}). To correct ^{224}Ra for radioactive decay, we multiply the activity of radium in the water by λ, the decay constant (0.189 d^{-1}), and the control volume (m^3). To correct for diffusive fluxes, we subtract the estimated ^{224}Ra diffusive flux ($^{224}J_{Ra\text{-}dif}$) in Eq.10, and ^{228}Ra diffusive flux ($^{228}J_{Ra\text{-}dif}$) in Eq. 11, following a diffusion estimation equation outlined in Rodellas et al. (2017). Each radium activity and salinity was run through the Monte Carlo simulation before being substituted into the equation. We assumed that any negative fluxes indicated seawater infiltration into the water.

4.5.1.3 Water Isotope Model

Oxygen isotopes in water can be used to calculate the percentage of FSGD and RSGD in sample using a two endmember mixing model. To do this we set up two equations:

$$f_{RSGD} + f_{FSGD} = f_{SGD} \quad (13)$$

$$\delta^{18}O_{Sound} \times f_{Sound} + \delta^{18}O_{FSGD} \times f_{FSGD} = \delta^{18}O_{SGD} \quad (14)$$

where f_{RSGD} is the fraction of Sound water circulating through the coastal aquifer resulting in recirculated seawater, f_{FSGD} is fresh groundwater fraction, and f_{SGD} is the total SGD fraction, equal to 1. $\delta^{18}O_{Sound}$, $\delta^{18}O_{FSGD}$, $\delta^{18}O_{SGD}$ are the average values of the $\delta^{18}O$ measured in the Sound, the fresh groundwater, and the SGD. Using these equations, we can then solve for the flux of water from FSGD and the recirculated seawater component (RSGD) by multiplying the fractions by the total SGD flux. The fresh groundwater endmember (-3.38 ‰) was determined by averaging $\delta^{18}O$ groundwater data between 0 – 3 salinity, the SGD endmember (-2.22 ‰) was determined by averaging $\delta^{18}O$ values

between 5 – 20 salinity, and the Sound endmember was taken from the average $\delta^{18}O$ in the total Sound, the west, central, and east Sound, and the seasons (Table 4.3).

In general, the RSGD component of SGD was more prevalent than that of FSGD (Table 4.3). This is similar to other SGD studies (Burnett et al., 2006), where the fresh component is typically much lower than that of the recirculated component. The average percentage of FSGD to the total SGD was ~ 7%, and the RSGD ~ 93% (Table 4.3). The central Sound had the highest average FSGD contribution to the Sound. This is interesting, as the majority of the SGD in the central Sound enters right by the coastline (Figure 4.4). Typically, the fresh groundwater portion of SGD is confined to nearshore, (Burnett et al., 2003; Michael et al., 2005), which means that the central Sound may experience higher fresh groundwater discharge due to the SGD proximity to the coastline.

Table 4.3 *Results of the two endmember $\delta^{18}O$ mixing model.*

	$\delta^{18}O$ (‰)	FSGD (%)	RSGD (%)
Total	-2.13	7	93
West	-2.15	5	95
Central	-1.37	42	58
East	-2.22	0	100
Dry	-1.6	35	65
Wet	-2.16	5	95

4.5.2 Model Results

The ranges of SGD water fluxes predicted by the radon and radium models are similar (Figure 4.15; Table B.4), with median (geometric mean) fluxes of 9.7×10^6 and 1.8×10^7 m^3 d^{-1}, respectively. These numbers are within range of values reported by other SGD studies (e.g., McCoy et al., 2011; Montiel et al., 2019; Sanial et al., 2021; Santos et

al., 2009). Our radium model picks a slightly higher median discharge rate than that of our radon model, but also has a larger error than that of the radon model. Both the radium and ^{222}Rn models indicate that the western Sound has the highest total SGD fluxes, with the ^{222}Rn model predicting that the eastern Sound would have the lowest SGD, and the radium model predicting the central and eastern Sound to have similar SGD fluxes (Figure 4.16). The Cohen's D shows that for the ^{222}Rn model, the western Sound had a large difference (D>0.5) from the central and eastern Sound, while the central Sound is weakly different from the eastern Sound (D=0.2). For the radium model, the Cohen's D indicates that there are negligible differences between the west, central, and east Sound (D<0.2). This most likely is due to high error in the radium model Monte Carlo simulation, and that ^{224}Ra activities were not highly variable depending on location. The negative values in the radium model either indicate seawater intrusion into the aquifer, or a result of the salinity effect on radium isotopes. In this instance, it is most likely a result of both. The opening of the BCS lowered salinity to a point where there was essentially no desorption of radium, reducing its ability as a tracer. A similar occurrence was described in Chapter 2, where during the BCS opening we were unable to use radium as an effective tracer of SGD.

For both models, the seasonal distribution differences are small (D<0.2), and therefore the majority of our variability in SGD was due to spatial changes rather than seasonal. Seasonal variation in SGD has been noted in multiple studies (McCoy and Corbett, 2009), and mainly is due to variations in the hydraulic head of the aquifer (Michael et al., 2005). The hydraulic head variation is due to changes in recharge and discharge throughout a seasonal cycle. There can be significant lag time between

recharge events and discharge for fresh groundwater, which can be anywhere from 0 – 3 months (Changnon et al., 1988; Eltahir et al., 1999), and saline discharge anywhere from 1 – 5 months (Michael et al., 2005). In our study site, the highest rainfall occurs typically in the summer months, with increased rainfall starting in May and ending in September. However, we are unable to see variations in the total SGD fluxes. Therefore, we look at the differences between the FSGD and RSGD components between the wet and dry seasons. The dry season had a higher fraction of FSGD compared to the wet season according to the $\delta^{18}O$ model (Table 4.3). Therefore, instead of a change in overall SGD fluxes, there may only be changes in the composition of the SGD throughout the Sound.

This is different from what was found in Chapter 2, where SGD fluxes seemed highest in the summer and fall compared to the winter and spring. This may have to do with the high ranges of uncertainty in our SGD fluxes for the entire Sound. Chapter 2 focused on nearshore fluxes in the western Sound, which may have a more prevalent seasonal variation than the entire Sound. Samples in Chapter 2 included time series sampling for radium and other tracers from the beach, close to where we expect the unconfined aquifer to release, whereas samples in this study were mainly from boat sampling slightly farther from the coast and therefore the aquifer source of SGD. If, for example, the changes in seasonal SGD fluxes, and the uncertainty, are both a factor of 2, it would be hard to detect the seasonal variation. However, although we do not see seasonal differences in the broad scope of the Sound, it does not preclude seasonal variability; just that the variability is within the range of uncertainty for the fluxes. There is also the possibility that short term flux variability due to winds, waves, rain events, and diurnal variations (i.e., tides) overshadow the seasonal pattern (Santos et al., 2009).

Santos et al., (2009) found that seasonal cycles of SGD were small compared short-term fluctuations in a coastal estuary in Florida that has similar climate conditions as the Sound. The lack of seasonal variability may be due to how much lower fresh groundwater input is compared to recirculated groundwater in this region, as well as the hydraulic gradient not having a well-defined cycle like it does in other regions (e.g., Lee and Kim, 2007).

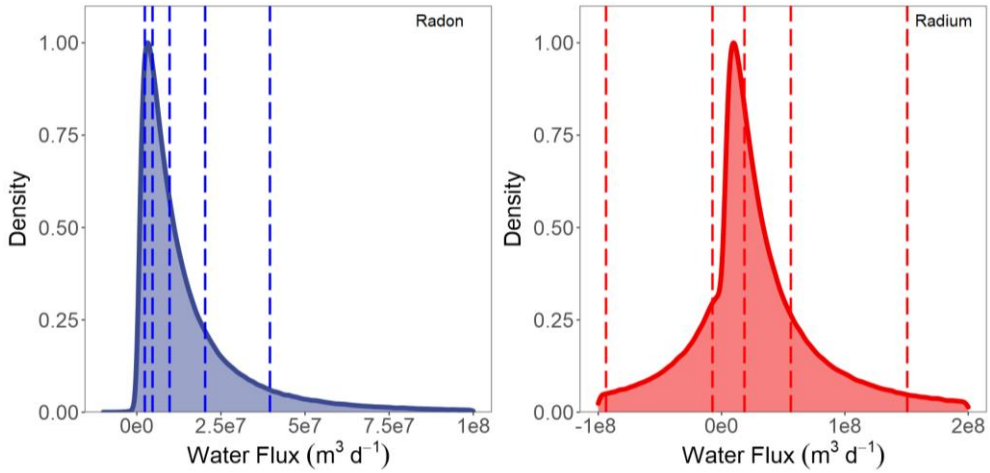

Figure 4.15 *SGD Monte Carlo simulation results for the total Sound (m^3 d^{-1}).*

The dashed lines represent the 10%, 25%, 50%, 75%, and 90% quantiles.

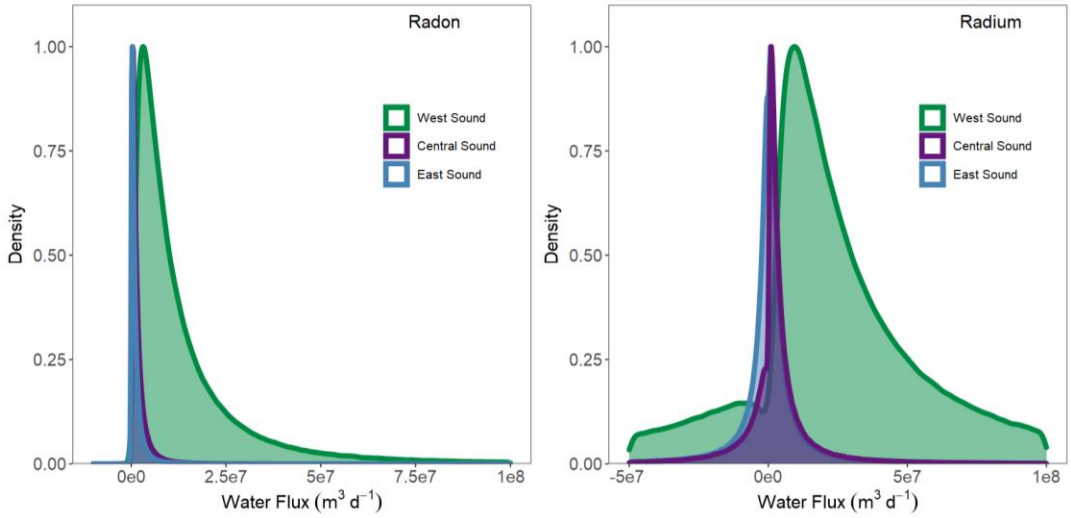

Figure 4.16 *SGD Monte Carlo simulation results for the west, central, and east Sound (m^3 d^{-1}).*

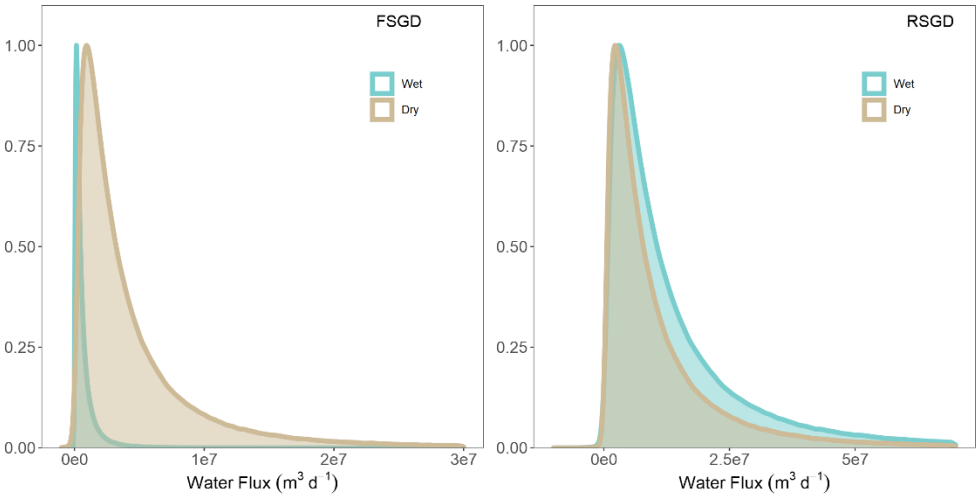

Figure 4.17 *FSGD and RSGD fluxes for wet and dry seasons using the radon Monte Carlo model errors (m^3 d^{-1}).*

While there were distinct differences in total fluxes (m^3 d^{-1}) in the west, central, and east Sound, when these fluxes were normalized by seepage area for each section

there are no differences between sections. The central and east Sound had a much smaller seepage area (~ 5×10^7 and 4×10^7 m^2, respectively) than the western Sound (~ 3×10^8 m^2). This highlights how much more groundwater affected area there was in the western Sound compared to the central and eastern Sound, which is reflected in the total water flux. Median area normalized discharges for the west, central, and east Sound were 0.03, 0.02, and 0.02, respectively. All area normalized discharges are shown in Table B.4.

4.5.3 SGD Distributions

There are distinct spatial differences for SGD fluxes in the Mississippi Sound based on our Monte Carlo results. The western Sound has higher discharge than the central and eastern sections of the Sound for all models. However, why this occurs is unknown. Often times, the presence of coarser buried materials can contribute to preferential flow of SGD compared to areas with smaller grain particles (Mulligan et al., 2007). This is important for both fresh groundwater flowing from the shore and the recirculating seawater in the aquifer (Mulligan et al., 2007). Previous work has indicated that buried paleochannels within incised valleys could be preferential pathways for both fresh groundwater discharge and seawater intrusion into aquifers (Mulligan et al., 2007; Spalt et al., 2018). With this in mind, we use geologic reconstructions (Adcock 2019; Gal et al., 2021; Hollis et al., 2019) and surficial sediment data (Sawyer et al., 2001) to determine if there are specific reasons for changes in the spatial distribution of SGD.

In the eastern Sound, there are incisional systems (Figure 4.18). These are associated with Marine Isotope Stage 2 (MIS2; ~22,000–17,000 cal yr BP; Late Pleistocene), when sea level was ~120 m lower than modern day (Gal et al., 2021; Hollis et al., 2019). Shallower, (≤ 5m) narrower incisional systems extend over the far eastern

section of the Sound, and continue offshore to connect with deeper (≥ 8 m) incised valleys (Figure 4.18). One incised valley runs between Horn and Ship Islands, and another through the Pas aux Heron connecting Mobile Bay and Mississippi Sound (Figure 4.18). The shallower incisional systems in the eastern Sound are mainly infilled with muddy to clayey sediments (Hollis et al., 2019). Deeper incised valleys in the Sound lead out towards Horn Island from the Pascagoula River and Biloxi River. The channel from the Pascagoula River runs perpendicular to the shore, but the Biloxi River incised valley follows the coastline, and then splits off, running perpendicular to the western part of Horn Island (Figure 4.18). These are continuations of low stand incised valleys from when the Pascagoula and Biloxi Rivers ran further offshore during MIS 2 (Gal et al., 2021). These valleys and the associated paleochannels are likely filled with fine to medium sand (Gal et al., 2021).

When comparing our ^{222}Rn data with the paleovalley and channel distribution, we noticed that several areas of high SGD line up with the deeper valleys near the Biloxi and Pascagoula Rivers. The shallow paleochannels in the far east do not seem to have an impact on SGD distribution. However, the deep valleys only seem to have an impact on the nearshore SGD fluxes (Figure 4.19). This could be due to direct aquifer connection with the paleochannels, leading to increased discharge nearshore (Mulligan et al., 2007). There is also the possibility that surficial sediments could act as a barrier to SGD if they are non-permeable (Douglas et al., 2020). Sedimentary data for the Sound indicates that the majority of the nearshore is primarily composed of sandy sediments, the mid-Sound is primarily composed of silts and clays, and when moving offshore the sediments become sandy again near the islands (Figure 4.18). The far western section of the Sound, however

does not have a primarily silty/clay layer, and remains mostly sandy (Figure 4.18). Interestingly, we do not see enhanced SGD near the islands, which could be due to a few reasons. The first possibility is that the paleochannels are not carrying the groundwater farther offshore as most of it is discharged directly along the coast. This would mean that while their presence along the coast is important for fresh discharge, the confining surficial sediments force the majority of it to be expended close to shore. Another possibility is that the groundwater is simply bypassing the Sound side of the islands and is being discharged on the Bight side due to hydraulic gradients and the base elevation flow (Mulligan et al., 2007). ^{222}Rn data collected offshore from the islands out towards the open Gulf of Mexico seems to indicate the latter (Figure 4.9). Indeed, a recent study by Sanial et al. (2021) showed that the islands seemed a major source of SGD to the Bight, along with freshened ponds and artesian wells observed on the islands, which could be indicative of paleochannel processes releasing SGD offshore.

In the western Sound, the paleochannel and paleovalley data is more limited, but still shows that they are present (Adcock, 2019; Figure 4.20). These channels mainly run parallel to the shoreline, with a few extending offshore towards Cat Island (Figure 4.20). High activities of ^{222}Rn run along the beaches west of St. Louis Bay where there is a cluster of smaller paleochannels running along the shoreline, indicating that these may play a role in SGD. Like the other islands, we do not see higher SGD signals near Cat Island, which would be expected if paleochannels were a source. However, the surficial sediments again are silt/clay on the beaches to the east of SLB out towards Cat Island, which may be why we do not see elevated SGD signatures. The combination of surface sediment composition and paleochannel location seem to play a role in SGD distribution

in the Mississippi Sound. However, the infill of the paleochannels also is important, as we have abundant buried valleys and channels in the far east of the Sound, but little to no SGD. Our surficial sediment data may also be skewed due to the artificial nature of the beaches along the coastline. Therefore, where we see sandy sediments that are along the entire shoreline may be just due to the sand that was placed there migrating offshore during storm events. If under this sediment is all silt/clay material, then there may not be much of correlation between the surface sediments and the high radon anomalies. However, surface sediments can play a role, because if they are not permeable, then the SGD will not breach the sediments and make it into the estuary. Therefore, both the location of paleochannels, the infill sediments, and the surficial sediments need to be taken into consideration when considering paleochannels as potential conduits of SGD.

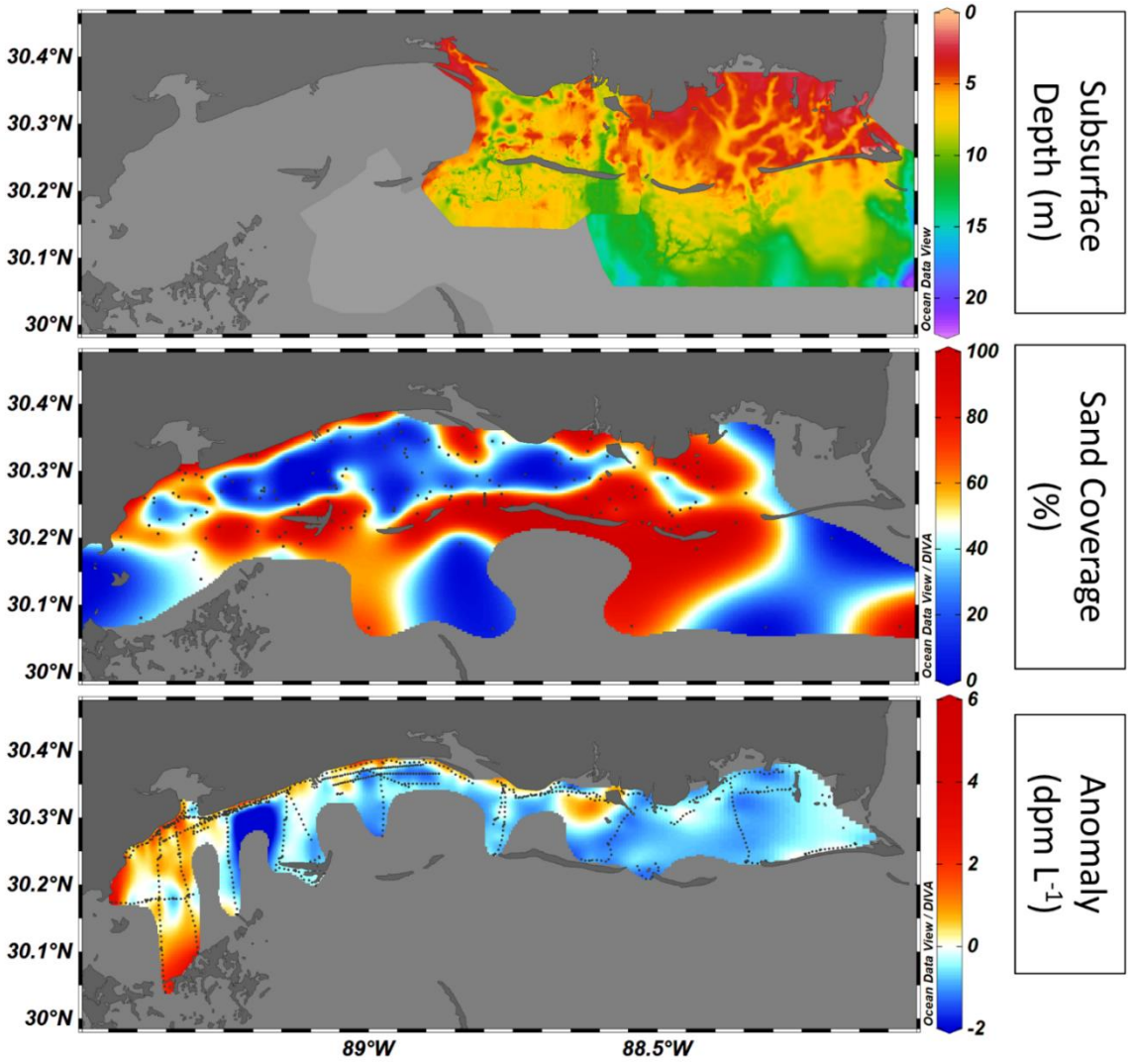

Figure 4.18 *Qualitative evaluation of incisional systems, sand coverage, and ^{222}Rn anomalies.*

a) Seismic data of the eastern Sound showing the MI2 surface with depth below the surface (from Gal et al., 2021; Hollis et al., 2019).

b) surface sediment sand percentage coverage, with above 50% sand in red, and below in blue (from Northern Gulf Littoral Initiative (NGLI), Sawyer et al., 2001).

c) radon anomaly plot in dpm L^{-1}.

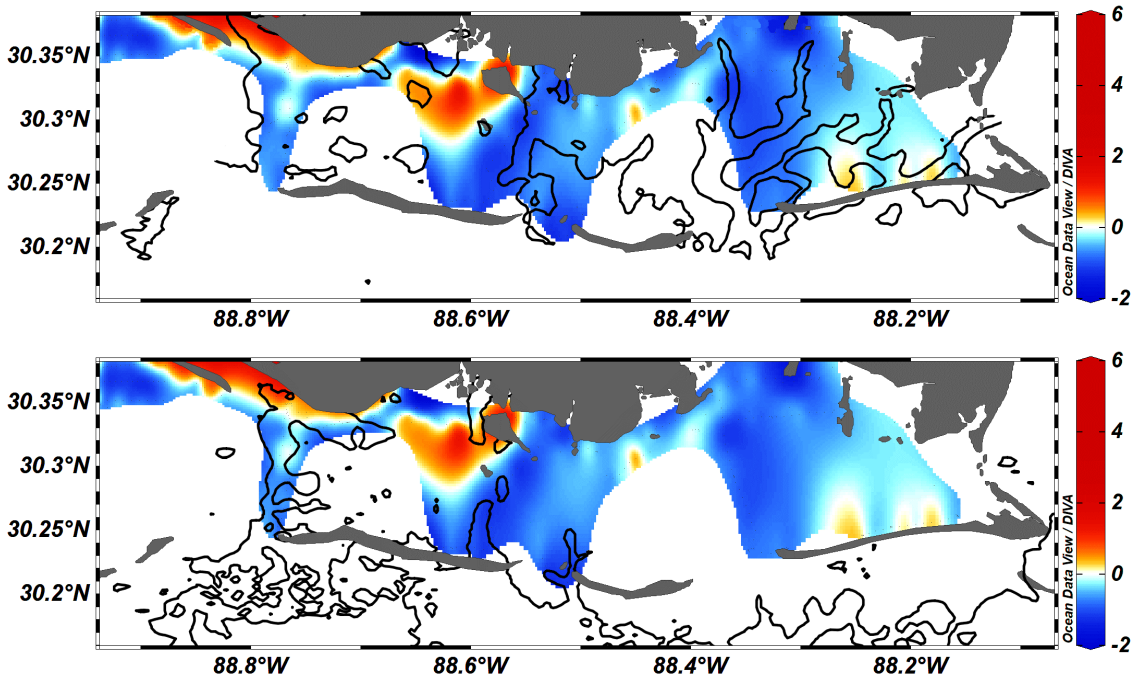

Figure 4.19 *MIS2 contours over ^{222}Rn anomalies.*

Top: Contours of 5 m MIS2 subsurface overlain on the radon anomaly; Bottom: contours of 8 m MIS2 subsurface overlain on the radon anomaly.

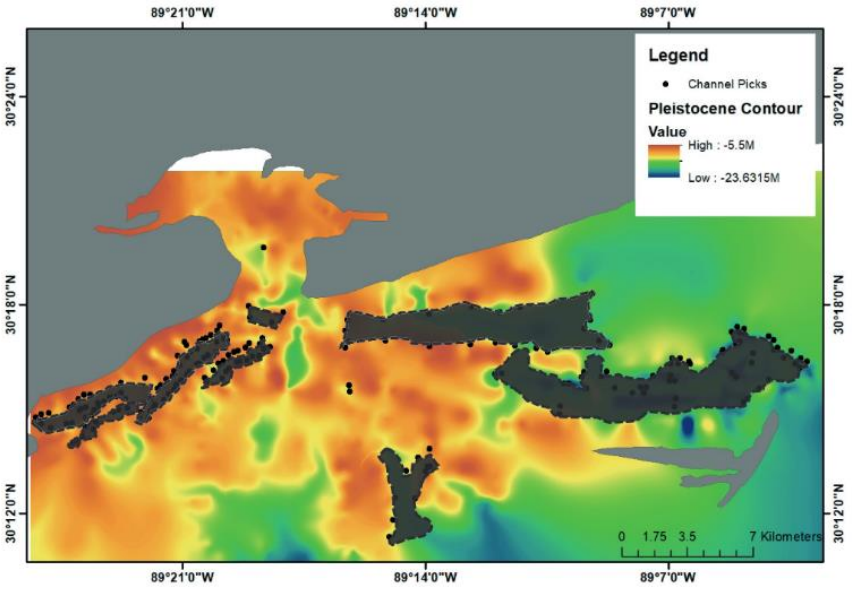

Figure 4.20 *Paleochannel locations and MIS2 layer depth in the western Sound.*

From Adcock, 2019

4.5.4 Nutrient Distributions

The opening of the BCS occurred in two stages within our study period; February 27, to April 11, 2019, and May 10 to July 27, 2019 (https://www.mvn.usace.army.mil/Missions/Mississippi-River-Flood-Control/Bonnet-Carre-Spillway-Overview/Spillway-Operation-Information/). Our open BCS samples are from the first of the openings, which should show a clearer picture of moving from a "normal" state to one that is severely affected, and the directly after closure samples are from after the second time the BCS was closed that year. During the opening and directly after the closing there was severe organism mortality due to both input of low salinity water and hypoxia (McConnaughey, 2019; Lee, 2019; Parra et al., 2020). After the input of high nutrients, there was also a large HAB that caused even more mortality and, additional societal and economic impacts (Byrd, 2019).

Inorganic nutrient concentrations showed trends associated with the opening and closing of the BCS, most notably for the nitrate+nitrite (NO_x) concentrations (Figure 4.21. Before the opening of the BCS, the NO_x concentrations were relatively low, and experienced a spike in concentration after the BCS opening, and subsequent decline when the BCS closed. The major increase of NO_x is in the core of where the BCS water would enter into the Sound. When the BCS was open, dissolved silicate (DSi) experienced a decline (Figure 4.21). The DSi endmember for groundwater is ~70% higher than that of the Mississippi River endmember (Table 4.2), therefore this decline may be due to a lower DSi signal entering the Sound. There also may be a decline due to excess nitrate from the BCS, which could lead to an increase in primary productivity, causing a higher DSi utilization (Sigleo and Frick, 2007). Diatoms have been found to be component of

blooms triggered by the BCS (Roy et al., 2016), and therefore, the decline in DSi was a result due of the algal bloom in Lake Pontchartrain or the western Mississippi Sound (Parra et al., 2020). Dissolved phosphate (DIP) and ammonium (NH_4^+) also experienced a decline with the BCS opening. The DIN:DIP molar ratio implies that the Sound was nitrogen limiting before the BCS opening (Figure 4.22), and the drop in DIP could be due to increased primary production. The NH_4^+ decline is due to either the Mississippi River waters having lower NH_4^+ than some of the local rivers and of the SGD, or preferential NH_4^+ uptake and nitrification. Dissolved organic nitrogen (DON) and dissolved organic phosphorus (DOP) do not show as clear trends as the inorganic nutrients, but it does seem that with intrusion of BCS waters, the DON tends to decline and DOP increased slightly (Figure 4.23). After closure of the BCS, the DON concentration spikes, which may be due to increased phytoplankton production and death (Yao et al., 2020).

The NH_4^+:DIN molar ratio before the BCS opening is high along the coast and offshore except for samples that are near river sources (Figure 4.22). This is indicative that the majority of the DIN in the Sound was in the reduced form along the coast, suggesting that the source water is also reducing (Sanial et al., 2021) or there were high rates of bacterial re-mineralization or nitrogen fixation (Voss et al., 2011; Wenjuan et al., 2011). The local river NH_4^+:DIN molar ratio is 0.3 (Table 4.2), and therefore is not the source of the reduced nitrogen. Since SGD has been shown to be a major source of reduced constituents (Slomp and Van Cappellen, 2004), and considering that the NH_4^+:DIN molar ratio in the groundwater is 0.8 (Table 4.2), it is possible that the high ratios near the coast are due to SGD input. There is a decline in the NH_4^+:DIN molar ratio

in the location where the BCS water infiltrates the Sound, indicating the change in source waters (Figure 4.22). Once the BCS was closed, the entire Sound had a ratio above 0.5, indicating that almost all waters had a reduced inorganic nitrogen source (Figure 4.22). This could be due to either the water being low in oxygen from stratification and hypoxia, that there was extensive nitrogen fixation from primary producers, or that there was input from SGD. Before the BCS, the majority of the Sound DIN:DIP molar ratio was below 16, indicating that the water was nitrogen limiting (Howarth et al., 1988). The waters entering the Sound from the BCS were above 16, showing that they are bringing an abundance of inorganic nitrogen into the Sound (Figure 4.22). This again implies that the BCS switched the Sound from a nitrogen limiting system to a phosphorus limiting system. After the closing of the BCS, the Sound returned to nitrogen limiting (Figure 4.22). Another interesting ratio is the DON to total dissolved nitrogen (TDN) ratio, which shows if samples are organic or inorganic dominated (Caffrey et al., 2007). Before the BCS, the samples were mainly DON dominated along the coastline, and declined offshore and near the Pascagoula River (Figure 4.23). BCS waters had a much lower DON:TDN molar ratio, indicating that the waters are mainly inorganic nitrogen. After the closing of the BCS, the ratio remains above 0.5 across the entire Sound, which is most likely due to the HAB, and excess production.

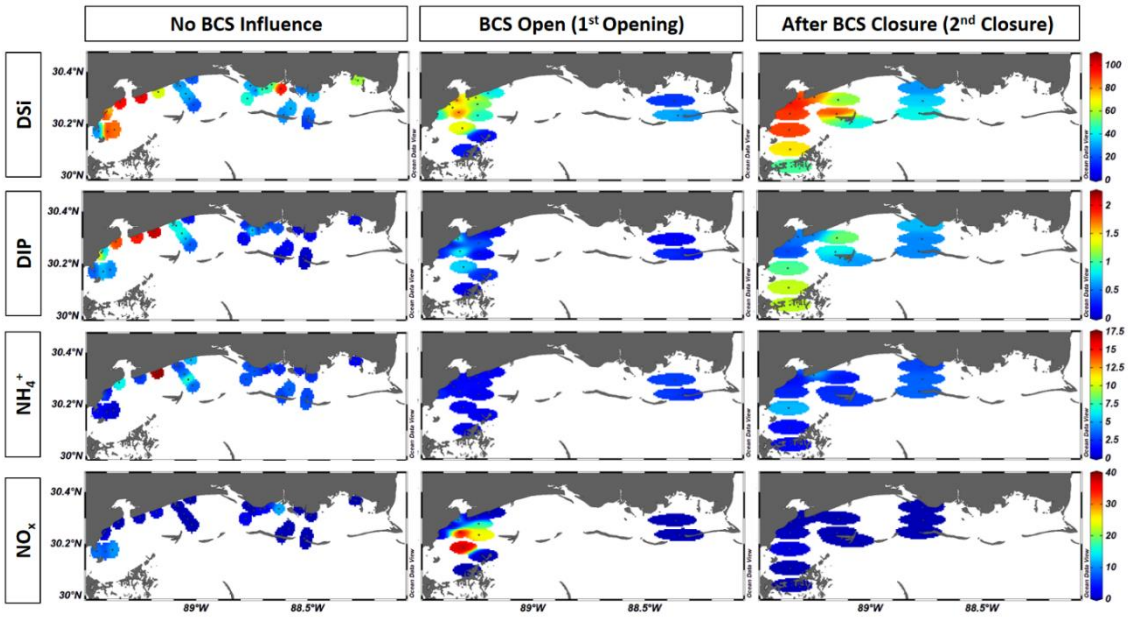

Figure 4.21 *Inorganic nutrient distributions (µM) from when there is no BCS influence, during the first opening, and after the final closure in 2019.*

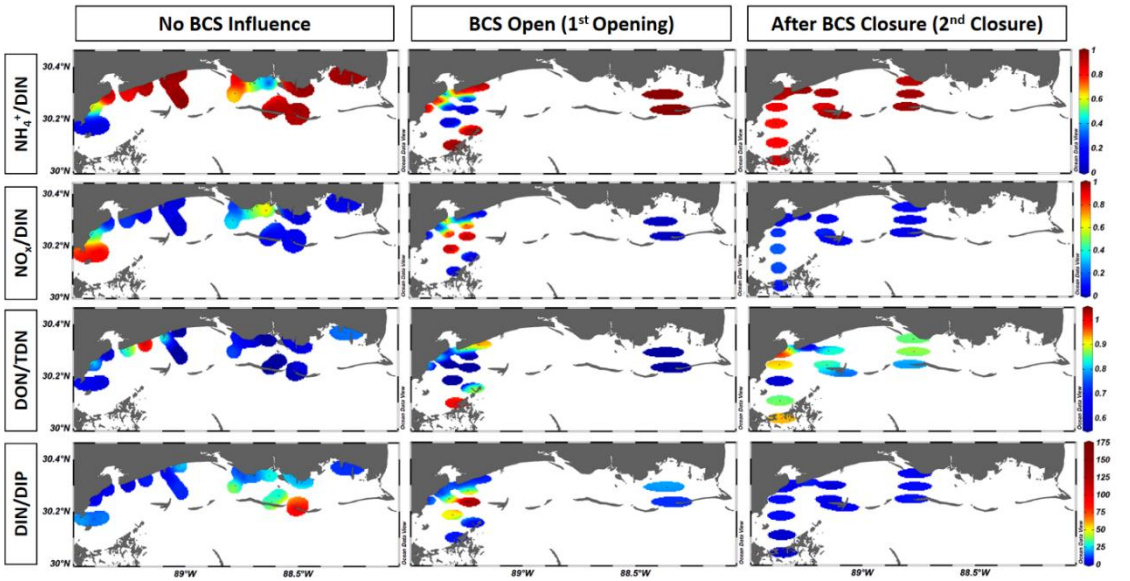

Figure 4.22 *Nutrient molar ratios when there was no BCS influence, when the BCS first opened in 2019, and directly after closure in 2019.*

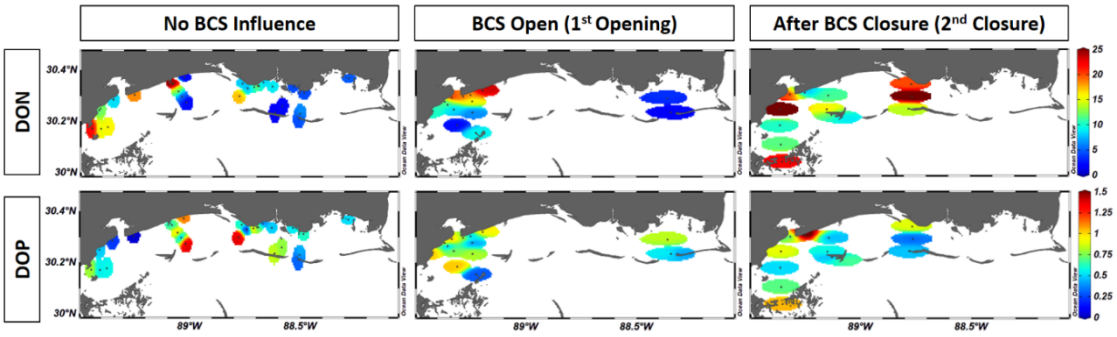

Figure 4.23 *Organic nutrient distributions (µM) from no BCS influence, during the first BCS opening in 2019, and after the final closure in 2019.*

4.5.5 Nutrient Risk Assessment

We conducted an environmental risk assessment by calculating risk quotients (RQ; e.g., Mohtar et al., 2019) based on observed nutrient data in the Sound and the predicted no effect concentration (PNEC) of total dissolved nitrogen (TDN) and total dissolved phosphorus (TDP). These were calculated by:

$$RQ = \frac{Obs_{conc}}{PNEC} \tag{15}$$

where Obs_{conc} is the observed concentration in a sample, and PNEC is the predicted no effect concentration. In the case of nitrogen and phosphorus, the PNEC would indicate the cutoff for eutrophication. The PNECs were obtained from Bricker et al. (1999), who list the TDN PNEC as 71 µM, and the TDP PNEC as 3.2 µM. The PNEC was based on the medium threshold for estuaries across the country (Bricker et al., 1999). Low RQs are 0.01 – 0.1, medium is 0.1 – 1.0, and high is >1.0. A low RQ indicates that the concentrations in the water column will not cause organism mortality or function suppression (Hernando et al., 2006), while high RQs indicate risk to organisms. For TDN

and TDP, there are no RQs that exceed the medium range. Before the BCS, the majority of medium risk was from the Pearl River plume for TDN, and along the coastline and out from the Port of Gulfport for TDP (Figure 4.24). During the opening, the BCS water had a high RQ for TDN in the core of the infiltrating water, which is where the majority of the oyster reef population of the western Sound is located (Linhoss and Mickle, 2022; Figure 4.2). There is some slight increase in phosphorus RQ in the core of the BCS waters, but it is similar to what was there before the opening. After the second closure, the TDP RQ increased in all of the western Sound, while the TDN RQ declined. All of this indicates that there is moderate risk for eutrophication by TDN and TDP during the opening of the BCS. Before the BCS opening, the majority of the Sound, except near rivers, was nitrogen limiting according to the TDN:TDP ratio, but when the BCS opened, the entire western Sound became phosphorus limiting. The excess nutrients from the opening, especially that of the TDN since the system is nitrogen limiting, drove an algae bloom across the majority of the Sound. However, when the BCS is closed, there is limited risk associated with the TDN compared to the TDP, again reinforcing that excess nitrogen into the system can lead to HABs.

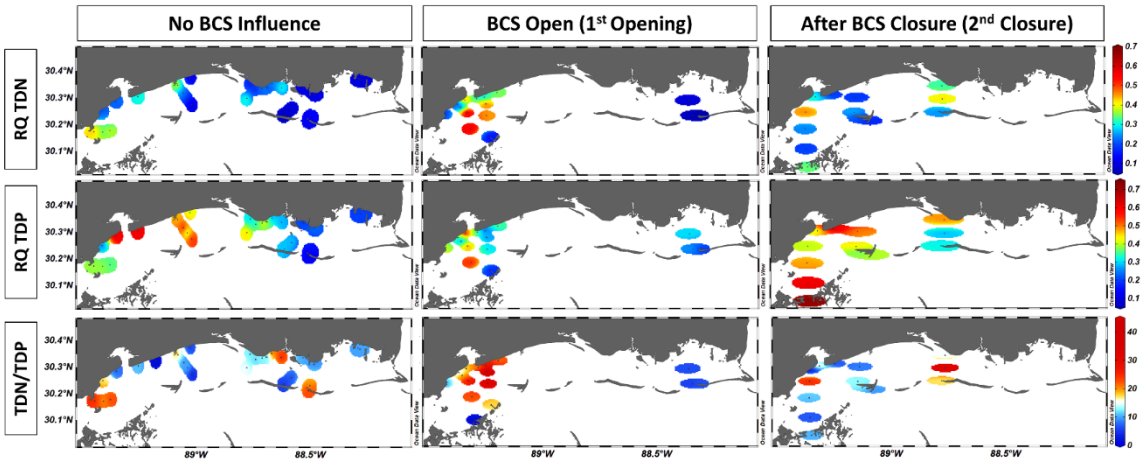

Figure 4.24 *Risk assessment of TDN and TDP, and TDN:TDP when the BCS is closed, after the first opening, and directly after the second closure.*

4.5.6 Nutrient Fluxes

Using the calculated RSGD and FSGD fluxes from the total SGD, we can determine a range of nutrient fluxes to the Sound and compare them to those from the local rivers and the BCS. Using data from the USGS (local rivers), and the Army Corp of Engineers (BCS), a distribution of fluxes was determined and compared to that of the FSGD and RSGD (Figure 4.25). To be able to compare the short term BCS input to the others, we normalized the flux to the entire year. Using $\delta^{18}O$ data collected during the BCS (Gilbert unpublished), it was determined that the percentage of Mississippi River water of the total freshwater in the Sound during the opening of the BCS was between 12 – 42% (10 – 90% quantiles). The water fluxes of the BCS, local rivers, FSGD, and RSGD were compared (Figure 4.25), and show that the local rivers and RSGD were the two dominant water sources to the Sound. The BCS flux was only considered for 2019, the largest opening to date, and was comparable to the input of FSGD to the Sound. Over the course of a year, FSGD water flux and RSGD water flux were ~ 2-3 orders of magnitude

lower than that of the local rivers. This is consistent with the literature (Moore, 2010), as the SGD water flux is often much lower than that of river input.

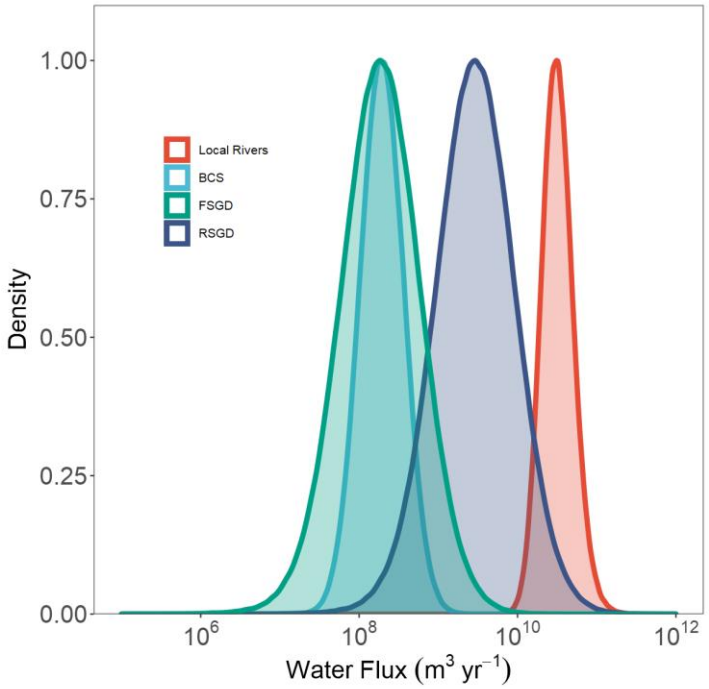

Figure 4.25 *Water fluxes (m^3 yr^{-1}) of the local rivers, FSGD, and RSGD into the Mississippi Sound during the study period (2018-2021).*

BCS input was normalized over the year of 2019 as an event. Note that the x scale is logarithmic.

Using the water flux distributions and nutrient endmember distributions (Figures 4.13 and 4.25), the nutrient input to the Sound can be calculated (Figure 4.26). From the nutrient export distributions, it can be seen that the local rivers dominate the DON input and are higher than other sources for DIN and DSi. The BCS is highest in NO_x input, which makes sense when comparing the NO_x:DIN distributions before, during, and after the BCS opening. Both the RSGD and local rivers are about 3 orders of magnitude higher than the FSGD and BCS with the NH_4^+ input. When looking at the NH_4^+:DIN distribution when the BCS had no influence, the ratio was extremely high near the coastline, which

can be indicative of the high NH_4^+ export due to SGD. SGD oxygen concentrations are often hypoxic or anoxic (e.g., Kroeger et al., 2007; Sanial et al., 2021), and thus the reduced form of dissolved constituents dominates within the coastal aquifer. The BCS input was also lower than SGD and local rivers for PO_4 and DSi on an annual basis. However, during the event, the BCS will dominate nutrient inputs to the Sound, which was shown in Chapter 2. This was also assuming that the water of the BCS entering the Sound had the same concentrations as the Mississippi River, which would not be the case after biological modification in Lake Pontchartrain; therefore the impact may be even lower on an annual basis than what was calculated through Monte Carlo simulation.

For the SGD nutrient fluxes, the RSGD component dominates over the FSGD component (Figure 4.26). This highlights the importance of the recirculated seawater in recycling nutrients in estuaries. The FSGD is a source of 'new' nutrients, while RSGD is a source of 'recycled' nutrients, that otherwise may remain buried in the sediments. This 'recycling' can be on extremely long time (>10 k years) scales due to buried organics in sediments; usually nutrient isotopes are needed to differentiate the sources in nutrients, which could help to determine if the recycling in the Sound is a shorter term (<yr) basis, or from buried organics (e.g., Wang et al., 2021). In terms of 'new' nutrients, we can compare the river and FSGD input into the Sound. For all nutrients the local rivers dominate over the FSGD. However, 'recycled' nutrient input by SGD rivals or was higher than that of rivers for PO_4 and NH_4^+.Therefore, combined, SGD was extremely important for nutrient input to the Sound, especially when our river fluxes may be lower during the dry season.

In terms of oyster reef restoration, substantial nutrient flux increases, especially when a limiting nutrient suddenly becomes available, can lead to occurrences such as HABs. While a small, localized bloom may not cause too much impact, the bloom that occurred due to the 2019 BCS opening was widespread over the western and central Sound (Gledhill, 2020; Morgan and Rakocinski, 2022), and it ended up causing hypoxia throughout the Sound (Pace et al., 2020). The large blooms can also release toxins that can affect the ability of larval oysters to survive (Wolny et al., 2020).

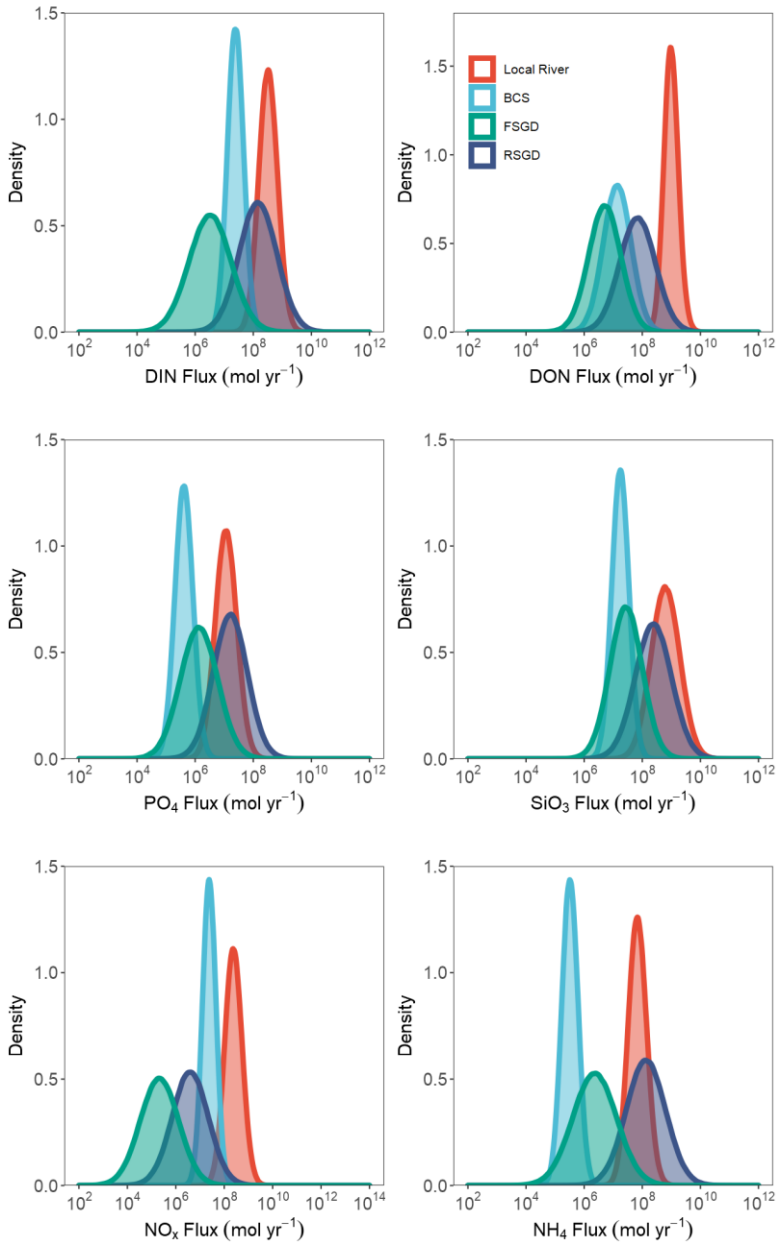

Figure 4.26 *Nutrient input distributions (mol yr^{-1}).*

Note that the x axis is logarithmic.

4.5.7 Trace element distributions

Throughout sampling, the main driver of trace element composition was the variety of water sources, including local rivers, the BCS, and groundwater, as well as

salinity. Dissolved oxygen for all surface samples did not fall below 80% saturation, and therefore was not expected to have any impact on trace metal distributions. However, other redox indicators, such as the ratio of reduced nitrogen (NH_4^+) to TDN can be used to determine if reduction/oxidation conditions are influencing the distribution of trace elements.

4.5.7.1 Dissolved Cs, Mo, U, and Re

Dissolved cesium (Cs) concentrations are conservative in seawater with an average concentration of about 2.2 nM (Brewer et al., 1972; Spencer et al., 1970). River water is often lower in Cs concentration compared to seawater in this region, and is often conservative in the Mississippi River plume (Joung and Shiller, 2016; Shim, 2011; Shim et al., 2012). However, SLB, which feeds into the Sound, can be a source of high Cs due to the outfall from a TiO_2 refinery (Bera et al., 2015). When examining Cs concentrations in the surface waters (Figure 4.27), there is an increase of Cs beyond 2.2 nM right outside the Bay, with the majority of the enhanced concentrations tracking eastward due to the mean surface currents in the western Sound that push water exiting the Bay eastward (Cobb and Blain, 2002). The concentrations in the central Sound are similar to those of seawater, which makes sense due to the main influence on this area being the Bight, and since the SLB is a relatively minor freshwater source to the Sound. Low Cs concentrations occur in the eastern Sound and far western Sound due to river influences. Groundwater Cs largely follows the mixing line between river influences and offshore waters (Figure 4.28), meaning that the main influence on elevated (>2.2 nM) Cs concentrations was SLB water.

Trace elements such as molybdenum (Mo), uranium (U), and rhenium (Re) can exhibit both conservative and nonconservative behavior in estuaries (e.g., Anbar et al., 1992; Dalai et al., 2005; Dellwig et al., 2007; Moore and Shaw, 2008; Ho et al., 2018; Ho et al., 2019; Joung and Shiller, 2016; Owens et al., 2011; Santos et al., 2011; Swarzenski and Baskaran, 2006; Wang et al., 2016). For all three of these trace elements, there was a distinct switch between Mississippi River sources and local river sources. Therefore, they may be useful in deconvolving water sources to the Sound. Groundwater concentrations of these elements are scattered along the salinity gradient (Figure 4.29), and there does not seem to be any clear excess in the U and Mo plots from groundwater sources. There were some high Re concentrations at low to mid salinities after the closure of the BCS in October 2019 in the western Sound. Some of the low salinity groundwater as well had high Re; all of these samples were collected after the opening of the BCS. This suggests the possibility of FSGD recharge from a Mississippi River source. This is corroborated by Re having a strong correlation with ^{228}Ra; when the BCS was open, the relationship is negative, but when closed it was positive (Figure B.4). This highlights how with the opening of the BCS, the influence of SGD was overshadowed. Both U and Mo have slight positive relationships with the NH_4^+:TDN ratio, especially when the BCS was open (Figure 4.30). Re does not have a clear relationship with this ratio, though there does seem to be a decline with Re as NH_4^+:TDN increases when the BCS was open. The slight

relationships indicate that the system may not be reducing enough be the main process affecting trace element distributions.

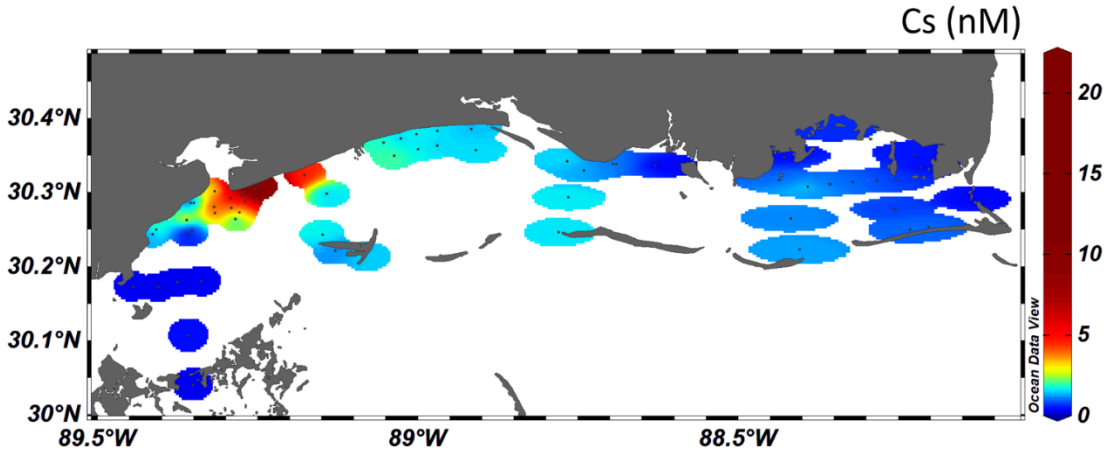

Figure 4.27 *Surface water Cs concentrations.*

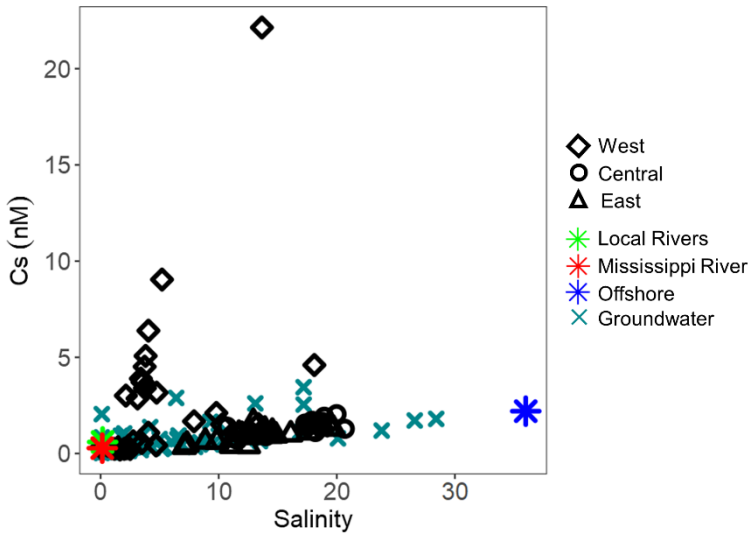

Figure 4.28 *Cs along the salinity gradient.*

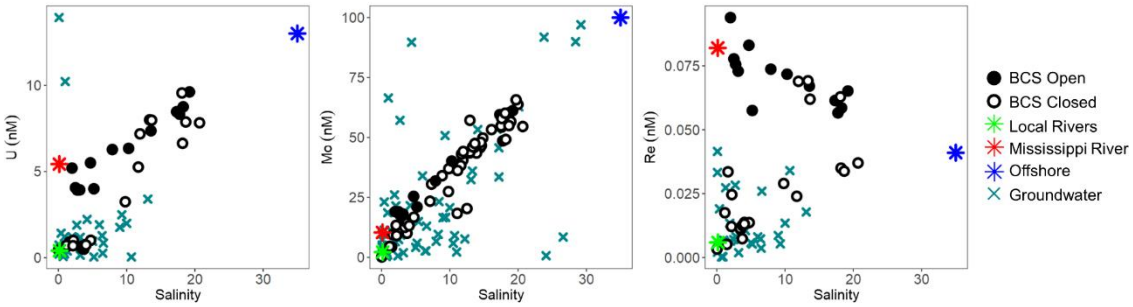

Figure 4.29 *U, Mo and Re vs Salinity*

The distributions of U, Mo, and Re along the salinity gradient under conditions of BCS influence, and when the BCS was closed, as well as groundwater and endmember concentrations.

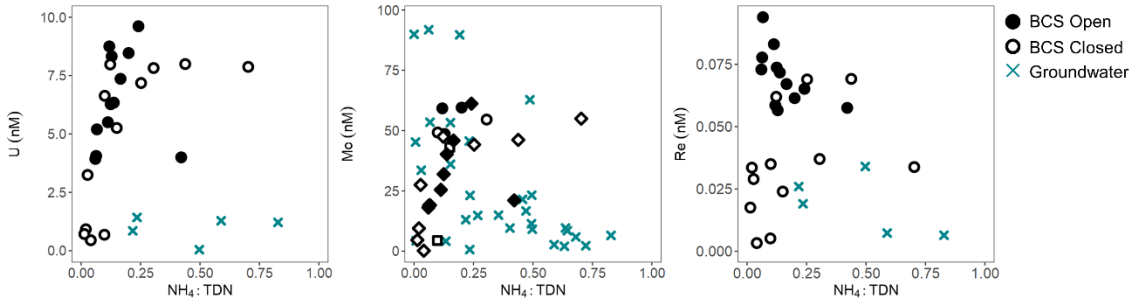

Figure 4.30 *U, Mo, and Re vs NH_4^+:TDN*

U, Mo, and Re vs NH_4^+:TDN ratio under conditions of BCS influence, when the BCS was closed, and groundwater.

4.5.7.2 Ba

The dissolved Ba in the Sound changed behavior when the BCS was opened and with seasons, indicating multiple endmember mixing (Figure 4.31). Concentrations were generally highest at low salinity, which is indicative of a fluvial source that is enriched in Ba (Ho et al., 2019). The local river concentrations can have a narrow or wide range, depending on the season (Figure 4.31). Spring and winter months had the lowest Ba concentrations, with concentrations falling between the local river concentrations and offshore, and seemingly not influenced by groundwater or Mississippi River. During the

summer months, samples taken during the BCS opening are enriched compared to the local rivers, showing the effect of the Mississippi River water entering the Sound. However, samples collected at the Chef Menteur and Rigolets Passes during the BCS opening are lower than the Mississippi River, possibly due to Ba removal as the waters move through Lake Pontchartrain (Figure 4.31). This trend continues into the Sound, with samples below salinity 10 falling under the conservative mixing line. Removals of Ba have been associated with diatom blooms (Coffey et al., 1997; Stecher and Kogut, 1999; Sternberg et al., 2005), and the HAB that occurred after the BCS in Lake Pontchartrain and the western Sound may have been a driver of this depletion. When the BCS was closed during the summer, samples were still slightly elevated above the local river endmembers; this observation may have been due to residual BCS enrichment, or potentially groundwater influence at mid-salinities. Indeed, the Ba groundwater concentrations show input along the salinity gradient, with the highest concentrations at mid-salinity (Figure 4.31). The Ba concentrations are also elevated at mid-salinity during the fall (Figure 4.31), which again may be due to groundwater. Fall is often when the local river flow is lowest, and therefore this may be indicative of SGD.

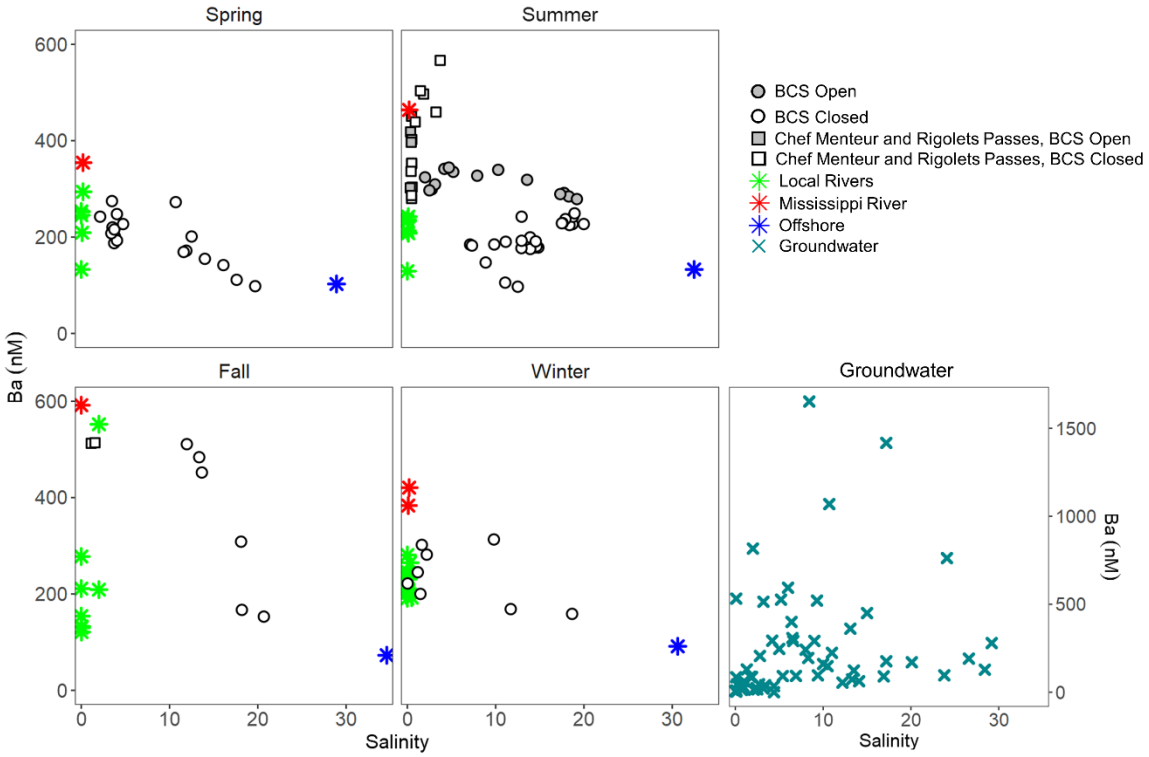

Figure 4.31 *Ba concentrations along the salinity gradient*

Ba concentrations along the salinity gradient during the four seasons, and in the groundwater. Endmember concentrations are represented by the stars.

Previous work in the Sound has estimated that Ba input from the sediments is ~ 35 µmol m^{-2} d^{-1}, and previous work in the Bight calculated that total SGD flux of Ba from the sediments to the Bight was ~ 18 µmol m^{-2} d^{-1} (Ho et al., 2019; Sanial et al., 2021). Using our FSGD and RSGD flux estimates (Figure 4.25), the Ba endmember distribution (Figure B.5), and seepage face area (~ 4×10^{8} m^{2}) we estimated the median flux of Ba from SGD in µmol m^{-2} d^{-1}. For FSGD, the Ba flux was ~ 0.75 µmol m^{-2} d^{-1}, and for RSGD the flux of Ba was ~ 16 µmol m^{-2} d^{-1} when saline groundwater

concentrations were corrected for Ba in the seawater. These values are similar to the previous studies, and also highlight how important seawater recirculation may be for Ba input into the Sound.

Processes that can control Ba cycling in the aquifer sediments can include ion exchange, weathering of minerals that contain Ba, evaporation and dilution, and Fe/Mn hydroxide precipitation and dissolution (Charette and Sholkovitz, 2006; Charette et al., 2005; Coffey et al., 1997; Sanders et al., 2012). Our groundwater Ba vs salinity plot does show that there may have been desorption in the mid salinity ranges (Figure 4.31), but this cannot be the only controlling factor as a good portion of Ba samples stay relatively low even as salinity increases. The groundwater Ba was well correlated with Mn (Figure 4.32; $r^2 = 0.51$), which may indicate that there was a redox control on the dissolution of Mn hydroxides, leading to elevated Ba concentrations. There was no relationship between Ba and Fe; other studies have found that often the redox chemistry of Mn is more important for forming elevated Ba concentrations in the subterranean estuary (e.g., Charette and Sholkovitz, 2006).

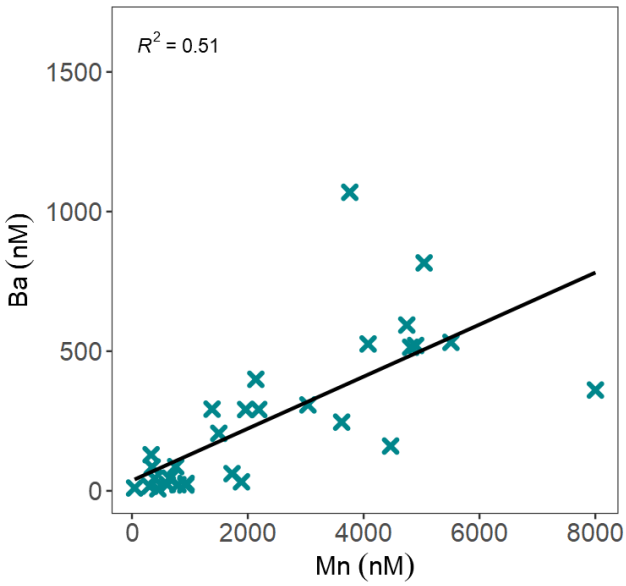

Figure 4.32 *Ba vs Mn in groundwater.*

4.5.7.3 Mn and Fe

Both Mn and Fe experience depletion in the Sound along the salinity gradient, indicating that there was removal in the water column (Figure 4.33). The lower salinity samples when the BCS was closed show an enrichment, which may be due to fluvial sources entering the Sound. Previous work on Fe and Mn in the Pearl and Mississippi Rivers has shown that the Pearl River and St. Louis Bay (SLB) have much higher concentrations of dissolved Fe and Mn than the Mississippi River (Shiller, 1997; Shiller and Stephens, 2005; Shim, 2011; Stolpe et al., 2010). The Pascagoula River, according to CONCORDE data, also has a higher Fe and Mn concentrations than that of the Mississippi River. When the BCS was open, the concentrations of Fe and Mn fell below the mixing line of Mississippi River water and offshore water, again indicating a removal process.

Groundwater and porewater Mn and Fe oxide formation and dissolution are often the main controls on many processes in the subterranean estuary, and can control the release of other trace metals from SGD (Charette and Sholkovitz, 2006; Pan et al., 2019). The dissolved Fe concentrations in the groundwater were higher than dissolved Mn concentrations (Figure 4.33), and groundwater Fe showed significant correlations with other metals such as Cr, V, U, Pb, Cu, and Re ($p < 0.05$, Table B.5), suggesting that the mobility of these trace elements from groundwater was driven by Fe cycling. Dissolved Mn was significantly correlated with Ba and Cs ($p < 0.05$, Table B.5), indicating that the Mn hydroxide cycle was the driver for the release of these trace elements from the coastal aquifer. Arsenic has been shown to be mobilized by both the dissolution of Mn and Fe hydroxides (e.g., Huq et al., 2020), and therefore it is unsurprising that it was well correlated with both dissolved Mn and Fe ($p < 0.05$, Table B.5).

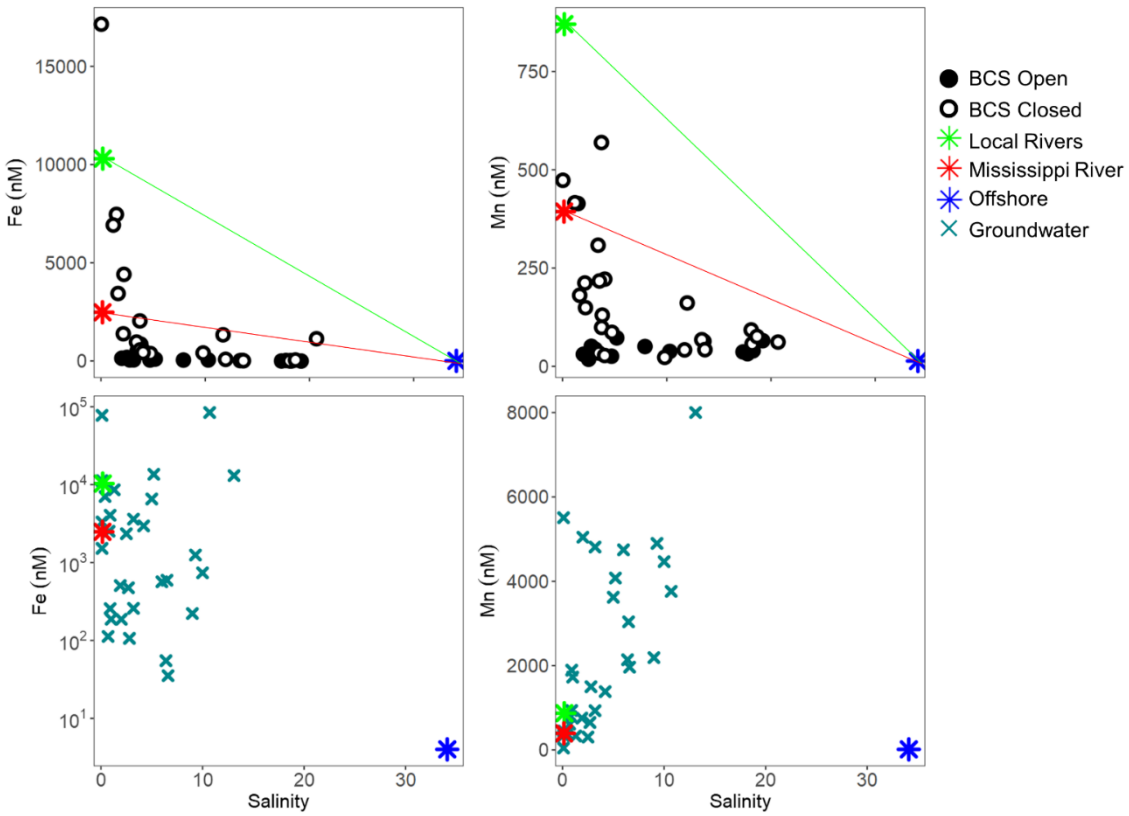

Figure 4.33 *Mn and Fe along the salinity gradient for surface and groundwater.*

The red and green lines correspond to the conservative mixing lines when the BCS was open and closed, respectively. River and offshore endmembers are shown on the groundwater plots. Note the logarithmic axis on the Fe groundwater plot.

4.5.7.4 V

In the Mississippi Sound, when the BCS was closed, the average concentration of V was 19 nM, and average dissolved V in seawater is between 32 – 36 nM (e.g., Ho et al., 2018). The concentrations of V for both the local rivers and the Mississippi River have large ranges, aligning with previous studies (e.g., Shiller, 1997). When the BCS was open, there appeared to be excess V above conservative mixing of offshore water and the Mississippi River (Figure 4.34). However, when the BCS was closed, there seems to be

depletion of V, except for samples collected in the fall. Depletions and enrichments in V have been noted in the Mississippi Sound before (e.g., Ho et al., 2019), where the enrichments were higher than the Mississippi River, Pearl River, SLB, and the Bight (Shiller, 1997; Shim, 2011; Shim et al., 2017). Previous studies have reported that V can experience removal in bottom waters due to oxygen depletion (e.g., Shiller and Mao, 1999), with other possible influences such as biological uptake, adsorption onto particles, and sedimentary uptake (Ho et al., 2019). Since the low V occurred in the winter and spring, biological uptake is not considered a primary driving factor, as this is when chlorophyll a (a proxy for primary production) is at its lowest. The highest river inputs do occur during the spring and winter though (Ho et al., 2019), which could increase SPM input into the Sound, causing an increase in particle adsorption. However, if this was the case, we would also expect that the BCS input would cause an increase in SPM as well, leading to a V depletion, but this is not observed.

The highest concentrations of V in the Sound occur in the summer and fall, with the lowest concentrations in the spring. This aligns with the seasonal change of SGD seen in Chapter 2, where the summer and fall had the highest discharge rates. Similar seasonal patterns of V have been observed before (Ho et al., 2019), with the explanation that sediments switch from sink to source due to changes in DO (e.g., Ho et al., 2019), pH (e.g., O'Connor et al., 2015), organic complexation (e.g., Beck et al., 2008), or V speciation changes driven by microbial processes (e.g., Huang et al., 2015). Another potential explanation is SGD, which Ho et al. (2019), suggested to be the cause of the sediment switch in the bottom waters of the Mississippi Sound. Further investigation into

how SGD may play a role in this sedimentary switch is necessary, including addressing the input of RSGD.

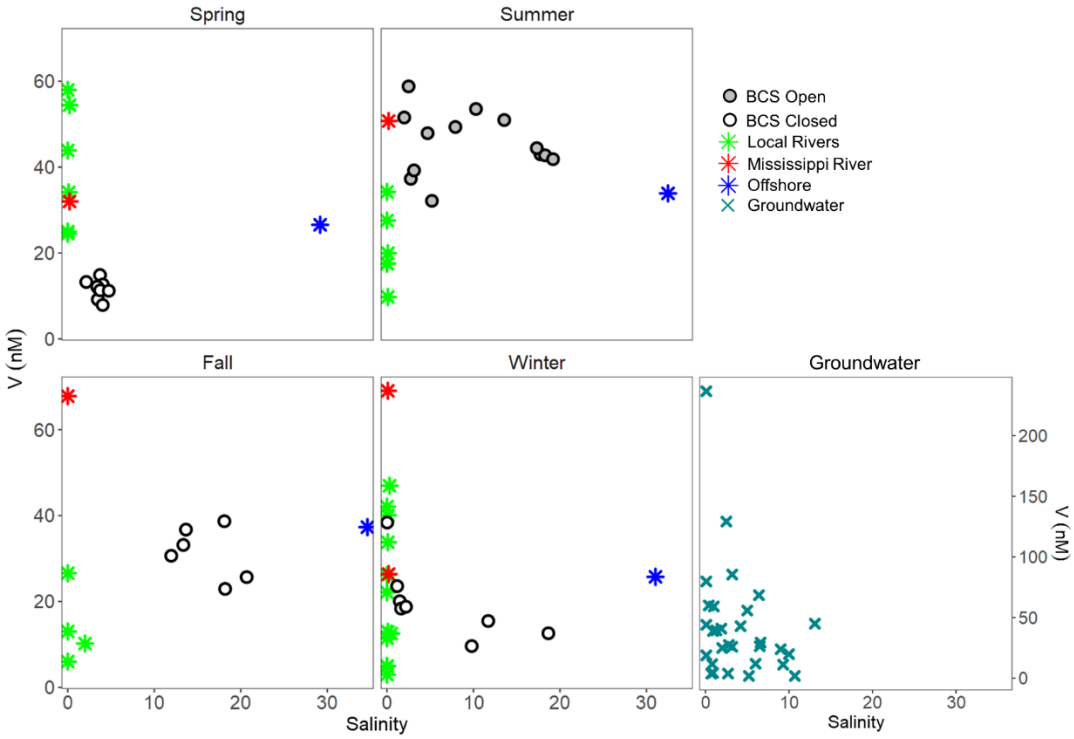

Figure 4.34 *V concentrations along the salinity gradient for the seasons in surface water and in groundwater.*

River and offshore endmember concentrations are denoted by the stars.

4.5.7.5 As, Cd, Cr, Cu, Pb, and Ni

There are various trace metals that are considered harmful in large amounts in the environment. In particular, arsenic (As), cadmium (Cd), chromium (Cr), copper (Cu), lead (Pb), and nickel (Ni), have all been documented to have adverse effects on the coastal environment (e.g., Conrad et al., 2019; Pan and Wang, 2012), including on oyster reef environments (e.g., Lu et al., 2017; Wang et al., 2018). Copper as well can also play

a vital role in the larval stage of oysters (e.g., Weng et al., 2019). While Cu is a necessary trace element for healthy oysters, high levels can lead to toxicity and mortality (Cao et al., 2019; Pinel, 2021).

The trace elements Cu, Cr, Pb, and Ni all have a similar trend of high concentrations at low salinities with declining concentrations offshore (Figure 4.35). There was removal along the mixing curves for Pb and Cr. Groundwater concentrations of all elements had wide ranges, from near zero to the highest observed concentrations (Figure 4.35).

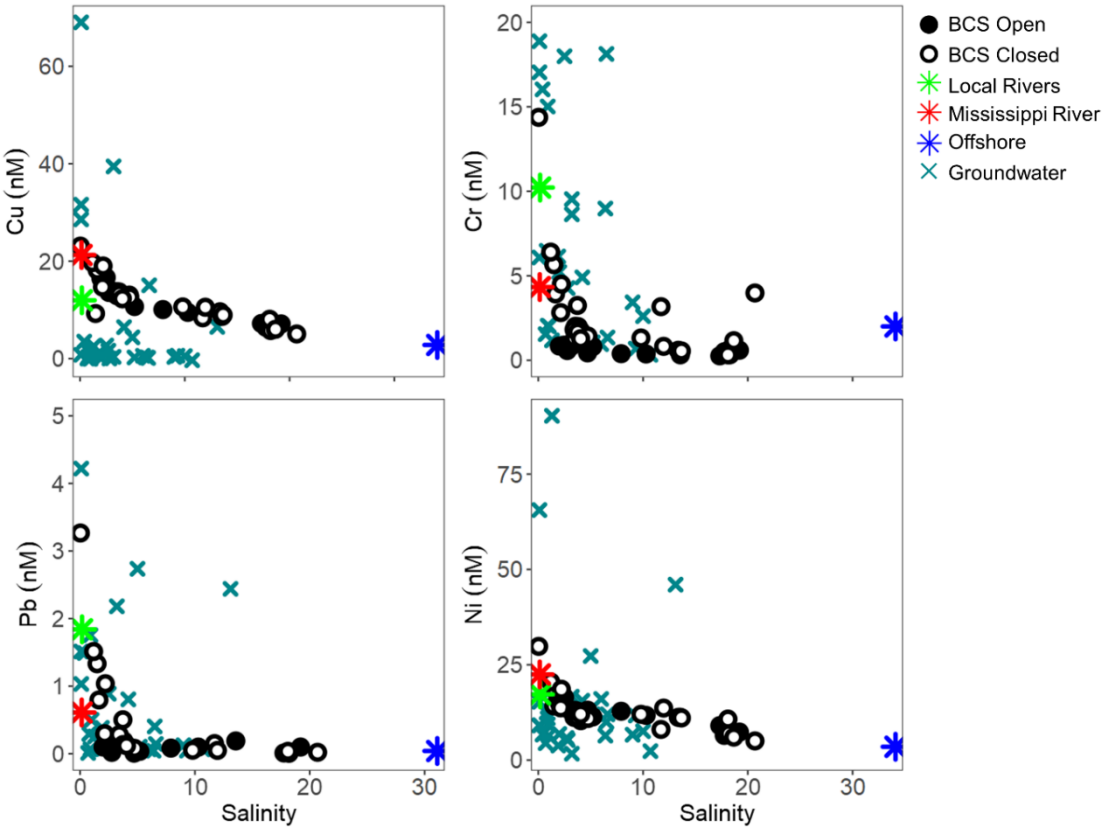

Figure 4.35 *Surface and groundwater Cu, Cr, Pb, and Ni along the salinity gradient.*

Arsenic concentrations had excess at mid-salinities, which coincides with high groundwater concentrations (Figure 4.36). Even when the BCS was open, there was excess As that cannot be accounted for by just Mississippi River water. Therefore, this excess was likely due to input of SGD. Cadmium concentrations also experienced excess at mid-salinities, but the groundwater concentrations were relatively low, indicating that other processes were occurring along the salinity gradient (Figure 4.36). One possibility is Cd desorption from particles in the water column or sediments with increasing salinity. Similar trends in Cd have been seen before (e.g., Du Laing et al., 2008; Waeles et al., 2004) and our trends may be due to particle desorption at higher salinities (Waeles et al., 2004).

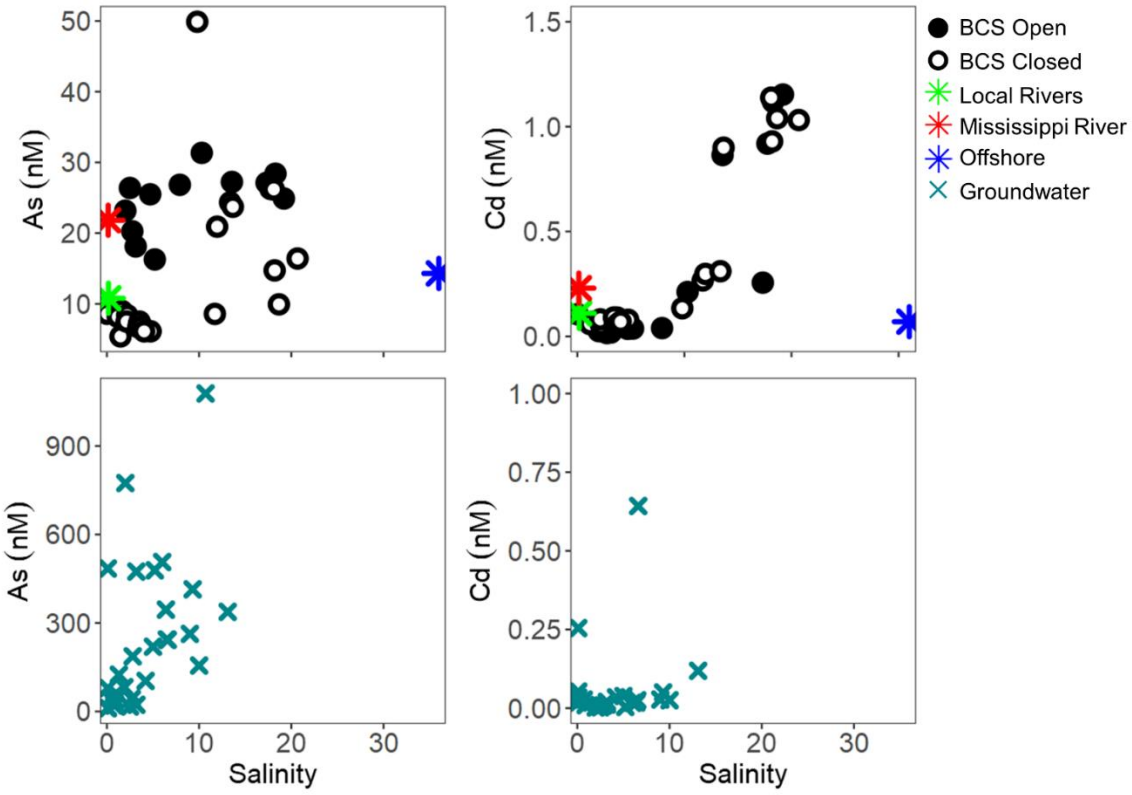

Figure 4.36 *Surface and groundwater As and Cd concentrations along the salinity gradient.*

4.6 Conclusion

Multi-year spatial and temporal surveys provided insight into the factors that affect the geochemical makeup of the Mississippi Sound. This study investigated the importance of SGD and river sources on an estuary that can experience extreme shifts in geochemical makeup. Rapid changes can cause organisms that cannot adapt quickly to experience mortality. During this study period, the Bonnet Carré Spillway was open for an unprecedented 123 days in 2019, causing inputs of water that had characteristics similar to the Mississippi River. The salinity levels throughout the western Sound dropped drastically, and the input of nutrients, primarily NO_x, caused the Sound chemistry to switch from a nitrogen limiting to a phosphorus limiting system.

From the radon surveys, we were able to calculate the SGD flux for the total Sound, the western, central, and eastern Sound, and for the wet and dry season. The western Sound, which had the highest radon anomalies also had a significantly higher SGD flux than the rest of the Sound. When comparing the total water fluxes of the local rivers, the BCS, FSGD, and RSGD, the BCS and local rivers dominated. However, the high concentration of constituents in the groundwater allowed the SGD to rival these surface water fluxes, and even dominate PO_4 and NH_4^+ nutrient exports to the Sound. During periods of low river flow, SGD most likely dominates all nutrient input. The opening and closing of the BCS influenced nutrient concentrations across the Sound, and affected how high of a risk the system was to eutrophication. When the BCS was closed, the Sound had a low RQ for TDN, and high along the coast for TDP, indicating that SGD is extremely important for phosphorus input. However, when the BCS was open, the RQ for TDN was elevated in the core of the infiltrating water, and ended up causing an algae

bloom that led to hypoxic conditions across the Sound. Trace elements were influenced mainly by either local rivers or the Mississippi River, though several trace elements such as Ba, Re, and V seem to have some influence from SGD as well. In the groundwater, the dissolution of Fe and Mn hydroxides seems to control the majority of metal distributions.

To determine why SGD fluxes changed spatially, we investigated seismic and sediment data from across the Sound. From the paleochannel and surface sediment data, we could link several near shore paleovalleys to SGD input, and determined that small grained surficial sediments can play a role in confining SGD to the subsurface. This may help to explain not only SGD spatial coverage in the Sound, but could also be important for future SGD work along other paleovalley influenced regions such as other passive margins.

Important questions remaining for this work are to determine the role of SGD on trace metals fluxes to the Sound. The recycling of the metals may be very important, especially metals such as Cu that can have both a positive and negative impact on oyster reef communities.

4.7 References

Adcock, D., 2019. Stratigraphic Characterization of the Pleistocene Paleodrainage Network in the Western Mississippi Sound. Mississippi State University. Masters Thesis. Mississippi State University.

Anbar, A.D., Creaser, R.A., Papanastassiou, D.A., Wasserburg, G.J., 1992. Rhenium in seawater: confirmation of generally conservative behavior. Geochim. Cosmochim. Acta 56, 4099–4103.

Attisano, K. K., Santos, I. R., Ferreira De Andrade, C. F., Lopes De Paiva, M., Milani, I. C. B., Niencheski, L. F. H., 2013. Submarine groundwater discharge revealed by radium isotopes (Ra-223 and Ra-224) near a paleochannel on the southern Brazilian continental shelf. Brazilian J. Oceanogr. 61, 195–200.

Beck, M., Dellwig, O., Schnetger, B., Brumsack, H.-J., 2008. Cycling of trace metals (Mn, Fe, Mo, U, V, Cr) in deep pore waters of intertidal flat sediments. Geochim. Cosmochim. Acta 72, 2822–2840. https://doi.org/10.1016/j.gca.2008.04.013.

Becker, L.A. 2000. Effect size [online]. Available from URL: https://www.uv.es/~friasnav/EffectSizeBecker.pdf [Accessed 2022 September 30]

Bianchi, T. S., J. R. Pennock, R. R. Twilley. 1999. Biogeochemistry of Gulf of Mexico Estuaries. John Wiley & Sons.

Brewer, P.G., Spencer, D.W., Robertson, D.E., 1972. Trace element profiles from the Geosecs-II test station in the Sargasso Sea. Earth Planet. Sci. Lett. 16, 111–116.

Bricker, S.B., C.G. Clement, D.E. Pirhalla, S.P. Orlando, and D.R.G. Farrow. 1999. National Estuarine Eutrophication Assessment: Effects of Nutrient Enrichment in the Nation's Estuaries. NOAA, National Ocean Service, Special Projects Office and the National Centers for Coastal Ocean Science. Silver Spring, MD: 71 pp.

Bonnet Carr´e Spillway Overview, 2019. 2019 Bonnet Carr´e Spillway Monitoring Update. Northern Gulf Institute. Mississippi State University, 2019, June 21). https://www.ngi.msstate.edu/portal/media/docs/2019/2019_Bonnet_Carre_Spillway_ Overview _-_June_21_2019_-_Final_Version_v2.pdf.

Bouchard, C., 2021. Exploring the Influence of Diurnal Forcing on Tidal Inlet Exchange and the Impact on the movement of Oxygen Depleted Waters in the Mississippi Sound and Bight Region. Masters thesis, Univ. of Southern Mississippi.

Burnett, W.C., Aggarwal, P.K., Aureli, A., Bokuniewicz, H., Cable, J.E., Charette, M.A., Kontar, E., Krupa, S., Kulkarni, K.M., Loveless, A., Moore, W.S., Oberdorfer, J.A., Oliveira, J., Ozyurt, N., Povinec, P., Privitera, A.M.G., Rajar, R., Ramessur, R.T., Scholten, J., Stieglitz, T., Taniguchi, M., Turner, J. V, 2006. Quantifying submarine groundwater discharge in the coastal zone via multiple methods. Sci. Total Environ. 367, 498–543. https://doi.org/10.1016/j.scitotenv.2006.05.009

Burnett, W.C., Bokuniewicz, H., Huettel, M., Moore, W.S., Taniguchi, M., 2003. Groundwater and pore water inputs to the coastal zone. Biogeochemistry 66, 3–33. https://doi.org/10.1023/B:BIOG.0000006066.21240.53

Byrd, J., 2019. Fishery Disaster Due to the Opening of the Bonnet Carré Spillway. Water Log 39:4, 10-12. http://masglp.olemiss.edu/waterlog/pdf/dec19/wl39.4_article3.pdf

Caffrey, J., Younos, T., Connor, M.S., Kohlhepp, G., Robertson, D.M., Sharp, J.H.,

Whitall, D., 2007. Nutrient Requirements for the National Water Quality Monitoring Network for US Coastal Waters and their Tributaries. National Water Quality Monitoring Network.
Cao, R., Zhang, T., Li, X., Zhao, Y., Wang, Q., Yang, D., Qu, Y., Liu, H., Dong, Z., Zhao, J., 2019. Seawater acidification increases copper toxicity: A multi-biomarker approach with a key marine invertebrate, the Pacific Oyster Crassostrea gigas. Aquat. Toxicol. 210, 167–178. https://doi.org/10.1016/J.AQUATOX.2019.03.002
Changnon, S. A., Huff, F. A., Hsu, C. F., 1988. Relations between precipitation and shallow groundwater in Illinois. J. Clim. 1, 1239–-1250.
Charette, M.A., Sholkovitz, E.R., Hansel, C.M., 2005. Trace element cycling in a subterranean estuary: Part 1. Geochemistry of the permeable sediments. Geochim. Cosmochim. Acta, 69(8), pp.2095-2109. https://doi.org/10.1016/j.gca.2004.10.024
Charette, M.A., Sholkovitz, E.R., 2006. Trace element cycling in a subterranean estuary: Part 2. Geochemistry of the pore water. Geochim. Cosmochim. Acta 70, 811–826. https://doi.org/10.1016/j.gca.2005.10.019
Cobb, M. and Blain, C.A., 2002. A coupled hydrodynamic-wave model for simulating wave and tidally-driven 2D circulation in inlets. In Estuarine and Coastal Modeling (2001) (pp. 725-742).
Coen, L.D., Brumbaugh, R.D., Bushek, D., Grizzle, R., Luckenbach, M.W., Posey, M.H., Powers, S.P., Tolley, S.G., 2007. Ecosystem services related to oyster restoration. Mar. Ecol. Prog. Ser. 341, 303–307. https://doi.org/10.3354/MEPS341303
Coffey, M., Dehairs, F., Collette, O., Luther, G., Church, T., Jickells, T., 1997. The behaviour of dissolved barium in estuaries. Estuar. Coast. Shelf Sci. 45, 113–121. https://doi.org/10.1006/ecss.1996.0157.
Conrad, S.R., Santos, I.R., White, S., Sanders, C.J., 2019. Nutrient and Trace Metal Fluxes into Estuarine Sediments Linked to Historical and Expanding Agricultural Activity (Hearnes Lake, Australia). Estuaries and Coasts 42, 944–957. https://doi.org/10.1007/S12237-019-00541-1/FIGURES/8
Dalai, T.K., Nishimura, K., Nozaki, Y., 2005. Geochemistry of molybdenum in the Chao Phraya River estuary, Thailand: role of suboxic diagenesis and porewater transport. Chem. Geol. 218, 189–202. https://doi.org/10.1016/j.chemgeo.2005.01.002.
Danish, M., Tripathy, G.R., Mitra, S., Rout, R.K., Raskar, S., 2021. Non-conservative removal of dissolved rhenium from a coastal lagoon: Clay adsorption versus biological uptake. Chem. Geol., 580, 120378.
Davenport, F.V. and Diffenbaugh, N.S., 2021. Using machine learning to analyze physical causes of climate change: A case study of US Midwest extreme precipitation. Geophysical Research Letters, 48(15), p.e2021GL093787.
Dellwig, O., Beck, M., Lemke, A., Lunau, M., Kolditz, K., Schnetger, B., Brumsack, H.-J., 2007. Non-conservative behaviour of molybdenum in coastal waters: coupling geochemical, biological, and sedimentological processes. Geochim. Cosmochim. Acta 71, 2745–2761. https://doi.org/10.1016/j.gca.2007.03.014.
Dortch, M.S., Zakikhani, M., Noel, M.R., Kim, S. C., 2007. Application of a Water

Quality Model to Mississippi Sound to Evaluate Impacts of Freshwater Diversions. US Army Corps of Engineers (2007) [online] Available from: https://apps.dtic.mil/docs/citations/ADA472574, Accessed 11th Oct 2022.

Douglas, A.R., Murgulet, D., Peterson, R.N., 2020. Submarine groundwater discharge in an anthropogenically disturbed, semi-arid estuary. J. Hydrol. 580, 124369. https://doi.org/10.1016/J.JHYDROL.2019.124369

Du Laing, G., De Vos, R., Vandecasteele, B., Lesage, E., Tack, F.M., Verloo, M.G., 2008. Effect of salinity on heavy metal mobility and availability in intertidal sediments of the Scheldt estuary. Estuarine, Coastal and Shelf Science, 77(4), 589-602.

Dulaiova, H., Camilli, R., Henderson, P.B., Charette, M.A., 2010. Coupled radon, methane and nitrate sensors for large-scale assessment of groundwater discharge and non-point source pollution to coastal waters. J. Environ. Radioact. 101, 553–563. https://doi.org/10.1016/j.jenvrad.2009.12.004

Dzwonkowski, B., Fournier, S., Reager, J.T., Milroy, S., Park, K., Shiller, A.M., Greer, A.T., Soto, I., Dykstra, S.L., Sanial, V., 2018. Tracking sea surface salinity and dissolved oxygen on a river-influenced, seasonally stratified shelf, Mississippi Bight, northern Gulf of Mexico. Cont. Shelf Res. 169, 25–33. https://doi.org/10.1016/j.csr.2018.09.009

Eleuterius, C.K., 1978. Classification of Mississippi Sound as to Estuary Hydrological Type. GulfResearch Reports 6, 185–187. https://doi.org/10.18785/grr.0602.12

Elliott, M., Day, J.W., Ramachandran, R., Wolanski, E., 2019. Chapter 1 – a synthesis: what future for coasts, estuaries, deltas, and other transitional habitats in 2050 and beyond? In: Wolanski, E., Day, J.W., Elliott, M., Ramachandran, R. (Eds.), Coasts and Estuaries: the Future. Elsevier, Amsterdam, pp. 1–28. Escobar, H., 2019. https://doi.org/10.1016/B978-0-12-814003-1.00001-0

Eltahir, E. A. B. and Yeh, P. A. J. F. 1999. On the asymmetric response of aquifer water level to floods and droughts in Illinois. Wat. Resour. Res. 35, 1199–1217.

Gal, N.S., Wallace, D.J., Miner, M.D., Hollis, R.J., Dike, C., Flocks, J.G., 2021. Influence of antecedent geology on the Holocene formation and evolution of Horn Island, Mississippi, USA. Mar. Geol. 431, 106375. https://doi.org/10.1016/J.MARGEO.2020.106375

Garcia-Solsona, E., Garcia-Orellana, J., Masqué, P., Dulaiova, H., 2008. Uncertainties associated with 223Ra and 224Ra measurements in water via a Delayed Coincidence Counter (RaDeCC). Mar. Chem. 109, 198–219. https://doi.org/10.1016/J.MARCHEM.2007.11.006

Gledhill, J.H., Barnett, A.F., Slattery, M., Willett, K.L., Easson, G.L., Otts, S.S. and Gochfeld, D.J., 2020. Mass mortality of the Eastern Oyster Crassostrea virginica in the western Mississippi Sound following unprecedented Mississippi River flooding in 2019. Journal of Shellfish Research, 39(2), pp.235-244.

Gore, R.H., 1992. Gulf of Mexico: A Treasury of Resources in the American Mediterranean. Pineapple Press, Inc., Sarasota, FL.

Goswami, V., Singh, S.K., Bhushan, R., 2012. Dissolved redox sensitive elements, Re, U and Mo in intense denitrification zone of the Arabian Sea. Chem. Geol., 291, 256-268.

Griffin, C., A. Kaufman, and W. Broecker. 1963. Delayed coin-cidence counter for the assay of actinon and thoron. J. Geo-phys. Res. 68:1749-1757.
Hernando, M.D., Mezcua, M., Fernández-Alba, A.R., Barceló, D., 2006. Environmental risk assessment of pharmaceutical residues in wastewater effluents, surface waters and sediments. Talanta 69, 334–342. https://doi.org/10.1016/J.TALANTA.2005.09.037
Ho, P., Lee, J.-M., Heller, M.I., Lam, P.J., Shiller, A.M., 2018. The distribution of dissolved and particulate Mo and V along the U.S. GEOTRACES East Pacific Zonal Transect (GP16): the roles of oxides and biogenic particles in their distributions in the oxygen deficient zone and the hydrothermal plume. Mar. Chem. 201, 242–255. https://doi. org/10.1016/j.marchem.2017.12.003.
Ho, P., Shim, M.J., Howden, S.D., Shiller, A.M., 2019. Temporal and spatial distributions of nutrients and trace elements (Ba, Cs, Cr, Fe, Mn, Mo, U, V and Re) in Mississippi coastal waters: Influence of hypoxia, submarine groundwater discharge, and episodic events. Cont. Shelf Res. 175, 53–69. https://doi.org/10.1016/j.csr.2019.01.013
Hode, L., 2019. Establishing the Role of the Mississippi-Alabama Barrier Islands in Mississippi Sound and Bight Circulation Using Observational Data Analysis and a Coastal Model. Dissertation. University of Southern Mississippi.
Hollis, R.J., Wallace, D.J., Miner, M.D., Gal, N.S., Dike, C., Flocks, J.G., 2019. Late Quaternary evolution and stratigraphic framework influence on coastal systems along the north-central Gulf of Mexico, USA. Quat. Sci. Rev. 223, 105910. https://doi.org/10.1016/J.QUASCIREV.2019.105910
Howarth, R.W., Marino, R. and Cole, J.J., 1988. Nitrogen fixation in freshwater, estuarine, and marine ecosystems. 2. Biogeochemical controls. Limnology and Oceanography, 33(4), 688-701.
Huang, J.-H., Huang, F., Evans, L., Glasauer, S., 2015. Vanadium: global (bio)geochem-istry. Chem. Geol. 417, 68–89. https://doi.org/10.1016/j.chemgeo.2015.09.019.
Huq, M.E., Fahad, S., Shao, Z., Sarven, M.S., Khan, I.A., Alam, M., Saeed, M., Ullah, H., Adnan, M., Saud, S. and Cheng, Q., 2020. Arsenic in a groundwater environment in Bangladesh: Occurrence and mobilization. J. Environ. Manage., 262, 110318.
Joung, D.J., Shiller, A.M., 2014. Dissolved barium behavior in Louisiana Shelf waters affected by the Mississippi/Atchafalaya River mixing zone. Geochim. Cosmochim. Acta 141, 303–313. https://doi.org/10.1016/j.gca.2014.06.021
Kennish, M.J., 2002. Environmental threats and environmental future of estuaries. Environmental conservation, 29(1), 78-107.
Kim, G., Ryu, J.-W., Yang, H.-S., Yun, S.-T., 2005. Submarine groundwater discharge (SGD) into the Yellow Sea revealed by 228Ra and 226Ra isotopes: Implications for global silicate fluxes. Earth Planet. Sci. Lett. 237, 156–166. https://doi.org/10.1016/J.EPSL.2005.06.011
Knee, K.L., Crook, E.D., Hench, J.L., Leichter, J.J., Paytan, A., 2016. Assessment of Submarine Groundwater Discharge (SGD) as a Source of Dissolved Radium and Nutrients to Moorea (French Polynesia) Coastal Waters. Estuaries and Coasts 39, 1651–1668. https://doi.org/10.1007/S12237-016-0108-Y/FIGURES/6

Kroeger, K.D., Swarzenski, P.W., Greenwood, Wm.J., Reich, C., 2007. Submarine groundwater discharge to Tampa Bay: nutrient fluxes and biogeochemistry of the coastal aquifer. Mar. Chem. 104, 85–97. https://doi.org/10.1016/j.

Ku, T. L., Knauss, K. G., Mathieu, G. G., 1977. Uranium in the open ocean: concentration and isotopic composition. Deep-Sea Research 24, 1005-1017.

Lee, A., 2019. Bonnet Carre spillway opening is causing a fisheries disaster in Mississippi, governor says, SunHerald. published on June 7. https://www.sunherald.com/news /local/article231300853.html#storylink¼cpy.

Linhoss, A., Mickle, P., 2022. A Field Validated Model of Temporal Variability in Oyster Habitat Suitability. Front. Mar. Sci. 9, 40. https://doi.org/10.3389/FMARS.2022.778936/BIBTEX

Lowe, M.R., Sehlinger, T., Soniat, T.M., Peyre, M.K.L., 2017. Interactive Effects of Water Temperature and Salinity on Growth and Mortality of Eastern Oysters, Crassostrea virginica: A Meta-Analysis Using 40 Years of Monitoring Data. https://doi.org/10.2983/035.036.0318 36, 683–697. https://doi.org/10.2983/035.036.0318

Lu, G.Y., Ke, C.H., Zhu, A., Wang, W.X., 2017. Oyster-based national mapping of trace metals pollution in the Chinese coastal waters. Environ. Pollut. 224, 658–669. https://doi.org/10.1016/J.ENVPOL.2017.02.049

McConnaughey, J., 2019. NOAA: 279 Dolphins Dead on Gulf Coast, Triple Usual Number. Associated Press. June 14. https://apnews.com/d18ced7257f34d5ba84 6fa3c08038048.

McCoy, C.A., Corbett, D.R., 2009. Review of submarine groundwater discharge (SGD) in coastal zones of the Southeast and Gulf Coast regions of the United States with management implications. J. Environ. Manage. 90, 644–651. https://doi.org/10.1016/j.jenvman.2008.03.002

McCoy, C., Viso, R., Peterson, R.N., Libes, S., Lewis, B., Ledoux, J., Voulgaris, G., Smith, E., Sanger, D., 2011. Radon as an indicator of limited cross-shelf mixing of submarine groundwater discharge along an open ocean beach in the South Atlantic Bight during observed hypoxia. Cont. Shelf Res. 31, 1306–1317. https://doi.org/10.1016/j.csr.2011.05.009

Michael, H.A., Mulligan, A.E., Harvey, C.F., 2005. Seasonal oscillations in water exchange between aquifers and the coastal ocean. Nat. 2005 4367054 436, 1145–1148. https://doi.org/10.1038/nature03935

Mohtar, W.H.M.W., Maulud, K.N.A., Muhammad, N.S., Sharil, S., Yaseen, Z.M., 2019. Spatial and temporal risk quotient based river assessment for water resources management. Environmental Pollution, 248, 133-144.

Moore, W.S. 2000. Determining coastal mixing rates using radium iso- topes. Continental Shelf Research 20 (15): 1993–2007.

Moore, W.S., Arnold, R., 1996. Measurement of ^{223}Ra and ^{224}Ra in coastal waters using a delayed coincidence counter. J. Geophys. Res. 101, 1321–1329.

Moore, W.S., Shaw, T.J., 1998. Chemical signals from submarine fluid advection onto the continental shelf. J. Geophys. Res. Ocean. 103, 21543–21552. https://doi.org/10.1029/98JC02232

Moore, W.S., Shaw, T.J., 2008. Fluxes and behavior of radium isotopes, barium, and

uranium in seven Southeastern US rivers and estuaries. Mar. Chem. 108, 236–254. https://doi.org/10.1016/j.marchem.2007.03.004.
Montiel, D., Lamore, A., Stewart, J., Dimova, N., 2019. Is Submarine Groundwater Discharge (SGD) Important for the Historical Fish Kills and Harmful Algal Bloom Events of Mobile Bay? Estuaries and Coasts 42, 470–493. https://doi.org/10.1007/s12237-018-0485-5
Morgan, L.M., Rakocinski, C.F., 2022. Predominant factors limiting the recovery of the eastern oyster (Crassostrea virginica) in western Mississippi Sound, USA. Estuar. Coast. Shelf Sci. 264, 107652. https://doi.org/10.1016/J.ECSS.2021.107652
Mulligan, A.E., Evans, R.L., Lizarralde, D., 2007. The role of paleochannels in groundwater/seawater exchange. J. Hydrol. 335, 313–329. https://doi.org/10.1016/J.JHYDROL.2006.11.025
National Oceanic and Atmospheric Administration (NOAA). 1997. NOAA's Estuarine Eutrophication Survey, Volume 4: Gulf of Mexico Region. Silver Spring, MD: Office of Ocean Resources Conservation and Assessment. 77 pp.
Neff, J.M., 1997. Ecotoxicology of arsenic in the marine environment. Environ. Toxicol. Chem., 16(5), 917-927.
Neuzil, C.E., 1986. Groundwater Flow in Low-Permeability Environments. Water Resour. Res. 22, 1163–1195. https://doi.org/10.1029/WR022i008p01163
O'Connor, A.E., Luek, J.L., McIntosh, H., Beck, A.J., 2015. Geochemistry of redox-sensitive trace elements in a shallow subterranean estuary. Mar. Chem. 172, 70–81. https://doi.org/10.1016/j.marchem.2015.03.001.
Owens, S.A., Buesseler, K.O., Sims, K.W.W., 2011. Re-evaluating the 238U-salinity relationship in seawater: implications for the 238U-234Th disequilibrium method. Mar. Chem. 127, 31–39. https://doi.org/10.1016/j.marchem.2011.07.005.
Pace, S.M., Poussard, L.M., Powell, E.N., Ashton-Alcox, K.A., Kuykendall, K.M., Solinger, L.K., Hemeon, K.M., Soniat, T.M., 2020. Dying, Decaying, and Dissolving into Irrelevance: First Direct in-the-Field Estimate of Crassostrea virginica Shell Loss—a Case History from Mississippi Sound. Journal of Shellfish Research, 30(2), 245-256. https://doi.org/10.2983/035.039.0206 39
Pan, K., Wang, W.X., 2012. Trace metal contamination in estuarine and coastal environments in China. Sci. Total Environ. 421–422, 3–16. https://doi.org/10.1016/J.SCITOTENV.2011.03.013
Parra, S.M., Sanial, V., Boyette, A.D., Cambazoglu, M.K., Soto, I.M., Greer, A.T., Chiaverano, L.M., Hoover, A., Dinniman, M.S., 2020. Bonnet Carré Spillway freshwater transport and corresponding biochemical properties in the Mississippi Bight. Cont. Shelf Res. 199, 104114. https://doi.org/10.1016/J.CSR.2020.104114
Pinel, R., 2021. Impacts of Water Quality and Reef Restoration on Oysters in Naples Bay, Florida, with a Focus on Copper Pollution (Doctoral dissertation, Florida Gulf Coast University).
Rabalais, N.N. and Turner, R.E. (2001) Hypoxia in the Northern Gulf of Mexico: Description, Causes and Change. In: Rabalais, N.N. and Turner, R.E., Eds., Coastal Hypoxia: Consequences for Living Resources and Ecosystems, Coastal and Estuarine Studies 58, American Geophysical Union, Washington DC, 1-36. http://dx.doi.org/10.1029/CE058p0001

Raychaudhuri, S., 2008. Introduction to Monte Carlo simulation. In Proceedings of the 2008 Winter Simulation Conference, Miami, FL, USA, 7–10 December 2008; pp. 91–100.
Renken, R.A., 1998. Ground Water Atlas of the United States: Segment 5, Arkansas, Louisiana, Mississippi (No. 730-F, pp. F1-F28). US Geological Survey.
Rodellas, V., Garcia-Orellana, J., Masqué, P., Font-Muñoz, J.S., 2015. The influence of sediment sources on radium-derived estimates of Submarine Groundwater Discharge. Mar. Chem. 171. https://doi.org/10.1016/j.marchem.2015.02.010
Rodellas, V., Garcia-Orellana, J., Trezzi, G., Masqué, P., Stieglitz, T.C., Bokuniewicz, H., Cochran, J.K., Berdalet, E., 2017. Using the radium quartet to quantify submarine groundwater discharge and porewater exchange. Geochim. Cosmochim. Acta 196, 58–73. https://doi.org/10.1016/J.GCA.2016.09.016
Roy, E.D., Smith, E.A., Bargu, S., White, J.R., 2016. Will Mississippi River diversions designed for coastal restoration cause harmful algal blooms? Ecol. Eng. 91, 350–364. https://doi.org/10.1016/J.ECOLENG.2016.02.030
Sanders, C.J., Santos, I.R., Barcellos, R., Silva Filho, E.V., 2012. Elevated concentrations of dissolved Ba, Fe and Mn in a mangrove subterranean estuary: consequence of sea level rise?. Cont. Shelf Res., 43, 86-94.
Sanial, V., Moore, W.S., Shiller, A.M., 2021. Does a bottom-up mechanism promote hypoxia in the Mississippi Bight? Mar. Chem. 235, 104007. https://doi.org/10.1016/J.MARCHEM.2021.104007
Sanial, V., Shiller, A.M., Joung, D.J., Ho, P., 2019. Extent of Mississippi River water in the Mississippi Bight and Louisiana Shelf based on water isotopes. Estuar. Coast. Shelf Sci. 226, 106196. https://doi.org/10.1016/j.ecss.2019.04.030
Santos, I.R., Burnett, W.C., Misra, S., Suryaputra, I.G.N.A., Chanton, J.P., Dittmar, T., Peterson, R.N., Swarzenski, P.W., 2011. Uranium and barium cycling in a salt wedge subterranean estuary: The influence of tidal pumping. Chem. Geol. 287, 114–123. https://doi.org/10.1016/j.chemgeo.2011.06.005
Santos, I.R., Dimova, N., Peterson, R.N., Mwashote, B., Chanton, J., Burnett, W.C., 2009. Extended time series measurements of submarine groundwater discharge tracers (^{222}Rn and CH_4) at a coastal site in Florida. Mar. Chem. 113, 137–147. https://doi.org/10.1016/J.MARCHEM.2009.01.009
Santos, I.R., Eyre, B.D., Huettel, M., 2012. The driving forces of porewater and groundwater flow in permeable coastal sediments: A review. Estuar. Coast. Shelf Sci. 98, 1–15. https://doi.org/10.1016/J.ECSS.2011.10.024
Savoie, A., 2020. Freshwater Endmembers Impacting Carbonate Chemistry in the Mississippi Sound. Master's Thesis. The University of Southern Mississippi.
Sawyer, W.B., Vaughan, C., Lavoie, D., Furukawa, Y., Carnaggio, N., Maclean, J., Populis, E., 2001. Northern Gulf Littoral Initiative (NGLI), Geology and Physical Properties of Marine Sediments in the N.E. Gulf of Mexico: Data Report.
Schulte, D.M., Burke, R.P. and Lipcius, R.N., 2009. Unprecedented restoration of a native oyster metapopulation. Science, 325(5944), 1124-1128.
Shiller, A.M., 1997. Dissolved trace elements in the Mississippi River: seasonal, inter-annual, and decadal variability. Geochim. Cosmochim. Acta 61, 4321–4330. https:// doi.org/10.1016/s0016-7037(97)00245-7.

Shiller, A.M., Mao, L.J., 1999. Dissolved vanadium on the Louisiana Shelf: effect of oxygen depletion. Cont. Shelf Res. 19, 1007–1020. https://doi.org/10.1016/s0278-4343(99)00005-9.
Shiller, A.M., Stephens, T.H., 2005. Microbial manganese oxidation in the lower Mississippi River: methods and evidence. Geomicrobiol. J. 22, 117–125. https://doi. org/10.1080/01490450590945924.
Shim, M.J., 2011. Dissolved and Collidal Element Transport through the Coastal Transition Zone (Ph.D. Dissertation). The University of Southern Mississippi, Hattiesburg, Mississippi.
Shim, M.J., Cai, Y., Guo, L., Shiller, A.M., 2017. Floodplain effects on the transport of dissolved and colloidal trace elements in the East Pearl River, Mississippi. Hydrol. Process. 31, 1086–1099. https://doi.org/10.1002/hyp.11093.
Shim, M.J., Swarzenski, P.W., Shiller, A.M., 2012. Dissolved and colloidal trace elements in the Mississippi River delta outflow after Hurricanes Katrina and Rita. Cont. Shelf Res. 42, 1–9. https://doi.org/10.1016/j.csr.2012.03.007.
Sigleo, A.C., Frick, W.E., 2007. Seasonal variations in river discharge and nutrient export to a Northeastern Pacific estuary. Estuar. Coast. Shelf Sci. 73, 368–378. https://doi.org/10.1016/J.ECSS.2007.01.015
Sholkovitz, E., Herbold, C. and Charette, M., 2003. An automated dye-dilution based seepage meter for the time-series measurement of submarine groundwater discharge. Limnology and Oceanography: Methods, 1(1), 16-28.
Sikora, W. B. and B. Kjerfve. 1985. Factors influencing the salinity regime of Lake Pontchartrain, Lousiana, a shallow coastal lagoon: Analysis of a long-term data set. Estuaries 8, 170–180.
Slomp, C.P., Van Cappellen, P., 2004. Nutrient inputs to the coastal ocean through submarine groundwater discharge: Controls and potential impact. J. Hydrol. 295, 64–86. https://doi.org/10.1016/j.jhydrol.2004.02.018
Spaid, H., 2020. Contribution of Submarine Groundwater Discharge to Select Biogeochemical Fluxes in St. Louis Bay, Mississippi. Master's Thesis. The University of Southern Mississippi.
Spalt, N., Murgulet, D., Hu, X., 2018. Relating estuarine geology to groundwater discharge at an oyster reef in Copano Bay, TX. J. Hydrol. 564, 785–801. https://doi.org/10.1016/J.JHYDROL.2018.07.048
Spencer, D.W., Robertson, D.E., Turekian, K.K.T., Folsom, R., 1970. Trace element calibrations and profiles at the Geosecs Test Station in the northeast Pacific Ocean. J. Geophys. Res. 75, 7688–7696.
Stecher, H.A., Kogut, M.B., 1999. Rapid barium removal in the Delaware estuary. Geochim. Cosmochim. Acta 63, 1003–1012. https://doi.org/10.1016/s0016-7037(98)00310-x.
Sternberg, E., Tang, D.G., Ho, T.Y., Jeandel, C., Morel, F.M.M., 2005. Barium uptake and adsorption in diatoms. Geochim. Cosmochim. Acta 69, 2745–2752. https://doi.org/ 10.1016/j.gca.2004.11.026.
Stolpe, B., Guo, L.D., Shiller, A.M., Hassellov, M., 2010. Size and composition of colloidal organic matter and trace elements in the Mississippi River, Pearl River and the northern Gulf of Mexico, as characterized by flow field-flow

fractionation. Mar. Chem. 118, 119–128. https://doi.org/10.1016/j.marchem.2009.11.007.
Swarzenski, P.W., Baskaran, M., 2006. Uranium distribution in the coastal waters and pore waters of Tampa Bay, Florida. Mar. Chem. 102, 252–266. https://doi.org/10.1016/j.marchem.2006.06.016.
van Geldern, R., Barth, J.A.C., 2012. Optimization of instrument setup and post-run corrections for oxygen and hydrogen stable isotope measurements of water by isotope ratio infrared spectroscopy (IRIS). Limnol Oceanogr. Methods 10, 1024–1036. https://doi.org/10.4319/lom.2012.10.1024.
Voss, M., Baker, A., Bange, H.W., Conley, D., Deutsch, B., Engel, A., Heiskanen, A.-S., Jickells, T., Lancelot, C., McQuatters-Gollop, A., 2011. Nitrogen Processes in Coastal and Marine Ecosystems. Cambridge University Press, UK.
Waeles, M., Riso, R.D., Maguer, J.F., Le Corre, P., 2004. Distribution and chemical speciation of dissolved cadmium and copper in the Loire estuary and North Biscay continental shelf, France. Estuarine, Coastal and Shelf Science, 59(1), pp.49-57.
Wang, W.X., Meng, J., Weng, N., 2018. Trace metals in oysters: molecular and cellular mechanisms and ecotoxicological impacts. Environ. Sci. Process. Impacts 20, 892–912. https://doi.org/10.1039/C8EM00069G
Wang, Q., Wang, X., Xiao, K., Zhang, Y., Luo, M., Zheng, C., Li, H., 2021. Submarine groundwater discharge and associated nutrient fluxes in the Greater Bay Area, China revealed by radium and stable isotopes. Geosci. Front. 12, 101223. https://doi.org/10.1016/J.GSF.2021.101223
Wang, D., Xia, W., Lu, S., Wang, G., Liu, Q., Moore, W.S., Arthur Chen, C.-T., 2016. The nonconservative property of dissolved molybdenum in the western Taiwan Strait: relevance of submarine groundwater discharges and biological utilization. Geochem. Geophys. Geosyst. 17, 28–43. https://doi.org/10.1002/2014gc005708.
Wang, X., Zhang, Y., Luo, M., Xiao, K., Wang, Q., Tian, Y., Qiu, W., Xiong, Y., Zheng, C., Li, H., 2021. Radium and nitrogen isotopes tracing fluxes and sources of submarine groundwater discharge driven nitrate in an urbanized coastal area. Sci. Total Environ., 763, 144616.
Weng, N., Jiang, H., Wang, W.X., 2019. Novel Insights into the Role of Copper in Critical Life Stages of Oysters Revealed by High-Resolution NanoSIMS Imaging. Environ. Sci. Technol. 53, 14724–14733. https://doi.org/10.1021/ACS.EST.9B05877/SUPPL_FILE/ES9B05877_SI_001.PDF
Wenjuan, X., Wang, J., Liju, T., Qiulu, W., n.d. Variation of Bacteria Biomass and its Possible Controlling Factors in the East China Sea. J. Ocean Univ. China Oceanic Coast. Sea Res. https://doi.org/10.1007/s11802-011-1732-6
Wolny, J.L., Tomlinson, M.C., Schollaert Uz, S., Egerton, T.A., McKay, J.R., Meredith, A., Reece, K.S., Scott, G.P., Stumpf, R.P., 2020. Current and Future Remote Sensing of Harmful Algal Blooms in the Chesapeake Bay to Support the Shellfish Industry. Front. Mar. Sci. 7, 337. https://doi.org/10.3389/FMARS.2020.00337/BIBTEX
Yao, X., Zhang, Y., Zhang, L., Zhu, G., Qin, B., Zhou, Y., Xue, J., 2020. Emerging role

of dissolved organic nitrogen in supporting algal bloom persistence in Lake Taihu, China: Emphasis on internal transformations. Sci. Total Environ. 736, 139497. https://doi.org/10.1016/J.SCITOTENV.2020.139497

CHAPTER V – CONCLUSION

Submarine groundwater discharge has been shown to play a role in nutrient and trace metal cycles in a variety of coastal systems around the world. This dissertation examined the role of groundwater on two trace metals (Ba and U) in a coastal acid sulfate soil (CASS) system, and the role of SGD on nutrient and trace metal distributions and fluxes in the Mississippi Sound. In the Tuckean Swamp, Australia, I demonstrated that Ba and U fluxes from groundwater during flood events made up a considerable portion of total fluxes to the region in New South Wales where the Tuckean Swamp is located. In the Mississippi Sound, I used two tracers, 222Rn and radium to quantify SGD water fluxes for a nearshore time series and across the entire Sound. These water fluxes were then used to calculate the impact of SGD on nutrient and trace metal input. For both studies, the fluxes of groundwater derived constituents were compared to river fluxes, which is necessary in order to consider how important groundwater is to these fluxes on a global scale.

In Chapter 2, I assessed the importance of groundwater on Ba and U fluxes to the Tuckean Swamp during a 117 day time series. Previous work on this system has shown that the high acidity in the soils after flood events can lead to elevated trace metal levels in the surface waters, mainly through the input of metal enriched, low pH groundwaters (de Weys et al., 2011; Santos et al., 2011a). Barium and U are two trace metals that have been studied in subterranean estuaries due to their contrasting behavior, and the influence that groundwater may play in their global fluxes (Santos et al., 2011b). Calculated Ba and U fluxes out of the Tuckean Swamp were elevated compared to rivers on a square meter basis, implying that on a regional scale, CASS systems are highly important for these

fluxes. Therefore, studies that are using Ba and U as proxies for other oceanic processes in regions affected by CASS need to understand how this may affect the overall concentrations of trace metals. When extrapolating out on a global scale, CASS Ba and U fluxes were only 1.0% and 2.5%, respectively. At the moment, CASS systems only cover ~0.1% of the Earth's surface, but as demand for arable land increases, and climate change becomes more extreme, there is the likelihood for CASS coverage to increase as well. With this in mind, it is probable that these systems will cause enhancement of trace metal fluxes to the coastal ocean. To improve the understanding of acidic groundwater on the coastal ocean, studies must focus on monitoring these types of systems over extended time periods, and understand how they may play a role in regional studies. While CASS occurs globally, not many studies have examined how they may affect proxy trace metals such as Ba and U.

In Chapter 3, I used radium isotopes during a time series in the Mississippi Sound that was conducted from 2017 – 2019 to calculate the impact of SGD in locations that have previously had localized fish kills, known as 'jubilees'. Previous work in Mobile Bay indicated that 'jubilees' could be caused by anoxic groundwater input along the coastline, and it was possible a similar process may be occurring in the Sound as well (Montiel et al., 2019). During the time series, there was also an unprecedented opening of the Bonnet Carré Spillway (BCS) that caused salinity in the Sound to drop to near zero. In this study, I was able to show that while the BCS, when open, was a controlling factor on nutrient inputs, during more normal years, SGD and local rivers have changing regimes of dominance. During times of the year when river flow was low, SGD was a main source of nutrients, and when river flow was high, SGD was not as important.

Radon surveys in the western Sound showed that areas that have higher groundwater influence coincide with regions where fish kills occur, mainly right along the coastline. Additionally, there were even anomalies of higher groundwater input further offshore, where previous work has found bottom water hypoxia to occur regularly (Ho et al., 2019). The radium excess in the surface waters was used to calculate a potential oxygen demand from SGD. When the BCS was open, the influence of SGD was essentially negligible, but during times of the year when SGD input was high (summer and fall), the potential oxygen demand was nearly half of observed oxygen levels, indicating that groundwater can be an important factor in oxygen levels.

In Chapter 4, I conducted ^{222}Rn surveys across the entirety of the Mississippi Sound, which included collecting discrete samples of radium, nutrients, and trace metals. This data was used to determine differences in SGD impact between three sections of the Sound; west, central, and east, each of which have distinct river and offshore influences. The radon anomalies across the Sound showed that the western Sound had the highest SGD, and the eastern Sound had the lowest SGD. Monte Carlo analysis was used on both the ^{222}Rn and radium data to calculate a range of error on the SGD fluxes in order to constrain the high variability on the mass balance calculations. Oxygen isotopes were used to distinguish fresh and recirculated groundwater input, and found that recirculated groundwater was the majority of all SGD. SGD was highly important for DIP and NH_4^+, while local rivers dominated DON and NO_x fluxes. Distributions of nutrients were highly impacted by the opening of the BCS in 2019, and signals of the local rivers and SGD were completely wiped out, showing that the BCS can have major impacts on the Sound when open for long periods of time. Trace metal distributions and inputs were dominated

by local rivers, though distributions were impacted by both the local rivers and the BCS. This chapter also investigated why SGD was higher in the western Sound compared to the eastern Sound. Seismic and surficial sediment data indicated that several near shore incisional systems may be linked to SGD input, and that small grained surface sediments may play a role in confining SGD to the subsurface.

All three studies concluded that SGD played an important role in nutrient and/or trace metal dynamics in a coastal system. The importance of groundwater on trace metals, and how this importance may change with continued anthropogenic stressing and climate change, needs to be evaluated. Future work with more long term studies in areas affected by CASS systems would help to identify how these areas evolve with time, and how we may be able to mitigate their impacts. Future work in areas like the Mississippi Sound where nutrient and trace metal sourcing has not been fully identified would benefit from usage of isotopes, such as nitrogen, which can trace the source of dissolved constituents. Both nutrient and trace metal isotope work can help to deconvolute water mass sources, and future work in this area would benefit from this.

5.1 References

De Weys, J., Santos, I.R., Eyre, B.D., 2011. Linking groundwater discharge to severe estuarine acidification during a flood in a modified wetland. Environ. Sci. Technol. 45, 3310–3316. https://doi.org/10.1021/es104071r

Ho, P., Shim, M.J., Howden, S.D., Shiller, A.M., 2019. Temporal and spatial distributions of nutrients and trace elements (Ba, Cs, Cr, Fe, Mn, Mo, U, V and Re) in Mississippi coastal waters: Influence of hypoxia, submarine groundwater discharge, and episodic events. Cont. Shelf Res. 175, 53–69. https://doi.org/10.1016/j.csr.2019.01.013

Montiel, D., Lamore, A., Stewart, J., Dimova, N., 2019. Is Submarine Groundwater Discharge (SGD) Important for the Historical Fish Kills and Harmful Algal Bloom Events of Mobile Bay? Estuaries and Coasts 42, 470–493. https://doi.org/10.1007/s12237-018-0485-5

Santos, I.R., Burnett, W.C., Misra, S., Suryaputra, I.G.N.A., Chanton, J.P., Dittmar, T., Peterson, R.N., Swarzenski, P.W., 2011b. Uranium and barium cycling in a salt wedge subterranean estuary: The influence of tidal pumping. Chem. Geol. 287, 114–123. https://doi.org/10.1016/j.chemgeo.2011.06.005

Santos, I.R., De Weys, J., Eyre, B.D., 2011a. Groundwater or floodwater? Assessing the pathways of metal exports from a coastal acid sulfate soil catchment. Environ. Sci. Technol. 45, 9641–9648. https://doi.org/10.1021/es202581h

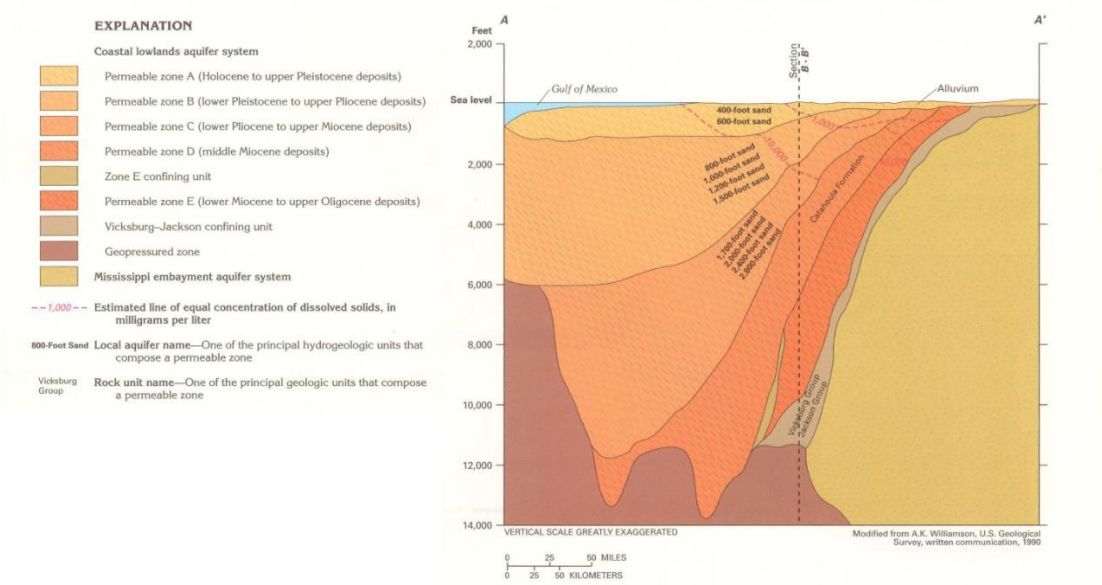

Figure A.1 *Aquifer units along coastline of Mississippi. Modified from Renken, 1998.*

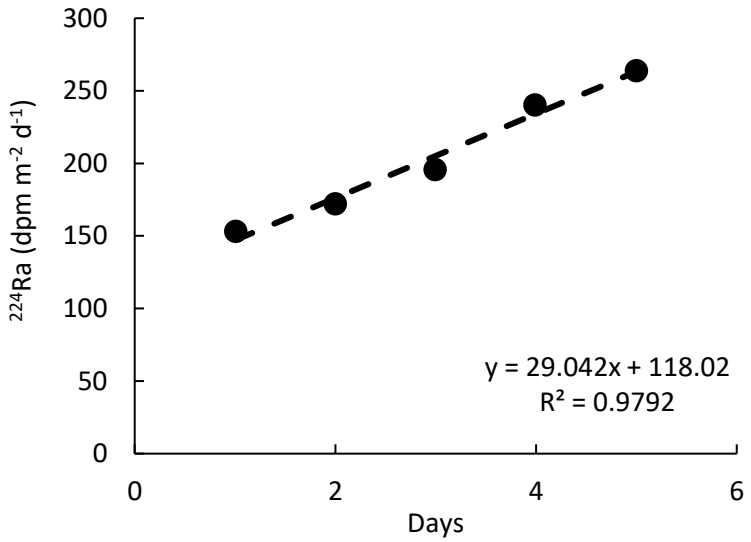

Figure A.2 *^{224}Ra (dpm m^{2} d^{-1}) diffusive flux vs days of the diffusion experiment.*

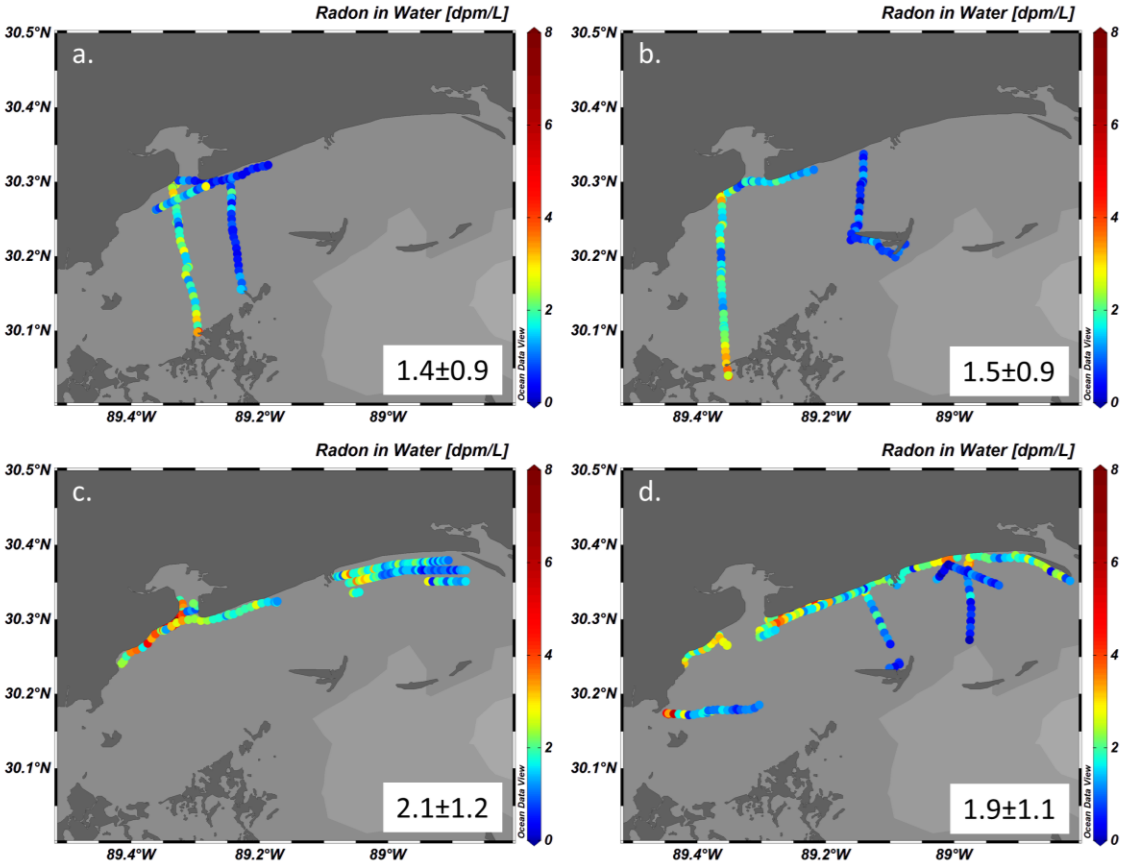

Figure A.3 *Radon in water in the western Mississippi Sound.*

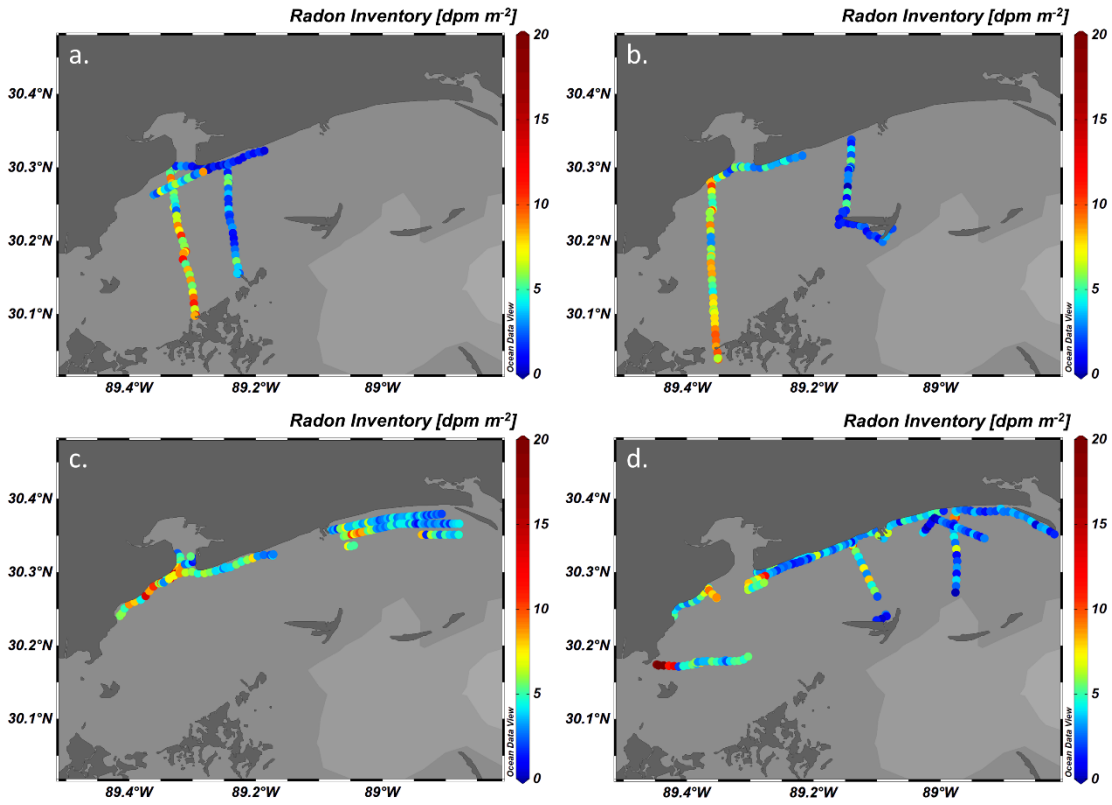

Figure A.4 *Radon inventories in the western Mississippi Sound*

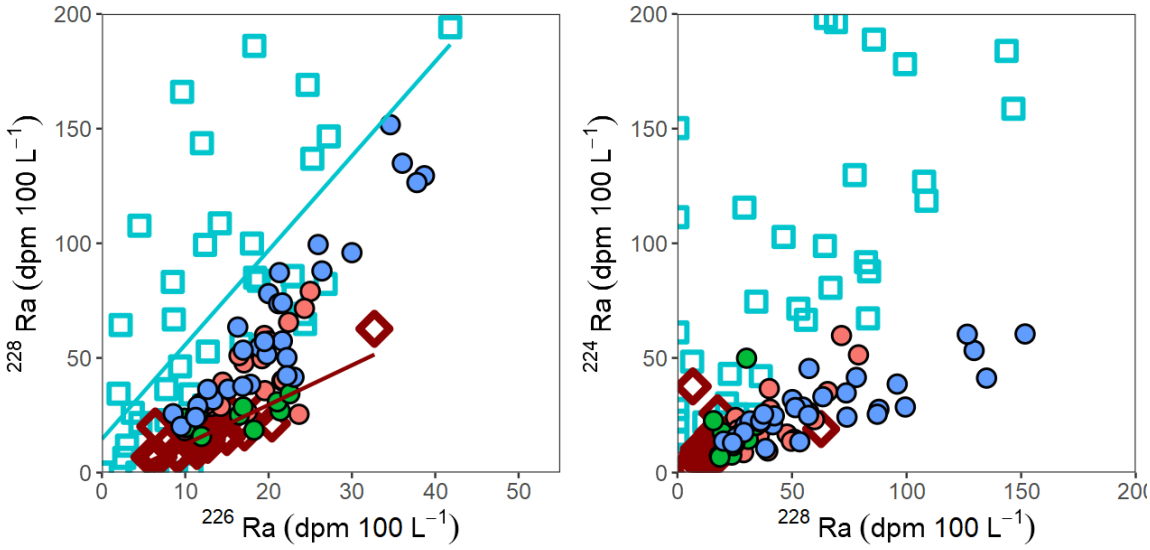

Figure B.1 *Linear axis radium activity ratios.*

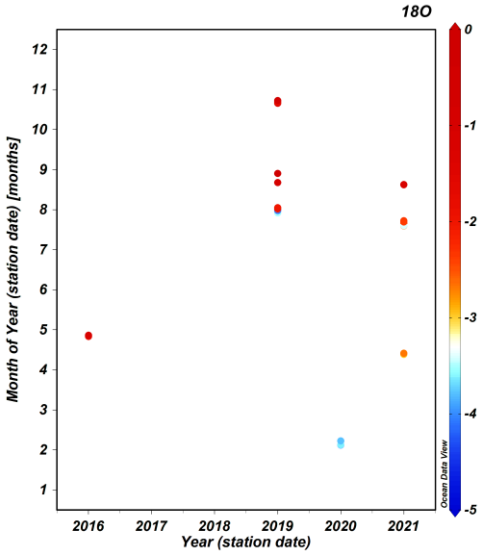

Figure B.2 *^{18}O sampling schedule.*

Table B.1 *Sound endmembers after Monte Carlo for ^{224}Ra, ^{228}Ra, salinity, and ^{222}Rn.*

	Mean	STDV	Median	IQR	25%	75%
Total Sound ^{224Ra} (dpm 100 L-1)	24.5	12	22	14	16.1	30.1
Total Sound ^{228Ra} (dpm 100 L-1)	50.2	30.5	42.9	33.2	29.4	62.6
Total Sound Salinity	14.1	8.8	11.9	9.5	8.1	17.6
Total Sound ^{222Rn} (dpm L-1)	1.5	1	1.2	1.1	0.8	1.9
West Sound ^{224Ra} (dpm 100 L-1)	25.3	11.3	23.1	13.5	17.4	30.8
West Sound ^{228Ra} (dpm 100 L-1)	63.5	33.8	56.1	38.4	40.1	78.5
West Sound Salinity	8.6	7.8	6.4	7	3.8	10.7
West Sound ^{222Rn} (dpm L-1)	1.8	1.1	1.6	1.2	1.1	2.3
Central Sound ^{224Ra} (dpm 100 L-1)	21.8	12.1	19.1	13.6	13.5	27.1
Central Sound ^{228Ra} (dpm 100 L-1)	43.2	15.6	40.6	19.3	32.1	51.4
Central Sound Salinity	21.7	4.6	21.3	6	18.5	24.5
Central Sound ^{222Rn} (dpm L-1)	1.4	0.8	1.2	0.9	0.9	1.7
East Sound ^{224Ra} (dpm 100 L-1)	23.2	9	21.6	11	16.8	27.8
East Sound ^{228Ra} (dpm 100 L-1)	25.5	4.7	25.1	6.2	22.2	28.4
East Sound Salinity	17.3	5.8	16.4	7.2	13.2	20.4
East Sound ^{222Rn} (dpm L-1)	0.7	0.6	0.5	0.5	0.3	0.8
Wet Season ^{224Ra} (dpm 100 L-1)	24.8	11.3	22.6	13.4	16.8	30.2
Wet Season ^{228Ra} (dpm 100 L-1)	55.4	30	48.7	33.9	34.6	68.5
Wet Season Salinity	9.7	7.2	7.8	7.2	5	12.2

Table B1 (continued)

Wet Season ^{222Rn} (dpm L-1)	1.3	0.9	1.1	1	0.7	1.7
Dry Season ^{224Ra} (dpm 100 L-1)	23.5	11.3	21.2	13.3	15.6	28.8
Dry Season ^{228Ra} (dpm 100 L-1)	40.7	22.4	35.7	25.2	25.2	50.5
Dry Season Salinity	18.4	8.1	16.8	9.7	12.6	22.3
Dry Season ^{222Rn} (dpm L-1)	1.6	1.2	1.3	1.2	0.9	2

Table B.2 *River, Bight, and groundwater endmembers for ^{224}Ra, ^{228}Ra, and salinity.*

	Mean	STDV	Median	IQR	25%	75%
^{224}Ra Rivers (dpm 100 L^{-1})	11.7	6.1	10.3	7	7.4	14.4
^{228}Ra Rivers (dpm 100 L^{-1})	17	8.2	15.3	9.6	11.3	20.9
Salinity Rivers	0.1	0.4	0	0.1	0	0.1
^{224}Ra Bight (dpm 100 L^{-1})	6.7	6.3	4.8	5.5	2.8	8.3
^{228}Ra Bight (dpm 100 L^{-1})	20.9	11.4	18.3	12.9	13	25.8
Salinity Bight	31.7	5	31.3	6.6	28.2	34.8
^{224}Ra GW (dpm 100 L^{-1})	163.4	169.6	113.3	138.6	63.5	202.1
^{228}Ra GW (dpm 100 L^{-1})	145.1	146	102.3	121.9	58.1	179.9
Salinity GW	7.6	7.2	5.5	6.3	3.2	9.4

Table B.3 *Nutrient endmembers for NO_x, NH_4^+, DIN, PO_4, SiO_3, and DON for the local rivers, the Mississippi River, and the groundwater.*

Nutrient (μM)	Mean	STDV	Median	IQR	25%	75%
Local River NO_x	9.5	7.3	7.6	7.2	4.8	12.0
Local River NH_4^+	2.5	1.6	2.1	1.7	1.4	3.2
Local River DIN	12.2	7.8	10.3	8.3	6.9	15.2
Local River PO_4	0.5	0.4	0.4	0.4	0.2	0.6
Local River SiO_3	34.1	47.6	19.8	30.3	9.8	40.1
Local River DON	32.5	11.4	30.7	14.2	24.3	38.6
Mississippi River NO_x	122.8	22.5	120.8	29.7	106.8	136.5
Mississippi River NH_4^+	1.6	0.3	1.6	0.4	1.4	1.8
Mississippi River DIN	124.9	22.4	122.9	29.6	109.0	138.6
Mississippi River PO_4	2.1	0.8	2.0	1.0	1.6	2.6
Mississippi River SiO_3	91.6	26.9	87.9	34.3	72.3	106.6
Mississippi River DON	107.4	124.4	70.2	93.0	37.7	130.7
FSGD NO_x	2.6	7.3	0.9	2.0	0.3	2.4
FSGD NH_4^+	29.8	64.6	12.2	25.1	5.0	30.1
FSGD DIN	35.4	69.9	16.0	30.6	6.8	37.4
FSGD PO_4	9.5	12.8	5.6	8.4	2.8	11.2
FSGD SiO_3	158.7	120.3	126.5	119.1	80.3	199.3
FSGD DON	29.0	22.6	22.9	22.1	14.4	36.5
RSGD NO_x	2.7	6.2	1.1	2.3	0.4	2.7
RSGD NH_4^+	73.9	111.1	40.7	65.5	19.5	85.0
RSGD DIN	79.7	114.1	45.5	70.8	22.3	93.1
RSGD PO_4	7.1	6.8	5.2	5.9	3.0	8.9
RSGD SiO_3	116.6	141.4	74.4	101.7	39.2	141.0
RSGD DON	29.3	33.6	19.3	25.3	10.4	35.7

Table B.4 *Monte Carlo model results.*

Water Flux (m^3 d^{-1})	Mean	STDV	Median	IQR	25%	75%	Seepage (m^3 m^{-2} d^{-1})	Mean	STDV	Median	IQR	25%	75%
Total Sound Radon	2.0E+07	1.6E+08	9.7E+06	1.7E+07	4.4E+06	2.2E+07		0.06	0.45	0.03	0.05	0.01	0.06
Total Sound Radium	1.3E+08	9.2E+10	1.8E+07	6.1E+07	-5.8E+06	5.5E+07		0.37	263	0.05	0.17	-0.02	0.16
West Sound Radon	1.4E+07	4.7E+07	7.6E+06	1.2E+07	3.7E+06	1.6E+07		0.05	0.18	0.03	0.05	0.01	0.06
West Sound Radium	2.8E+07	3.9E+10	1.9E+07	4.7E+07	3.9E+06	5.1E+07		0.11	149	0.07	0.18	0.02	0.20
Central Sound Radon	1.7E+06	2.7E+07	9.3E+05	1.5E+06	4.5E+05	1.9E+06		0.04	0.55	0.02	0.03	0.01	0.04
Central Sound Radium	2.2E+06	2.9E+09	1.9E+06	7.1E+06	-1.2E+06	5.9E+06		0.05	60	0.04	0.14	-0.02	0.12
East Sound Radon	2.4E+06	2.1E+07	8.9E+05	2.2E+06	2.6E+05	2.4E+06		0.06	0.53	0.02	0.05	0.01	0.06
East Sound Radium	2.4E+07	2.2E+10	6.7E+05	6.6E+06	-2.6E+06	3.9E+06		0.62	555	0.02	0.16	-0.07	0.10
Wet Season Radon	1.4E+07	3.7E+07	7.2E+06	1.2E+07	3.4E+06	1.5E+07		0.04	0.11	0.02	0.03	0.01	0.04

Table B4 (continued)

West Season Radium	7.0E+07	5.2E+10	2.3E+07	6.3E+07	3.3E+05	6.4E+07	0.20	149	0.06	0.18	0.00	0.18
Dry Season Radon	2.6E+07	8.2E+07	1.3E+07	2.2E+07	5.7E+06	2.8E+07	0.07	0.24	0.04	0.06	0.02	0.08
Dry Season Radium	1.3E+07	2.1E+10	1.4E+07	5.6E+07	-1.0E+07	4.6E+07	0.04	61	0.04	0.16	-0.03	0.13

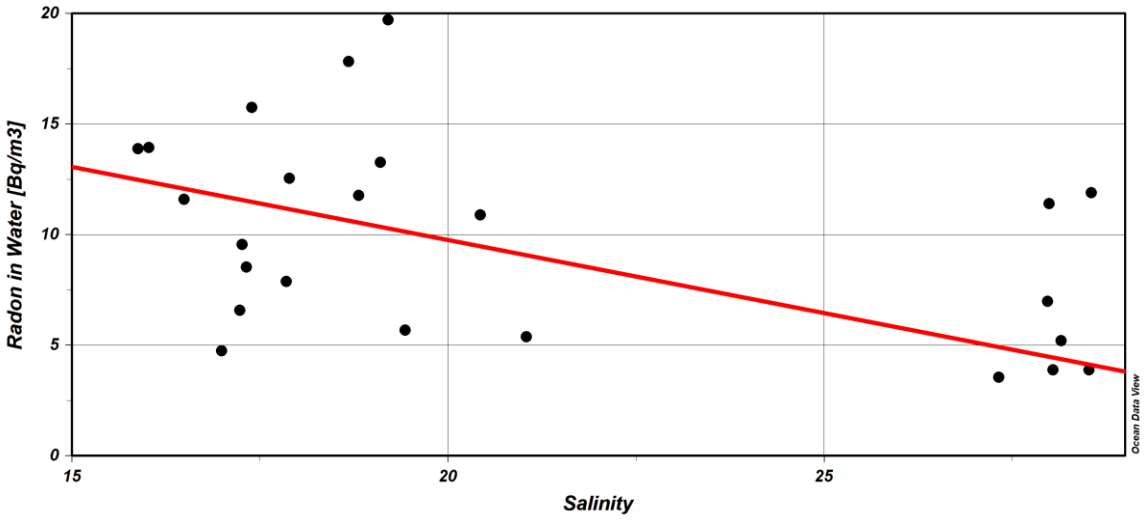

Figure B.3 *Radon vs salinity at the boundary between the Sound and Bight.*

Slope of the line is -0.661. Average Rn activity is 8.4 Bq/m3, average salinity is 22.

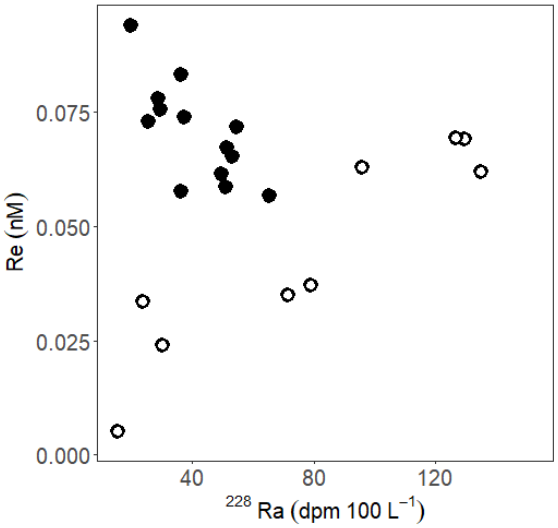

Figure B.4 *Re vs* ^{228}*Ra.*

Open circles indicate when the BCS was closed, filled circles are when the BCS was open.

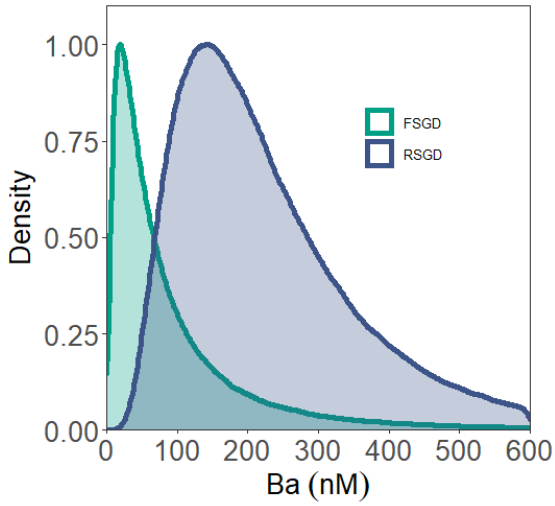

Figure B.5 *Ba distribution plot after Monte Carlo.*

Table B.5 *Trace element regression of groundwater samples.*

P<0.05 = *, p < 0.01 = **, p < 0.001 = ***, p < 0.0001 = **.

	Ba	Cd	Cs	Re	Pb	U	V	Cr	Mn	Fe	Co	Ni	Cu	Mo	As
Ba	1														
Cd	-0.09	1													
Cs	0.38**	-0.08	1												
Re	0.02	0.32	0.18	1											
Pb	-0.17	0	0.33	0.49**	1										
U	-0.17	-0.06	0.32	0.38*	0.77****	1									
V	-0.31	0.03	0.34	0.31	0.83****	0.68****	1								
Cr	-0.16	-0.04	0.36	0.39*	0.96****	0.70****	0.85****	1							
Mn	0.71****	-0.18	0.46*	-0.22	-0.19	-0.08	-0.3	-0.12	1						
Fe	0.33	0.03	0.22	0.63***	0.65***	0.43*	0.43*	0.59***	0	1					
Co	-0.14	0.90****	0.09	0.48**	0.43*	0.27	0.38*	0.39*	-0.21	0.29	1				
Ni	-0.15	0.77****	0.25	0.47**	0.51**	0.37*	0.45*	0.50**	-0.06	0.32	0.92****	1			
Cu	-0.31	0.01	0.17	0.49**	0.81****	0.55**	0.75****	0.74****	-0.34	0.48**	0.34	0.42*	1		
Mo	-0.03	-0.07	0.24	0.17	-0.08	0.43*	-0.08	-0.16	0.1	-0.12	-0.12	-0.04	-0.11	1	
As	0.99****	-0.08	0.26	0.06	-0.16	-0.17	-0.3	-0.15	0.69****	0.38*	-0.13	-0.15	-0.3	-0.1	1